Tuning Giant Magnetocaloric Materials

A Study of (Mn,Fe)2(P,Si) and NiCoMnTi Heusler Compounds

Zhang, F.

Important note
To cite this publication, please use the final published version (if applicable).
Please check the document version above.

Tuning Giant Magnetocaloric Materials

A Study of (Mn,Fe)$_2$(P,Si) and NiCoMnTi Heusler Compounds

Dissertation

for the purpose of obtaining the degree of doctor

at Delft University of Technology

by the authority of the Rector Magnificus, Prof.dr.ir. T.H.J.J. van der Hagen,

chair of the Board for Doctorates

to be defended publicly on

Monday 19 September 2022 at 10:00 o'clock

by

Fengqi ZHANG

Master of Engineering in Environmental Engineering,

South China University of Technology, Guangzhou, China

born in Shandong, China

This dissertation has been approved by the promotors.

Composition of the doctoral committee:

Rector Magnificus   chairperson

Prof. dr. E. H. Brück   Delft University of Technology, promotor

Dr. ir. N. H. van Dijk   Delft University of Technology, promotor

…………………………………………………………..

Independent members:

Prof. dr. C. Pappas   Delft University of Technology, the Netherlands

Prof. dr. F. M. Mulder   Delft University of Technology, the Netherlands

Dr. N. Dempsey   Néel Institute (CNRS), France

Prof. dr. L. Caron   Bielefeld University, Germany

Prof. dr. X. Kang   South China University of Technology, China

Prof. dr.ir. J. L. Kloosterman   Delft University of Technology, the Netherlands

Dedicated to my parents and my wife Ziying

Contents

Chapter 1 Introduction

Materials exhibiting a large magnetocaloric effect, have the potential to transform technology in several areas of applications. In this chapter, we summarize the historic development of the magnetic refrigeration technique, which is very promising to replace the present compressor based technology and has received broad attention from the research community. Here we provide the current state of research in the field. Additionally, we discuss some characteristic materials which exhibit a giant magnetocaloric effect, especially (Mn,Fe)$_2$(P,Si) based intermetallic compounds with a magnetoelastic-coupling and NiMn - based Heusler compounds with a magnetostructural-coupling. Finally, the outline of the thesis can be found at the end of this chapter.

1.1 Potential applications based on magnetocaloric materials

The magnetocaloric effect (MCE) is an intrinsic property of all magnetic materials. The magnetocaloric effect is the physical phenomenon where a magnetic material is heated or cooled when an external magnetic field is applied or removed [1, 2]. Based on this effect, several promising potential applications, such as magnetic refrigeration (cooling) [3-5], magnetocaloric heat pumps (heating) [6] and thermomagnetic generators for harvesting waste heat [7, 8] have been proposed. Amongst these applications, the magnetic refrigeration technique has a relatively long history as it was first demonstrated almost 100 years ago [9]. For low-temperature cooling (below 1 K) Giauque and MacDougall have first reached a temperature of 0.25 K by demagnetizing the paramagnetic salt $Gd(SO_4)_3 \cdot 8H_2O$ [10]. This thesis will mainly focus on heat-pumping near room temperature. Revisiting the history of magnetocaloric cooling will help us catch the lifeline of this field [11].

Experimental observations for the magnetocaloric effect started from Pierre Weiss and Auguste Piccard's work in 1917 [9]. In their experiment the magnetic field-induced heating effect had been noticed in ferromagnetic nickel around its Curie temperature ($T_C \approx 354\ ^oC$). Simultaneously, theoretical investigations on adiabatic demagnetization at low temperature had been proposed independently by Debye in 1926 [12] and by Giauque in 1927 [13]. Subsequently, the experimental realization of magnetic cooling was first reported by Giauque and MacDougall in 1933 [10]. For this important accomplishment, Giauque received the 1949 Nobel Prize in Chemistry for his work on the thermodynamic properties of substances at low temperatures. As specifically mentioned during his presentation speech, magnetic cooling makes it possible to reach temperatures nearer to absolute zero than was possible by any earlier technique [14]. Interestingly, Giauque states himself that the first successful attempt was carried out between 3 and 9 a.m. on the morning of the 19th of March, 1933. After that many researchers have worked on getting even closer to absolute zero temperature by nuclear demagnetization. Room temperature applications were left aside until the 1970s, and rare earth Gd-based prototypes had been developed [15, 16]. At the start of the 1990s there were sporadic, but influential studies that started to focus on magnetic cooling near room temperature, in systems like FeRh [17, 18] and perovskite-type manganese oxide [19]. In Mn-perovskites [19] a large magnetic entropy change (ΔS_m) of 5.5 $Jkg^{-1}K^{-1}$ was observed with an applied magnetic field change ($\Delta \mu_0 H$) of 1.5 T at 230 K. It was pointed out that this candidate material could be suitable for magnetic refrigeration near room temperature. In the same year the breakthrough in this field came by the pioneering work on the giant magnetocaloric effect (GMCE), firstly proposed by V. K. Pecharsky *et al.*, near room temperature in $Gd_5(Si_2Ge_2)$ material [3, 20].

2

Due to the stronger first-order magnetostructural coupling of the phase transition (orthorhombic to monoclinic structural transition coupled with magnetic transition) the ΔS_m of $Gd_5(Si_2Ge_2)$ can reach 18.5 $Jkg^{-1}K^{-1}$ for a field change of $\Delta\mu_0H$ = 5 T at 276 K. Surprisingly the strong first-order magnetic transition (FOMT) properties are close to reversible because of the very low thermal hysteresis (ΔT_{hys} = 2 K). After that, numerous FOMT magnetocaloric materials (MCMs) that demonstrate a GMCE have sprung up, including $(Mn,Fe)_2(P,X)$-based compounds (X = As, Ge, Si) [4], $La(Fe,Si)_{13}$-based materials [5, 21], Ni-Mn-X-based magnetic Heusler compounds (X = Ga, In, Sn, Sb) [22, 23] and Mn-M-X (M = Co, Ni and X = Si, Ge) compounds [24, 25]. In the last 25 years continuously growing interest has resulted in growing efforts in searching for FOMT MCMs. These research activities are motivated by the potential use of magnetic refrigerants near room temperature as replacement working materials for future solid-state gas-free cooling engines, which could be more environmentally-friendly and hold a higher energy efficiency compared with traditional air-compression refrigerators. As presented in **Figure. 1.1**, the total research publications and citations about "magnetocaloric" have shown a continuous growth during the last 25 years.
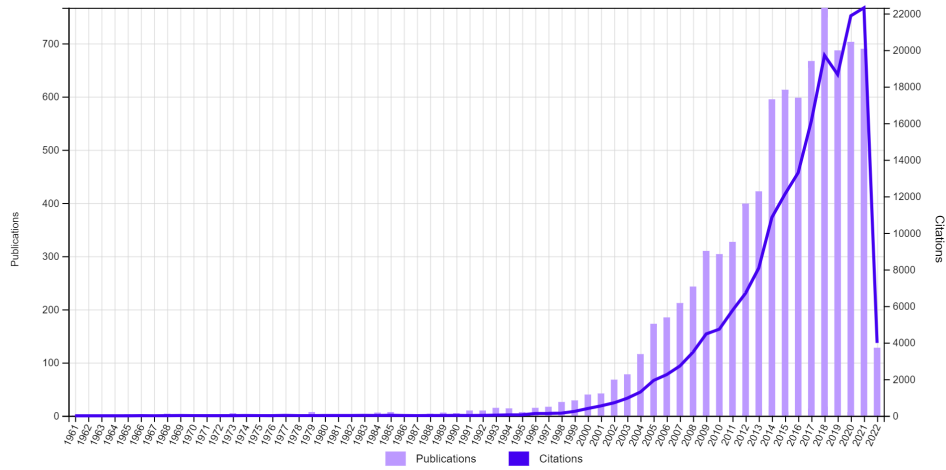
Figure 1.1 Research publications and citations for different years (Data from Web of Science, 2022).

1.2 Giant magnetocaloric materials and phase transition classification

With respect to giant magnetocaloric materials, one can approximately classify them into first-order magnetic phase transition (FOMT) and second-order magnetic phase transition (SOMT) types. Particularly, the first-order magnetic phase transition materials, which are rare in natural compounds, can be achieved by tailoring structural or elastic transitions to

couple with a magnetic transition (e.g. ferromagnetic to paramagnetic; ferromagnetic to antiferromagnetic; ferrimagnetic to antiferromagnetic). Correspondingly, these are so-called magnetostructural coupling and magnetoelastic coupling strategies. Typically, in the near room-temperature range the magnetostructurally coupled systems mainly include Gd$_5$(Si$_2$Ge$_2$) based compounds, Ni-Mn-X based Heusler compounds (X = Ga, In, Sn, Sb) and Mn-M-X based ferromagnets (M = Co, Ni and X = Si, Ge). For magnetoelastically coupled systems it can be extended to (Mn,Fe)$_2$(P,X) based compounds (X = As, Ge, Si), La(Fe,Si)$_{13}$ based materials, FeRh based and Mn$_2$Sb based compounds. In terms of practical near room temperature applications, some desirable properties should further be considered: for instance, a low heat capacity (to maximize the adiabatic temperature change (ΔT_{ad})), a relatively good thermal conductivity (rapid heat transfer), good corrosion resistance, shape-ability, low cost, toxicity and the abundance of the used elements. In addition, the magnetic and thermal hysteresis should also be regulated to minimize energy losses upon magnetic cycling. These criteria often require that the FOMT material can be tuned to its critical point, which is the border between the FOMT and SOMT, in order to combine a large magnetocaloric effect with a low hysteresis. In this thesis, different optimization strategies have been applied to reduce the hysteresis, such as nanostructuring, doping (interstitial light elements) and decoupling (SOMT), for the representative (Mn,Fe)$_2$(P,Si)-based and Ni(Co)MnTi-based compounds. The results of these experiments will be discussed in detail in the following chapters. Moreover, considering the technological routes from materials production to practical commercial application [26], as demonstrated in **Figure 1.2**, it can be estimated that the room temperature magnetic refrigeration technique is currently located at step 4 and still needs further development to approach real life application.
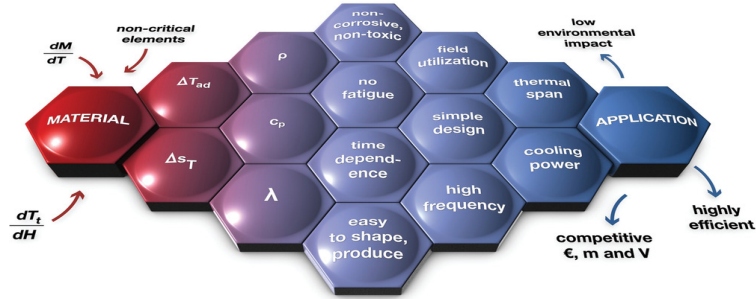
Figure 1.2 Illustration of the different challenges for room temperature magnetic refrigeration with respect to applications [26].

The benchmark material for the MCE near room temperature is pure Gd, which shows a SOMT with a good MCE performance around 294 K: $|\Delta S_m|$= 3.2(6.1) Jkg^{-1}K^{-1} and ΔT_{ad} =

2.9(5.2) K with $\Delta\mu_0H$ = 1(2) T [27]. Thus, it is also important to distinguish the difference between first-order and second-order magnetic phase transitions. According to the Ehrenfest classification [28], which defines the order of the transition by whether the first or second order derivative of the Gibbs energy G exhibits a discontinuity. As shown in **Figure 1.3**, the volume V, enthalpy H_E, entropy S, heat capacity C_p and magnetization M as a function of the temperature T for the first-order and second-order phase transition are compared. It is obvious that for first-order magnetic phase transitions the first order derivatives of these variables show a discontinuity at the transition temperature T_0, while for comparison the first order derivatives of second order transitions change smoothly at T_0. Therefore, based on the above properties magnetic or thermodynamic measurements allow us to distinguish the difference between these two types of phase transition. For the transition at critical point several theoretical evaluation methods based on different models can be utilized. For example, the Banerjee criterion and ΔS_m-H relations (Bean–Rodbell model [29] or the Landau model [30])
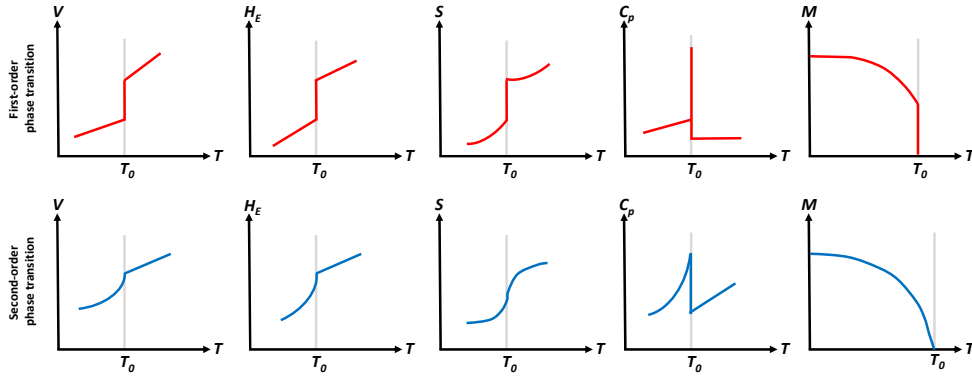
Figure 1.3 Volume V, enthalpy H_E, entropy S, heat capacity C_p and magnetization M for the first-order and second-order phase transition.

1.3 Typical magneto-coupling giant magnetocaloric materials

1.3.1 Fe$_2$P-type (Mn,Fe)$_2$(P,Si) based materials

Although the first-row transition metal elements (Ti to Zn) are chemically simple, the overlapping of partially filled 3d and 4s bands provides them uniqueness and complexity [31]. For example, for the transition-metal systems $(M_{1-x},M'_x)_2X$, where X= P, As or Sb and M, M' are first-row transition elements, some interesting physical properties have been discovered. Goodenough pointed out that the itinerant electron model of this system assumes that only the 3d bands have a finite density of states at the Fermi level, whereas

the $4s$ band is empty [31]. On the other hand, the magnetic properties only reflect the number of $3d$ electrons per transition metal atom, and the existence of metalloids can sufficiently stabilize the material systems. The Fe_2P prototype material, a strongly anisotropic hexagonal ferromagnet (space group *P-62m*) [32], shows a first-order ferromagnetic transition with a T_C at around 216 K [33, 34]. As one of the derivatives of Fe_2P the magnetic and structural properties of quarternary $(Mn,Fe)_2(P,As)$ compounds were studied by Fruchart and co-workers [35, 36]. The MCE properties of the $(Mn,Fe)_2(P,As)$ compounds were originally studied by Brück and co-workers in 2000 [4]. Within this work the $(Mn,Fe)_2(P_{0.45}As_{0.55})$ compound was found to present a giant magnetocaloric effect at the transition from the low-temperature ferromagnetic (FM) state to the high-temperature paramagnetic (PM) state with a large ΔS_m (at about 300 K) of 14.5 $Jkg^{-1}K^{-1}$ and 18.0 $Jkg^{-1}K^{-1}$ for $\Delta\mu_0H$ of 2 T and 5 T, respectively [4]. Subsequently, in response to the requirement of removing the toxic arsenic content, different $(Mn,Fe)_2(P,X)$ based intermetallic compounds (X = Ge, Si) have been developed. For instance, the so-called second generation $(Mn,Fe)_2(P,Ge)$ and third generation $(Mn,Fe)_2(P,Si)$ alloys were produced in 2007 and 2008, respectively [37, 38]. Interestingly, the GMCE performance was almost kept stable after the metalloids replacement of As by Ge/Si [39, 40]. Compared with other giant magnetocaloric materials some advantages can be highlighted: an excellent GMCE performance, rare-earth free, relative low economic costs and the absence of toxic elements. More valuable characteristics of this series of compounds are the tunable Curie temperature and the easily reduced hysteresis by compositional optimization. Simultaneously, an improved understanding of the physical mechanism associated with this strong magnetoelastic coupling in GMCE $(Mn,Fe)_2(P,Si)$ based materials has been achieved. On the one hand, from the fundamental crystal structure aspect, the site occupancy of different atoms have been distinguished unambiguously, as demonstrated in **Figure 1.4**. Mn atoms prefer the $3g$ site and Fe atoms prefer the $3f$ site while P/Si atoms randomly distribute on the $1b/2c$ sites (for the Si-rich case Si atoms show a preference for the $2c$ site) [41]. On the other hand, from theoretical investigations the so-called "mixed magnetism" mechanism has been found to be responsible for the GMCE in the $(Mn,Fe)_2(P,Si)$ based MCMs. The crystallographic $3g$ and $3f$ sites of the hexagonal lattice, represent layers with relatively large stable Mn magnetic moments and relatively weak unstable Fe magnetic moments, respectively. The latter shows an interesting "moment-quenching" property across the magnetic transition, as indicated by density functional theory (DFT) [40], neutron diffraction (ND) [41, 43] and X-ray magnetic circular dichroism (XMCD) [44]. Combined DFT calculations and synchrotron high-resolution X-ray diffraction (HRXRD) [45] experiments show a significant electronic charge redistribution around the Fe atoms across the ferromagnetic transition, which was attributed to the competition between magnetism and covalent bonding. Moreover, it is

6

found that the change in the c/a ratio of the hexagonal unit cell is closely related to thermal hysteresis, which could be ascribed to a change in the transition-induced elastic strain energy [46]. Finally, returning to the material properties, typical advantages and disadvantages of $(Mn,Fe)_2(P,Si)$ based MCMs are presented in **Figure 1.5**. Remaining weaknesses of these materials are the intrinsic brittleness and the relatively low thermal conductivity.
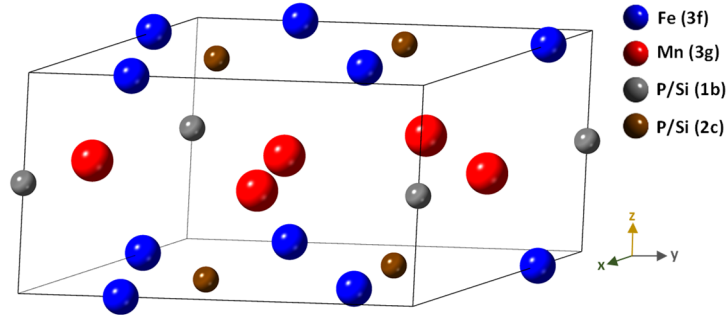
Figure 1.4 Schematic representation of the crystal structure for the $(Mn,Fe)_2(P,Si)$ based MCMs.
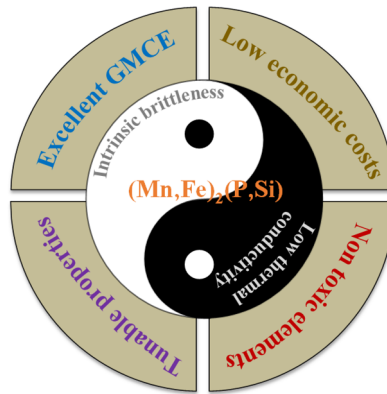
Figure 1.5 Schematic figure related to typical advantages and disadvantages of material properties about $(Mn,Fe)_2(P,Si)$ based MCMs.

1.3.2 Ni-Mn-X based magnetic Heusler compounds (X = Ga, In, Sn, Sb)

The Heusler compounds, X_2YZ (where X, Y are transition metals and Z is a main-group element), are well known for their multi-functional properties: shape memory effect, superelasticity, magneto-optical effect, magnetocaloric effect, spin polarization,

superconductivity, thermoelectric effect, topological insulators, *etc.* [47, 48]. This material family started from the discovery of the Cu_2MnAl ferromagnet in 1903 by the Germany scientist Fritz Heusler [49] and nowadays it has been expanded to more than 1000 related-compounds. As presented in **Figure 1.6**, the Heusler compounds X_2YZ always crystallize in the fcc cubic $Fm\overline{3}m$ structure (space group 225) with the highly ordered $L2_1$ structure. For the fully stoichiometric Heusler compounds, the X atoms occupy the 8*c* (¼, ¼, ¼), while the Y and the Z atoms preferentially occupy the 4*a* (0, 0, 0) and 4*b* (½, ½, ½) sites, respectively. When a magnetic field is applied or when the temperature is changed, a martensitic transition can be triggered due to the magnetic difference between the weakly magnetic (paramagnetic or antiferromagnetic) martensite and strongly magnetic (ferromagnetic) austenite. The change in Zeeman energy ($E_{Zeeman} = -\mu_0 \int MH\, dV$, where M is the-magnetization, V the- cell volume and H the- external magnetic field) will destabilize the system and make the martensitic or inverse martensitic (diffusionless) phase transition happen, as illustrated in **Figure 1.7**. Note that different chemical compositions could generate different low-temperature modulated and non-modulated (NM) martensite structures [50]. A giant magnetocaloric effect was already reported in poly-crystalline [51] and in single-crystalline [52] NiMnGa materials, before an inverse giant magnetocaloric effect was found by Krenke and co-workers [53]. The $|\Delta S_m|$ value of single crystalline $Ni_{52.6}Mn_{23.1}Ga_{24.3}$ can reach 18.0 $Jkg^{-1}K^{-1}$ for $\Delta\mu_0H$ of 5 T at 300 K [52]. Later on, more NiMn-based MCMs like NiMnIn/Sb [54-56] and NiMnSn -based [57] Heusler compounds have been discovered. In this thesis, we mainly focus on the another novel group of Heusler compounds- coined as the all-*d*-metal Ni(Co)MnTi system because they contain no main group elements. They are stabilized by covalent *d-d* hybridization, rather than *p-d* hybridization between transition elements and main-group elements [58].
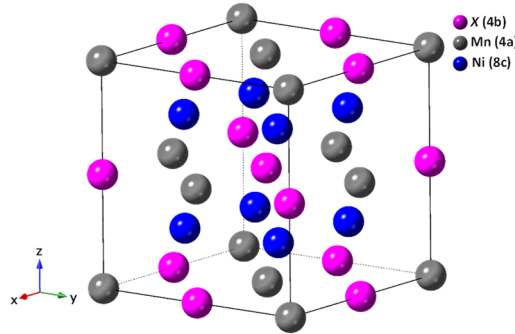
Figure 1.6 Schematic representation of the fcc cubic $Fm\overline{3}m$ structure (space group 225) for Ni-Mn-*X* based magnetic Heusler compounds (*X* = Ga, In, Sn, Sb), where the 4*a* site (0,0,0) is occupied by Mn, the 4*b* site (½, ½, ½) is occupied by *X*, and the 8*c* site (¼, ¼, ¼) by Ni.
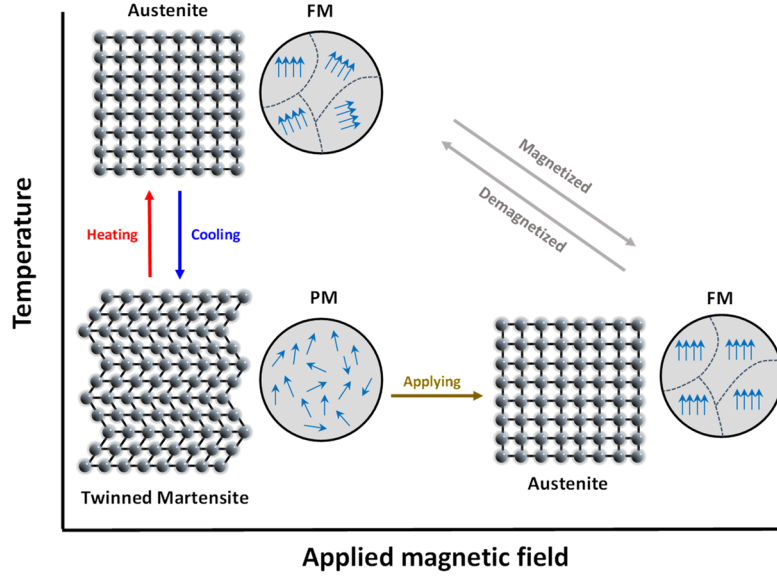
Figure 1.7 Schematic figures of the temperature- and magnetic field-induced martensitic transformation for Ni-Mn-*X* based magnetic Heusler compounds (*X* = Ga, In, Sn, Sb).

1.5 Outline of this thesis

The main aim of this thesis is to systematically study the fundamental physical (thermodynamics, magnetic and (micro)structural) properties among magnetoelastic and magnetostructural giant MCMs.

In **Chapter 2**, the experimental methods and techniques, as well as the theoretical background for the MCE, will be introduced.

In **Chapter 3**, different from the traditional bulk materials, it is of interest to investigate how the magnetoelastic coupling changes under low dimension (nano-scale) and the corresponding (micro)structure changes for nanoscale particle size for $(Mn,Fe)_2(P,Si)$ based MCMs. This has been done by applying a "top-down" method, which also allows us to further extend the potential applications of these materials into nanoscale scenarios.

In **Chapter 4**, we explore the influence of doping with light elements like fluorine and sulfur on the change of the magnetic transition temperature T_C and the magnetocaloric properties for $(Mn,Fe)_2(P,Si)$ based MCMs. For this metal-metalloid itinerant-electron system, the effect of F and S doping is studied by neutron diffraction and first-principle theoretical

calculations. The aim is to unravel how the strong electronegativity of these elements influences these functional materials.

In **Chapter 5**, we propose a decoupling strategy to separate the magnetostructural coupling and then aim to achieve a single second-order magnetic transition (SOMT) in all-*d*-metal NiCoMnTi based Heusler compounds. By optimizing the ratio among different metallic elements and by doping (e.g. Cu), the transition temperature T_C and the saturation magnetization M_S can be controlled adequately. Compositional maps for T_C and M_S have been established experimentally. By combining XRD, SQUID, SEM experiments and DFT calculations, the (micro)structural and magnetocaloric properties have been investigated systematically.

In **Chapter 6**, we investigate the influence of interstitial boron atoms on the magnetocaloric properties for NiCoMnTi based Heusler compounds. The obtained significant reduction in the thermal hysteresis ΔT_{hys} and increase in M_S are attributed to an enhancement of the GMCE. Due to the very low ΔT_{hys} the reversibility of MCE cycles exhibits a superior MCE performance compared with traditional magnetic Heusler compounds. Together with the experimental results, first-principles calculation clarifies the atomic occupancy of boron and the changes in the electronic configuration.

10

References

[1] O. Gutfleisch, M.A. Willard, E. Brück, C.H. Chen, S.G. Sankar, J.P. Liu, Magnetic materials and devices for the 21st century: Stronger, lighter, and more energy efficient, *Adv Mater* 23 (2011) 821-842.

[2] V. Franco, J.S. Blazquez, J.J. Ipus, J.Y. Law, L.M. Moreno-Ramirez, A. Conde, Magnetocaloric effect: From materials research to refrigeration devices, *Prog Mater Sci* 93 (2018) 112-232.

[3] V.K. Pecharsky, K.A. Gschneidner, Giant magnetocaloric effect in $Gd_5(Si_2Ge_2)$, *Phys Rev Lett* 78 (1997) 4494-4497.

[4] O. Tegus, E. Brück, K.H.J. Buschow, F.R. de Boer, Transition-metal-based magnetic refrigerants for room-temperature applications, *Nature* 415 (2002) 150-152.

[5] F.X. Hu, B.G. Shen, J.R. Sun, X.X. Zhang, Great magnetic entropy change in $La(Fe, M)_{13}(M = Si, Al)$ with Co doping, *Chinese Phys* 9 (2000) 550-553.

[6] H. Johra, K. Filonenko, P. Heiselberg, C. Veje, S. Dall'Olio, K. Engelbrecht, C. Bahl, Integration of a magnetocaloric heat pump in an energy flexible residential building, *Renew Energ* 136 (2019) 115-126.

[7] M. Gueltig, F. Wendler, H. Ossmer, M. Ohtsuka, H. Miki, T. Takagi, M. Kohl, High-performance thermomagnetic generators based on Heusler alloy films, *Adv Energy Mater* 7 (2017) 1601879.

[8] A. Waske, D. Dzekan, K. Sellschopp, D. Berger, A. Stork, K. Nielsch, S. Fahler, Energy harvesting near room temperature using a thermomagnetic generator with a pretzel-like magnetic flux topology, *Nat Energy* 4 (2019) 68-74.

[9] P. Weiss, A. Piccard, Le phénomène magnétocalorique, *Journal of Theoretical and Applied Physics* 7 (1917) 103-109.

[10] W.F. Giauque, D.P. MacDougall, Attainment of temperatures below 1 degrees absolute by demagnetization of $Gd_2(SO_4)_3 \cdot 8H_2O$, *Phys Rev* 43 (1933) 0768-0768.

[11] A. Smith, Who discovered the magnetocaloric effect?, *Eur Phys J H* 38 (2013) 507-517.

[12] P. Debye, Einige bemerkungen zur magnetisierung bei tiefer temperatur, *Annalen der Physik* 386 (1926) 1154-1160.

[13] W.F. Giauque, A thermodynamic treatment of certain magnetic effects. A proposed method of producing temperatures considerably below 1° absolute, *J Am Chem Soc* 49 (1927) 1864-1870.

[14] A. Tiselius, Nobel prize in chemistry, Presentation Speech: Nobel prize chem (1949).

[15] G. V. Brown, Magnetic heat pumping near room temperature, *J App Phy* 47 (1976) 3673.

[16] S. S. Rosenblum, W. A. Steyert, W. P. Pratt, Jr., A continuous magnetic refrigerator operating near room temperature, Los Alamos National Lab (LANL) (1977).

[17] M.P. Annaorazov, K.A. Asatryan, G. Myalikgulyev, S.A. Nikitin, A.M. Tishin, A.L. Tyurin, Alloys of the FeRh system as a new class of working material for magnetic refrigerators, *Cryogenics* 32 (1992) 867-872.

[18] M.P. Annaorazov, S.A. Nikitin, A.L. Tyurin, K.A. Asatryan, A.K. Dovletov, Anomalously high entropy change in FeRh alloy, *J Appl Phys* 79 (1996) 1689-1695.

[19] Z.B. Guo, Y.W. Du, J.S. Zhu, H. Huang, W.P. Ding, D. Feng, Large magnetic entropy change in perovskite-type manganese oxides, *Phys Rev Lett* 78 (1997) 1142-1145.

[20] V.K. Pecharsky, Karl A. Gschneidner Jr (1930–2016), *Nature Mater* 15 (2016) 1059-1059.

[21] F.X. Hu, B.G. Shen, J.R. Sun, Z.H. Cheng, G.H. Rao, X.X. Zhang, Influence of negative lattice expansion and metamagnetic transition on magnetic entropy change in the compound $LaFe_{11.4}Si_{1.6}$, *Appl Phys Lett* 78 (2001) 3675-3677.

[22] A. Planes, L. Mañosa, M. Acet, Magnetocaloric effect and its relation to shape-memory properties in ferromagnetic Heusler alloys, *J Phys-Condens Mat* 21 (2009) 233201.

[23] J. Liu, T. Gottschall, K.P. Skokov, J.D. Moore, O. Gutfleisch, Giant magnetocaloric effect driven by structural transitions, *Nature Materials* 11 (2012) 620-626.

[24] N.T. Trung, L. Zhang, L. Caron, K.H.J. Buschow, E. Brück, Giant magnetocaloric effects by tailoring the phase transitions, *Appl Phys Lett* 96 (2010) 172504.

[25] E.K. Liu, W.H. Wang, L. Feng, W. Zhu, G.J. Li, J.L. Chen, H.W. Zhang, G.H. Wu, C.B. Jiang, H.B. Xu, F. de Boer, Stable magnetostructural coupling with tunable magnetoresponsive effects in hexagonal ferromagnets, *Nat Commun* 3 (2012) 873.

[26] T. Gottschall, K.P. Skokov, M. Fries, A. Taubel, I. Radulov, F. Scheibel, D. Benke, S. Riegg, O. Gutfleisch, Making a cool choice: the materials library of magnetic refrigeration, *Adv Energy Mater* 9 (2019) 1901322.

[27] J. Lyubina, Magnetocaloric materials for energy efficient cooling, *J Phys D Appl Phys* 50 (2017) 053002.

[28] G. Jaeger, The Ehrenfest classification of phase transitions: Introduction and evolution, *Arch Hist Exact Sci* 53 (1998) 51-81.

[29] J.Y. Law, V. Franco, L.M. Moreno-Ramirez, A. Conde, D.Y. Karpenkov, I. Radulov, K.P. Skokov, O. Gutfleisch, A quantitative criterion for determining the order of magnetic phase transitions using the magnetocaloric effect, *Nat Commun* 9 (2018) 2680.

[30] N.H. van Dijk, Landau model evaluation of the magnetic entropy change in magnetocaloric materials, *J Magn Magn Mater* 529 (2021) 167871.

[31] J.B. Goodenough, Interpretation of structure and magnetism in transition-metal pnictides M_2X and $(M_{1-x}M'_x)_2X$, *J Solid State Chem* 7 (1973) 428-447.

[32] S. Rundqvist, F. Jellinek, The structures of Ni_6Si_2B, Fe_2P and related phases, *Acta Chemica Scandinavica* 13 (1959) 425-432.

[33] R. Wappling, L. Haggstrom, T. Ericsson, S. Devanarayanan, E. Karlsson, B. Carlsson, S. Rundqvist, First-order magnetic transition, magnetic-structure, and vacancy distribution in Fe_2P, *J Solid State Chem* 13 (1975) 258-271.

[34] L. Lundgren, G. Tarmohamed, O.f. Beckman, B. Carlsson, S. Rundqvist, First order magnetic phase transition in Fe_2P, *Physica Scripta* 17 (1978) 39-48.

[35] R. Zach, M. Guillot, R. Fruchart, The influence of high magnetic fields on the first order magneto-elastic transition in $MnFe(P_{1-y}As_y)$ systems, *J Magn Magn Mater* 89 (1990) 221-228.

[36] M. Bacmann, J.L. Soubeyroux, R. Barrett, D. Fruchart, R. Zach, S. Niziol, R. Fruchart, Magnetoelastic transition and antiferro-ferromagnetic ordering in the system $MnFeP_{1-y}As_y$, *J Magn Magn Mater* 134 (1994) 59-67.

[37] D.T.C. Thanh, E. Brück, O. Tegus, J.C.P. Klaasse, K.H.J. Buschow, Influence of Si and Ge on the magnetic phase transition and magnetocaloric properties of MnFe(P,Si,Ge), *J Magn Magn Mater* 310(2) (2007) e1012-e1014.

13

[38] D.T.C. Thanh, E. Brück, N.T. Trung, J.C.P. Klaasse, K.H.J. Buschow, Z.Q. Ou, O. Tegus, L. Caron, Structure, magnetism, and magnetocaloric properties of $MnFeP_{1-x}Si_x$ compounds, *J Appl Phys* 103 (2008) 07B318.

[39] N.T. Trung, Z.Q. Ou, T.J. Gortenmulder, O. Tegus, K.H.J. Buschow, E. Brück, Tunable thermal hysteresis in MnFe(P,Ge) compounds, *Appl Phys Lett* 94 (2009) 102513.

[40] F. Guillou, G. Porcari, H. Yibole, N. van Dijk, E. Brück, Taming the first-order transition in giant magnetocaloric materials, *Adv Mater* 26 (2014) 2671-2675.

[41] X.F. Miao, L. Caron, P. Roy, N.H. Dung, L. Zhang, W.A. Kockelmann, R.A. de Groot, N.H. van Dijk, E. Brück, Tuning the phase transition in transition-metal-based magnetocaloric compounds, *Phys Rev B* 89 (2014) 174429.

[42] N.H. Dung, Z.Q. Ou, L. Caron, L. Zhang, D.T.C. Thanh, G.A. de Wijs, R.A. de Groot, K.H.J. Buschow, E. Brück, Mixed magnetism for refrigeration and energy conversion, *Adv Energy Mater* 1 (2011) 1215-1219.

[43] N.H. Dung, L. Zhang, Z.Q. Ou, L. Zhao, L. van Eijck, A.M. Mulders, M. Avdeev, E. Suard, N.H. van Dijk, E. Brück, High/low-moment phase transition in hexagonal Mn-Fe-P-Si compounds, *Phys Rev B* 86 (2012) 045134.

[44] H. Yibole, F. Guillou, L. Caron, E. Jimenez, F.M.F. de Groot, P. Roy, R. de Groot, N.H. van Dijk, E. Brück, Moment evolution across the ferromagnetic phase transition of giant magnetocaloric $(Mn, Fe)_2(P, Si,B)$ compounds, *Phys Rev B* 91 (2015) 014429.

[45] M.F.J. Boeije, P. Roy, F. Guillou, H. Yibole, X.F. Miao, L. Caron, D. Banerjee, N.H. van Dijk, R.A. de Groot, E. Brück, Efficient room-temperature cooling with magnets, *Chem Mater* 28 (2016) 4901-4905.

[46] P. Roy, E. Torun, R.A. de Groot, Effect of doping and elastic properties in $(Mn,Fe)_2(Si,P)$, *Phys Rev B* 93 (2016) 094110.

[47] T. Graf, C. Felser, S.S.P. Parkin, Simple rules for the understanding of Heusler compounds, *Prog Solid State Ch* 39 (2011) 1-50.

[48] C. Felser, A. Hirohata, Heusler alloys properties, growth, applications preface, *Springer Ser Mater S* 222 (2016) book.

[49] F. Heusler, Über magnetische manganlegierungen, *Verh. DPG* 5 (1903) 219.

[50] X.Z. Liang, X.J. Jiang, J.L. Gu, J. Bai, Z.Q. Guan, Z.Z. Li, H.L. Yan, Y.D. Zhang, C. Esling, X. Zhao, L. Zuo, 5M and 7M martensitic stability and associated physical properties in $Ni_{50}Mn_{35}In_{15}$ alloy: first-principles calculations and experimental verification, *Scripta Mater* 204 (2021) 114140.

[51] F.X. Hu, B.G. Shen, J.R. Sun, Magnetic entropy change in $Ni_{51.5}Mn_{22.7}Ga_{25.8}$ alloy, *Appl Phys Lett* 76 (2000) 3460-3462.

[52] F.X. Hu, B.G. Shen, J.R. Sun, G.H. Wu, Large magnetic entropy change in a Heusler alloy $Ni_{52.6}Mn_{23.1}Ga_{24.3}$ single crystal, *Phys Rev B* 64 (2001) 132412.

[53] K.G. Sandeman, S. Takei, Magnetocaloric materials and applications, Handbook of Magnetism and Magnetic Materials, Springer International Publishing, Cham, 2020, pp. 1-38.

[54] Y. Sutou, Y. Imano, N. Koeda, T. Omori, R. Kainuma, K. Ishida, K. Oikawa, Magnetic and martensitic transformations of NiMnX (X=In,Sn,Sb) ferromagnetic shape memory alloys, *Appl Phys Lett* 85 (2004) 4358-4360.

[55] R. Kainuma, Y. Imano, W. Ito, Y. Sutou, H. Morito, S. Okamoto, O. Kitakami, K. Oikawa, A. Fujita, T. Kanomata, K. Ishida, Magnetic-field-induced shape recovery by reverse phase transformation, *Nature* 439 (2006) 957-960.

[56] Z.D. Han, D.H. Wang, C.L. Zhang, S.L. Tang, B.X. Gu, Y.W. Du, Large magnetic entropy changes in the $Ni_{45.4}Mn_{41.5}In_{13.1}$ ferromagnetic shape memory alloy, *Appl Phys Lett* 89 (2006) 182507.

[57] T. Krenke, E. Duman, M. Acet, E.F. Wassermann, X. Moya, L. Mañosa, A. Planes, Inverse magnetocaloric effect in ferromagnetic Ni-Mn-Sn alloys, *Nature Mater* 4 (2005) 450-454.

[58] Z.Y. Wei, E.K. Liu, J.H. Chen, Y. Li, G.D. Liu, H.Z. Luo, X.K. Xi, H.W. Zhang, W.H. Wang, G.H. Wu, Realization of multifunctional shape-memory ferromagnets in all-*d*-metal Heusler phases, *Appl Phys Lett* 107 (2015) 022406.

Chapter 2 Experimental techniques and theoretical background

This thesis mainly focuses on the magnetoelastic-coupling type (Mn,Fe)$_2$(P,Si) based intermetallic compounds and the magnetostructural-coupling type all-d-metal Ni(Co)MnTi-based Heusler compounds. In this chapter, the experimental techniques with regard to sample preparation, (micro)structural- and, magnetic- characterization will be introduced. In addition some theoretical background about the magnetocaloric effect is presented.

High-energy ball milling and vacuum arc-melting techniques in combination with subsequent heat treatments are powerful methods to synthesize good quality polycrystalline alloys. X-ray diffraction provides insight into the crystal-structure changes associated with the phase transition. Supplementary neutron diffraction can determine the magnetic structure and resolve the sublattice magnetic moments. The magnetic properties, like the magnetocaloric performance, can be characterized by magnetometry (SQUID and VSM). To further explore the processing-structure-property relationship for magnetic phase transition materials, microstructural characterization like SEM and TEM, and quantum mechanical calculations have been applied. The combination of these experimental techniques and theoretical modelling can provide insight and provides the basic framework for the magnetocaloric materials in different material systems.

17

2.1 Experimental techniques

2.1.1 Sample preparation

a. High-energy ball milling

In the field of powder metallurgy, high-energy ball milling (HEBM) is a mechanical deformation process that is frequently used to produce nanocrystalline metals or powdered alloys (so-called pre-alloying process). The synthesis of materials by HEBM of powders was first developed by John Benjamin (1970) and his co-workers at the International Nickel Company in the late 1960's [1]. The kinetics of HEBM strongly depends on the energy transferred from the balls to the powder during high-speed milling. Generally speaking, the energy transfer is governed by many parameters such as the type of mill (planetary, vibratory), the total powder mass in one milling jar, the milling speed, the milling time, the ball-sample ratio, the conditions of milling (protective atmosphere, certain working temperature, dry or wet condition). One advantage of the HEBM technique is that it is relatively simple and has high potential to scale up to produce large quantities (metric tons or more) of materials, which is appealing for industrial production. The schematic view of a high-energy ball milling device is shown in **Figure. 2.1.1**.

In this thesis, a planetary high-energy ball mill (PM400, MA-type, Retsch) was used to synthesize $(Mn,Fe)_2(P,Si)$-type compounds. The detailed synthesis methods can be found in **Chapters 3** and **4**. The starting raw materials were grinded in tungsten-carbide jars (V ≈ 380 ml) with tungsten-carbide balls (m ≈ 8 g) under argon atmosphere to prevent surface oxidation during production. Note that a protective atmosphere is especially important for nano-materials. A ball-milling time of 10 hours (in 15 minutes milling intervals separated by 10 minutes cool-down periods) at a rotation speed of 380 rpm was chosen.
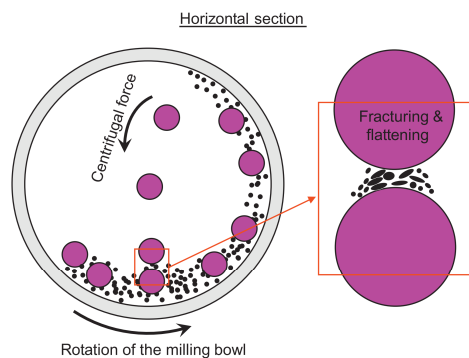
Figure 2.1.1 Schematic view of the high-energy ball milling [2].

b. Plasma-arc-melting

Plasma-arc-melting is an electro-thermal metallurgical method that uses electric energy to generate a discharge plasma arc between the water-cooled electrode and the material lying on a water-cooled Cu crucible under a protective Ar atmosphere, which can melt metals and alloys at temperatures in excess of 3000°C. Arcs can be generated with direct current or alternating current. For our home-built arc-melter a DC power supply is used to produce stable arcs [3]. Meanwhile, a non-consumable tungsten (W) electrode is used. In this thesis, the arc-melting technique is mainly utilized to synthesize NiMn-based Heusler compounds. More experimental details about the melting process can be found in **Chapters 5** and **6**. The melted ingot is flipped and re-melted several times to guarantee homogeneity of the sample, and then quickly cooled down to room temperature within minutes. The experimental arc-melting set-up is presented in **Figure 2.1.2**.
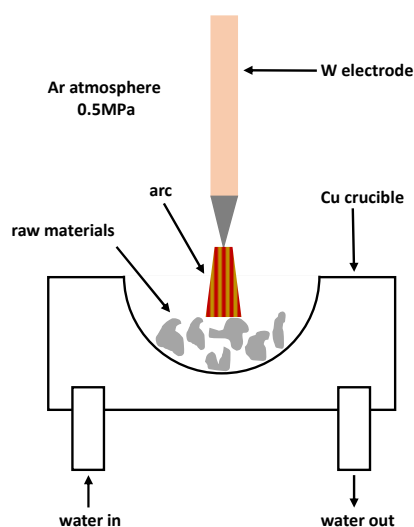
Figure 2.1.2. Experimental set-up of the arc-melting technique.

c. Heat treatment

After samples were produced by ball-milling or arc-melting, often certain heat treatments are required to make samples more homogeneous. First, the samples are sealed in quartz ampoules under an Ar atmosphere of 200 mbar, and then the samples are put into vertical electrical-furnaces for a holding time ranging from several hours up to several days. Finally, these annealed samples are quickly quenched by dropping them into cold water.

19

2.1.2 Structural and thermal-dynamic measurements

a. X-ray diffraction

X-ray diffraction is a nondestructive technique used to determine the atomic crystal structure of inorganic/organic compounds. After fitting the XRD patterns by Rietveld analysis the crystal information can be derived, including the lattice parameters, the preferential crystal orientation, the average crystalline size, residual stresses and the impurities phases in the sample. In this thesis, a PANalytical X-pert Pro diffractometer [4] with a Cu -K_α beam source (λ = 1.5406 Å) is used. For variable temperature (non-ambient) measurements the XRD patterns were collected using an Anton Paar TTK450 tunable-temperature sample chamber. The crystal structure refinement of the XRD patterns was performed using Fullprof's implementation [5] of the Rietveld refinement method.

b. Neutron diffraction

Different from X-ray diffraction, neutron diffraction (ND) is another crystallographic method for the determination of the atomic and magnetic structure of materials. In this thesis, by applying the ND technique the atomic occupation of light atoms (e.g. F and S) within the Fe-rich $(Mn,Fe)_2(P,Si)$ type compounds can be determined. Simultaneously, useful structural details of the site occupation of Mn/Fe and P/Si atoms can be obtained. Additionally, the magnetic structure and the sub-lattice magnetic moments have been investigated systematically in **Chapter 4**. The ND data presented in **Chapter 4** were recorded on the time-of-flight high-resolution neutron diffractometer [6] (Polaris) at the ISIS pulsed neutron source facility (Rutherford Appleton Laboratory, UK).

c. Differential scanning calorimetry

The calorimetry measurements at zero magnetic field were carried out on a commercial differential scanning calorimeter (DSC, TA Instrument Q2000) [7] equipped with a liquid nitrogen cooling system. This calorimeter allows us a direct determination of the heat capacity of these phase transition materials with a high precision using the so-called Tzero DSC technology.

2.1.3 Magnetic measurements

a. Superconducting quantum interference device

The magnetic measurements were carried out using superconducting quantum interference device (SQUID) magnetometers (Quantum Design; MPMS-5S and MPMS-XL) [8]. The

temperature can be varied from 1.5 to 370 K and the applied magnetic field up to 5(7) T. Samples were put into a gelatine capsule and then mounted in a transparent plastic straw. The temperature sweep rate for the cooling and heating process was set to 2 K/min for all the measurements performed in this thesis.

b. Vibrating sample magnetometer

If the transition temperature of the sample is above 370 K, then the vibrating sample magnetometer (VSM) is applied. The VSM machine (Quantum Design VersaLab) [9] oscillates the sample (at 40 Hz) between the compact gradiometer pickup coils, while sweeping through a temperature or magnetic field range. VersaLab is a cryogen-free instrument, so no costly liquid cryogens are required to operate the instrument. Instead, VersaLab (50-650K; 0- 3T) uses a cryocooler to achieve cryogenic temperatures.

2.1.4 Microstructural measurements

a. Scanning electron microscopy

Scanning Electron Microscope (SEM) utilizes a focused beam of high-energy electrons (15 KeV), which can generate a variety of signals at the surface of solid specimens. These signals derived from the electron-sample interactions can reveal useful microstructural information about the sample, including the external morphology, the chemical composition, the element distribution, the grain size and the grain orientation inside the material. In this thesis the microstructure of samples was analyzed by a SEM (JEOL JSM IT100LA) equipped with Energy Dispersive X-ray Spectroscopy (EDS), and line-scans were used to determine the elemental distribution of the different phases present in the material.

b. Transmission electron microscopy

Transmission electron microscopy (TEM) is an excellent tool to investigate the structure of materials, especially for nanoscale materials. In this thesis (**Chapter 3**), high-resolution TEM (HRTEM) was performed using a JEOL JEM 2200FS (200 keV) to investigate the element distribution with the energy dispersive X-ray (EDX) detector (256 x 256 pixels) in mapping mode.

2.1.5 Theoretical calculations

a. First-principles calculations

The basic properties of electrical conductivity, thermal conductivity and magnetism in solids can be studied based on the band theory of solids. Density Functional Theory (DFT) treats the behavior of all particles as a function of a functional, and can therefore simplify the complex multi-electron interactions [10, 11].

The Hohenberg-Kohn theory and the Kohn-Sham equation are the theoretical basis of DFT [10, 11]. The Hohenberg-Kohn theory proves that the energy functional of the system in the ground state can be determined by the variation of the charge density. And the Kohn-Sham equation transformed the multi-electron system into a single-electron theory. In the DFT theory there are mainly two approximations adapted to solve this problem: the Local Density Approximation (LDA) and the General Gradient Approximation (GGA) [12, 13]. LDA is an approximation of the exchange-correlation energy where the density distribution function of a uniform electron gas can be replaced by the corresponding energy of inhomogeneous electron gas. LDA can get good calculation results for most semiconductors and metals. On the basis of LDA, the developed GGA, which is a semi-localized approximation, can give more accurate calculation results. At present, the most commonly used exchange-correlation energy functionals in GGA are PBE and PW91.

In this thesis the Vienna *Ab-initio* Simulation Package (VASP) has been applied for first-principles calculations of different material systems [14]. More calculations details can be found in the following chapters.

2.2 Thermodynamic derivation for ΔS_m

According to the basic theory of thermodynamics, the relationship between magnetization, applied magnetic field, temperature and entropy can be established. Currently, one of the most popular ways to derivate of ΔS_m is based on the Maxwell equations, which transforms the magnetization versus temperature (*M-T*) curves of different magnetic fields under isofield conditions (applied in this thesis) or the magnetization versus magnetic fields (*M-H*) curves of different temperatures under isothermal conditions. Below we will derive this Maxwell expression from the basic thermodynamic formulas.

Based on the first law of thermodynamics (energy conservation law), when the external fields are introduced into a thermodynamic system, the total differential of the internal energy of the system corresponds to:

$$dU = dQ - dW \qquad\qquad (2.1)$$

where Q is thermal energy and W is the work from an external force. For example, for the applied magnetic field, the differential of the work is $dW_{mag} = -\mu_0 H d\mathrm{M}$ where H is magnetic field, μ_0 is permeability of vacuum and M is the magnetization. When considering the thermal variation of a closed system (when there is no thermal exchange then $dQ = TdS$, where T is the temperature and S is the entropy), the differential of U can be rewritten as the following relation:

$$dU = TdS - PdV + \mu_0 H dM \qquad\qquad (2.2)$$

The thermal properties of a material system can be described by the Gibbs free energy G. For a system which has variables that depend on temperature T, pressure P and applied magnetic field $\mu_0 H$, the Gibbs free energy G is defined as:

$$G = U - TS + PV - \mu_0 HM \qquad\qquad (2.3)$$

Correspondingly, by implementing equation (2.2) into (2.3), then the differential dG is obtained:

$$dG = -SdT + VdP - Md(\mu_0 H) \qquad\qquad (2.4)$$

Therefore, when certain state variables are kept constant the following relations can be obtained in terms of the partial derivatives of G:

$$S(T,H,P) = -\left(\frac{\partial G}{\partial T}\right)_{H,P} \qquad\qquad (2.5)$$

$$V(T,H,P) = -\left(\frac{\partial G}{\partial P}\right)_{H,T} \qquad\qquad (2.6)$$

$$M(T,H,P) = -\left(\frac{\partial G}{\partial \mu_0 H}\right)_{T,P} \qquad\qquad (2.7)$$

Based on above relations, for constant pressure equation (2.4) can be rewritten as:

$$dG(T,H) = \left(\frac{\partial G}{\partial T}\right)_H dT + \left(\frac{\partial G}{\partial \mu_0 H}\right)_T d(\mu_0 H) \qquad\qquad (2.8)$$

Because of the Maxwell relation, the crossed second derivatives of G should be equal:

23

$$\left(\frac{\partial}{\partial \mu_0 H}\left(\frac{\partial G}{\partial T}\right)_H\right)_T = \left(\frac{\partial}{\partial T}\left(\frac{\partial G}{\partial \mu_0 H}\right)_T\right)_H \qquad (2.9)$$

Consequently, the Maxwell expression corresponds to equation (2.10). The isothermal magnetic entropy change ΔS_m between $\mu_0 H_0$ and $\mu_0 H_1$ can be determined by equation (2.11):

$$\left(\frac{\partial S}{\partial \mu_0 H}\right)_T = \left(\frac{\partial M}{\partial T}\right)_H \qquad (2.10)$$

$$\Delta S(T, \Delta \mu_0 H) = \int_{\mu_0 H_0}^{\mu_0 H_1} \left(\frac{\partial M}{\partial T}\right)_H d\mu_0 H \qquad (2.11)$$

References

[1] J.S. Benjamin, Dispersion strengthened superalloys by mechanical alloying, *Metall Trans* 1 (1970) 2943–2951.

[2] G. Faraji, H.S. Kim, H.T. Kashi, Severe plastic deformation: Methods, processing and properties, Book Elsevier 2018.

[3] M. Boeije, Electron density studies on magnetic systems, TU Delft PhD thesis (2017).

[4] Introduciton to X'Pert Pro https://labs.jhu.edu/wp-content/uploads/2016/04/Introduction-to-XPert-Pro.pdf.

[5] J. Rodríguez-Carvajal, An introduction to the program FullProf 2000, (2001).

[6] R.I. Smith, S. Hull, M.G. Tucker, H.Y. Playford, D.J. McPhail, S.P. Waller, S.T. Norberg, The upgraded Polaris powder diffractometer at the ISIS neutron source, *Rev Sci Instrum* 90 (2019) 115101.

[7] TA instruments thermal analysis https://www.tainstruments.com/pdf/brochure/2012%20DSC%20Brochure%20r1.pdf

[8] Quantum Design, System & options –magnetic propterty measurement systems.

[9] Quantum Design, Vibrating sample magnetometer –application note.

[10] P. Hohenberg, W. Kohn, Inhomogeneous electron gas, *Phys Rev B* 136 (1964) B864.

[11] W. Kohn, L.J. Sham, Self-consistent equations including exchange and correlation effects, *Phys Rev* 140 (1965) A1133.

[12] J.P. Perdew, A. Zunger, Self-interaction correction to density-functional approximations for many-electron systems, *Phys Rev B* 23 (1981) 5048-5079.

[13] J.P. Perdew, K. Burke, M. Ernzerhof, Generalized gradient approximation made simple, *Phys Rev Lett* 77 (1996) 3865-3868.

[14] G. Kresse, J. Furthmuller, Efficient iterative schemes for *ab initio* total-energy calculations using a plane-wave basis set, *Phys Rev B* 54 (1996) 11169-11186.

25

Chapter 3 Magnetocaloric effect in the (Mn,Fe)$_2$(P,Si) system: From bulk to nano
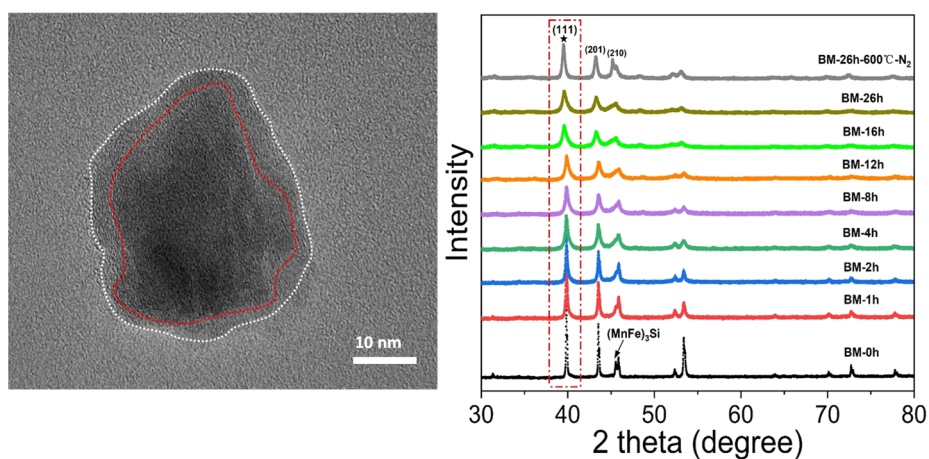
This chapter is based on:

Abstract

In the field of nanoscale magnetocaloric materials, novel concepts like micro-refrigerators, thermal switches, microfluidic pumps, energy harvesting devices and biomedical applications have been proposed. However, reports on nanoscale $(Mn,Fe)_2(P,Si)$-based materials, which are one of the most promising bulk materials for solid-state magnetic refrigeration, are rare. In this study we have synthesized $(Mn,Fe)_2(P,Si)$-based nanoparticles, and systematically investigated the influence of crystallite size and microstructure on the giant magnetocaloric effect. The results show that the decreased saturation magnetization (M_s) is mainly attributed to the increased concentration of an atomically disordered shell, and with a decreased particle size, both the thermal hysteresis and T_c are reduced. In addition, we determined an optimal temperature window for annealing after synthesis of 300-600 °C and found that gaseous nitriding can enhance M_s from 120 to 148 Am^2kg^{-1} and the magnetic entropy change (ΔS_m) from 0.8 to 1.2 $Jkg^{-1}K^{-1}$ in a field change of $\Delta \mu_0 H$ = 1 T. This improvement can be attributed to the synergetic effect of annealing and nitration, which effectively removes part of the defects inside the particles. The produced superparamagnetic particles have been probed by high-resolution transmission electron microscopy, Mössbauer spectra and magnetic measurements. Our results provide important insight into the performance of giant magnetocaloric materials at the nanoscale.

28

3.1 Introduction

The magnetocaloric effect (MCE) describes the fundamental phenomenon that when a magnetic compound is exposed to a change in the applied magnetic field under adiabatic conditions it shows an increase or decrease in temperature. This adiabatic temperature change ΔT_{ad} is associated with a transfer between magnetic and vibrational entropies. In magnetocaloric materials (MCMs) the strength of the MCE is affected by several intrinsic factors like the chemical composition, the crystal structure, the nature of the magnetic interactions and the stress state. Since the seminal work on the discovery of GdSiGe-based MCMs by Pecharsky and coworkers in 1997 [1], a growing number of first-order magnetic transition (FOMT) materials, which demonstrate a giant magnetocaloric effect (GMCE) have sprung up. This contrasts with most other magnetic materials that show a second order magnetic transition (SOMT). Currently, numerous promising GMCE candidate materials have been proposed, including (Mn,Fe)$_2$(P,X)-based compounds (X = As, Ge, Si) [2-4], La(Fe,Si)$_{13}$-based materials [5], NiMn-X based Heusler compounds (X = Ga, In, Sn, Sb) [6], FeRh based alloys [7], Mn$_2$Sb based alloys [8] and MnM-X (M= Co or Ni, X= Si or Ge) ferromagnets [9]. These MCMs with a GMCE exhibit the potential to design efficient devices for solid state magnetic refrigeration, magnetic heat pumps and energy harvesting.

Among these MCMs, the (Mn,Fe)$_2$(P,Si)-based alloys, together with the La(Fe,Si)$_{13}$-based alloys, are the most promising giant MCMs [10] and have been widely investigated because of their excellent GMCE performance, low economic costs and absence of toxic elements, in comparison with previous two-generation (Mn,Fe)$_2$(P,As) and (Mn,Fe)$_2$(P,Ge)-based compounds. Interestingly, the magneto-elastic coupling in (Mn,Fe)$_2$(P,Si)-based MCMs (accompanied by a change in c/a ratio at the FOMT) enables a reduction in thermal hysteresis (ΔT_{hys}) by doping [11]. In addition, the Curie temperature (T_C) can be tuned by composition within a wide temperature window (100-500 K) [12]. In MCMs like the NiMn-based Heusler compounds the magneto-structural coupling leads to a drastic change in crystal structure resulting in a relatively large value for ΔT_{hys}, which is detrimental for the cycling efficiency. The physical mechanism responsible for the GMCE in the (Mn,Fe)$_2$(P,Si)-based MCMs originates from the so-called "mixed magnetism". The interlayers of the crystallographic 3g (preferentially occupied by Mn) and the crystallographic 3f sites (preferentially occupied by Fe) of the hexagonal lattice, represent layers with relatively large stable magnetic moments and relatively weak unstable magnetic moments, respectively. The latter show an interesting "moment-quenching" property across the magnetic transition, as indicated by density functional theory (DFT) [13], neutron diffraction (ND) [14] and X-ray magnetic circular dichroism (XMCD) [15]. Combined DFT calculations and synchrotron high-resolution X-ray diffraction (HRXRD) [16] experiments show a significant

29

electronic charge redistribution around the Fe atoms across the ferromagnetic transition, which was attributed to the competition between magnetism and covalent bonding.

However, although extensive experimental and theoretical studies have focused on the characterization of bulk (Mn,Fe)$_2$(P,Si)-based GMCE materials, the relationship between the magneto-elastic coupling and a size reduction down to nanoscale particles is still pivotal and deserves further exploration. In the field of nanoscale GMCE materials, some novel devices have been proposed in the field of micro-refrigerators [17, 18], thermal switches [19], microfluidic pumps [20, 21], energy harvesting devices [22, 23] and biomedical applications (magnetic hyperthermia [24] or drug delivery [25]). Nano-sized particles have several properties that are distinctly different from bulk materials, like a high surface-to-volume ratio and a fast thermal response. Nonetheless, reports about nanoscale (Mn,Fe)$_2$(P,Si)-based GMCE materials are rare. In this paper, nanoscale (Mn,Fe)$_2$(P,Si)-based MCMs were produced by a "top-down" wet high-energy mechanical milling (HEMM) method [26], which is cheap and can be easily scaled up. The refined particle size distribution in this method is a result of repetitive fragmentation and coalescence events. The crystal structure, thermodynamics and magnetization are investigated as a function of crystallite size. A moderate post-milled annealing at a temperature of 300-600 °C under N$_2$ atmosphere was found to efficiently recover the bulk MCE as a result of the synergistic effect of gaseous nitridation and the removal of dislocations in the particles, as observed by High-resolution transmission electron microscopy (HRTEM). Combined HRTEM, temperature-dependent Mössbauer spectroscopy and magnetic measurements, reveal the presence of a mono-domain state in (Mn,Fe)$_2$(P,Si)-based superparamagnetic particles. Our findings shed new light on the properties of nanoscale GMCE materials and offer useful guidelines for practical engineering applications like ferro-fluids for self-pumping applications.

3.2 Experimental procedure

Bulk MnFeP$_{0.45}$Si$_{0.55}$ MCMs were synthesized from 10 g mixed powders of Mn (99.9%), Fe (99.9%), red-P (99.7%) and Si (99.9%) by milling for 10 h at 380 rpm. To prevent iron contamination, tungsten carbide (WC) balls were used during the pre-alloying procedure. The resulting powders were then pressed into cylindrical tablets sealed in quartz tubes under Ar atmosphere and then annealed for 25 h at 1373 K. After that, these samples were rapidly quenched in cold water, followed by a pre-cooling process in liquid nitrogen to remove the so-called "virgin effect" [27]. Subsequently, 5 g bulk samples and 3 ml oleic acid (chemical surfactant to passivate surface and prevent oxidation), were mixed together with 2-propanol under Ar atmosphere. The synthesis scheme is illustrated in **Figure S3.1** (Supplementary Information). During the whole procedure, we keep the same ball/powder

weight ratio (8:1). Correspondingly, 0.3 g ball-milled powder was taken out from the jar at different ball milling (BM) times ranging from 1 to 26 h (ball milling times of 1, 2, 4, 8, 12, 16, 20, 26 h were used). The residual surfactant and 2-propanol on the surface of milled-powders can be removed completely by mixing with an anhydrous ethanol solution and high-speed centrifugation (10000 rpm). To recover the magnetic properties after ball milling, we processed the milled powders (e.g. 26 h) in a horizontal tubular furnace under N$_2$ flow in different annealing temperatures (300, 500, 550, 600, 700 and 900 °C). For comparison, Ar atmosphere is also applied at an annealing temperature of 600 °C. The average powder size of the BM-0h raw material is around 100 μm. The SEM and corresponding EDS mapping images can be found in **Figure S3.2** (Supplementary Information).

Differential scanning calorimetry (DSC) measurements were carried out using a TA-Q2000 DSC calorimeter. In the high temperature paramagnetic (PM), state X-ray diffraction (XRD) patterns were collected using an Anton Paar TTK450 temperature-tunable sample chamber and a PANalytical X-pert Pro diffractometer with Cu K_α radiation. The crystal structure refinement of the XRD patterns was performed using Fullprof's implementation of the Rietveld refinement method [28]. The average crystallite size was calculated based on the Scherrer equation implemented in the X'pert Highscore software. Field-dependent magnetization (*M-H*) curves at a temperature of 5 K were measured in a magnetometer equipped with a superconducting quantum interference device (SQUID, Quantum Design MPMS 5S) and a vibrating-sample magnetometer (VSM, Quantum Design Versalab) was used to measure temperature-dependent magnetization (*M-T*) curves. Transmission [57]Fe Mössbauer spectroscopy experiments at 4.2 and 130 K were performed on a spectrometer using a [57]Co(Rh) source with a sinusoidal velocity transducer. The velocity calibration was carried out using an α-Fe foil at room temperature. The source and the absorbing samples were kept at the same temperature during measurements. The Mössbauer spectra were fitted using the Mösswinn 4.0 program. The spectra were fitted with a binomial distribution model, as previously described for the analysis of Mössbauer spectra of FeMnP$_{1-x}$As$_x$ compounds [29]. To prove the surface functionalization of surfactant, diffuse reflectance infrared Fourier transform (DRIFT) spectroscopy measurements were performed on a Thermo Nicolet Nexus 670 with a Harrick reflectance device with KBr as reference material, over the range 4000 to 400 cm^{-1}. DRIFT experiments show the used surfactant can be easily removed after a high-speed centrifugation process, as shown in **Figure S3.12** (Supplementary Information). All demonstrated samples went through this process. Scanning electron microscopy (SEM) was carried out on a JSM-7500F Field Emission Scanning Electron Microscope to study the particle distribution. HRTEM analysis was performed using a Jeol JEM 2200FS (200 keV) and the element distributions were measured

with the EDX detector of the same microscope in mapping mode. Digital image processing was performed by the DigitalMicrograph software (version 3.9.1, Gatan Inc).

3.3 Results and discussions

3.3.1 Crystal structural information and average crystallite size

The XRD patterns of original bulk MnFeP$_{0.45}$Si$_{0.55}$ material in the high-temperature PM state are shown in **Figure 3.1a**. The hexagonal Fe$_2$P-type (space group *P-62m*) phase was identified as the main phase. In addition, a cubic (Mn,Fe)$_3$Si-type impurity phase (space group *Fm-3m*) was observed with a weight fraction of 10.1(2) *wt.%*. In the inset of **Figure 3.1a**, the hexagonal (Mn,Fe)$_2$(P,Si) crystal structure has been illustrated, where the Mn atoms (red) preferentially occupy the pyramidal coordinated 3*g* sites with five nonmetal nearest neighbors, while the Fe atoms (blue) favor the tetragonal coordinated 3*f* sites surrounded by four nonmetal coordination atoms and the P (Si) atoms are randomly distributed on the 2*c* and 1*b* sites [30].

To investigate the influence of the high-energy ball milling (HEBM) process on the crystal structure, the XRD patterns of MnFeP$_{0.45}$Si$_{0.55}$ powders were obtained for different BM times in the PM state, as shown in **Figure 3.1b**. The three strongest reflections (111), (201) and (210) of the hexagonal structure in the milled powders indicate that the overall structure is largely unchanged. In **Figure 3.1c** the hexagonal lattice parameters ratio *c/a* are presented (*a*, *c* and the volume *V* can be found in **Figure S3.3** (Supplementary Information)). It can be seen that *c/a* only slightly changes for BM times up to 4 h and it decreases dramatically for longer BM times. As seen in **Figure 3.1b**, the XRD peak-heights decrease, while the peaks broaden for increasing BM times. The peak broadening results from a decreased particle size and introduced micro-strains during BM process. The average crystallite size of the ball-milled samples is estimated based on Scherrer equation $D_{hkl} = K\lambda/(B_{hkl}\cos(\vartheta))$, where D_{hkl} is the average crystallite size, *hkl* are Miller indices of the crystal planes, *K* is the crystallite-shape factor (0.9), λ is the wavelength of the X-rays (0.154 nm for Cu $K_{\alpha 1}$ radiation), B_{hkl} is the full-width at half-maximum (FWHM) of the diffraction peak in radians and ϑ is the Bragg angle [31]. Note, that estimation of the crystallite size from the peak width in the XRD patterns is only reliable up to a crystallite size of about 200 nm. The influence of microstrains on the peak width was not considered during calculation because: (*i*) the crystallite size generally contributes more to the peak broadening than the microstrains when crystallite size is below 100 nm [32] and (*ii*) the strongest low-angle XRD peak ((111) reflection) was chosen to estimate the crystallite size as the contribution of microstrains to peak broadening is relatively small in the low-angle range [33, 34].
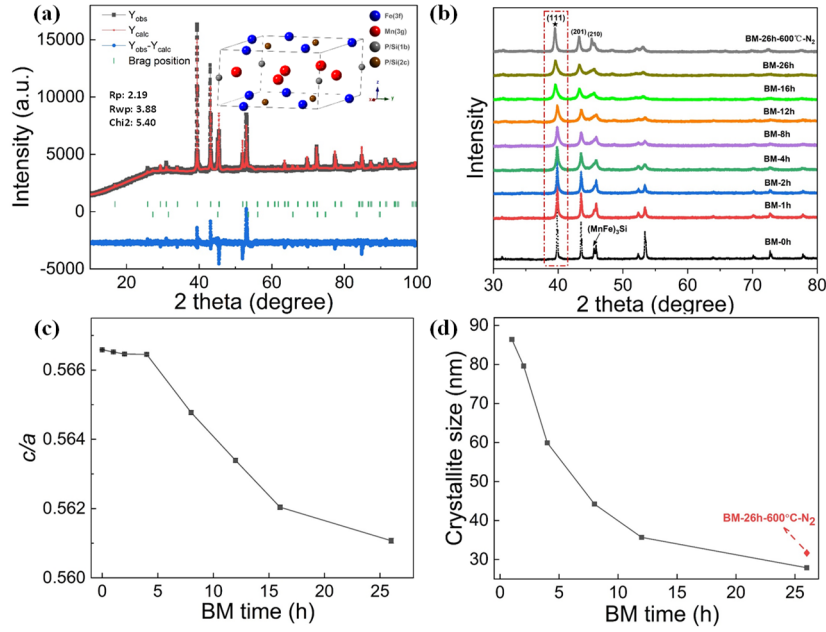
Figure 3.1 (a) High-temperature XRD patterns of bulk MnFeP$_{0.45}$Si$_{0.55}$ material in the PM state. (b) XRD patterns of MnFeP$_{0.45}$Si$_{0.55}$ samples as a function of the BM times (0, 1, 2,4, 8, 12, 16, 20 and 26 h) and post-annealed condition (600°C and N$_2$ atmosphere) in the PM state. (c) The c/a ratio as a function of BM times. (d) Average crystallite size as a function of the BM time obtained from the peak width of the diffraction peaks.

As shown in **Figure 3.1d**, the average crystallite size gradually reduces from 86 nm (BM-1h) to 28 nm (BM-26h), with a slight increase to 32 nm for the sample that was annealed after ball milling (BM-26h-600°C-N$_2$). Previous studies showed that the crystallite size increases exponentially with increasing annealing temperature [35]. The slower increase for our samples may result from the moderate annealing temperature and from the nitrogen surface passivation, which is also observed in steels and Li-ion battery materials [36, 37]. The average crystallite size for bulk (Mn,Fe)$_2$(P,Si) based MCMs with coarse grains is around 27 μm [38]. Here it is found that even a BM time of 1 h significantly decreases the crystallite size to nanoscale, which might be caused by the drastic plastic deformation and the continuous fracturing during the HEBM process. In contrast to the significant reduction in crystallite size for BM times up to 4 h, successive ball milling results in a slow decrease in crystallite size towards a limiting value of around 30 nm, this may be governed by the hardening rate introduced by the dislocation generation and the recovery rate arising from dislocation annihilation and recombination [39]. Additionally, the continuous decrease in crystallite size in **Figure 3.1d** is correlated with the decrease in c/a ratio in **Figure 3.1c**

33

because the *c/a* ratio is closely related to the magnetic exchange coupling [40]. The microstructure of the BM samples will be investigated in detail in section 3.4.

3.3.2 Thermodynamic properties

Figure 3.2a shows the DSC curves of different BM samples performed on cooling/heating processes between 360 and 415 K. The sharp exothermic and endothermic peaks for samples with a short BM time (less than 12 h) correspond to the presence of a FOMT, while the samples with a longer BM time (e.g. 26 h) show a less pronounced specific heat peak. This indicates that long BM times shift the FOMT towards the boundary between the FOMT and the SOMT. The total entropy change (ΔS_{tot}) at T_C is determined by equation $\Delta S_{tot} = L/T_C$, where L is the latent heat, which was derived from the temperature integral of the specific heat (after subtraction of a linear background). As shown in **Figure 3.2b**, compared with the bulk sample (ΔS_{tot} = 20.93 Jkg^{-1}K^{-1}), the sample with a BM time of 26 h only shows roughly 10 % (ΔS_{tot} = 2.03 Jkg^{-1}K^{-1}) of the original bulk value, but the post-annealed sample (BM-26h-600°C-N$_2$) shows a partial recovery (ΔS_{tot} = 2.86 Jkg^{-1}K^{-1}). From **Figure 3.2c**, it is observed that ΔT_{hys} (which is determined by the distance between exothermic and endothermic peaks) sharply decreases from 15.9 to 7.8 K for increasing BM times up to 12 h. For longer BM times it increases slightly, which may be ascribed to the growing amount of defects like dislocations introduced in the material (see HRTEM results in section 3.3). The $<T_C>$ = (T_C ^{heating} + T_C ^{cooling})/2 exhibits a similar decreasing tendency with increasing BM time.

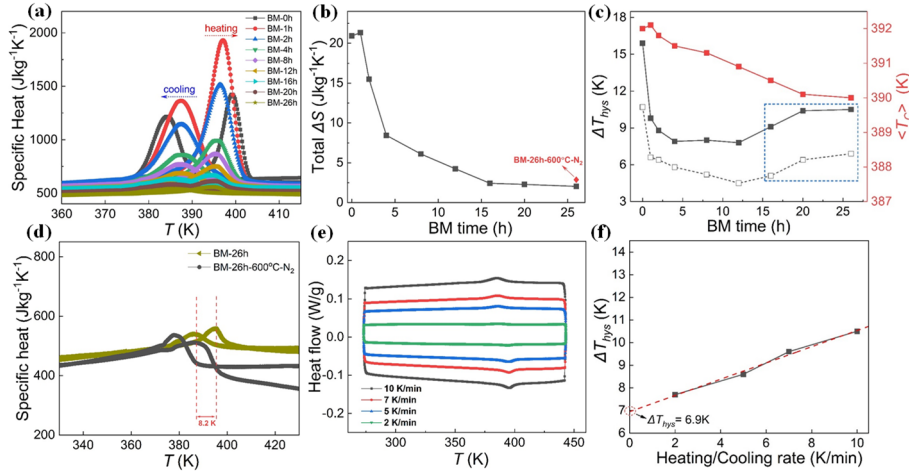**Figure 3.2** (a) Zero-field DSC curves of MnFeP$_{0.45}$Si$_{0.55}$ samples for different BM times along with heating and cooling process. (b) The ΔS_{tot} as a function of BM times; (c) The changes in the thermal hysteresis ΔT_{hys} and the average Curie temperature $<T_C>$ = (T_C ^{heating} + T_C ^{cooling})/2 for different BM times. (d) DSC curves of the BM-26h and BM-26h-

600°C-N$_2$ samples. (e) DSC curves at different heating/cooling rates for BM-26h sample. (f) Linear fitting of ΔT_{hys} obtained from different sweep rates for the BM-26h sample.

This reflects that the BM effectively reduces the atomic exchange interaction energy and the exchange integral (J_{ex}) that controls the Curie temperature (T_C) [41]. In **Figure 3.2d** the post-annealed BM-26h-600°C-N$_2$ sample holds a 8.2 K decrease in T_C^{heating}, compared with BM-26h sample. The origin of ΔT_{hys} can be distinguished into intrinsic (e.g. electronic properties) and extrinsic contributions (e.g. dynamic sweeping rate) [42]. To get the intrinsic ΔT_{hys} and exclude extrinsic factors for the BM-26h sample, in **Figure 3.2e** different DSC sweeping rates (10, 7, 5, 2 K/min) have been chosen. From these curves an extrapolated value of ΔT_{hys} = 6.9 K is found at zero sweep rate, as shown in **Figure 3.2f**. The data for the other BM samples derived by the same method are presented (dashed line) in **Figure 3.2c**. **Table 3.1** summarizes the changes in ΔT_{hys}, T_C^{heating}, T_C^{cooling}, $<T_C>$ and ΔS_{tot} at different BM times.

Table 3.1 Summary of thermal hysteresis (ΔT_{hys}), heating Curie temperature (T_C^{heating}), cooling Curie temperature (T_C^{cooling}), $<T_C>$ and total entropy change (ΔS_{tot}).

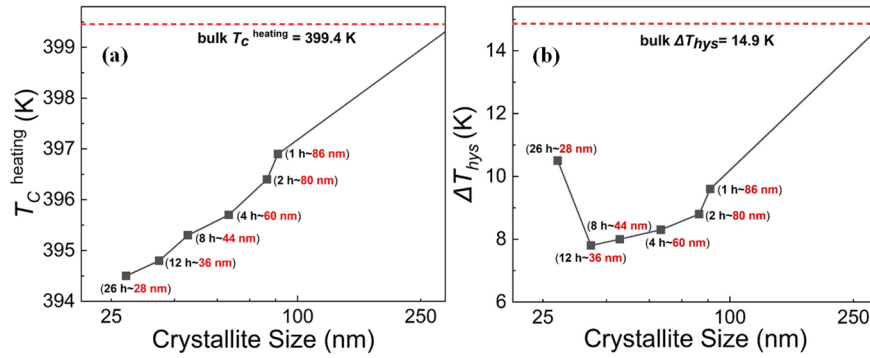| BM time (h)	ΔT_{hys} (K)	T_C^{heating} (K)	T_C^{cooling} (K)	$<T_C>$ (K)	ΔS_{tot} (Jkg^{-1}K^{-1})
0	14.9	399.4	384.5	392.0	20.93
1	9.6	396.9	387.3	392.1	21.33
2	8.8	396.2	387.4	391.8	15.49
4	8.3	395.7	387.4	391.5	8.44
8	8.0	395.3	387.3	391.3	6.10
12	7.8	394.8	387.0	390.9	4.23
16	9.1	395.1	386.0	390.5	2.42
20	10.4	395.3	384.9	390.1	2.28
26	10.5	395.3	384.8	390.0	2.03
26 (+600°C-N$_2$)	8.7	386.5	377.8	382.1	2.86

Figure 3.3 (a) T_C^{heating} and (b) ΔT_{hys} as a function of the average crystallite size derived from XRD. The horizontal axis is in log scale. The dashed lines reflect the bulk value obtained for zero BM time.

The correlation between crystallite size and T_C^{heating} is displayed in **Figure 3.3a**. With decreasing size from 86 nm (BM time of 1 h) to 28 nm (BM time of 26 h) T_C^{heating} shows a decrease. This trend is in agreement with other reduced-dimension nanomaterials [43-46], for instance when in DyCuAl the crystallite size is reduced from 90 to 38 nm T_C reduces from 27 to 24 K [47] and in the La$_{0.6}$Ca$_{0.4}$MnO$_3$ nano-system T_C shifts from 270 to 258 K when the particle size decreases from 223 to 45 nm [48]. The reduced crystallite size also affects the hysteresis behavior in the form of thermal hysteresis [49], magnetic hysteresis [50] as well as stress hysteresis [51]. As shown in **Figure 3.3b**, with decreasing crystallite size, ΔT_{hys} reduces from 14.9 K at a BM time of 0h to 7.8 K at a BM time of 12 h, with a slight enhancement to 10.5 K at a BM time of 26 h.

3.3.3 Microstructural characterization

In order to investigate the microstructure evolution as a result of the nano-sizing SEM and HRTEM were performed, as shown in **Figure 3.4**. In **Figure 3.4a**, a SEM image of a collection of particles for the BM-16h sample is shown. An obvious particle size distribution is observed with sizes ranging from several nanometer up to around 3 μm. Within some of the bigger particles several small nanoparticles (NPs) can be identified, as indicated inside the red boxes. **Figure 3.4b** shows the HRTEM image of one isolated spherical particle with a diameter of about 35 nm for the BM-26h sample, which is composed of a darker crystalline core and brighter amorphous shell. A fast Fourier transform (FFT) is applied which confirms that the core is single crystalline. **Figure 3.4c** indicates the inter-planar spacing is 0.20 nm. In **Figure 3.4d** the bright-field HRTEM of one of the bigger particles (with a diameter of about 170 nm) from the same BM-26h sample presents a similar shell layer. This shell layer is also found for the post-annealed particles (BM-26h-600°C-N$_2$ sample) shown in **Figure**

S3.5b (Supplementary Information). The formation of an amorphous shell in NPs was also observed in nano Gd (inert-gas evaporation) [52], LaFeSi (pulsed laser deposition (PLD); or spark ablation) [53, 54], Heusler compounds (PLD) [55], manganese perovskite (sol-gel method) [48] and other oxide compounds (HEBM) [56]. By using a FFT and comparing the diffraction patterns we can evaluate the crystallite sizes within a polycrystalline particle. For instance in **Figure 3.4e**, four single-domain areas have been indicated with crystallite sizes of 36.8, 40.0, 22.4 and 25.6 nm, respectively. The average crystallite size (31.2 nm) from HRTEM is in good agreement with the value estimated from XRD (28 nm). **Figure 3.4f** and **3.4g** show different electron diffraction patterns corresponding to single crystalline areas 4 and 2 in **Figure 3.4e**, respectively. These two single crystalline areas have a different crystallographic orientation. The diffraction patterns from the crystalline cores are consistent with a pure hexagonal structure along the [1,-1,0] zone axis, while the shell presents amorphous diffraction rings, as shown in **Figure S3.4** (Supplementary Information). The corresponding inverse fast Fourier transform (IFFT) image for the diffraction pattern of **Figure 3.4g** is shown in **Figure 3.4h**. In this figure some dislocation defects marked with "T" are observed along the $(11\bar{1})$ direction, which could be ascribed to severe plastic
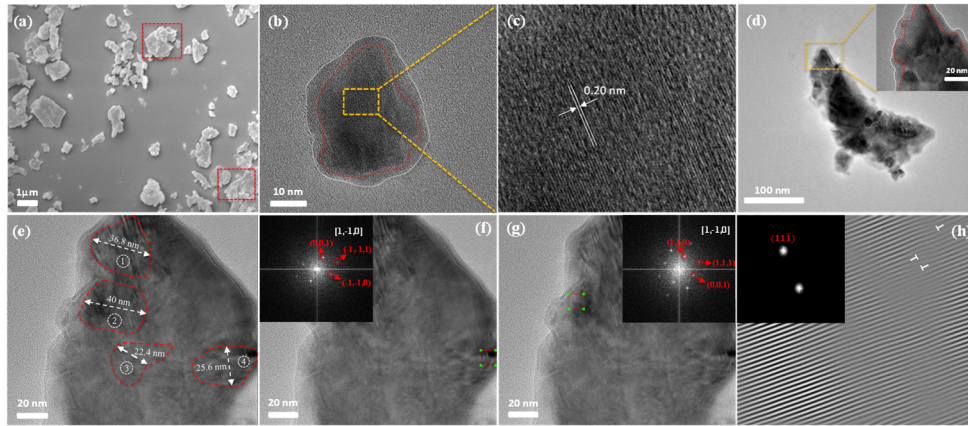
Figure 3.4 (a) SEM image for the BM-16h sample. (b) HRTEM image of isolated "core-shell" single domain particle for the BM-26h sample. (c) Partial enlarged image collected from the yellow box in (b) together with the interplanar spacing. (d) Bright-field HRTEM image of one of the bigger particles in the BM-26h sample. Inset demonstrates the shell layer. (e) Different single-crystalline areas within one particle. (f-g) Corresponding FFT patterns in the regions indicated by the red circles in (e) for the BM-26h sample (region 4 in (f) and region 2 in (g)). (h) Corresponding IFFT pattern of (g) consisting of numerous dislocations marked with "T" along the $(11\bar{1})$ direction.

deformation during the HEBM process. The formation of such defects has also been observed in other HEBM nanomaterials [57, 58]. The presence of dislocations may result in changes in structural, thermodynamic and magnetic properties. In contrast, widely

distributed dislocations have not been observed in the corresponding IFFT image of the post-annealed sample (BM-26h-600°C-N$_2$), as shown in **Figure S3.5e** (Supplementary Information). This is expected to be a result of the annealing at a moderate temperature of 600°C. To study the homogeneity of elemental distributions, energy-dispersive X-ray spectroscopy (EDS) mapping was performed in the HRTEM for the BM-26h sample, as shown in **Figure S3.6** (Supplementary Information). It was found that the metal (Mn-Fe) and non-metal (P-Si) elements are homogeneously distributed in the matrix and that there is no obvious element segregation. The EDS mapping of sample BM-26h-600°C-N$_2$ in **Figure S3.7** (Supplementary Information), also reveals the amount of doped nitrogen within one of the particles. For this sample annealing under a nitrogen environment results in a reduction in unit-cell volume (from 111.9 to 110.8 Å^3), indicating that N atoms enter the structure substitutionally [59]. Image analysis of **Figure S3.7** indicates that the particle shell contains a higher N concentration compared to the particle core, which may be attributed to the amorphous structure of the particle shell. N doping during annealing generally presents some positive effects [60-62], which is expected to be responsible for the optimization of magnetic properties discussed in the section below.

3.3.4 Magnetic properties

The change in crystallite size and microstructure upon nano-sizing can also bring different magnetic properties with respect to the bulk behavior. For instance, from the *M-T* curves in **Figure 3.5a**, it is observed that for increasing BM times the characteristic sharp FOMT for the bulk sample gradually disappears and the transition area significantly broadens, which is expected to be related to the evolution of the particle size distribution. The isothermal *M-H* curves in **Figure 3.5b** illustrate that the M_s decreases with increasing BM times, which can be ascribed to the gradual loss in long-range ferromagnetic order for smaller crystallite sizes. The gradual reduction in M_s with BM times is more pronounced after 4 h.
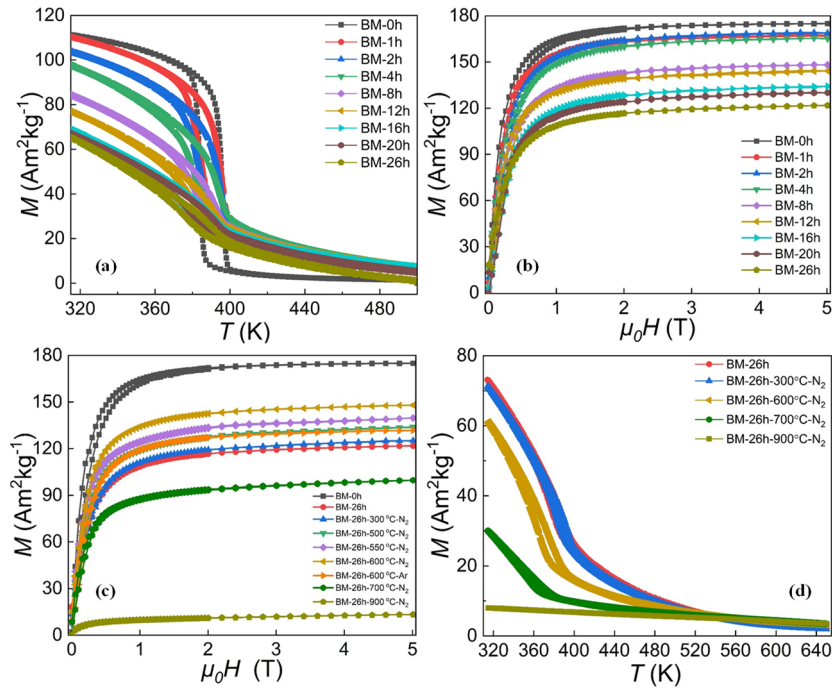
Figure 3.5 (a) Temperature-dependent magnetization (M-T) curves at 1 T for MnFeP$_{0.45}$Si$_{0.55}$ samples with different BM times. (b) Isothermal field-dependent magnetization (M-H) curves at 5 K for samples with different BM times. (c) M-H curves at 5 K for the BM-0h sample, the BM-26h sample and post-annealed samples for BM-26h after annealing at various temperatures and protective atmospheres. (d) M-T curves at 1 T for the BM-26h sample and the corresponding post-treatment samples annealed in N$_2$ at different temperatures.

In **Figure 3.5c** the saturation magnetization M_s at 5 K and 5 T decreases from 175 to 122 Am^{2}kg^{-1} for a BM time from 0 to 26 h, respectively. Interestingly, except for the bulk sample (BM-0h), the 1st cycle magnetization and demagnetization curves almost overlap each other for all BM samples. This suggests that successive milling results in a decrease in magnetocrystalline anisotropy [41], which can be observed by the correspondence between the 1st cycle demagnetization and 2nd cycle magnetization process in subsequent M-H curves, presented in **Figure S3.8** (Supplementary Information). Because the decrease in M_s (~30%) will be detrimental to the MCE, we tried to recover this loss in M_s while maintaining the small crystallite size by N$_2$ gaseous nitriding. The approach was inspired by previous studies, which noticed an enhancement of the magnetic moments [62] and a refinement of the microstructure [60]. As exhibited in **Figure 3.5c**, an optimal temperature window of 300-600 °C for annealing under N$_2$ atmosphere has been found where a clear enhancement in M_s is found for all post-annealed samples. For annealing temperatures above 600 °C the saturation magnetization M_s is reduced rapidly as the higher temperature leads to the

formation of metal-nitride and the destruction of the hexagonal structure. Specifically, the M_s value for the BM-26h-600°C-N_2 sample increased 22% from 127.5 to 147.9 (5 T) Am^2kg^{-1} in comparison to BM-26h sample. However, for an annealing temperature above 600°C (see the data for 700-900 °C in **Figure 3.5d**), the ferromagnetic phase transition is gradually suppressed due to the collapse of the hexagonal structure.

The relationship between M_s and the average crystallite size has been shown in **Figure 3.6a**. It is found that M_s decreased continuously with decreasing crystallite size. This phenomenon has been widely investigated in different nanomaterials systems [63, 64]. The decrease in M_s with the reduction in crystallite size might (partially) be ascribed to the existence of a so-called magnetic dead layer (MDL) on the surface [65], which means the surface shell becomes highly frustrated, leading to a reduced magnetic moment of the particle. The MDL is directly proportional to increased surface-volume ratio related to the decreased crystallite size. From HRTEM results in **Figure 3.4** an amorphous MDL has also been observed at the surface of the magnetic nanoparticles. Experimentally, the polarized small-angle neutron scattering (SANS) technique has proven that for maghemite/magnetite NPs a gradual decrease in magnetization can result from an enhanced tendency for spin canting near the surface [66, 67]. As shown in **Figure 3.6b**, the relationship between M_s and crystallite size can be well estimated by the following relation [63, 68]:

$$M_s = M_{s0}\left(1 - \frac{6\gamma}{D}\right) \qquad (3.1)$$

where M_s is the saturation magnetization of the nanomaterial, M_{s0} is the saturation magnetization of the bulk material, γ is the thickness of MDL (approximately 2–3 nm) and D is the average crystallite size.
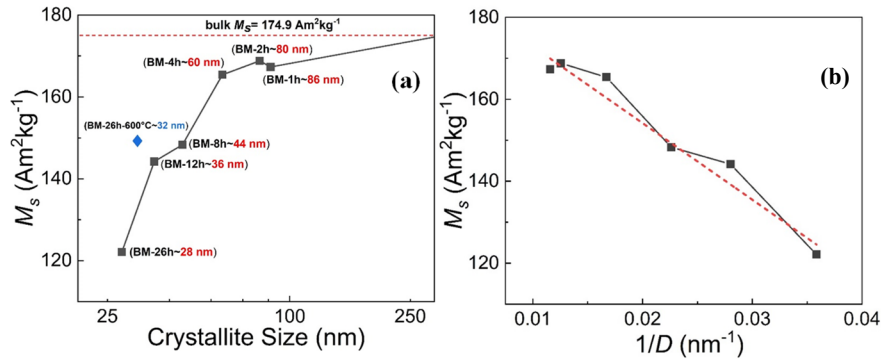

Figure 3.6 (a) Saturation magnetization M_s measured in a field of 5 T at a temperature of 5 K as a function of the average crystallite size D (for different BM times). (b) Linear fitting between the M_s and 1/D.

The hysteresis loops in the FM state were obtained in **Figure 3.7a**. As shown in **Figure 3.7b**, the coercive field $\mu_0 H_c$ (negative intersection of the horizontal axis in the *M-H* curve for reducing field) for the BM-0h, BM-26h and BM-26h-600°C-N$_2$ samples are 1.80, 17.6 and 6.50 mT, respectively. Compared to bulk (Mn,Fe)$_2$(P,Si) and other soft magnetic MCMs [69], the BM-26h sample exhibits a pronounced 10 times increase in coercive field $\mu_0 H_c$. The increase in $\mu_0 H_c$ with decreasing crystallite size *D* is also observed in some other polycrystalline materials where a $\mu_0 H_c \propto 1/D$ relation was reported [41, 70]. The mechanically reduced crystallite size is expected to create more pinning sites, which are the main source for the enhanced value for $\mu_0 H_c$ [71]. As the mechanically reduced particle size can pin the magnetic domain wall movement, an additional driving force in the form of a higher applied magnetic field is needed to overcome the pinning of the magnetic domain walls before they start to move. The thickness of the magnetic domain wall (κ) in (Mn,Fe)$_2$(P,Si) system can be estimated by following formula [72]:

$$\kappa = Na \qquad\qquad (3.2)$$

$$N = \sqrt{\pi^2 J S^2 / K a^3} \qquad\qquad (3.3)$$

$$J = 3 k_B T_c / 2 z S(S+1) \qquad\qquad (3.4)$$

where *N* is the number of atomic planes contained within the magnetic domain wall; *a* is the effective lattice parameter ($a = \sqrt[3]{V/3}$ for an hexagonal system and *V* is the unit-cell volume); *J* is the exchange integral; *S* is the electron spins, which is deduced from $\mu_{eff} = 2\sqrt{S(S+1)}$ and μ_{eff} is the effective (average) spin moment of the Mn and Fe atoms; *K* is the magneto-crystalline anisotropy constant (0.28×10^6 J/m^3 for (Mn,Fe)$_2$(P,Si) system [73]); k_B is Boltzmann's constant; T_C is the Curie temperature and *z* is the number of nearest neighbors. The estimated magnetic domain wall thickness δ is 13 nm for the BM-26h sample, which is of the same order of magnitude as the average crystallite size (28 nm). In addition, dislocations can also pin the motion of magnetic domain walls [74]. As a consequence it can cause a partial increase in $\mu_0 H_c$. For comparison, the BM-26h-600°C-N$_2$ sample, which has a decreased dislocation density with respect to the BM-26h sample shows a distinctly lower value for $\mu_0 H_c$, even though its value is still higher than that of the original BM-0h bulk sample. In addition, the weak magnetic hysteresis in **Figure 3.7b** is expected to be ascribed to the presence of a fraction of larger particles in the superparamagnetic material.
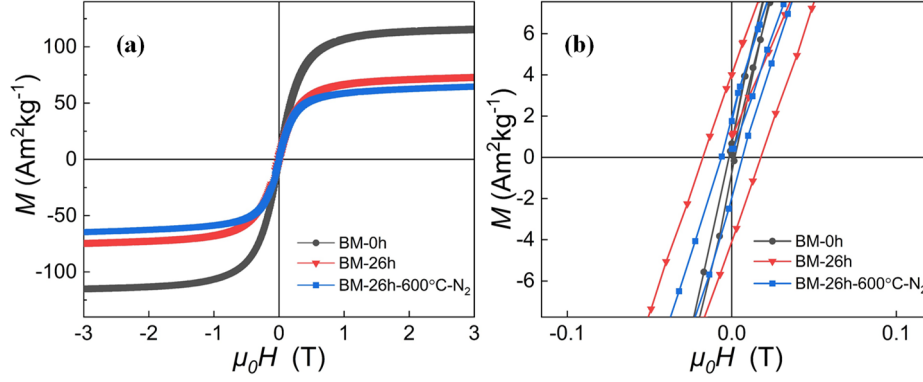
Figure 3.7 (a) Magnetic hysteresis loops for the BM-0h, BM-26h and BM-26h-600°C-N$_2$ samples at a temperature of 320 K. (b) Magnification of the magnetization loops of (a) near the origin.

Based on the isothermal *M-T* curves presented in **Figure S3.9** (Supplementary Information), the magnetic field induced entropy change ΔS_m can be evaluated using the Maxwell relation $\Delta S_m = \int_0^H (\frac{\partial M}{\partial T})_H dH$, which is associated with the configuration entropy arising from spin disorder [75]. **Figure 3.8a-b** shows the negative ΔS_m values (conventional MCE) of three samples as a function of temperature measured with increasing temperature for magnetic field changes $\mu_0 \Delta H$ of 1, 2 and 3 T, respectively. For a field change of $\mu_0 \Delta H$ = 1 T (characteristic for applications), the maximum value of $|\Delta S_m|$ decreases from 6.8 Jkg^{-1}K^{-1} for the original bulk BM-0h sample to 0.8 Jkg^{-1}K^{-1} (88% loss) for the BM-26h sample, which can be ascribed to a significant reduction in ΔM and a broadening of the phase transition. In comparison with the BM-26h sample, the BM-26h-600°C-N$_2$ sample shows an improvement in the maximum value of $|\Delta S_m|$ from 0.8 to 1.2 Jkg^{-1}K^{-1} (1.6 to 2.3 Jkg^{-1}K^{-1} for $\mu_0 \Delta H$ =2 T). This is consistent with the increasing trend of the transformation peak in the DSC experiments and can originate from the synergistic effect of the reduced dislocation density and the nitrogen doping.

In **Figure 3.9** a map of $|\Delta S_m|$ versus T_C is shown for some representative nano MCMs. For La(Fe,Si)$_{13}$, the other most promising MCMs, no data are reported, although several nano-compounds exist [53, 54]. The post-annealed nano MnFeP$_{0.45}$Si$_{0.55}$ sample (BM-26h-600°C-N$_2$) shows competitive $|\Delta S_m|$ values for field changes of 1 and 2 T, compared with the benchmark MCE material Gd in the form of nano-compounds.
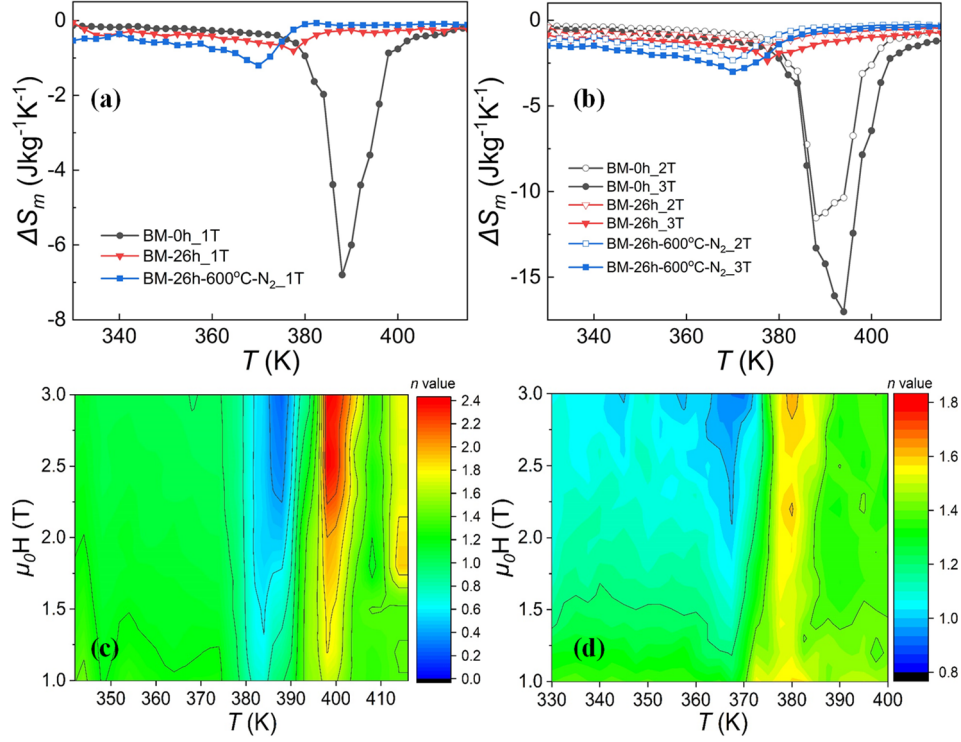
Figure 3.8 Temperature dependence of ΔS_m for the BM-0h, BM-26h and BM-26h-600°C-N$_2$ samples for a magnetic field change $\mu_0\Delta H$ of (a) 1 T and (b) 2 and 3 T (with respect to zero field); 2D contour plots of the field exponent n as a function of magnetic field and temperature for the (c) BM-0h and (d) BM-26h samples.

Furthermore, ΔT_{ad} based on indirect measurements and the relative cooling power (*RCP*) used for evaluating the refrigeration capacity of a magnetic refrigerant can be obtained by expressions (3.5) [76] and (3.6) [48], respectively, as shown below:

$$\Delta T_{ad} \cong -\frac{T}{Cp}\Delta S_m(T,H) \qquad (3.5)$$

$$RCP = \left|\Delta S_{m,max}\right|\delta T_{FWHM} \qquad (3.6)$$

where C_P is zero-field specific heat and δT_{FWHM} is temperature difference between T_2 and T_1 at FWHM. All MCE parameters including T_{trans}, ΔS_m, ΔT_{ad}, *RCP*, *D*, and synthesis methods for our works and some classical nano MCMs are summarized in **Table 3.2**. Note that some nanomaterials focused on cryogenic magnetic refrigeration like Gd$_2$O$_3$ [77] and GdNi$_5$ [78] are not included due to their extreme low working temperature (< 30 K), even though they present a relatively high ΔS_m at high field changes.
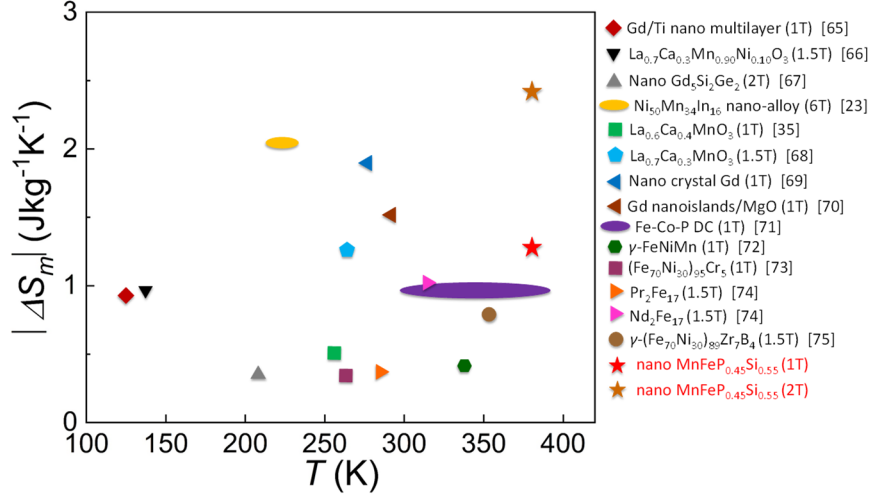
Figure 3.9 Map of the absolute magnetic entropy change |ΔS_m| for different field changes $\mu_0\Delta H$ as a function of the magnetic transition temperature for nano MCMs [35, 48, 79-89]. The stars correspond to the present data for the BM-26h-600°C-N₂ sample.

In addition, to distinguish the FOMT or SOMT nature of the phase transition, Arrott plots ($\mu_0 H/M$ versus M^2) were constructed for the BM-0h, BM-26h and BM-26h-600°C-N₂ samples. The Arrott plots were made from the isothermal *M-H* curves presented in **Figure S3.9** (Supplementary Information), assuming a demagnetization factor of *N* = 1/3 (assuming an equiaxed powder sample volume). Although the BM-0h sample represents clear FOMT characteristics (with a "S-shaped" curve as predicted by the Banerjee criterion), the other two samples appear to be of SOMT type, which is in conflict with the observed hysteresis. Hence, the recently proposed field exponent *n* for the magnetic entropy change [90] is applied to further identify the nature of the magnetic transition. This field exponent is defined as:

$$n\,(T,H) = \frac{d\ln|\Delta S_M|}{d\ln H} \qquad\qquad (3.7)$$

2D-plots of exponent *n*(*T*,*H*) as a function of temperature *T* and applied magnetic field *H* have been shown in **Figure 3.8c-d** for the BM-0h and BM-26h samples. Close to the magnetic transition the *n* value peaks at a value above the value obtained for the paramagnetic state at higher temperature, a characteristic feature for a FOMT [91, 92]. We therefore conclude that: (1) the BM-0h sample is a strong FOMT (*n* > 2) in agreement with the Banerjee criterion in the Arrott plot and (2) the BM-26h sample shows a weak FOMT, rather than a SOMT.

Table 3.2 Transition temperature (T_{trans}), magnetic entropy change $|\Delta S_m|$, adiabatic temperature change ΔT_{ad}, RCP, crystallite size D and synthesis method for selected nano MCMs reported in the literature.

Nano MCMs system	T_{trans} (K)	$|\Delta S_m|$ (Jkg⁻¹K⁻¹)	ΔT_{ad} (K)	RCP (Jkg⁻¹)	D (nm)	Synthesis methods	References
Pr_2Fe_{17} and Nd_2Fe_{17}	~285; ~337	0.6 (1.5 T);	-	60 (1.5 T)	11;11	BM 40h	[88]
γ-FeNiMn	340	0.41 (1 T)	-	78 (1 T)	17	BM 10h	[86]
$(Fe_{70}Ni_{30})_{95}Cr_5$	258	~0.3 (1 T)	-	77 (1 T)	13	BM method	[87]
Fe-Co-P DC	300-390	0.907 (1 T)	0.77 (1 T)	52 (1 T)	<100	electrodeposition	[85]
γ-$(Fe_{70}Ni_{30})_{89}Zr_7B_4$	353	0.7 (1.5 T)	-	65 (1.5 T)	20	BM method	[89]
Nano Gd	-	~0.4 (0.1 T)	-	-	12	alkalide reduction	[93]
Gd nanoislands/MgO	296.2	~1.5 (1 T)	-	-	~131	solid-state dewetting	[84]
$La_{0.7}Ca_{0.3}MnO_3$	266	1.2 (1.5 T)	-	44 (1.5 T)	65	sol-gel method	[82]
$La_{0.7}Ca_{0.3}Mn_{0.9}Ni_{0.1}O_3$	145	0.95 (1.5 T)	-	-	15	BM method	[80]
$La_{0.6}Ca_{0.4}MnO_3$	258	0.6 (1 T)	-	50 (1 T)	45	sol-gel method	[48]
Nano crystal Gd	285.6	~1.8 (1 T)	-	-	12	inert gas condensation	[83]
Gd/Ti nano multilayer	130	~0.9 (1 T）	-	-	-	sputtering deposition	[79]
Nano $Gd_5Si_2Ge_2$	~225	0.45 (2 T)	-	-	85	BM method	[81]
Nano $LaFe_{11.5}Si_{1.5}$	200-340	-	-	-	~6.5	spark ablation	[54]
$Ni_{50}Mn_{34}In_{16}$ nano-alloy	226-241	2 (6 T)	-	150 (6 T)	150	BM method	[35]
$MnFeP_{0.45}Si_{0.55}$ BM-26h-600°C-N₂	~382	1.2 (1 T); 2.4 (2 T)	0.9 (1 T) 1.74 (2 T)	29 (1 T) 77 (2 T)	31.6	BM 26h	this work

3.3.5 Mössbauer spectra and superparamagnetic particles

When the dimension of a magnetic particle is below a certain size (e.g. 50 nm) it will be single magnetic domain and presents superparamagnetism (SPM) above the so-called blocking temperature T_B [94]. As mentioned, the HRTEM results (**Figure 3.4b**) show individual nanoscale crystallites, which based on their size are expected to behave as

superparamagnetic particles (SPP). Because Mössbauer spectroscopy is very sensitive to the magnetic properties of nanoscale particles, it is an excellent technique to provide more details about SPM in (Mn,Fe)$_2$(P,Si)-based nano MCMs. The Mössbauer spectra at 4.2 K for the BM0h, BM-26h and BM-26h-600°C-N$_2$ samples are shown in **Figure 3.10**. The fitted hyperfine parameters include the average isomer shift (δ), the average quadrupole splitting (QS), the hyperfine field and linewidth (Γ) and are presented in **Table 3.3**. Obviously, the values of δ and QS for the main phase remain almost unchanged, but the reduced hyperfine fields for the BM samples indicate a decrease in Fe moment. The line width Γ is enhanced with increasing BM time, reflecting the development of a wide distribution of magnetic fields acting on the Fe nuclei [95]. The five sets of sextets observed in **Figure 3.10** correspond to five types of chemical coordination environment of Fe. Simultaneously, the phase fraction of the SPP for the BM samples of 18% for the BM-26h sample and 10% for the BM-26h-600°C-N$_2$ sample is clearly enhanced. In **Figure 3.10** a typical ferromagnetic sextet (middle brown curve) appears due to the existence of collective magnetic interactions below T_B [96]. For comparison, in **Figure S3.10** (Supplementary Information) the hyperfine lines at 130 K become asymmetrically broadened and a single line appears. These are fundamental features of SPM for nanoscale particles, as seen in the Mössbauer spectra [56, 95, 97, 98].
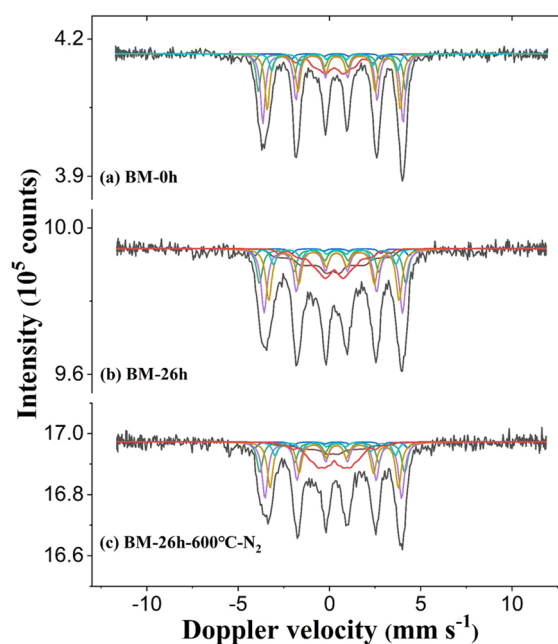

Figure 3.10 Mössbauer spectra for the (a) BM-0h, (b) BM-26h and (c) BM-26h-600°C-N$_2$ samples recorded at 4.2 K.

Note that the five middle sextets (blue, green, purple, dark yellow, cyan) correspond to the FM components of the main phase, the red curves correspond to the $(Mn,Fe)_3Si$ impurity phase, the middle brown curves correspond to the SPP phase and the black curves represent the sum.

This phenomenon can be understood by considering the SPM relaxation time estimated by the Néel–Brown–Arrhenius expression [99]:

$$\tau_R = \tau_0 \exp(KV/k_BT) \qquad (3.8)$$

where τ_R is the relaxation time of the magnetization vector in a particle, τ_0 is a characteristic time constant that is roughly equal to 1×10^{-9} s, K is the magnetic anisotropy constant, V is volume of the crystallite and k_BT corresponds to the thermal energy. If $\tau_R < \tau_L$ then a superparamagnetic doublet/singlet will appear, where $\tau_L \approx 10^{-8}$ - 10^{-9} s is the Larmor precession time of the nucleus. For $\tau_R > \tau_L$ a minor sextet structure is observed, while for the intermediate range with $\tau_R \approx \tau_L$ complex spectra with broadened lines are found. Other evidence for the presence of SPM can be found in the *M-T* curves at 0.1 T for ZFC-FC conditions, as presented in **Figure S3.11** (Supplementary Information) for the BM-26h and BM-26h-600°C-N₂ samples. Typical magnetization divergences were observed, which are characteristic of SPM in nanoscale particles [100]. The blocking temperature T_B (at 0.1 T) is determined to be 72 and 61 K for the BM-26h and BM-26h-600°C-N₂ samples, respectively. Annealing is found to reduce T_B, which in agreement with observations for other nano-

Table 3.3 Mössbauer fit parameters for the BM-0h, BM-26h and BM-26h-600°C-N₂ samples at 4.2 K. (F- ferromagnetic phase; IM- impurity phase (Mn,Fe)₃Si; SPP- superparamagnetic particles)

Sample	IS (mm·s⁻¹)	QS (mm·s⁻¹)	Hyperfine field (T)	Γ (mm·s⁻¹)	Phase	Spectral contribution (%)
BM-0h	0.30(1)	-0.19(1)	23.6(1)	0.30(1)	F	85(3)
	0.27(2)	-	8.8(5)	0.30(1)	IM	15(3)
BM-26h	0.31(1)	-0.17(1)	23.3(1)	0.39(1)	F	67(3)
	0.27(2)	-	8.8(5)	0.30(1)	IM	15(3)
	0.19(2)	-	12.0(5)	0.39(1)	SPP	18(3)
BM-26h-	0.31(1)	-0.17(1)	23.0(1)	0.37(1)	F	71(3)
600°C-N2	0.27(2)	-	8.8(5)	0.30(1)	IM	19(3)
	0.17(2)	-	10.9(5)	0.37(1)	SPP	10(3)

systems [101]. The critical diameter for single magnetic domain behavior (D_{sd}) for

(Mn,Fe)$_2$(P,Si)-based compounds can be estimated by [72]:

$$D_{sd} = 2R_{sd} \cong 9\gamma_w/k_d \qquad (3.9)$$

where R_{sd} is the single domain radius, $\gamma_w = 2\sqrt{AK}$ is the surface energy of a Bloch wall and $k_d = J_s^2/2\mu_0 = \frac{1}{2}\mu_0 M_s^2$ is the stray field energy (J_s is the saturation magnetization). Thus D_{sd} can be deduced from (8):

$$D_{sd} = 36\sqrt{AK}/\mu_0 M_S^2 \qquad (3.10)$$

$$A = nJ_{ex}S^2/a \qquad (3.11)$$

where A is the exchange stiffness constant, n is the number of atoms in one unit cell, J_{ex} is the exchange integral, S is the spin, a is the lattice parameter, K is the magnetocrystalline anisotropy constant, μ_0 is the permeability of vacuum and M_s is the saturation magnetization. The value for D_{sd} is estimated to be 29.8 nm for (Mn,Fe)$_2$(P,Si)-based compounds. This is in accordance with our XRD results where the crystallite size was estimated to be about 28 nm for the BM-26h sample and the HRTEM results of **Figure 3.4e** with an average crystallite size of 31.2 nm.

3.4 Conclusions

In summary, we have systematically studied the crystalline structure, thermodynamic-, microstructure- and magnetic properties in (Mn,Fe)$_2$(P,Si)-based nano MCMs derived from bulk alloys by XRD, DSC, HRTEM, SQUID and Mössbauer spectrocopy. The change in crystallite size as a result of the HEBM process is found to be responsible for changes in T_C, ΔT_{hys}, ΔS_{tot} and the magnetization. Nano-sizing MCMs can be used to regulate T_C and $\Delta T_{hys,}$ similarly as with certain doping elements, tuning composition, optimizing annealing conditions and adjusting physical pressure. An efficient sample treatment after the HEBM process was adopted, which consists of annealing in a temperature window of $300 - 600$ °C with gaseous nitriding. Even though the $|\Delta S_m|$ of the bulk material (6.8 Jkg^{-1}K^{-1} with $\mu_0\Delta H$ =1 T) is found to be significantly reduced by nanostructuring, the nitriding procedure was found to result in a significant recovery of the lost magnetization with an improvement in $|\Delta S_m|$ ($\mu_0\Delta H$ = 1 T) from 0.8 to 1.2 Jkg^{-1}K^{-1}. During this procedure the crystallite size remained almost constant, which demonstrates competitive MCE characteristics among the reported nano MCMs systems. A core-shell type nanostructure, with a crystalline core and an atomically disordered shell, has been observed for the first time in (Mn,Fe)$_2$(P,Si)-based nano MCMs. The existence of superparamagnetic NPs has been proved by HRTEM, Mössbauer spectroscopy and magnetic measurement. Our study provides essential insight

in (Mn,Fe)$_2$(P,Si)-based nano MCMs and opens the possibility to further develop its potential for future applications in the field of microrefrigerators, ferrofluids, nanocomposites, heterogeneous catalysis and magnetic hyperthermia.

References

[1] V.K. Pecharsky, K.A. Gschneidner, Giant magnetocaloric effect in Gd$_5$(Si$_2$Ge$_2$), *Phys Rev Lett* 78 (1997) 4494-4497.

[2] O. Tegus, E. Brück, K.H.J. Buschow, F.R. de Boer, Transition-metal-based magnetic refrigerants for room-temperature applications, *Nature* 415 (2002) 150-152.

[3] N.T. Trung, Z.Q. Ou, T.J. Gortenmulder, O. Tegus, K.H.J. Buschow, E. Brück, Tunable thermal hysteresis in MnFe(P,Ge) compounds, *Appl Phys Lett* 94 (2009) 1-3.

[4] F. Guillou, G. Porcari, H. Yibole, N. van Dijk, E. Brück, Taming the first-order transition in giant magnetocaloric materials, *Adv Mater* 26 (2014) 2671-2675.

[5] F.X. Hu, B.G. Shen, J.R. Sun, Z.H. Cheng, G.H. Rao, X.X. Zhang, Influence of negative lattice expansion and metamagnetic transition on magnetic entropy change in the compound LaFe$_{11.4}$Si$_{1.6}$, *Appl Phys Lett* 78 (2001) 3675-3677.

[6] A. Planes, L. Mañosa, M. Acet, Magnetocaloric effect and its relation to shape-memory properties in ferromagnetic Heusler alloys, *J Phys-Condens Mat* 21 (2009) 1-29.

[7] A. Chirkova, K.P. Skokov, L. Schultz, N.V. Baranov, O. Gutfleisch, T.G. Woodcock, Giant adiabatic temperature change in FeRh alloys evidenced by direct measurements under cyclic conditions, *Acta Mater* 106 (2016) 15-21.

[8] P.A.E. Murgatroyd, K. Routledge, S. Durdy, M.W. Gaultois, T.W. Surta, M.S. Dyer, J.B. Claridge, S.N. Savvin, D. Pelloquin, S. Hebert, J. Alaria, Chemically controllable magnetic transition temperature and magneto-elastic coupling in MnZnSb compounds, *Adv Funct Mater* 31 (2021) 1-9.

[9] J. Liu, Y.Y. Gong, Y.R. You, X.M. You, B.W. Huang, X.F. Miao, G.Z. Xu, F. Xu, E. Brück, Giant reversible magnetocaloric effect in MnNiGe-based materials: minimizing thermal hysteresis via crystallographic compatibility modulation, *Acta Mater* 174 (2019) 450-458.

[10] T. Gottschall, K.P. Skokov, M. Fries, A. Taubel, I. Radulov, F. Scheibel, D. Benke, S. Riegg, O. Gutfleisch, Making a cool choice: the materials library of magnetic refrigeration, *Adv Energy Mater* 9 (2019) 1-13.

[11] J.W. Lai, B.W. Huang, X.F. Miao, N.V. Thang, X.M. You, M. Maschek, L. van Eijck, D.C. Zeng, N. van Dijk, E. Brück, Combined effect of annealing temperature and vanadium substitution for mangetocaloric $Mn_{1.2-x}V_xFe_{0.75}P_{0.5}Si_{0.5}$ alloys, *J Alloy Compd* 803 (2019) 671-677.

[12] J.W. Lai, X. Tang, H. Sepehri-Amin, K. Hono, Tuning transition temperature of magnetocaloric $Mn_{1.8}Fe_{0.2}(P_{0.59}Si_{0.41})_x$ alloys for cryogenic magnetic refrigeration, *Scripta Mater* 183 (2020) 127-132.

[13] N.H. Dung, Z.Q. Ou, L. Caron, L. Zhang, D.T.C. Thanh, G.A. de Wijs, R.A. de Groot, K.H.J. Buschow, E. Brück, Mixed magnetism for refrigeration and energy conversion, *Adv Energy Mater* 1 (2011) 1215-1219.

[14] X.F. Miao, L. Caron, P. Roy, N.H. Dung, L. Zhang, W.A. Kockelmann, R.A. de Groot, N.H. van Dijk, E. Brück, Tuning the phase transition in transition-metal-based magnetocaloric compounds, *Phys Rev B* 89 (2014) 1-6.

[15] H. Yibole, F. Guillou, L. Caron, E. Jimenez, F.M.F. de Groot, P. Roy, R. de Groot, N.H. van Dijk, E. Brück, Moment evolution across the ferromagnetic phase transition of giant magnetocaloric (Mn,Fe)₂(P,Si,B) compounds, *Phys Rev B* 91 (2015) 1-10.

[16] M.F.J. Boeije, P. Roy, F. Guillou, H. Yibole, X.F. Miao, L. Caron, D. Banerjee, N.H. van Dijk, R.A. de Groot, E. Brück, Efficient room-temperature cooling with magnets, *Chem Mater* 28 (2016) 4901-4905.

[17] V. Chaudhary, Z. Wang, A. Ray, I. Sridhar, R.V. Ramanujan, Self pumping magnetic cooling, *J Phys D Appl Phys* 50 (2017) 03LT03

[18] D.J. Silva, B.D. Bordalo, A.M. Pereira, J. Ventura, J.P. Araujo, Solid state magnetic refrigerator, *Appl Energ* 93 (2012) 570-574.

[19] K. Klinar, M.M. Rojo, Z. Kutnjak, A. Kitanovski, Toward a solid-state thermal diode for room-temperature magnetocaloric energy conversion, *J Appl Phys* 127 (2020) 234101

[20] A. Kitanovski, P.W. Egolf, Innovative ideas for future research on magnetocaloric technologies, *Int J Refrig* 33 (2010) 449-464.

[21] S. Pal, A. Datta, S. Sen, A. Mukhopdhyay, K. Bandopadhyay, R. Ganguly, Characterization of a ferrofluid-based thermomagnetic pump for microfluidic applications, *J Magn Magn Mater* 323 (2011) 2701-2709.

[22] D.N. Ba, L. Becerra, N. Casaretto, J.E. Duvauchelle, M. Marangolo, S. Ahmim, M. Almanza, M. LoBue, Magnetocaloric gadolinium thick films for energy harvesting applications, *Aip Adv* 10 (2020) 1-4.

[23] D.N. Ba, Y.L. Zheng, L. Becerra, M. Marangolo, M. Almanza, M. LoBue, Magnetocaloric effect in flexible, free-standing gadolinium thick films for energy conversion applications, *Phys Rev Appl* 15 (2021) 064045.

[24] X.L. Liu, Y.F. Zhang, Y.Y. Wang, W.J. Zhu, G.L. Li, X.W. Ma, Y.H. Zhang, S.Z. Chen, S. Tiwari, K.J. Shi, S.W. Zhang, H.M. Fan, Y.X. Zhao, X.J. Liang, Comprehensive understanding of magnetic hyperthermia for improving antitumor therapeutic efficacy, *Theranostics* 10 (2020) 3793-3815.

[25] J.B. Li, Y. Qu, J. Ren, W.Z. Yuan, D.L. Shi, Magnetocaloric effect in magnetothermally-responsive nanocarriers for hyperthermia-triggered drug release, Nanotechnology 23 (2012) 505706

[26] T. Yadav, R. Yadav, D. Singh, Mechanical milling: A top down approach for the synthesis of nanomaterials and nanocomposites, *Nanoscience and Nanotechnology* 2 (2012) 22-48.

[27] F. Guillou, H. Yibole, Z.Q. Ou, E. Brück, O. Tegus, Large recalescence-like event at the first cooling across the magnetic transition of (Mn,Fe)$_2$(P,Si) magnetocaloric materials, *Scripta Mater* 160 (2019) 81-85.

[28] H.M. Rietveld, A profile refinement method for nuclear and magnetic structures, *J Appl Crystallogr* 2 (1969) 65-71.

[29] R.P. Hermann, O. Tegus, E. Brück, K.H.J. Buschow, F.R. de Boer, G.J. Long, F. Grandjean, Mössbauer spectral study of the magnetocaloric FeMnP$_{1-x}$As$_x$ compounds, *Phys Rev B* 70 (2004) 1-9.

[30] X.F. Miao, S.Y. Hu, F. Xu, E. Brück, Overview of magnetoelastic coupling in (Mn, Fe)$_2$(P, Si)-type magnetocaloric materials, *Rare Metals* 37 (2018) 723-733.

[31] U. Holzwarth, N. Gibson, The Scherrer equation versus the 'Debye-Scherrer equation', *Nat Nanotechnol* 6 (2011) 534-534.

[32] G.S. Song, M. Staiger, M. Kral, Some new characteristics of the strengthening phase in beta-phase magnesium-lithium alloys containing aluminum and beryllium, *Mat Sci Eng a-Struct* 371 (2004) 371-376.

[33] H.G. Jiang, M. Ruhle, E.J. Lavernia, On the applicability of the x-ray diffraction line profile analysis in extracting grain size and microstrain in nanocrystalline materials, *J Mater Res* 14 (1999) 549-559.

[34] Z. Zhang, F. Zhou, E.J. Lavernia, On the analysis of grain size in bulk nanocrystalline materials via X-ray diffraction, *Metall Mater Trans A* 34a (2003) 1349-1355.

[35] V. Sanchez-Alarcos, V. Recarte, J.I. Perez-Landazabal, S. Larumbe, R. Caballero-Flores, I. Unzueta, J.A. Garcia, F. Plazaola, J.A. Rodriguez-Velamazan, Mechanically induced disorder and crystallization process in Ni-Mn-In ball-milled alloys, *J Alloy Compd* 689 (2016) 983-991.

[36] D. Wu, H. Kahn, J.C. Dalton, G.M. Michal, F. Ernst, A.H. Heuer, Orientation dependence of nitrogen supersaturation in austenitic stainless steel during low-temperature gas-phase nitriding, *Acta Mater* 79 (2014) 339-350.

[37] Y.Z. Li, Y.B. Li, Y.M. Sun, B. Butz, K. Yan, A.L. Koh, J. Zhao, A. Pei, Y. Cui, Revealing nanoscale passivation and corrosion mechanisms of reactive battery materials in gas environments, *Nano Lett* 17 (2017) 5171-5178.

[38] M. Fries, L. Pfeuffer, E. Bruder, T. Gottschall, S. Ener, L.V.S. Diop, T. Grob, K.P. Skokov, O. Gutfleisch, Microstructural and magnetic properties of Mn-Fe-P-Si (Fe₂P-type) magnetocaloric compounds, *Acta Mater* 132 (2017) 222-229.

[39] F.A. Mohamed, A dislocation model for the minimum grain size obtainable by milling, *Acta Mater* 51 (2003) 4107-4119.

[40] Z. Gercsi, E.K. Delczeg-Czirjak, L. Vitos, A.S. Wills, A. Daoud-Aladine, K.G. Sandeman, Magnetoelastic effects in doped Fe₂P, *Phys Rev B* 88 (2013) 024417.

[41] B.D. Cullity, C.D. Grahem, Introduction to Magnetic Materials, 2008.

[42] O. Gutfleisch, T. Gottschall, M. Fries, D. Benke, I. Radulov, K.P. Skokov, H. Wende, M. Gruner, M. Acet, P. Entel, M. Farle, Mastering hysteresis in magnetocaloric materials, *Philos T R Soc A* 374 (2016) 1-21.

[43] D. Michels, C.E. Krill, R. Birringer, Grain-size-dependent Curie transition in nanocrystalline Gd: the influence of interface stress, *J Magn Magn Mater* 250 (2002) 203-211.

[44] A.S. Bolokang, M.J. Phasha, Thermal analysis on the curie temperature of nanocrystalline Ni produced by ball milling, *Adv Powder Technol* 22 (2011) 518-521.

[45] Z. Zhao, V. Buscaglia, M. Viviani, M.T. Buscaglia, L. Mitoseriu, A. Testino, M. Nygren, M. Johnsson, P. Nanni, Grain-size effects on the ferroelectric behavior of dense nanocrystalline BaTiO$_3$ ceramics, *Phys Rev B* 70 (2004) 1-8.

[46] A.F. Manchon-Gordon, R. Lopez-Martin, A. Vidal-Crespo, J.J. Ipus, J.S. Blazquez, C.F. Conde, A. Conde, Distribution of transition temperatures in magnetic transformations: sources, effects and procedures to extract information from experimental data, *Metals-Basel* 10 (2020) 1-23.

[47] Q.Y. Dong, B.G. Shen, S.L. He, H.W. Jiang, W. Zheng, J.R. Sun, Effect of crystal grain dimension on the magnetic properties and magnetocaloric effects in DyCuAl compound, *J Nanosci Nanotechno* 12 (2012) 1040-1043.

[48] V.M. Andrade, R.J.C. Vivas, S.S. Pedro, J.C.G. Tedesco, A.L. Rossi, A.A. Coelho, D.L. Rocco, M.S. Reis, Magnetic and magnetocaloric properties of La$_{0.6}$Ca$_{0.4}$MnO$_3$ tunable by particle size and dimensionality, *Acta Mater* 102 (2016) 49-55.

[49] T. Gottschall, D. Benke, M. Fries, A. Taubel, I.A. Radulov, K.P. Skokov, O. Gutfleisch, A matter of size and stress: Understanding the first-order transition in materials for solid-state refrigeration, *Adv Funct Mater* 27 (2017) 1-6.

[50] F.X. Hu, L. Chen, J. Wang, L.F. Bao, J.R. Sun, B.G. Shen, Particle size dependent hysteresis loss in La$_{0.7}$Ce$_{0.3}$Fe$_{11.6}$Si$_{1.4}$C$_{0.2}$ first-order systems, *Appl Phys Lett* 100 (2012) 1-4.

[51] X.B. Shi, F.M. Guo, J.S. Zhang, H.L. Ding, L.S. Cui, Grain size effect on stress hysteresis of nanocrystalline NiTi alloys, *J Alloy Compd* 688 (2016) 62-68.

[52] I. Aruna, B.R. Mehta, L.K. Malhotra, S.M. Shivaprasad, Stability and hydrogenation of "bare" gadolinium nanoparticles, *Adv Funct Mater* 15 (2005) 131-137.

[53] N.R. Checca, W.S. Torres, R.J. Caraballo-Vivas, M.A.V. Heringer, D.R. Sanchez, A. Rossi, M.S. Reis, D.L. Rocco, Off-stoichiometry LaFe$_5$Si$_x$ cubic phase induced by the reduced size of the nanoparticles produced by pulsed laser deposition, *J Alloy Compd* 803 (2019) 417-423.

[54] J.C. Feng, R. Geutjens, N.V. Thang, J.J. Li, X.A. Guo, A. Keri, S. Basak, G. Galbacs, G. Biskos, H. Nirschl, H.W. Zandbergen, E. Brück, A. Schmidt-Ott, Magnetic phase transition in spark-produced ternary LaFeSi nanoalloys, *Acs Appl Mater Inter* 10 (2018) 6073-6078.

[55] N.R. Checca, R.J. Caraballo-Vivas, A.A. Coelho, A. Rossi, N.M. Fortunato, F. Mohseni, J.N. Goncalves, J.S. Amaral, D.L. Rocco, M.S. Reis, Experimental realisation of off-stoichiometric Fe-Mn-Si full Heusler alloy with hexagonal crystal structure by pulsed laser deposition, *Mater Design* 143 (2018) 268-273.

[56] V. Sepelak, I. Bergmann, A. Feldhoff, P. Heitjans, F. Krumeich, D. Menzel, F.J. Litterst, S.J. Campbell, K.D. Becker, Nanocrystalline nickel ferrite, NiFe$_2$O$_4$: Mechanosynthesis, nonequilibrium cation distribution, canted spin arrangement, and magnetic behavior, *J Phys Chem C* 111 (2007) 5026-5033.

[57] F.L. Zhang, C.Y. Wang, M. Zhu, Nanostructured WC/Co composite powder prepared by high energy ball milling, *Scripta Mater* 49 (2003) 1123-1128.

[58] D. Raabe, S. Ohsaki, K. Hono, Mechanical alloying and amorphization in Cu-Nb-Ag in situ composite wires studied by transmission electron microscopy and atom probe tomography, *Acta Mater* 57 (2009) 5254-5263.

[59] N.V. Thang, X.F. Miao, N.H. van Dijk, E. Brück, Structural and magnetocaloric properties of (Mn,Fe)$_2$(P,Si) materials with added nitrogen, *J Alloy Compd* 670 (2016) 123-127.

[60] P.D. Nezhadfar, K. Anderson-Wedge, S.R. Daniewicz, N. Phan, S. Shao, N. Shamsaei, Improved high cycle fatigue performance of additively manufactured 17-4 PH stainless steel via in-process refining micro-/defect-structure, *Addit Manuf* 36 (2020) 1-15.

[61] K. Koyama, H. Fujii, Nitrogen gas-solid reaction process and basic magnetism of the interstitially modified rare-earth 3d transition-metal nitrides R$_2$Fe$_{17}$N$_3$ (R = Y, Ce, Nd, Sm) and Y$_2$Co$_{17}$N$_3$, *Phys Rev B* 61 (2000) 9475-9493.

[62] T.K. Kim, M. Takahashi, New magnetic material having ultrahigh magnetic-moment, *Appl Phys Lett* 20 (1972) 492-494.

[63] P.A. Yadav, A.V. Deshmukh, K.P. Adhi, B.B. Kale, N. Basavaih, S.I. Patil, Role of grain size on the magnetic properties of La$_{0.7}$Sr$_{0.3}$MnO$_3$, *J Magn Magn Mater* 328 (2013) 86-90.

[64] J.A. Turcaud, H.N. Bez, E. Ruiz-Trejo, C.R.H. Bahl, K.K. Nielsen, A. Smith, L.F. Cohen, Influence of manganite powder grain size and Ag-particle coating on the magnetocaloric effect and the active magnetic regenerator performance, *Acta Mater* 97 (2015) 413-418.

[65] J. Curiale, M. Granada, H.E. Troiani, R.D. Sanchez, A.G. Leyva, P. Levy, K. Samwer, Magnetic dead layer in ferromagnetic manganite nanoparticles, *Appl Phys Lett* 95 (2009) 1-3.

[66] K.L. Krycka, R.A. Booth, C.R. Hogg, Y. Ijiri, J.A. Borchers, W.C. Chen, S.M. Watson, M. Laver, T.R. Gentile, L.R. Dedon, S. Harris, J.J. Rhyne, S.A. Majetich, Core-shell magnetic morphology of structurally uniform magnetite nanoparticles, *Phys Rev Lett* 104 (2010) 1-4.

[67] S. Disch, E. Wetterskog, R.P. Hermann, A. Wiedenmann, U. Vainio, G. Salazar-Alvarez, L. Bergstrom, T. Bruckel, Quantitative spatial magnetization distribution in iron oxide nanocubes and nanospheres by polarized small-angle neutron scattering, *New J Phys* 14 (2012) 1-11.

[68] T. Sarkar, A.K. Raychaudhuri, A.K. Bera, S.M. Yusuf, Effect of size reduction on the ferromagnetism of the manganite $La_{1-x}Ca_xMnO_3$ (x=0.33), *New J Phys* 12 (2010) 123026.

[69] F.M. Li, J.Q. Feng, J. Yi, G. Wang, J.Q. Wang, J.T. Huo, Magnetocaloric properties of $LaFe_{11.4}Si_{1.6}$ based amorphous alloys, *J Alloy Compd* 845 (2020) 1-7.

[70] J.F. Loffler, J.P. Meier, B. Doudin, J.P. Ansermet, W. Wagner, Random and exchange anisotropy in consolidated nanostructured Fe and Ni: Role of grain size and trace oxides on the magnetic properties, *Phys Rev B* 57 (1998) 2915-2924.

[71] S.A. Majetich, J.H. Scott, E.M. Kirkpatrick, K. Chowdary, K. Gallagher, M.E. McHenry, Magnetic nanoparticles and magnetocrystalline anisotropy, *Nanostruct Mater* 9 (1997) 291-300.

[72] C. Kittel, Introduction to solid state physics, (1976).

[73] H. Yibole, F. Guillou, Y.K. Huang, G.R. Blake, A.J.E. Lefering, N.H. van Dijk, E. Brück, First-order ferromagnetic transition in single-crystalline (Mn,Fe)₂(P,Si), *Appl Phys Lett* 107 (2015) 1-5.

[74] X.W. Zhou, R.A. Johnson, H.N.G. Wadley, Misfit-energy-increasing dislocations in vapor-deposited CoFe/NiFe multilayers, *Phys Rev B* 69 (2004) 1-10.

[75] M.E. Gruner, W. Keune, B. Roldan Cuenya, C. Weis, J. Landers, S.I. Makarov, D. Klar, M.Y. Hu, E.E. Alp, J. Zhao, M. Krautz, O. Gutfleisch, H. Wende, Element-resolved thermodynamics of magnetocaloric LaFe$_{13-x}$Si$_x$, *Phys Rev Lett* 114 (2015) 1-6.

[76] Y.H. Qu, D.Y. Cong, X.M. Sun, Z.H. Nie, W.Y. Gui, R.G. Li, Y. Ren, Y.D. Wang, Giant and reversible room-temperature magnetocaloric effect in Ti-doped Ni-Co-Mn-Sn magnetic shape memory alloys, *Acta Mater* 134 (2017) 236-248.

[77] A. Zelenakova, P. Hrubovcak, O. Kapusta, V. Zelenak, V. Franco, Large magnetocaloric effect in fine Gd$_2$O$_3$ nanoparticles embedded in porous silica matrix, *Appl Phys Lett* 109 (2016) 122412.

[78] J. Li, S. Ma, H. Wang, W.J. Gong, J.J. Jiang, S.J. Li, Y. Wang, D.Y. Geng, Z.D. Zhang, Enhanced cryogenic magnetocaloric effect induced by small size GdNi$_5$ nanoparticles, *J Mater Sci Technol* 30 (2014) 973-978.

[79] D. Doblas, L.M. Moreno-Ramirez, V. Franco, A. Conde, A.V. Svalov, G.V. Kurlyandskaya, Nanostructuring as a procedure to control the field dependence of the magnetocaloric effect, *Mater Design* 114 (2017) 214-219.

[80] A.F. Manchon-Gordon, A. Gomez, J.J. Ipus, J.S. Blazquez, C.F. Conde, A. Conde, Milling effects on the distribution of Curie temperatures and magnetic properties of Ni-doped La$_{0.7}$Ca$_{0.3}$MnO$_3$ compounds, *J Alloy Compd* 848 (2020) 1-7.

[81] D.M. Rajkumar, M.M. Raja, R. Gopalan, V. Chandrasekaran, Magnetocaloric effect in high-energy ball-milled Gd$_5$Si$_2$Ge$_2$ and Gd$_5$Si$_2$Ge$_2$/Fe nanopowders, *J Magn Magn Mater* 320 (2008) 1479-1484.

[82] H. Yang, Y.H. Zhu, T. Xian, J.L. Jiang, Synthesis and magnetocaloric properties of La$_{0.7}$Ca$_{0.3}$MnO$_3$ nanoparticles with different sizes, *J Alloy Compd* 555 (2013) 150-155.

[83] S.P. Mathew, S.N. Kaul, Tuning magnetocaloric effect with nanocrystallite size, *Appl Phys Lett* 98 (2011) 1-3.

[84] J.M. Logan, D. Rosenmann, T. Sangpo, M.V. Holt, P. Fuesz, I. McNulty, Tungsten-encapsulated gadolinium nanoislands with enhanced magnetocaloric response, *Appl Phys Lett* 111 (2017) 1-5.

[85] J.Y. Cheng, T. Li, S. Ullah, F. Luo, H. Wang, M. Yan, G.P. Zheng, Giant magnetocaloric effect in nanostructured Fe-Co-P amorphous alloys enabled through pulse electrodeposition, *Nanotechnology* 31 (2020) 1-9.

[86] V. Chaudhary, R.V. Ramanujan, Magnetic and structural properties of high relative cooling power $(Fe_{70}Ni_{30})_{92}Mn_8$ magnetocaloric nanoparticles, *J Phys D Appl Phys* 48 (2015) 1-7.

[87] V. Chaudhary, R.V. Ramanujan, Magnetocaloric properties of Fe-Ni-Cr nanoparticles for active cooling, *Sci Rep* 6 (2016) 1-9.

[88] P. Alvarez-Alonso, J.L.S. Llamazares, C.F. Sanchez-Valdes, G.J. Cuello, V. Franco, P. Gorria, J.A. Blanco, On the broadening of the magnetic entropy change due to Curie temperature distribution, *J Appl Phys* 115 (2014) 1-3.

[89] J. Ipus, H. Ucar, M. McHenry, Near room temperature magnetocaloric response of an (FeNi)ZrB alloy, *IEEE transactions on magnetics* 47 (2011) 2494-2497.

[90] J.Y. Law, V. Franco, L.M. Moreno-Ramirez, A. Conde, D.Y. Karpenkov, I. Radulov, K.P. Skokov, O. Gutfleisch, A quantitative criterion for determining the order of magnetic phase transitions using the magnetocaloric effect, *Nat Commun* 9 (2018) 1-9.

[91] V. Franco, J.S. Blazquez, A. Conde, Field dependence of the magnetocaloric effect in materials with a second order phase transition: a master curve for the magnetic entropy change, *Appl Phys Lett* 89 (2006) 1-3.

[92] V. Franco, A. Conde, Scaling laws for the magnetocaloric effect in second order phase transitions: from physics to applications for the characterization of materials, *Int J Refrig* 33 (2010) 465-473.

[93] J.A. Nelson, L.H. Bennett, M.J. Wagner, Solution synthesis of gadolinium nanoparticles, *J Am Chem Soc* 124 (2002) 2979-2983.

[94] A.H. Lu, E.L. Salabas, F. Schuth, Magnetic nanoparticles: Synthesis, protection, functionalization, and application, *Angew Chem Int Edit* 46 (2007) 1222-1244.

[95] V. Sepelak, A. Feldhoff, P. Heitjans, F. Krumeich, D. Menzel, F.J. Litterst, I. Bergmann, K.D. Becker, Nonequilibrium cation distribution, canted spin arrangement, and enhanced magnetization in nanosized $MgFe_2O_4$ prepared by a one-step mechanochemical route, *Chem Mater* 18 (2006) 3057-3067.

[96] A.G. Roca, J.F. Marco, M.D. Morales, C.J. Serna, Effect of nature and particle size on properties of uniform magnetite and maghemite nanoparticles, *J Phys Chem C* 111 (2007) 18577-18584.

[97] P.C. Morais, A.L. Tronconi, K.S. Neto, Temperature-dependence of the mossbauer linewidth of superparamagnetic particles of ferric hydroxysulfate, *J Appl Phys* 57 (1985) 1291-1293.

[98] M.J.N. Isfahani, M. Myndyk, V. Sepelak, J. Amighian, A Mössbauer effect investigation of the formation of MnZn nanoferrite phase, *J Alloy Compd* 470 (2009) 434-437.

[99] Roggwill.P, W. Kundig, Mössbauer-spectra of superparamagnetic Fe_3O_4, *Solid State Commun* 12 (1973) 901-903.

[100] J.T. Batley, M. Nguyen, I. Kamboj, C. Korostynski, E.S. Aydil, C. Leighton, Quantitative understanding of superparamagnetic blocking in thoroughly characterized Ni nanoparticle assemblies, *Chem Mater* 32 (2020) 6494-6506.

[101] M. Tadic, S. Kralj, M. Jagodic, D. Hanzel, D. Makovec, Magnetic properties of novel superparamagnetic iron oxide nanoclusters and their peculiarity under annealing treatment, *Appl Surf Sci* 322 (2014) 255-264.

Supplementary Information for Chapter 3

Synthesis and structural analysis:
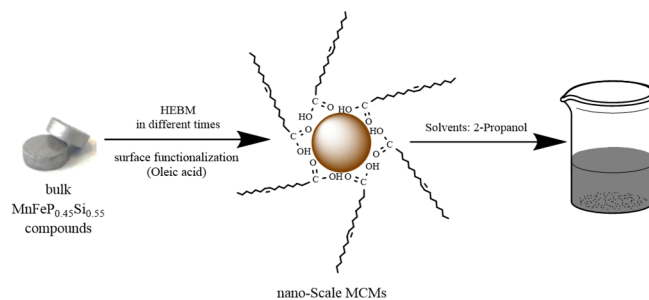
Figure S3.1 Schematic illustration of the synthesis of MnFeP$_{0.45}$Si$_{0.55}$ nanoscale magnetocaloric materials (MCMs).
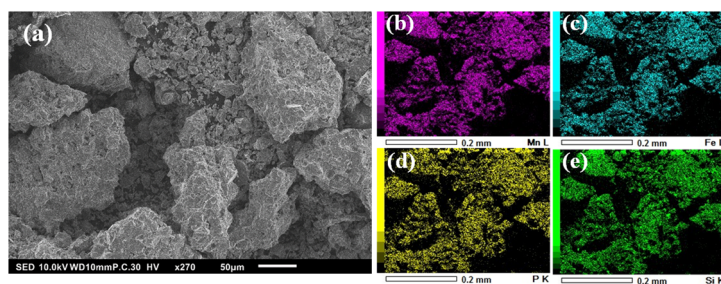

Figure S3.2 (a) Back-scattered SEM image of the raw BM-0h material. SEM-EDS mapping images for (b) Mn, (c) Fe, (d) P, (e) Si.
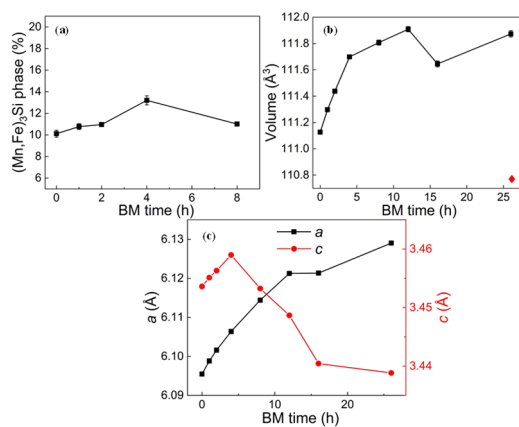

Figure S3.3 Crystal refinement results of (a) weight fraction of the (Mn,Fe)$_3$Si impurity phase, (b) volume change as a function of the ball milling (BM) time (The data point marked with the red diamond indicates the volume of the BM-26h-600°C-N$_2$ sample) and (c) the changes in the lattice parameters *a* and *c*.

Transmission electron microscopy:
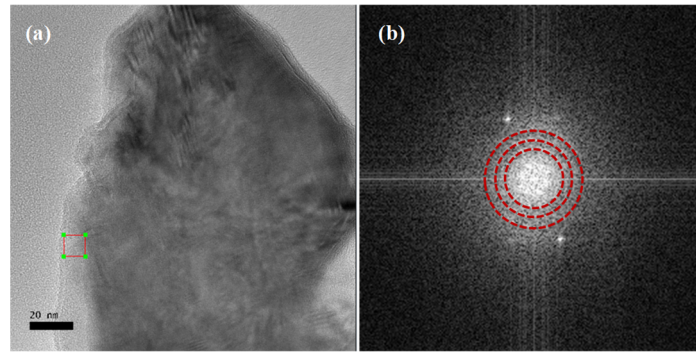
Figure S3.4 (a) HRTEM image of nanoparticles (NPs) from the sample with a BM time of 26 h (BM-26h). (b) Corresponding FFT patterns for the amorphous shell in the region of red box in (a).
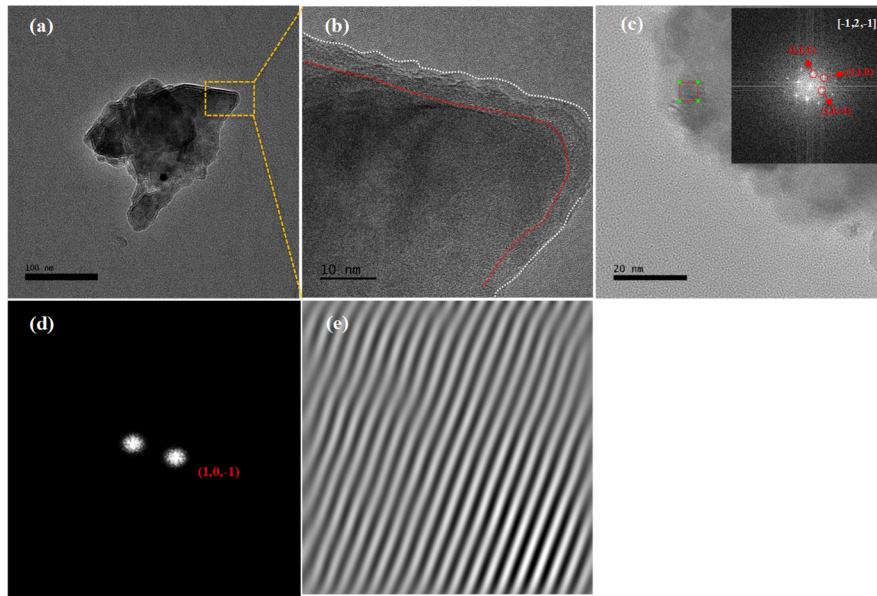

Figure S3.5 (a) HRTEM image of the BM-26h-600°C-N₂ sample. (b) Enlarged image from the region in (a). (c) Corresponding FFT patterns in the region of red box. (d) Selected diffraction spots from (c) as input for the IFFT. (e) IFFT image corresponding to the (1,0,-1) plane.
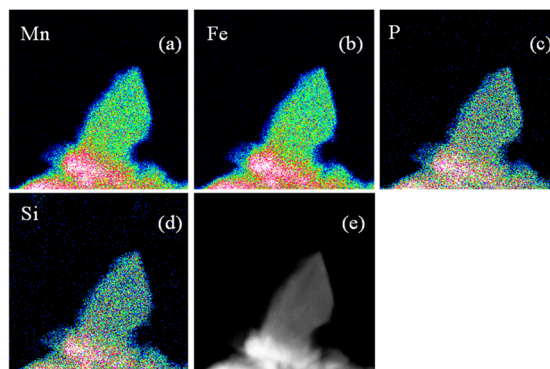
Figure S3.6 HRTEM-EDS elemental mapping of the BM-26h sample: (a) Mn; (b) Fe; (c) P; (d) Si; (e) original image.
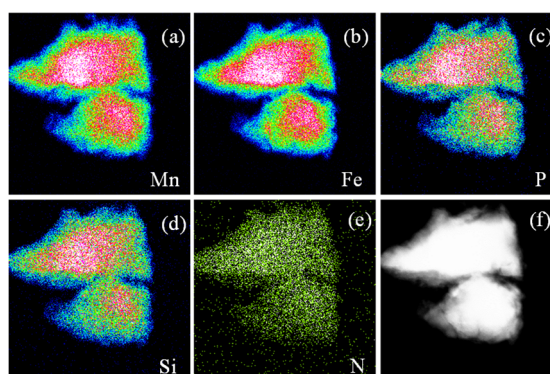

Figure S3.7 HRTEM-EDS elemental mapping of the post-annealed BM-26h-600°C-N$_2$ sample: (a) Mn; (b) Fe; (c) P; (d) Si; (e) N; (f) original image.

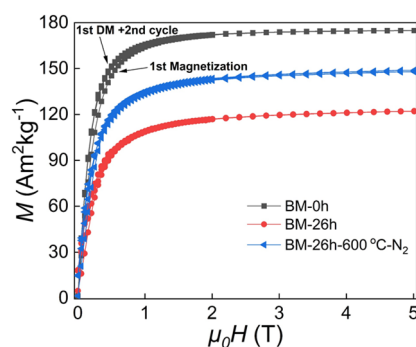## Magnetisation measurements and Mössbauer spectroscopy:

Figure S3.8 First and second cycle for the isothermal field dependence of magnetization (*M-H*) curves at a temperature of 5 K for the BM-0h, BM-26h and BM-26h-600°C-N$_2$ samples. (DM: demagnetization).
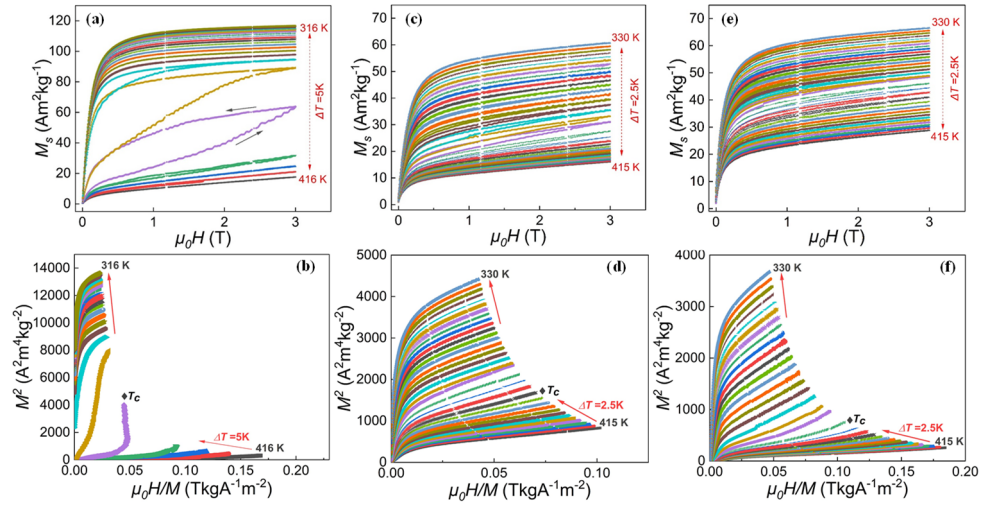
Figure S3.9 (a-c-e) Magnetisation as a function of the applied magnetic field (*M-H* curves) at different temperatures in applied fields up to 3 T for the BM-0h, BM-26h and BM-26h-600°C-N₂ samples, respectively. (b-d-f) Corresponding Arrott plots from (a-c-e).
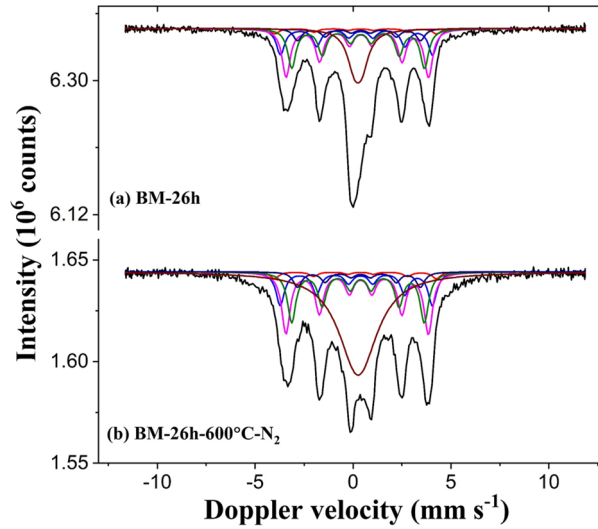

Figure S3.10 Mössbauer spectra for the (a) BM-0h, (b) BM-26h and (c) BM-26h-600°C-N₂ samples recorded at a temperature of 130 K.
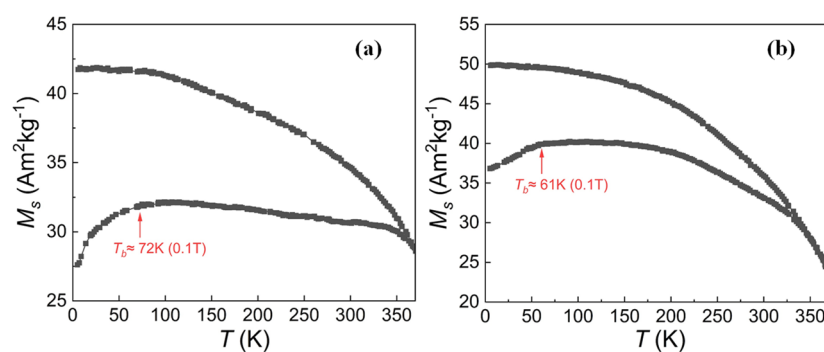
Figure S3.11 Magnetisation as a function of temperature in ZFC-FC condition in a field of 0.1 T for the (a) BM-26h and (b) BM-26h-600°C-N₂ samples.
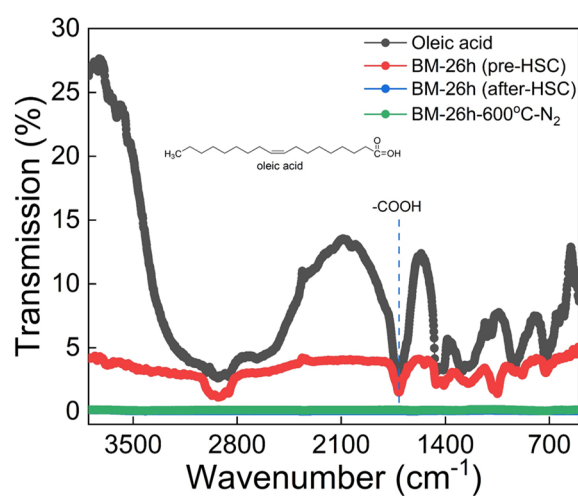
Infrared spectra:

Figure S3.12 The infrared spectra for pure surfactant with the BM-26h (pre-HSC), BM-26h (after HSC) and BM-26h-600°C-N₂ samples. The peaks at about 2931 and 2852 cm^{-1} are related to asymmetric and symmetric vibrations of the −CH₂ group and the peaks about 1412 and 1282 cm^{-1} are bending vibrations of the −CH₂ group. The specific peak at around 1712 cm^{-1} (marked by the blue dashed line) corresponds to a stretching vibration of the -C=O group. (HSC: high speed centrifugation)

Chapter 4 Impact of F and S doping on $(Mn,Fe)_2(P,Si)$ giant magnetocaloric materials
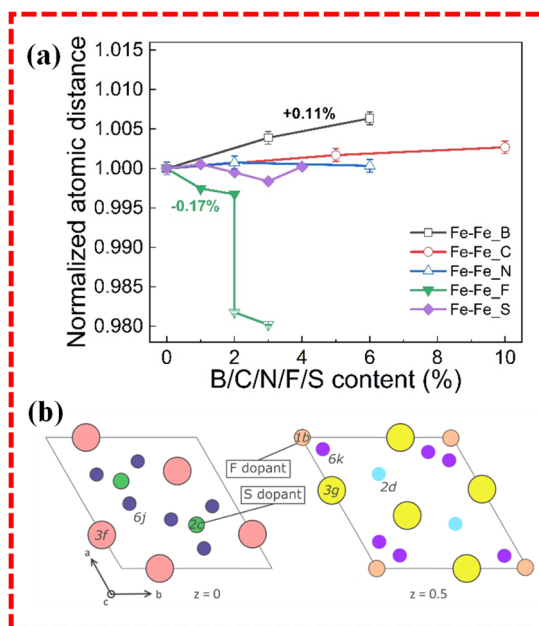
This chapter is based on:

Abstract

The quarternary $(Mn,Fe)_2(P,Si)$-based materials with a giant magnetocaloric effect (GMCE) at the ferromagnetic transition T_C are promising bulk materials for solid-state magnetic refrigeration. In the present study we demonstrate that doping with the light elements fluorine and sulfur can be used to adjust T_C near room temperature and tune the magnetocaloric properties. For F doping the first-order magnetic transition (FOMT) of $Mn_{0.60}Fe_{1.30}P_{0.64}Si_{0.36}F_x$ (x = 0.00, 0.01, 0.02, 0.03) is enhanced, which is explained by an enhanced magnetoelastic coupling. The magnetic entropy change $|\Delta S_m|$ at a field change $(\Delta\mu_0 H)$ of 2 T markedly improved by 30% from 14.2 $Jkg^{-1}K^{-1}$ (x = 0.00) at 335 K to 20.2 $Jkg^{-1}K^{-1}$ (x = 0.03) at 297 K. For the F doped material the value of $|\Delta S_m|$ for $\Delta\mu_0 H$ = 1 T reaches 11.6 $Jkg^{-1}K^{-1}$ at 294 K, which is consistent with the calorimetric data (12.4 $Jkg^{-1}K^{-1}$). Neutron diffraction experiments reveal enhanced magnetic moments by F doping in agreement with the prediction of DFT calculation. For S doping in $Mn_{0.60}Fe_{1.25}P_{0.66-y}Si_{0.34}S_y$ (y = 0.00, 0.01, 0.02, 0.03, 0.04) three impurity phases have been found from microstructural analysis, which reduce the stability of the FOMT in the main phase and decrease T_C, e.g. the $|\Delta S_m|$ reduces from 7.9(12.6) $Jkg^{-1}K^{-1}$ (332 K) for the undoped sample to 3.4(6.2) $Jkg^{-1}K^{-1}$ (313 K) for the maximum doped sample for $\Delta\mu_0 H$ = 1(2) T. Neutron diffraction experiments combined with first-principles theoretical calculation, distinguish the occupation of F/S dopants and the tuning mechanism for light element doping, corresponding to subtle structural changes and a strengthening of the covalent bonding between metal and metalloid atoms. It is found that the light elements F and S can effectively regulate the magnetocaloric properties and provide fundamental understanding of $(Mn,Fe)_2(P,Si)$-based intermetallic compounds.

66

4.1 Introduction

The giant magnetocaloric effect (GMCE), accompanied by an isothermal magnetic entropy change (ΔS_m) and an adiabatic temperature change (ΔT_{ad}), enables several promising applications in the form of: (*i*) magnetic refrigeration [1], (*ii*) magnetic heat pumps [2] and (*iii*) thermomagnetic motors and generators to covert low-temperature waste heat into electricity [3, 4]. In the last two decades, numerous first-order magnetic transition (FOMT) magnetocaloric materials (MCMs) that demonstrate a GMCE have sprung up, including Gd$_5$(Si$_2$Ge$_2$) [5], (Mn,Fe)$_2$(P,*X*)-based compounds (*X* = As, Ge, Si) [6], La(Fe,Si)$_{13}$-based materials [7], Ni-Mn-*X* based magnetic Heusler compounds (*X* = Ga, In, Sn, Sb) [8], FeRh [9], Mn$_2$Sb based alloys [10] and Mn-*M*-*X* (*M* = Co, Ni and *X* = Si, Ge) alloys [11]. Within these MCMs the (Mn,Fe)$_2$(P,Si)-based alloys with a hexagonal crystal structure have attracted considerable attention because they are rare-earth free, have no toxic elements, are low cost and have a tunable Curie temperature (T_C). This materials system demonstrates a strong magnetoelastic coupling controlled by the magnetic, structural and electronic degrees of freedom.

Different strategies have been proposed to further optimize the GMCE performance, for example engineering chemical pressure (by atom substitution or interstitial doping), applying hydrostatic pressure or multiple mechanical stimuli (multicaloric effect) [12, 13]. Doping with light elements (e.g. H, B, C, N) can be an effective method to tailor the magnetic properties. For example, in another prototypical magnetoelastic MCM system La(Fe,Si)$_{13}$ the insertion of H (as well as B and C) atoms significantly increases T_C [14]. For NiMn-based Heusler compounds substitutional B or interstitial C are both helpful to adjust the magnetostructural phase transition [15-18]. Specifically for (Mn,Fe)$_2$(P,Si)-based materials B/C/N atoms present positive effects. For example, substitution of B (up to 7.5%) in MnFe$_{0.95}$P$_{0.595}$B$_{0.075}$Si$_{0.33}$ can dramatically reduce the thermal hysteresis (ΔT_{hys}) from 75 K to only 1.6 K, and thereby effectively improve the reversibility of the GMCE [19]. Compared to doping with metal elements (e.g. V, Ni, Co, Zr, Nb, Mo) [20-23], the doping with light elements provides a unique platform to investigate the nature of the magnetoelastic isostructural transition for this metal-metalloid system [24]. In addition to the B/C/N doping of (Mn,Fe)$_2$(P,Si)-based MCMs, doping with F and S, which have high electronegativity values of $\chi_F \approx 4.0$ and 2.5 respectively [25], enables a systematic exploration on the question of how light elements influence the fundamental magnetic properties. It is noteworthy that, from the classical Pauling's scale [26, 27], the element F ($\chi_F \approx 4$) possesses the highest electronegativity value [25] which can help us understand the role of the electrons within (Mn,Fe)$_2$(P,Si)-based MCMs, especially in comparison with other light elements like B. Additionally, S the neighboring element of P, is rarely reported for MCMs and the increase

in electronegativity from P ($\chi_F \approx 2.1$) to S ($\chi_F \approx 2.5$) can be considered dominant. For S the influence of the chemical pressure is expected to be limited as the atomic radius is very similar for P (r = 1.07 Å) and for S (r = 1.05 Å)[28]. These properties inspire and further motivate us to investigate the effects of F and S doping for (Mn,Fe)₂(P,Si)-based MCMs.

In the present study, the F and S doped $Mn_{0.60}Fe_{1.30}P_{0.64}Si_{0.36}F_x$ (x = 0.00, 0.01, 0.02, 0.03) and $Mn_{0.60}Fe_{1.25}P_{0.66-y}Si_{0.34}S_y$ (y = 0.00, 0.01, 0.02, 0.03, 0.04) alloys have successfully been produced. Here the thermodynamic, MCE and structural information is reported. It is found that F-doped materials show improved magnetic moments and GMCE performance. The increase in moments is in agreement with Density Functional Theory (DFT) calculations. Additional neutron diffraction (ND) experiments reveal that the MCE properties can be tuned by controlling the atomic distances among different metal-metal or metal-metalloid atom pairs. Electron Localization Function (ELF) calculations clarify that subtle changes in atomic distances as well as the covalent bonding, defined by the *p-d* hybridization, jointly control the GMCE properties of the (Mn,Fe)₂(P,Si)-based materials. Our current study illuminates how light elements affect the magnetoelastic coupling and the GMCE in metal-metalloid MCMs.

4.2 Experimental and computational procedures

The off-stoichiometric bulk $Mn_{0.60}Fe_{1.30}P_{0.64}Si_{0.36}F_x$ (x = 0.00, 0.01, 0.02, 0.03) and $Mn_{0.60}Fe_{1.25}P_{0.66-y}Si_{0.34}S_y$ (y = 0.00, 0.01, 0.02, 0.03, 0.04) MCMs were synthesized by solid-state chemical reaction [20]. Mn (99.9%), Fe (99.9%), red-P (99.7%), Si (99.9%), FeF₃ (97.0%) and FeS₂ (99.8%) powders with a total mass of 10 g were mixed and milled for 10 h at 380 rpm. The pressed cylindrical tablets were sealed in quartz tubes under 200 mbar Ar atmosphere and annealed for 25 h at 1373 K. Subsequently, these samples were rapidly quenched in cold water, followed by a pre-cooling process in liquid nitrogen to remove the so-called "virgin effect" [29]. Note that the ratio between metallic (Mn,Fe) and non-metallic (P,Si) in the nominal composition of the studied alloys has been chosen to deviate from 2:1 in order to achieve the smallest amount of impurity phases [30].

Differential scanning calorimetry (DSC) measurements were carried out using a commercial TA-Q2000 DSC calorimeter. The DSC measurements under different magnetic fields were performed in a home-built Peltier cell-based DSC, where the calorimetric ΔS_m and ΔT_{ad} were derived from specific heat measurements [31]. X-ray diffraction (XRD) patterns were collected using an Anton Paar TTK450 temperature-tunable sample chamber and a PANalytical X-pert Pro diffractometer with Cu K_α radiation. Neutron diffraction (ND) experiments were performed on the Polaris time-of-flight powder diffractometer at the ISIS

pulsed spallation neutron source (UK). About 6 g of powder sample was placed into a vanadium can (8 mm diameter) and neutron diffraction data were collected at room temperature (RT). Instrumental details can be found in ref. [32, 33]. The XRD and neutron patterns were analysed using Fullprof's implementation of the Rietveld refinement method [34]. Temperature-dependent magnetization (M-T) and field-dependent magnetization (M-H) curves were measured in a superconducting quantum interference device (SQUID, Quantum Design MPMS 5S) magnetometer. Scanning electron microscopy (SEM) was carried out on a JSM-7500F Field Emission Scanning Electron Microscope to study the morphology and composition.

First-principles calculations in the framework of the density functional theory (DFT) were performed using the Vienna *ab initio* simulation package (VASP) [35, 36]. The projector augmented wave (PAW) method [37, 38] was used with the generalized gradient approximation of Perdew-Burke-Ernzerhof [39] for the exchange correlation functional. Elastic constants are calculated by applying appropriate cell-volume conserving deformations [40-42]. In all calculations the following electrons were treated as valence electrons: $3p$, $4s$, $3d$ for Mn; $4s$ and $3d$ for Fe; $3s$ and $3p$ for P, Si and S; $2s$ and $2p$ for F. A 2×2×2 supercell based on a 9-atom unit cell with the composition $Mn_{0.5}Fe_{1.5}P_{0.67}Si_{0.33}$ was used in the calculations. All $3f$ sites were filled by Fe atoms while $3g$ sites were semi-randomly occupied by Fe and Mn atoms. Si atoms were inserted at the $1b$ site and P atoms at the $2c$ site in order to avoid the computational cost related to larger supercells to account for the positional disorder [42]. The structure was fully relaxed on a gamma-centered k-grid of 7×7×11 with the 2nd order Methfessel-Paxton method [43] and a smearing width of 0.05 eV. A smaller 1×1×2 supercell with a k-grid of 14×14×11 was used for calculations of the electron localization function. The kinetic energy cutoff was set at 500 eV, the force convergence tolerance was set to 0.1 meV/Å and the energies were converged to 1 μeV.

To determine the F and S site preference, the formation energies of the structures with dopants placed on all possible crystallographic sites were compared. The energy cost of forming each structure is calculated as the difference between the energies of doped (E_{doped}) and pure (E_{pure}) compounds minus the chemical potential of the dopant ($μ_d$) plus the chemical potential of the atom replaced by the dopant ($μ_s$):

$$E_f = E_{doped} + μ_s - (E_{pure} + μ_d) \hspace{2cm} (4.1)$$

Chemical potentials were calculated by first optimizing bcc iron, alpha manganese, diamond cubic silicon, orthorhombic sulfur and tetrahedral phosphorus and then using the resulting total energies per atom. For fluorine chemical potential was obtained from the total energy

of the isolated F$_2$ molecule. To investigate the type of the chemical bonds the electron localization function (ELF) [44] was analyzed. The ELF allows for an accurate characterization of the bond nature based on the electron densities. This characterization is based on a topological analysis of local quantum-mechanical functions related to the Pauli exclusion principle. The ELF represents the possibility of finding a second electron with the same spin in the vicinity of the reference electron. Higher ELF values correspond to areas with more localized electrons and indicate a stronger covalent bonding.

4.3 Results

The specific heat as a function of temperature (measured by zero-field DSC) for the Mn$_{0.60}$Fe$_{1.30}$P$_{0.64}$Si$_{0.36}$F$_x$ (x = 0.00, 0.01, 0.02, 0.03) materials is presented in **Figure 4.1a**. It is observed endothermic and exothermic peaks shift to lower temperatures with increasing F dopant content. The latent heat (L) of the phase transition has been estimated by $L = \int_{T_s}^{T_f} \frac{dQ}{dT} dT$, where dQ/dT is the change in heat flow with respect to temperature, and T_s and T_f are the start and end temperatures [45]. The entropy change at T_C corresponds to $\Delta S_{tot} = L/T_C$. The main thermodynamic parameters extracted from the DSC measurements are summarized in **Table 4.1**.
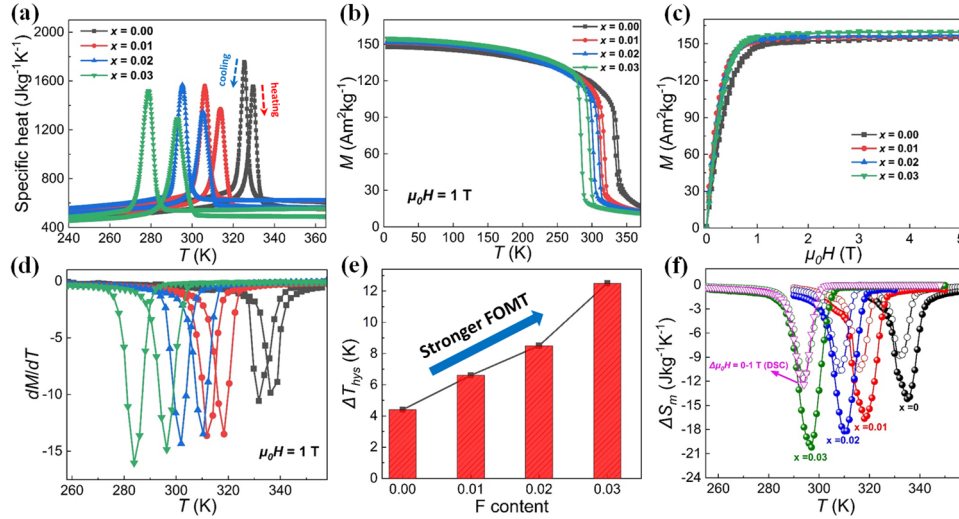

Figure 4.1 (a) Specific heat derived from DSC experiments for Mn$_{0.60}$Fe$_{1.30}$P$_{0.64}$Si$_{0.36}$F$_x$ (x = 0.00, 0.01, 0.02, 0.03) materials upon heating and cooling. (b) Isofield *M-T* curves for Mn$_{0.60}$Fe$_{1.30}$P$_{0.64}$Si$_{0.36}$F$_x$ (x = 0.00, 0.01, 0.02, 0.03) alloys in an applied field of 1 T. (c) Corresponding isothermal *M-H* curves as a function of applied field at 5 K. (d) Temperature dependence of *dM/dT* derived from the *M-T* curves. (e) ΔT_{hys} change for different F-doped materials. (f) ΔS_m change for a field change ($\Delta\mu_0 H$) of 1 T (open symbols) and 2 T (solid symbols) at different F contents. Note that the magenta curve is extracted from DSC under an applied field change of 1 T.

The *M-T* curves at 1 T for the Mn$_{0.60}$Fe$_{1.30}$P$_{0.64}$Si$_{0.36}$F$_x$ (x = 0.00, 0.01, 0.02, 0.03) materials are shown in **Figure 4.1b**. A giant FOMT from strong ferromagnetism at low temperature to paramagnetism at high temperature is observed with phase transitions near room temperature. (Mn,Fe)$_2$(P,Si)-based alloys are found to be sensitive to F doping with a sensitivity of the phase transition of dT_C/dx = -13.3 K/*at.%* F. In addition to the shift in T_C, two striking phenomena for F doping are found (*i*) a weak enhancement of the saturation magnetization and (*ii*) an enhancement of the FOMT. Furthermore, as shown in **Figure 4.1e**, the thermal hysteresis ΔT_{hys} continuously increases from 4.4 K (x = 0.00) to 12.5 K (x = 0.03), which is in line with the enhanced FOMT indicated in **Figure 4.1f**.

These findings are unusual as most doping elements in (Mn,Fe)$_2$(P,Si)-based alloys result in a decrease in saturation magnetization and a lower thermal hysteresis. In particular, it has been reported previously that B doping significantly reduces ΔT_{hys}, resulting in an excellent cyclic adiabatic temperature change (ΔT_{cyclic} = 2.8 K under $\Delta \mu_0 H$ = 1.1 T) [19]. Considering the difference in free electrons among B ($2s^2 2p^1$) and F ($2s^2 2p^5$) and the strong electronegativity ($\chi_F \approx$ 4.0) for F [25], the competition between covalent bonding and ferromagnetic exchange coupling [24] is expected to be responsible to the difference in magnetic response for these doping elements.

As shown in **Figure 4.1d** the value of T_C has been determined from the minimum in dM/dT and is collected in **Table 4.1** for comparison to DSC data. The value of ΔS_m for the Mn$_{0.60}$Fe$_{1.30}$P$_{0.64}$Si$_{0.36}$F$_x$ (x = 0.00, 0.01, 0.02, 0.03) samples, defined as the entropy change caused by a magnetic field change, has been obtained from the *M-T* curves in field and is shown in **Figure 4.1f**. The maximum value of $|\Delta S_m|$ for $\Delta \mu_0 H$ = 2 T shows a significant improvement of 30% from 14.2 Jkg^{-1}K^{-1} at 335 K for the undoped sample (x = 0.00) to 20.2 Jkg^{-1}K^{-1} at 297 K for the highest doped sample (x = 0.03). For a field change of $\mu_0 H$ = 1 T the entropy change $|\Delta S_m|$ reaches 11.6 Jkg^{-1}K^{-1} at 294 K for the x = 0.03 sample, which is consistent with the in-field DSC data (12.4 Jkg^{-1}K^{-1}). These values are higher than the values for the archetypical MCM Gd of 2.8 (5.2) Jkg^{-1}K^{-1} with $\Delta \mu_0 H$ = 1(2) T [46]. **Figure S4.1a** and **S4.1b** (Supplementary Information) illustrate the conventional MCE upon applying magnetic fields. The adiabatic temperature change for the x = 0.03 sample is extracted from calorimetric measurements in **Figure S4.1c** (Supplementary Information) and reaches ΔT_{ad} = 2.2(3.9) K with $\Delta \mu_0 H$ = 1(1.5) T, which is competitive with other MCMs [47].

Table 4.1 Summary of the Curie temperature upon cooling (T_C-cooling) and heating (T_C-heating), the thermal hysteresis ΔT_{hys}, the latent heat L and total entropy change (ΔS_{tot}) for $Mn_{0.60}Fe_{1.30}P_{0.64}Si_{0.36}F_x$ (x = 0.00, 0.01, 0.02, 0.03) materials, measured in DSC and SQUID.

Sample	Tc-cooling DSC (K)	Tc-cooling SQUID (K)	Tc-heating DSC (K)	Tc-heating SQUID (K)	ΔT_{hys} DSC (K)	ΔT_{hys} SQUID (K)	L (J/g)	$|\Delta S_{tot}|$ (Jkg⁻¹K⁻¹)
x = 0.00	325.4	331.8	329.7	336.2	4.3	4.4	4.8	14.8
x = 0.01	306.8	311.8	313.9	318.4	7.1	6.6	5.1	16.6
x = 0.02	295.3	301.9	305.2	310.4	9.9	8.5	5.4	18.3
x = 0.03	278.8	283.9	292.8	296.4	14.0	12.5	6.0	21.7

Similar to F doping discussed above also S doping can be considered. In **Figure 4.2a** the specific heat upon heating and cooling is shown for $Mn_{0.60}Fe_{1.25}P_{0.66-y}Si_{0.34}S_y$ (y = 0.00, 0.01, 0.02, 0.03, 0.04) samples. For all samples a FOMT is observed. For increasing S doping T_C shifts to lower temperature, ΔT_{hys} remains almost constant, while L and $|\Delta S_{tot}|$ continuously decreases, which indicates a weakening of the FOMT, as illustrated in **Table 4.2**. **Figure 4.2b** shows the M-T curves for the S-doped samples in an applied field of 1 T. By varying the S content, the T_C upon heating shifts from 332 K for the undoped sample (y = 0.00) to 313 K for the highest doped sample (y = 0.04). The effect of S doping on T_C is only dT_C/dy = -4.8 K/$at.$% S, which is significantly weaker than that of F doping with dT_C/dx = -13.3 K/$at.$% F. **Figure 4.2c** demonstrates the corresponding M-H curves at 5 K. M_S slightly decreases from y = 0.00 to y = 0.03, with a more rapid decline between y = 0.03 (151.5 Am²kg⁻¹) and y = 0.04 (132.8 Am²kg⁻¹). **Figure 4.2d** shows that $|\Delta S_m|$ gradually decreases with increasing S doping. The entropy change $|\Delta S_m|$ reduces from 7.9(12.6) Jkg⁻¹K⁻¹ for the undoped sample (y = 0) to 3.4(6.2) Jkg⁻¹K⁻¹ for the highest doped sample (y = 0.04) in a field change of $\Delta\mu_0H$ = 1(2) T.
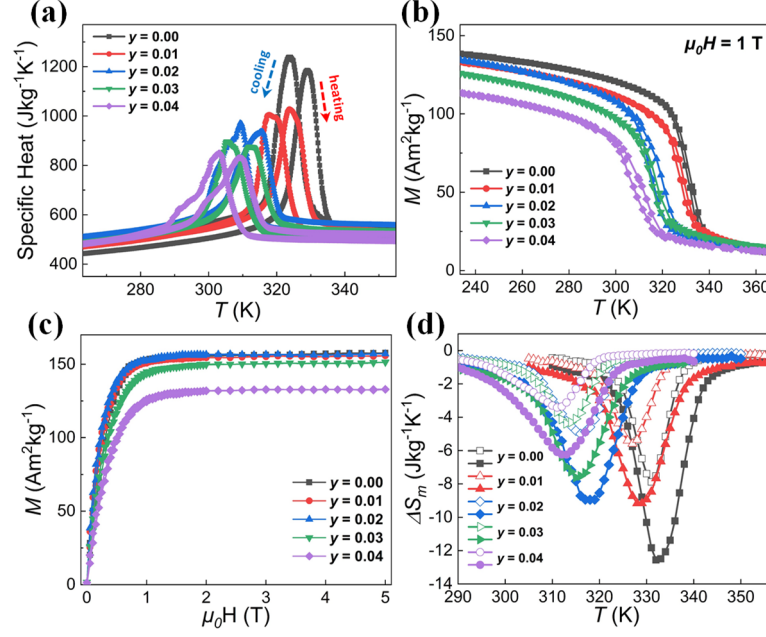
Figure 4.2 (a) Specific heat derived from DSC experiments for Mn$_{0.60}$Fe$_{1.25}$P$_{0.66-y}$Si$_{0.34}$S$_y$ (y = 0.00, 0.01, 0.02, 0.03, 0.04) materials upon heating and cooling. (b) Isofield M-T curves for Mn$_{0.60}$Fe$_{1.25}$P$_{0.66-y}$Si$_{0.34}$S$_y$ (y = 0.00, 0.01, 0.02, 0.03, 0.04) materials under 1 T. (c) Corresponding isothermal M-H curves at 5 K. (d) Entropy change ΔS_m for $\Delta\mu_0H$ = 1 T (open symbols) and 2 T (solid symbols) as a function of different S doping contents.

Table 4.2 Summary of T_C–cooling, T_C–heating, ΔT_{hys}, L and ΔS_{tot} for Mn$_{0.60}$Fe$_{1.25}$P$_{0.66-y}$Si$_{0.34}$S$_y$ (y = 0.00, 0.01, 0.02, 0.03, 0.04) materials, measured in DSC and SQUID.

Sample	Tc-cooling DSC (K)	Tc-cooling SQUID (K)	Tc-heating DSC (K)	Tc-heating SQUID (K)	ΔT_{hys} DSC (K)	ΔT_{hys} SQUID (K)	L (J/g)	$|\Delta S_{tot}|$ (Jkg^{-1}K^{-1})
y = 0.00	323.9	325.3	329.2	331.6	5.3	6.3	4.9	15.2
y = 0.01	319.9	323.2	325.8	328.0	5.7	4.8	4.2	13.2
y = 0.02	309.7	315.2	315.8	319.3	6.1	4.1	3.8	12.2
y = 0.03	305.6	308.8	312.2	316.1	6.6	7.3	3.6	11.7
y = 0.04	303.1	305.9	309.2	313.0	6.1	7.1	3.0	9.9

To further investigate the mechanism responsible for the weakening of the FOMT in Mn$_{0.60}$Fe$_{1.25}$P$_{0.66-y}$Si$_{0.34}$S$_y$ (y = 0.00, 0.01, 0.02, 0.03, 0.04) materials SEM measurements are applied. **Figure 4.3a** shows the backscattered electrons (BSE) SEM image from the

Mn$_{0.60}$Fe$_{1.25}$P$_{0.63}$Si$_{0.34}$S$_{0.03}$ sample, revealing three distinct impurities randomly distributed within the main phase matrix. The composition of these three types of impurities are determined as Mn$_{47.8}$Fe$_{8.3}$P$_{2.4}$Si$_{6.2}$S$_{35.3}$ (impurity 1: MnS-based), Mn$_{17.3}$Fe$_{19.8}$P$_{4.9}$Si$_{49.6}$S$_{8.4}$ (impurity 2: (Mn,Fe)Si-based) and Mn$_{20.5}$Fe$_{40.0}$P$_{14.7}$Si$_{24.0}$S$_{0.8}$ (impurity 3: (Mn,Fe)$_3$Si-based), respectively. Interestingly, besides the MnS-based and (Mn,Fe)$_3$Si-based impurities also observed by X-ray diffraction, another (Mn,Fe)Si-based impurity has been found in (Mn,Fe)$_2$(P,Si)-based MCMs [48]. The reason for the appearance of this (Mn,Fe)Si-based impurity could be the decomposition of (Mn,Fe)$_5$Si$_3$ below 800 °C into (Mn,Fe)$_3$Si and (Mn,Fe)Si [49, 50]. These closely arranged impurities within matrix might also be attributed to compositional fluctuations in the main phase, which may explain the appearance of shoulders in some of the specific heat measurement peaks in **Figure 4.2a**. Additionally, the corresponding composition line-scan profile in **Figure 4.3b** clearly illustrates the competition among (Mn,Fe)Si-based and MnS-based impurities.
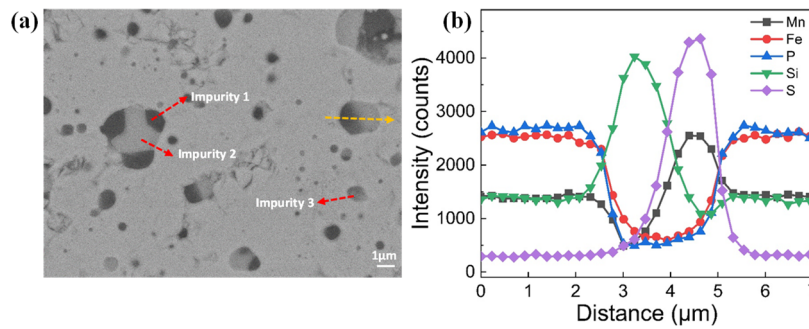

Figure 4.3 (a) Backscattered electron SEM image for the Mn$_{0.60}$Fe$_{1.25}$P$_{0.63}$Si$_{0.34}$S$_{0.03}$ alloy. (b) Corresponding composition line-scan profile along the yellow dashed line in (a).

In comparison to X-ray diffraction, neutron diffraction (ND) often possesses a higher sensitivity to light elements (e.g. H, B, C, N, O, F, S), therefore it has been successfully employed to resolve the occupation of B, C and N dopants within the (Mn,Fe)$_2$(P,Si)-based lattice structure [51, 52]. Due to the neutron spin ND is sensitive to both the lattice structure and the magnetic structure [53, 54]. Here, we present the crystal structures at RT for Mn$_{0.60}$Fe$_{1.30}$P$_{0.64}$Si$_{0.36}$F$_x$ (x = 0.00, 0.02) and Mn$_{0.60}$Fe$_{1.25}$P$_{0.66-y}$Si$_{0.34}$S$_y$ (y = 0.00, 0.02) refined from our ND data, **Figure 4.4(a-b)** and **4.4(c-d)**, respectively. Good fits to the data were obtained using a hexagonal unit cell (space group *P-62m*) with both Mn and Fe magnetic moments aligned parallel to the *c* axis. The orientation of the magnetic moments is different from previous studies of Mn-rich samples, where the moments were found to be oriented in the *a-b* plane [55]. The magnetic moments for Fe-rich samples are preferentially aligned along *c* axis, in a similar manner to its parent Fe$_2$P counterpart [56, 57]. This indicates that

the direction of moments is strongly determined by the Mn/Fe ratio in (Mn,Fe)$_2$(P,Si)-based materials. The fitted ND patterns for all F-doped and S-doped samples are exhibited in **Figure S4.2** and **S4.3**, respectively (Supplementary Information). The structural parameters (including the XRD data for comparison) and the magnetic moments derived from Rietveld refinement can be found in **Table S4.1** and **S4.2** (Supplementary Information).
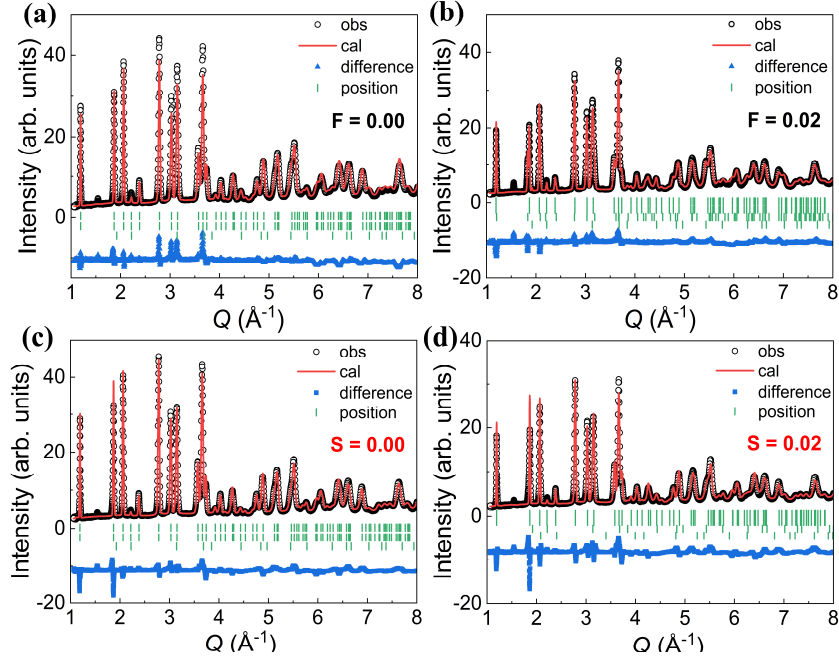

Figure 4.4 Fitted powder neutron diffraction patterns for Fe-rich (a) Mn$_{0.60}$Fe$_{1.30}$P$_{0.64}$Si$_{0.36}$F$_{0.00}$, (b) Mn$_{0.60}$Fe$_{1.30}$P$_{0.64}$Si$_{0.36}$F$_{0.02}$, (c) Mn$_{0.60}$Fe$_{1.25}$P$_{0.66}$Si$_{0.34}$S$_{0.00}$ and (d) Mn$_{0.60}$Fe$_{1.25}$P$_{0.64}$Si$_{0.34}$S$_{0.02}$ collected in the Polaris detector bank 3 ($<2\vartheta> \approx 40.4 - 66.4°$) at RT as a function of the wave vector transfer Q. Black circles indicate the observed data points, red lines the calculated profile, blue lines the difference and vertical lines the Bragg peak positions.

The lattice parameters a and c of the hexagonal Fe$_2$P type lattice structure for the F-doped and S-doped alloys, derived from the ND experiments, are shown in **Figure 4.5a** and **4.5b**. **Figure 4.5a** shows that at RT the lattice parameters exhibit discontinuous changes in a and c depending on their magnetic state (ferromagnetic (FM)/Coexistence/paramagnetic (PM)) with anomalies in $\Delta a/a$ ($\Delta c/c$) of the order of -0.91% (+1.73%), while lattice symmetry is conserved in different magnetic states. As shown in **Figure 4.5c**, combining the ND data with high-temperature PM X-ray data, one can easily distinguish the difference in c/a ratio among the FM state, two-phase coexistence and the PM state. The change in c/a ratio is

closely related to the magnetic exchange interactions that control the magnetoelastic coupling in these materials [58].
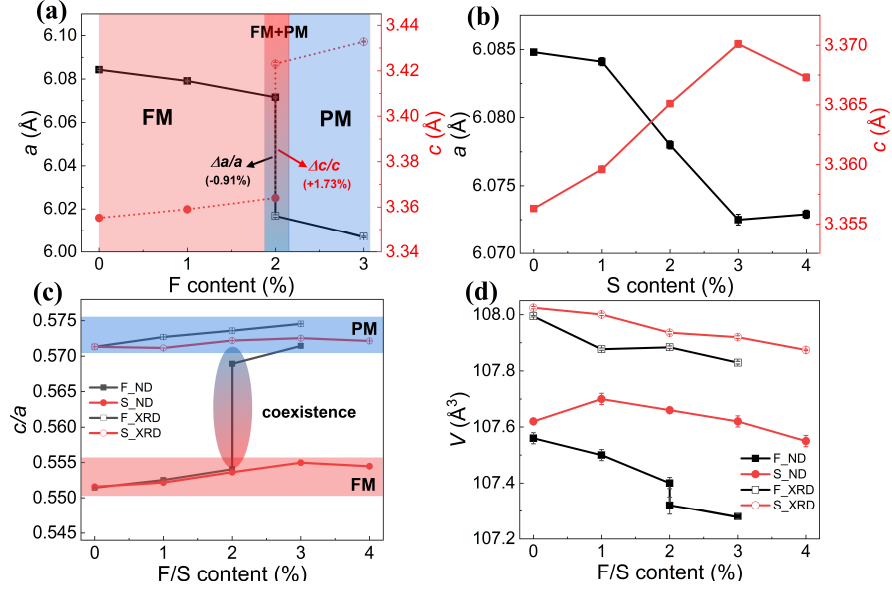

Figure 4.5 Lattice parameters *a* and *c* as a function of the F and S doping concentration for the (a) $Mn_{0.60}Fe_{1.30}P_{0.64}Si_{0.36}F_x$ (*x* = 0.00, 0.01, 0.02, 0.03) and (b) $Mn_{0.60}Fe_{1.25}P_{0.66-y}Si_{0.34}S_y$ (*y* = 0.00, 0.01, 0.02, 0.03, 0.04) alloys. Note that the F-doped samples have different magnetic states (FM, PM, phase coexistence), while the S-doped samples are all in the FM state. (c) *c/a* ratio and (d) unit-cell volume *V* as a function of the F/S doping concentration. Note that solid symbols correspond to ND data and open symbols to XRD data, respectively.

In **Figure 4.5c** the magnitude of the jump in *c/a* ratio for the F-doped sample with *x* = 0.02 is about 2.6 %, corresponding to a relatively low ΔT_{hys} of 9 K. Moreover, the cell volume *V* for the F-doped and S-doped samples derived from the ND and XRD data are presented in **Figure 4.5d**. The slight differences are caused by the thermal expansion of different experiment temperatures (ND at RT and XRD at T_C + 100 K).
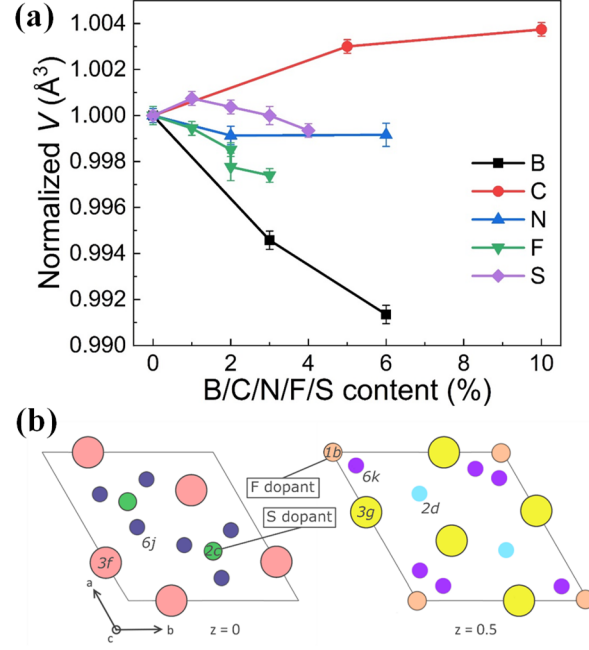
Figure 4.6 (a) Normalized volume as a function of the B, C, N, F and S doping concentration, obtained from ND data. (b) Schematic representation of (Mn,Fe)$_2$(P,Si)-type lattice structure and the corresponding potential atom positions of the F/S dopant in the basal plane at $z = 0$ and $z = 0.5$.

A comparison of the present data with those from Miao *et al.* [52] for B, C, N-doped (Mn,Fe)$_2$(P,Si)-based materials and with DFT calculations, makes it possible to further investigate the effect of doping (interstitial/substitutional) and site occupancy of F/S atoms. As demonstrated in **Figure 4.6a**, compared with C doping (red curve; interstitial site), F (green curve) and S (purple curve) atoms enter the structure as substitutional atoms because the covalent radius of F (0.57 Å) and S (1.05 Å), as well as B (0.84 Å), are smaller than the non-metal elements P (1.07 Å) and Si (1.11 Å) within the (Mn,Fe)$_2$(P,Si) structure [28], which leads to the decrease in normalized cell volume. The decrease in V for S is distinctly lower than that for F, which could be ascribed to the comparable atom radius among S, P and Si. In addition, based on our neutron diffraction results, accurate preferred sites for the F and S atoms have been obtained: F preferentially occupies the 1b site, while S preferentially occupies the 2c site with no evidence found for any preferential occupancy of the P and Si atoms on these sites. This preference is illustrated in the schematic representation in **Figure 4.6b** and matches the conclusions for doped Fe$_2$P [51]. According to DFT calculations, the formation energies E_f of various site occupation models for these

77

two systems confirm the experimentally obtained preferred sites, as shown in **Figure S4.6** (Supplementary Information).

4.4 Discussions

One interesting phenomenon about F doping is the surprisingly continuous enhancement of the MCE accompanied by an increase in thermal hysteresis. The thermal hysteresis is closely associated with the energy barrier for nucleation during the FOMT [59]. Different strategies to minimize the hysteresis have been proposed. For magnetostructural MCMs improving the structural compatibility between both phases is recommended [11, 60], while metal-element doping or introducing secondary phases are effective for (Mn,Fe)₂(P,Si)-type and La(Fe,Si)₁₃-type magnetoelastic MCMs [22, 23, 61]. The magnetoelastic transition is sensitive to the transition-induced elastic strain energy (U_E) because of the lattice mismatch between the PM and FM phases (no symmetry change) [42, 62]. U_E in a hexagonal system [63-65] can be estimated by the formula:

$$U_E = (C_{11} + C_{12})e_1^2 + 2C_{13}e_1e_3 + \frac{1}{2}C_{33}e_3^2 \qquad (4.2)$$

where the C_{ij} (i, j = 1,2,3,4,5,6) are the elastic constants (calculated with DFT, see Section. 2) and $e_{i,j}$ are the elastic strains ($e_1 = e_2 = \Delta a/a$ and $e_3 = \Delta c/c$ in an hexagonal system) [23, 42]. Consequently, the corresponding U_E for the Mn₀.₆₀Fe₁.₃₀P₀.₆₄Si₀.₃₆F₀.₀₂ sample (ΔT_{hys} = 8.5 K) is estimated to be 7.8 kJ/mol. The U_E for the parent Mn₀.₆₀Fe₁.₃₀P₀.₆₄Si₀.₃₆ sample (ΔT_{hys} = 4.4 K) is only around 4.1 kJ/mol (derived from temperature-dependent XRD at T_C). Therefore, the increase in ΔT_{hys} for F doping is correlated with the enhanced elastic transition energy.

Additionally, Arrott plots (μ_0H/M versus M^2) for F-doped and S-doped samples present in **Figure S4.7** and **S4.8** (Supplementary Information) were constructed to further analyze the nature of the transition. According to the Banerjee criterion [66] a clear FOMT feature is found for all samples because of the "S-shaped" curves, which confirms the other FOMT features (thermal hysteresis, peak in the specific heat and lattice discontinuities at the transition).

The magnetic moments for the Fe and Mn atoms as well as the total moment per formula unit for our Mn₀.₆₀Fe₁.₃₀P₀.₆₄Si₀.₃₆F$_x$ (x = 0.00, 0.01, 0.02) and Mn₀.₆₀Fe₁.₂₅P₀.₆₆₋$_y$Si₀.₃₄S$_y$ (y = 0.00,0.01, 0.02, 0.03, 0.04) alloys were determined from the neutron diffraction data by magnetic structure refinement and are shown in **Figure 4.7a** and **4.7b**. It shows that Mn(3g) atoms are responsible for the main magnetic moments, and that the Mn moments almost remain constant, while the Fe(3f) moments significantly decrease, especially near to the transition region (see the F-doped sample with x = 0.02 and the S-doped sample with y =

0.04). The so-called "mixed magnetism" [67] in the $(Mn,Fe)_2(P,Si)$ system was applied to explain that, compared with the robustness of Mn(3g) moments, the Fe(3f) moments are relatively sensitive to the phase transition reflected in the "Fe moment quenching" phenomenon, which has been demonstrated in theoretical calculations [67, 68]. The Fe(3f) intralayer coupling is easily influenced by external stimuli like chemical pressure (e.g. by heteroatomic doping), hence in the next section we will further investigate these atomic-scale variations among different doping systems. The total magnetic moments obtained from macroscopic magnetization measurements at RT are in good agreement with the neutron diffraction results at the same temperature. Interestingly, in comparison to the experimental results (red curve), the DFT calculations for the total moment (black curve) also confirm that F doping (in contrast with other elements) promotes a moment enhancement. This significant enhancement is ascribed to the increase in Fe moment, while the Mn moments maintain constant, as shown in **Figure 4.7c**. For S-doping **Figure 4.7d** shows that even though the moment hardly changes in the theoretical calculations, the magnetic moment from magnetization measurements show a decrease, which could be caused by the introduction of Mn-based secondary phases as DFT calculations didn't consider this effect, and a sudden increase in the amount of (Mn,Fe)Si- and MnS-based impurities has been observed in **Figure S4.4b** (Supplementary Information) considering Mn takes responsibility for largest magnetic moments in $(Mn,Fe)_2(P,Si)$-based MCMs [67].

Actually, the parent system for $(Mn,Fe)_2(P,Si)$ is the hexagonal Fe_2P metalloid material, for which itinerant ferromagnetism was found to occur based on the Rhodes–Wohlfarth criteria ($q_c/q_s \approx 1.8$) [69-71]. Single crystalline Fe_2P shows a mixture of itinerant and localized magnetism characteristics due to the presence of a strong magnetic anisotropy [72]. This itinerant-electron metamagnet also shows a moment instability for one of the Fe moments, which is similar to $(Mn,Fe)_2(P,Si)$. Also, for $(Mn,Fe)_2(P,Si)$-based MCMs high-resolution synchrotron powder diffraction experiments combined with DFT calculation infer that the metastable moment behavior (Fe moment destabilization) during the phase transition is mainly ascribed to the function of the metalloid atoms (P/Si) [24]. A remarkable electron-density redistribution around Fe atoms was experimentally observed, indicating that this strong magnetoelastic coupling system is dominated by the competition between covalent bonding and ferromagnetic exchange coupling [24]. The chemical coordination environment (like interatomic distances), directly strengthen/weaken the magnetic exchange interactions among various atoms, thereby effectively influencing the electronic configuration around the Fe(3f) sites [55].
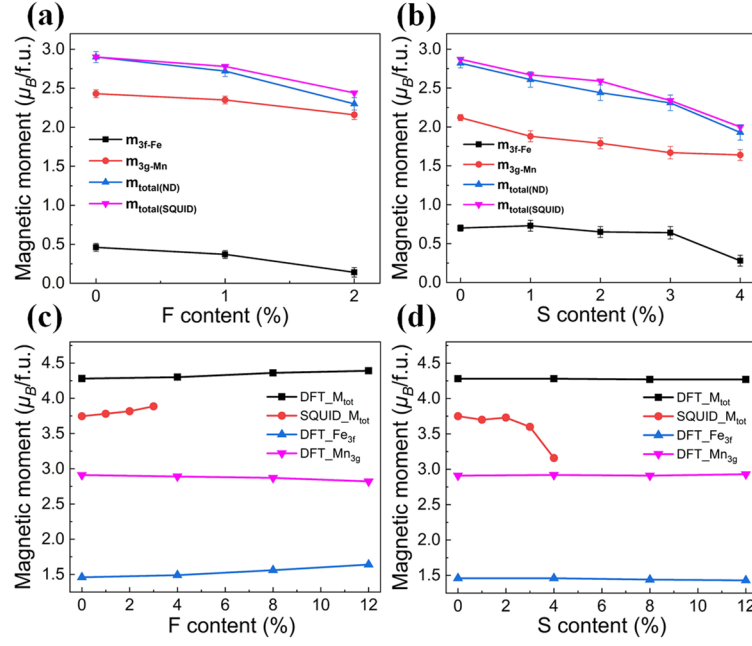
79

Figure 4.7 Experimental magnetic moments obtained from ND and SQUID magnetization measurements at RT for (a) $Mn_{0.60}Fe_{1.30}P_{0.64}Si_{0.36}F_x$ (x = 0.00, 0.01, 0.02) and (b) $Mn_{0.60}Fe_{1.25}P_{0.66-y}Si_{0.34}S_y$ (y = 0.00, 0.01, 0.02, 0.03, 0.04) alloys. The magnetic moments derived from DFT calculations and magnetization measurements at 5 K as a function of (c) F and (d) S content.

The Fe-Fe (3f intralayer), Mn-Mn (3g intralayer), Fe-Mn (3f-3g interlayer) and Fe-P/Si (3f intralayer) atomic distances with different B, C, N, F and S dopant concentrations determined experimentally from ND measurements are shown in **Figure 4.8(a-d)**. Note that the P/Si atoms are distributed randomly within 3g/3f layers. Compared with the isotropic deformations for B doping, the most significant atomic distance change for F dopant is the intralayer Fe(3f) - Fe(3f) spacing, where the normalized atomic distance changes by -0.17 % (per dopant concentration %), as shown in **Figure 4.8a**. This is most likely because the Fe(3f) atoms are metastable and the contracted Fe(3f) - Fe(3f) distance may consolidate the magnetic interaction, whereas the intralayer Mn(3g) - Mn(3g) distance shows a negligible effect, as shown in **Figure 4.8b**. Meanwhile, recent neutron powder diffraction studies of doping in (Mn,Fe)₂(P,Ge) alloys elucidate that coplanar Fe/Mn–Ge/P bond-length changes have a significant influence on T_C and ΔT_{hys} [73]. Thus, the comparatively small distance changes in the interlayer Fe(3f)-metalloid(2c) distance (-0.08%) and Fe(3f) - Mn(3g) distance (+0.10%) together with Fe(3f) - Fe(3f) distance (-0.17%) for F doping, resulting in a distortion of the tetrahedral Fe(3f) site, could contribute to this enhancement in exchange interaction as illustrated in **Figure 4.8(c-d)**.

For S doping, the most remarkable change is observed for the intralayer Mn($3g$)-Mn($3g$) distance (-0.11%). Based on electronic structure calculations, the Fe/Mn d electrons within the (Mn,Fe)$_2$(P,Si) structure are near the Fermi level, while the P/Si p electrons are located far below [55, 74]. As a consequence, similar to Si doping [55], free electrons would transfer from the metal d band to the metalloid p band due to the stronger electronegativity (ability to attract shared electrons) of F ($2s^2 2p^5$) and S ($3s^2 3p^4$) atoms, which further enhances the splitting of the d band, and therefore increase the magnetic moment. Unfortunately, the introduced impurities suppresses the increased moment potential for S doping.
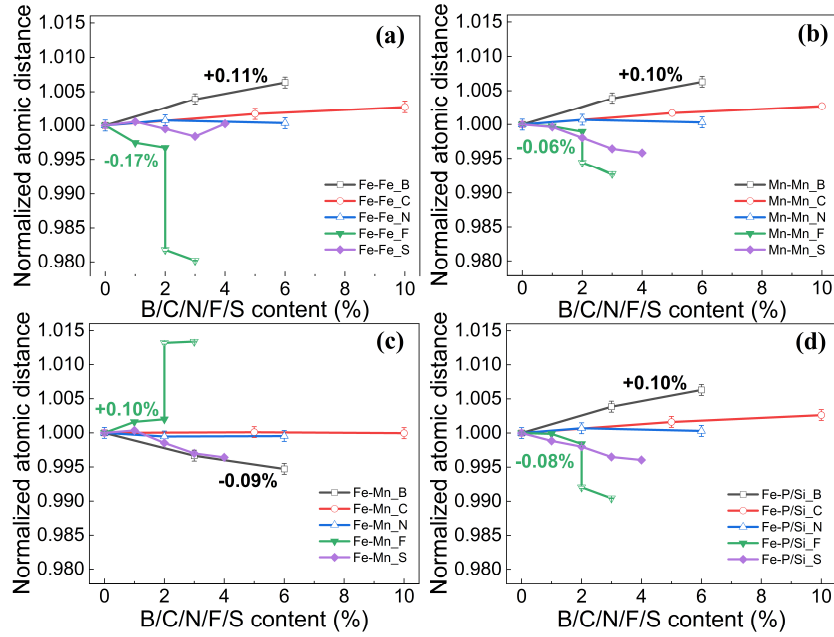

Figure 4.8 Normalized interatomic distances of (a) Fe-Fe, (b) Mn-Mn, (c) Fe-Mn and (d) Fe-P/Si as a function of different B, C, N, F and S dopant concentrations for (Mn,Fe)$_2$(P,Si)-based materials, determined from neutron diffraction. Note that the marked normalized atomic distance has been rescaled per dopant concentration (*at.%*).

The Electron Localization Function (ELF), a visualization of the valence shell electron pair repulsion theory, has been applied successfully in intermetallic compounds to distinguish the nature of the chemical covalent/metallic bonding [75-77]. This method is also suitable for the (Mn,Fe)$_2$(P,Si)-based itinerant FM system. In **Figure 4.9(a-c) and (d-f)**, the 2D ELF contour plots, sliced along (001) and (110) direction, are shown for (*i*) no dopant, (*ii*) F-doping and (*iii*) S-doping. From the topological analysis of the ELF in **Figure 4.9(b-c)** a significant electron localization around the P($2c$) atoms is confirmed for F and S doping in comparison with the undoped material (**Figure 4.9a**). This is in agreement with *K*-edge

81

phosphorus X-ray absorption spectroscopy (XAS) results which indicate that P is involved in a charge redistribution [78]. A similar phenomenon is seen in **Figure 4.9(e-f)**. Obviously, F/S atoms can effectively promote electron localization around the P(2c) atoms, while there is delocalization around the Si(1b) atoms. The ELF maps for the Mn surroundings are shown in **Figure S4.9** (Supplementary Information). The line profiles of the ELF values between the nearest-neighboring atoms are illustrated in **Figure 4.9g**. A higher value (close to maximum 1) means more electron localization. It is noteworthy that the maximum ELF values for nearest Fe-P atoms change from 0.49 to 0.58 (17.6% increase), which indicates a stronger covalent bonding upon F/S doping, while the ELF values for the nearest Fe-Si atoms decrease from 0.54 to 0.43 (20.5% decrease). These covalent bonding properties for F/S doped systems are essentially associated with the charge transfer from the *p-d* covalent hybridization. The combined atomic distance changes jointly contribute to the total moments enhancement for the F-doped (Mn,Fe)$_2$(P,Si) system and help to stabilize the hexagonal phase. Taking metalloids as the entry point, our current study on introducing non-metal species provide a new way to further optimize the MCE performance by regulating the metastability in bonding and atomic distances.
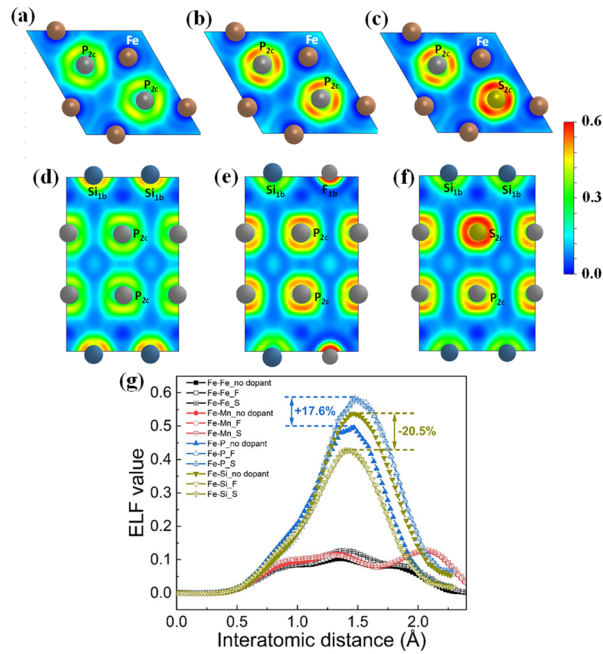

Figure 4.9 Calculated ELF contour maps for the *3f* Fe layer with (a) no dopant, (b) F-doping, (c) S-doping sliced along (001) direction and (c) no dopant, (d) F-doping, (e) S-doping sliced along (110) direction in the FM state of the (Mn,Fe)$_2$(P,Si)-based alloys. (g) Line profiles of the ELF values between Fe and its nearest neighbors. The stoichiometry of MnFeP$_{2/3}$Si$_{1/3}$ is assumed in the supercell for simplicity of the calculations.

4.5 Conclusions

In summary, the light elements F and S have successfully been introduced into (Mn,Fe)$_2$(P,Si)-based MCMs and the thermodynamic and magnetic properties of the new materials synthesised have been investigated. For these two dopant systems T_C can be moved sufficiently into the RT range. Interestingly, it is found that F doping enhances the magnetocaloric effect at the FOMT (by an increase in magnetic moments and in $|\Delta S_m|$), while for S doping the generated impurities slowly weaken the FOMT. By performing ND experiments the site occupancy has been resolved, indicating that F and S are substituted on the 1b and 2c site, respectively. This site preference has been confirmed by DFT calculations. The tunable MCE properties with F/S doping are analyzed in terms of the experimental atomic distances among different metal-metal or metal-metalloids atom pairs. Together with theoretical ELF calculations, these results clarify the subtle atomic distance changes, as well as the covalent bonding. Together they determine the change in GMCE with doping in these magnetoelastic (Mn,Fe)$_2$(P,Si)-based materials. Our results provide important insights and systematic understanding into the effect of doping with light elements on the GMCE properties of (Mn,Fe)$_2$(P,Si)-based MCMs.

References

[1] A. Kitanovski, Energy applications of magnetocaloric materials, *Adv Energy Mater* 10 (2020) 1903741.

[2] H. Johra, K. Filonenko, P. Heiselberg, C. Veje, S. Dall'Olio, K. Engelbrecht, C. Bahl, Integration of a magnetocaloric heat pump in an energy flexible residential building, *Renew Energ* 136 (2019) 115-126.

[3] A. Waske, D. Dzekan, K. Sellschopp, D. Berger, A. Stork, K. Nielsch, S. Fahler, Energy harvesting near room temperature using a thermomagnetic generator with a pretzel-like magnetic flux topology, *Nat Energy* 4 (2019) 68-74.

[4] D. Dzekan, A. Waske, K. Nielsch, S. Fahler, Efficient and affordable thermomagnetic materials for harvesting low grade waste heat, *Apl Mater* 9 (2021) 011105.

[5] V.K. Pecharsky, K.A. Gschneidner, Giant magnetocaloric effect in Gd$_5$(Si$_2$Ge$_2$), *Phys Rev Lett* 78 (1997) 4494-4497.

[6] O. Tegus, E. Brück, K.H.J. Buschow, F.R. de Boer, Transition-metal-based magnetic refrigerants for room-temperature applications, *Nature* 415 (2002) 150-152.

[7] F.X. Hu, B.G. Shen, J.R. Sun, Z.H. Cheng, G.H. Rao, X.X. Zhang, Influence of negative lattice expansion and metamagnetic transition on magnetic entropy change in the compound LaFe$_{11.4}$Si$_{1.6}$, *Appl Phys Lett* 78 (2001) 3675-3677.

[8] A. Planes, L. Mañosa, M. Acet, Magnetocaloric effect and its relation to shape-memory properties in ferromagnetic Heusler alloys, *J Phys-Condens Mat* 21 (2009) 233201.

[9] A. Chirkova, K.P. Skokov, L. Schultz, N.V. Baranov, O. Gutfleisch, T.G. Woodcock, Giant adiabatic temperature change in FeRh alloys evidenced by direct measurements under cyclic conditions, *Acta Mater* 106 (2016) 15-21.

[10] P.A.E. Murgatroyd, K. Routledge, S. Durdy, M.W. Gaultois, T.W. Surta, M.S. Dyer, J.B. Claridge, S.N. Savvin, D. Pelloquin, S. Hebert, J. Alaria, Chemically controllable magnetic transition temperature and magneto-elastic coupling in MnZnSb compounds, *Adv Funct Mater* 31 (2021) 2100108.

[11] J. Liu, Y.Y. Gong, Y.R. You, X.M. You, B.W. Huang, X.F. Miao, G.Z. Xu, F. Xu, E. Brück, Giant reversible magnetocaloric effect in MnNiGe-based materials: Minimizing thermal hysteresis via crystallographic compatibility modulation, *Acta Mater* 174 (2019) 450-458.

[12] L. Caron, N.T. Trung, E. Brück, Pressure-tuned magnetocaloric effect in Mn$_{0.93}$Cr$_{0.07}$CoGe, *Phys Rev B* 84 (2011) 020414.

[13] L. Mañosa, A. Planes, Solid-state cooling by stress: A perspective, *Appl Phys Lett* 116 (2020) 050501.

[14] V. Paul-Boncour, L. Bessais, Tuning the magnetocaloric properties of the La(Fe,Si)$_{13}$ compounds by chemical substitution and light element insertion, *Magnetochemistry* 7 (2021) 1-18.

[15] M.M. Cicek, S. Saritas, O. Yildirim, B. Emre, Effect of the low constituent boron on martensitic transformation, magnetic, and magnetocaloric properties of Ni$_{50}$Mn$_{35}$In$_{15}$ Heusler alloys, *J Alloy Compd* 845 (2020) 155493.

[16] H.Z. Luo, F.B. Meng, Q.X. Jiang, H.Y. Liu, E.K. Liu, G.H. Wu, Y.X. Wang, Effect of boron on the martensitic transformation and magnetic properties of $Ni_{50}Mn_{36.5}Sb_{13.5-x}B_x$ alloys, *Scripta Mater* 63 (2010) 569-572.

[17] S. Kavita, V.V. Ramakrishna, P. Yadav, S. Kethavath, N.P. Lalla, T. Thomas, P. Bhatt, R. Gopalan, Enhancement of martensite transition temperature and inverse magnetocaloric effect in $Ni_{43}Mn_{47}Sn_{11}$ alloy with B doping, *J Alloy Compd* 795 (2019) 519-527.

[18] Y. Zhang, J. Liu, Q. Zheng, J. Zhang, W.X. Xia, J. Du, A.R. Yan, Large magnetic entropy change and enhanced mechanical properties of Ni-Mn-Sn-C alloys, *Scripta Mater* 75 (2014) 26-29.

[19] F. Guillou, G. Porcari, H. Yibole, N. van Dijk, E. Brück, Taming the first-order transition in giant magnetocaloric materials, *Adv Mater* 26 (2014) 2671-2675.

[20] J.W. Lai, B.W. Huang, X.F. Miao, N.V. Thang, X.M. You, M. Maschek, L. van Eijck, D.C. Zeng, N. van Dijk, E. Brück, Combined effect of annealing temperature and vanadium substitution for mangetocaloric $Mn_{1.2-x}V_xFe_{0.75}P_{0.5}Si_{0.5}$ alloys, *J Alloy Compd* 803 (2019) 671-677.

[21] J.T. Feng, F.J. Qian, D.N. Shi, H. Yang, Effect of Zr substitution on the crystal structure, magnetoelastic transition and magnetocaloric properties of (Mn,Fe)₂(P,Si) alloys, *Applied Physics* 9 (2019) 358-364.

[22] S.Y. Hu, X.F. Miao, J. Liu, Z.Q. Ou, M.Q. Cong, O. Haschuluu, Y.Y. Gong, F.J. Qian, Y.R. You, Y.J. Zhang, F. Xu, E. Brück, Small hysteresis and giant magnetocaloric effect in Nb-substituted (Mn,Fe)₂(P,Si) alloys, *Intermetallics* 114 (2019) 106602.

[23] X.F. Miao, Y. Gong, F.Q. Zhang, Y.R. You, L. Caron, F.J. Qian, W.H. Guo, Y.J. Zhang, Y.Y. Gong, F. Xu, N.H. van Dijk, E. Brück, Enhanced reversibility of the magnetoelastic transition in (Mn,Fe)₂(P,Si) alloys via minimizing the transition-induced elastic strain energy, *J Mater Sci Technol* 103 (2022) 165-176.

[24] M.F.J. Boeije, P. Roy, F. Guillou, H. Yibole, X.F. Miao, L. Caron, D. Banerjee, N.H. van Dijk, R.A. de Groot, E. Brück, Efficient room-temperature cooling with magnets, *Chem Mater* 28 (2016) 4901-4905.

[25] W. Gordy, W.J.O. Thomas, Electronegativities of the elements, *J Chem Phys* 24 (1956) 439-444.

[26] L. Pauling, The nature of the chemical bond. IV. The energy of single bonds and the relative electronegativity of atoms, *J Am Chem Soc* 54 (1932) 3570-3582.

[27] K.Y. Li, D.F. Xue, Estimation of electronegativity values of elements in different valence states, *J Phys Chem A* 110 (2006) 11332-11337.

[28] B. Cordero, V. Gomez, A.E. Platero-Prats, M. Reves, J. Echeverria, E. Cremades, F. Barragan, S. Alvarez, Covalent radii revisited, *Dalton T* 21 (2008) 2832-2838.

[29] X.F. Miao, L. Caron, Z. Gercsi, A. Daoud-Aladine, N.H. van Dijk, E. Brück, Thermal-history dependent magnetoelastic transition in (Mn,Fe)₂(P,Si), *Appl Phys Lett* 107 (2015) 042403

[30] N.H. Dung, Moment formation and giant magnetocaloric effects in hexagonal Mn-Fe-P-Si compounds, TU Delft PhD Thesis (2012).

[31] G. Porcari, F. Cugini, S. Fabbrici, C. Pernechele, F. Albertini, M. Buzzi, M. Mangia, M. Solzi, Convergence of direct and indirect methods in the magnetocaloric study of first order transformations: the case of Ni-Co-Mn-Ga Heusler alloys, *Phys Rev B* 86 (2012) 104432.

[32] R.I. Smith, S. Hull, M.G. Tucker, H.Y. Playford, D.J. McPhail, S.P. Waller, S.T. Norberg, The upgraded Polaris powder diffractometer at the ISIS neutron source, *Rev Sci Instrum* 90 (2019) 115101.

[33] N.H. van Dijk, Resolving the site occupancy of nonmetal atoms in (Mn,Fe)₂(P,Si,F/S) magnetocaloric compounds, STFC ISIS Neutron and Muon Source (2020). https://doi.org/10.5286/ISIS.E.RB20900031, https://doi.org/10.5286/ISIS.E.RB20900041, https://doi.org/10.5286/ISIS.E.RB20900051, https://doi.org/10.5286/ISIS.E.RB20900061, https://doi.org/10.5286/ISIS.E.RB209000801, https://doi.org/10.5286/ISIS.E.RB209000811, https://doi.org/10.5286/ISIS.E.RB209000821, https://doi.org/10.5286/ISIS.E.RB209000831, https://doi.org/10.5286/ISIS.E.RB20900084-1.

[34] H.M. Rietveld, A profile refinement method for nuclear and magnetic structures, *J Appl Crystallogr* 2 (1969) 65-71.

[35] G. Kresse, J. Hafner, Ab initio molecular dynamics for liquid metals, *Phys Rev B* 47 (1993) 558-561.

[36] G. Kresse, J. Furthmuller, Efficiency of ab-initio total energy calculations for metals and semiconductors using a plane-wave basis set, *Comp Mater Sci* 6 (1996) 15-50.

[37] P.E. Blochl, Projector augmented-wave method, *Phys Rev B* 50 (1994) 17953-17979.

[38] G. Kresse, D. Joubert, From ultrasoft pseudopotentials to the projector augmented-wave method, *Phys Rev B* 59 (1999) 1758-1775.

[39] J.P. Perdew, K. Burke, M. Ernzerhof, Generalized gradient approximation made simple, *Phys Rev Lett* 77 (1996) 3865-3868.

[40] D.I. Bolef, N.T. Melamed, M. Menes, Elastic constants of hexagonal cadmium sulfide, *J Phys Chem Solids* 17 (1960) 143-148.

[41] L. Fast, J.M. Wills, B. Johansson, O. Eriksson, Elastic-constants of hexagonal transition-metals-theory, *Phys Rev B* 51 (1995) 17431-17438.

[42] P. Roy, E. Torun, R.A. de Groot, Effect of doping and elastic properties in (Mn,Fe)₂(Si,P), *Phys Rev B* 93 (2016) 094110.

[43] M. Methfessel, A.T. Paxton, High-precision sampling for Brillouin-Zone integration in metals, *Phys Rev B* 40 (1989) 3616-3621.

[44] B. Silvi, A. Savin, Classification of chemical-bonds based on topological analysis of electron localization functions, *Nature* 371 (1994) 683-686.

[45] P. Roy, E. Brück, R.A. de Groot, Latent heat of the first-order magnetic transition of MnFeSi$_{0.33}$P$_{0.66}$, *Phys Rev B* 93 (2016) 165101.

[46] T. Gottschall, K.P. Skokov, M. Fries, A. Taubel, I. Radulov, F. Scheibel, D. Benke, S. Riegg, O. Gutfleisch, Making a cool choice: the materials library of magnetic refrigeration, *Adv Energy Mater* 9 (2019) 1901322.

[47] J. Lyubina, Magnetocaloric materials for energy efficient cooling, *J Phys D Appl Phys* 50 (2017) 053002.

[48] J.W. Lai, Z.G. Zheng, B.W. Huang, H.Y. Yu, Z.G. Qiu, Y.L. Mao, S. Zhang, F.M. Xiao, D.C. Zeng, K. Goubitz, E. Brück, Microstructure formation and magnetocaloric effect of the Fe_2P-type phase in $(Mn,Fe)_2(P,Si,B)$ alloys, *J Alloy Compd* 735 (2018) 2567-2573.

[49] V. Johnson, D.B. Rogers, J.F. Weiher, C.G. Frederick, Magnetic and mössbauer-effect studies of $Mn_5Si_3:Fe_5Si_3$ solid-solutions, *J Solid State Chem* 4 (1972) 311-323.

[50] V. Singh, P. Bag, R. Rawat, R. Nath, Critical behavior and magnetocaloric effect across the magnetic transition in $Mn_{1+x}Fe_{4-x}Si_3$, *Sci Rep* 10 (2020) 1-17.

[51] Z. Gercsi, E.K. Delczeg-Czirjak, L. Vitos, A.S. Wills, A. Daoud-Aladine, K.G. Sandeman, Magnetoelastic effects in doped Fe_2P, *Phys Rev B* 88 (2013) 024417.

[52] X.F. Miao, N.V. Thang, L. Caron, H. Yibole, R.I. Smith, N.H. van Dijk, E. Brück, Tuning the magnetoelastic transition in $(Mn,Fe)_2(P,Si)$ by B, C, and N doping, *Scripta Mater* 124 (2016) 129-132.

[53] X.F. Miao, L. Caron, J. Cedervall, P.C.M. Gubbens, P.D. de Reotier, A. Yaouanc, F. Qian, A.R. Wildes, H. Luetkens, A. Amato, N.H. van Dijk, E. Brück, Short-range magnetic correlations and spin dynamics in the paramagnetic regime of $(Mn,Fe)_2(P,Si)$, *Phys Rev B* 94 (2016) 014426.

[54] X.F. Miao, Y. Mitsui, A.I. Dugulan, L. Caron, N.V. Thang, P. Manuel, K. Koyama, K. Takahashi, N.H. van Dijk, E. Brück, Kinetic-arrest-induced phase coexistence and metastability in $(Mn,Fe)_2(P,Si)$, *Phys Rev B* 94 (2016) 094426.

[55] X.F. Miao, L. Caron, P. Roy, N.H. Dung, L. Zhang, W.A. Kockelmann, R.A. de Groot, N.H. van Dijk, E. Brück, Tuning the phase transition in transition-metal-based magnetocaloric compounds, *Phys Rev B* 89 (2014) 174429.

[56] D. Scheerlinck, E. Legrand, Neutron diffraction study of the magnetic structure of Fe_2P, *Solid State Commun* 25 (1978) 181-184.

[57] J. Cedervall, M.S. Andersson, E.K. Delczeg-Czirjak, D. Iusan, M. Pereiro, P. Roy, T. Ericsson, L. Haggstrom, W. Lohstroh, H. Mutka, M. Sahlberg, P. Nordblad, P.P. Deen, Magnetocaloric effect in Fe_2P: Magnetic and phonon degrees of freedom, *Phys Rev B* 99 (2019) 174437.

[58] E.K. Delczeg-Czirjak, Z. Gercsi, L. Bergqvist, O. Eriksson, L. Szunyogh, P. Nordblad, B. Johansson, L. Vitos, Magnetic exchange interactions in B-, Si-, and As-doped Fe_2P from first-principles theory, *Phys Rev B* 85 (2012) 224435.

[59] L.F. Cohen, Contributions to hysteresis in magnetocaloric materials, *Phys Status Solidi B* 255 (2018) 1700317.

[60] J. Liu, X.M. You, B.W. Huang, I. Batashev, M. Maschek, Y.Y. Gong, X.F. Miao, F. Xu, N. van Dijk, E. Brück, Reversible low-field magnetocaloric effect in Ni-Mn-In-based Heusler alloys, *Phys Rev Mater* 3 (2019) 084409.

[61] J.W. Lai, H. Sepehri-Amin, X. Tang, J. Li, Y. Matsushita, T. Ohkubo, A.T. Saito, K. Hono, Reduction of hysteresis in $(La_{1-x}Ce_x)_y(Mn_zFe_{11.4-z})Si_{1.6}$ magnetocaloric compounds for cryogenic magnetic refrigeration, *Acta Mater* 220 (2021) 117286.

[62] M.F.J. Boeije, M. Maschek, X.F. Miao, N.V. Thang, N.H. van Dijk, E. Brück, Mixed magnetism in magnetocaloric materials with first-order and second-order magnetoelastic transitions, *J Phys D Appl Phys* 50 (2017) 174002.

[63] G.F. Cardinale, D.L. Medlin, P.B. Mirkarimi, K.F. McCarty, D.G. Howitt, Orientation-dependence of elastic strain energy in hexagonal and cubic boron nitride layers in energetically deposited BN films, *Journal of Vacuum Science & Technology a* 15 (1997) 196-200.

[64] J.Y. Shen, S. Johnston, S.L. Shang, T. Anderson, Calculated strain energy of hexagonal epitaxial thin films, *J Cryst Growth* 240 (2002) 6-13.

[65] J.F. Nye, Physical properties of crystals: their representation by tensors and matrices, Oxford university press 1985.

[66] B.K. Banerjee, On a generalised approach to first and second order magnetic transitions, *Physics Letters* 12 (1964) 16-17.

[67] N.H. Dung, Z.Q. Ou, L. Caron, L. Zhang, D.T.C. Thanh, G.A. de Wijs, R.A. de Groot, K.H.J. Buschow, E. Brück, Mixed magnetism for refrigeration and energy conversion, *Adv Energy Mater* 1 (2011) 1215-1219.

[68] M. Maschek, X. You, M.F.J. Boeije, D. Chernyshov, N.H. van Dijk, E. Brück, Charge redistribution and the magnetoelastic transition across the first-order magnetic transition in (Mn,Fe)$_2$(P,Si,B), *Phys Rev B* 98 (2018) 224413.

[69] S. Kumar, A. Krishnamurthy, B.K. Srivastava, On nature of magnetism in ferromagnetic alloys (Fe$_{1-x}$Co$_x$)$_2$P, *J Phys D Appl Phys* 41 (2008) 055001.

[70] O. Eriksson, J. Sjostrom, B. Johansson, L. Haggstrom, H.L. Skriver, Itinerant ferromagnetism in Fe$_2$P, *J Magn Magn Mater* 74 (1988) 347-358.

[71] E.P. Wohlfarth, Magnetic properties of crystallineand amorphous alloys: A systematic discussion based on the Rhodes-Wohlfarth plot, *J Magn Magn Mater* 7 (1978) 113-120.

[72] L. Caron, M. Hudl, V. Hoglin, N.H. Dung, C.P. Gomez, M. Sahlberg, E. Brück, Y. Andersson, P. Nordblad, Magnetocrystalline anisotropy and the magnetocaloric effect in Fe$_2$P, *Phys Rev B* 88 (2013) 094440.

[73] H.R. Zhang, D.M. Liu, Z.L. Zhang, S.B. Wang, M. Yue, Q.Z. Huang, J.W. Lynn, The correlation between the covalent bonds and magnetocaloric properties of the Mn$_{2-x}$Fe$_x$P$_y$Ge$_{1-y}$M$_z$ compounds, *J Appl Phys* 130 (2021) 133901

[74] P. Jernberg, A.A. Yousif, L. Häggström, Y. Andersson, A Mössbauer study of Fe$_2$P$_{1-x}$Si$_x$ (x≤0.35), *J Solid State Chem* 53 (1984) 313-322.

[75] A.D. Becke, K.E. Edgecombe, A simple measure of electron localization in atomic and molecular-systems, *J Chem Phys* 92 (1990) 5397-5403.

[76] A. Savin, R. Nesper, S. Wengert, T.F. Fassler, ELF: The electron localization function, *Angew Chem Int Edit* 36 (1997) 1809-1832.

[77] E.K. Liu, W.H. Wang, L. Feng, W. Zhu, G.J. Li, J.L. Chen, H.W. Zhang, G.H. Wu, C.B. Jiang, H.B. Xu, F.R. de Boer, Stable magnetostructural coupling with tunable magnetoresponsive effects in hexagonal ferromagnets, *Nat Commun* 3 (2012) 1-10.

[78] F. Guillou, K. Ollefs, F. Wilhelm, A. Rogalev, A.N. Yaresko, H. Yibole, N.H. van Dijk, E. Brück, Electronic and magnetic properties of phosphorus across the first-order ferromagnetic transition of (Mn,Fe)$_2$(P,Si,B) giant magnetocaloric materials, *Phys Rev B* 92 (2015) 224427.

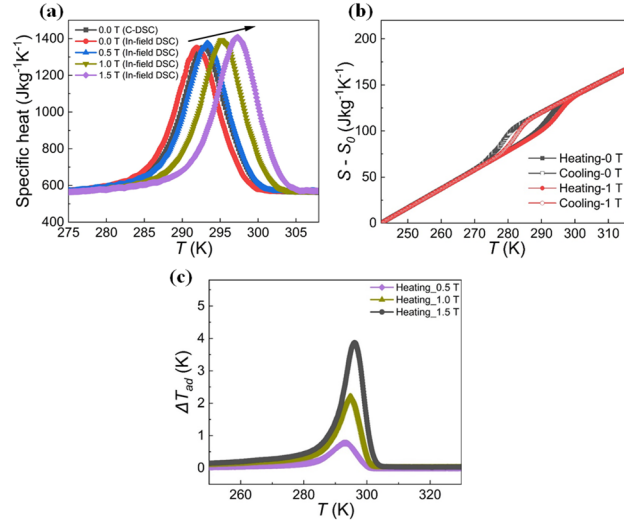## Supplementary Information for Chapter 4

Figure S4.1 (a) Specific heat as a function of temperature from DSC measurements in different applied magnetic fields for the $Mn_{0.60}Fe_{1.30}P_{0.64}Si_{0.36}F_{0.03}$ alloy. The black curve is added for comparison with data from a commercial zero-field DSC, indicating a good correspondence. (b) The $S-S_0(T,H)$ entropy curves obtained from heating (solid symbols) and cooling (open symbols) in applied magnetic fields of $\mu_0H = 0$ T and $\mu_0H = 1$ T for $Mn_{0.60}Fe_{1.30}P_{0.64}Si_{0.36}F_{0.03}$ alloy. S_0 corresponds to the entropy at $T = 242$ K. (c) Temperature dependence of the adiabatic temperature change ΔT_{ad} in different applied field changes derived from in-field DSC measurements.
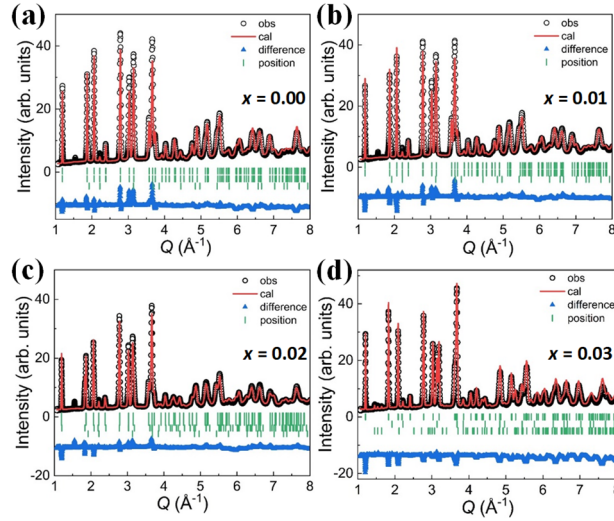

Figure S4.2 Fitted powder neutron diffraction patterns at room temperature for (a) $Mn_{0.60}Fe_{1.30}P_{0.64}Si_{0.36}F_{0.00}$, (b) $Mn_{0.60}Fe_{1.30}P_{0.64}Si_{0.36}F_{0.01}$, (c) $Mn_{0.60}Fe_{1.30}P_{0.64}Si_{0.36}F_{0.02}$, (d) $Mn_{0.60}Fe_{1.30}P_{0.64}Si_{0.36}F_{0.03}$, collected from detector bank 3 at

91

the Polaris instrument ($40.4° \leq 2\theta \leq 66.4°$). Black circles indicate the observed data points, red lines the calculated profile, blue lines the residuals and vertical lines the Bragg peak positions.
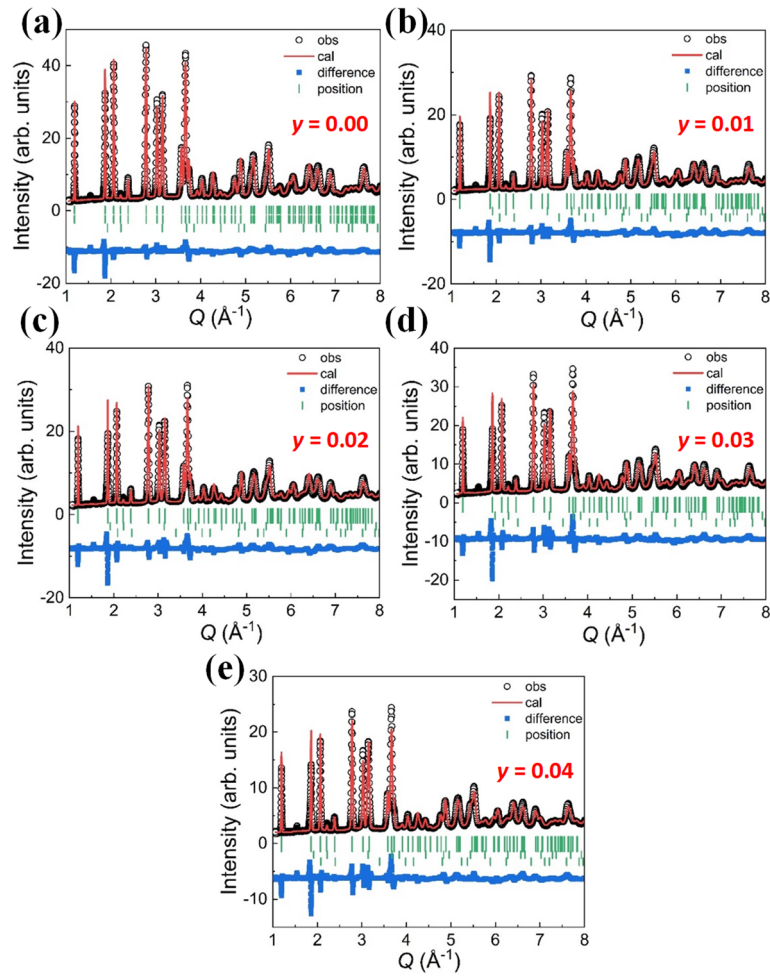

Figure S4.3 Fitted powder neutron diffraction patterns at room temperature for (a) $Mn_{0.60}Fe_{1.25}P_{0.66}Si_{0.34}S_{0.00}$ (b) $Mn_{0.60}Fe_{1.25}P_{0.65}Si_{0.34}S_{0.01}$ (c) $Mn_{0.60}Fe_{1.25}P_{0.64}Si_{0.34}S_{0.02}$ (d) $Mn_{0.60}Fe_{1.25}P_{0.63}Si_{0.34}S_{0.03}$ and (e) $Mn_{0.60}Fe_{1.25}P_{0.62}Si_{0.34}S_{0.04}$, collected from detector bank 3 at the Polaris instrument ($40.4° \leq 2\theta \leq 66.4°$). Black circles indicate the observed data points, red lines the calculated profile, blue lines the residuals and vertical lines the Bragg peak positions.

Table S4.1 Structural parameters for $Mn_{0.60}Fe_{1.30}P_{0.64}Si_{0.36}F_x$ (x = 0.00, 0.01, 0.02, 0.03) alloys derived from neutron diffraction. For comparison, the data within the square brackets show the corresponding results from X-ray diffraction at the same temperature.

Parameters	x = 0.00 (FM)	x = 0.01 (FM)	x = 0.02 (FM)	x = 0.02 (PM)	x = 0.03 (PM)
a	6.0843(4)	6.0791(3)	6.0716 (3)	6.0168 (6)	6.0072(3)
	[6.08834 (7)]	[6.08091 (10)]	[6.0765 (1)]	[6.0141 (1)]	[6.00824 (7)]
c	3.3552(3)	3.3590 (3)	3.3640 (3)	3.4231(6)	3.4328(2)
	[3.35359 (5)]	[3.35821 (7)]	[3.36466 (9)]	[3.4301 (1)]	[3.43882 (4)]
V	107.56(2)	107.50(2)	107.40(2)	107.32(3)	107.28(1)
	[107.66 (1)]	[107.54 (1)]	[107.59 (1)]	[107.44 (1)]	[107.51 (1)]
c/a	0.55145(6)	0.552542 (6)	0.554053 (5)	0.568926 (11)	0.571451 (5)
	[0.55082 (1)]	[0.55226 (1)]	[0.55372 (2)]	[0.57035 (2)]	[0.57235 (1)]
$3f$-x_1	0.2563 (3)	0.2559 (3)	0.2560 (2)	0.2545 (3)	0.2545 (1)
Occ-Fe_{3f}	0.250	0.250	0.250	0.250	0.250
Occ-Mn_{3f}	0	0	0	0	0
$M_{3f\text{-}Fe}(\mu_B)$	0.46 (5)	0.37 (5)	0.14 (6)	-	0
$3g$-x_2	0.6007 (3)	0.6013 (4)	0.6017 (3)	0.6058 (2)	0.6058 (3)
Occ-Fe_{3g}	0.078 (1)	0.081 (4)	0.086 (3)	0.078 (3)	0.078 (2)
Occ-Mn_{3g}	0.147 (1)	0.144 (2)	0.139 (4)	0.147 (4)	0.147 (3)
$M_{3g\text{-}Mn}(\mu_B)$	2.43 (5)	2.35 (5)	2.16 (6)	-	0
Occ-P_{2c}	0.10667	0.10667	0.10667	0.10667	0.10667
Occ-Si_{2c}	0.06000	0.06000	0.06000	0.06000	0.06000
Occ-P_{1b}	0.05333	0.05333	0.05333	0.05333	0.05333
Occ-Si_{1b}	0.03000	0.02916	0.02833	0.02833	0.02750
Occ-F_{1b}	-	0.00084	0.00167	0.00167	0.00250
Impurity1 (3:1; wf %)	2.56 [1.8 (2)]	3.05 [4.8 (3)]	5.71 [8.3 (2)]	-	3.77 [8.5 (2)]
FM state	97.44 [98.2 (7)]	96.95 [95.2 (9)]	61.06 (1) [38.6 (7)]	-	-
PM state	-	-	33.22 [53.1 (7)]	-	96.23 [78.6 (7)]
SiO_2 (wf %)	0	0	0	0	[12.9 (4)]
Rp (%)	5.98	7.43	5.65	5.65	5.02
Rwp (%)	7.60	8.39	6.37	6.37	5.52
M_{total} (M-T) (μ_B/f.u.)	2.90	2.78	2.44	-	1.12
M_{total} (Neutron) (μ_B/f.u.)	2.90 (7)	2.72 (7)	2.30 (8)	-	-

Table S4.2. Structural parameters for $Mn_{0.60}Fe_{1.25}P_{0.66-y}Si_{0.34}S_y$ (y = 0.00, 0.01, 0.02, 0.03, 0.04) alloys derived from neutron diffraction. For comparison, the data marked within the square brackets show the corresponding results from X-ray diffraction at the same temperature.

| Parameters	y = 0.00 (FM)	y = 0.01 (FM)	y = 0.02 (FM)	y = 0.03 (FM)	y = 0.04 (FM)
a	6.0848 (2)	6.0841 (3)	6.0780 (3)	6.0725 (4)	6.0729 (3)
	[6.0855 (10)]	[6.0866 (7)]	[6.0814 (1)]	[6.0776 (1)]	[6.0793 (1)]
c	3.3563 (2)	3.3596 (3)	3.3651 (2)	3.3701 (3)	3.3673 (3)
	[3.35498 (7)]	[3.3558 (5)]	[3.3610 (1)]	[3.3633 (1)]	[3.3614 (1)]
V	107.62 (1)	107.70 (2)	107.66 (1)	107.62 (2)	107.55 (2)
	[107.60 (1)]	[107.67 (1)]	[107.65 (1)]	[107.59 (1)]	[107.58 (1)]
c/a	0.551586 (3)	0.552184 (5)	0.553650 (4)	0.554975 (6)	0.554487 (5)
	[0.551304 (1)]	[0.55134 (1)]	[0.55268 (1)]	[0.55339 (1)]	[0.55292 (1)]
$3f$-x_1	0.2555 (3)	0.2559 (3)	0.2561 (1)	0.2564 (2)	0.2567 (3)
Occ-Fe$_{3f}$	0.25	0.25	0.25	0.25	0.25
Occ-Mn$_{3f}$	0	0	0	0	0
$M_{3f\text{-}Fe}(\mu_B)$	0.70 (4)	0.73 (7)	0.65 (7)	0.64 (8)	0.28 (7)
$3g$-x_2	0.6045 (3)	0.6050 (4)	0.6003 (1)	0.6012 (3)	0.6011 (5)
Occ-Fe$_{3g}$	0.080 (2)	0.089 (4)	0.090 (4)	0.088 (4)	0.089 (3)
Occ-Mn$_{3g}$	0.133 (3)	0.149 (1)	0.150 (1)	0.150 (2)	0.150 (2)
$M_{3g\text{-}Mn}(\mu_B)$	2.12 (4)	1.88 (7)	1.79 (7)	1.67 (8)	1.64 (7)
Occ-P$_{2c}$	0.11000	0.10833	0.10667	0.10500	0.10333
Occ-Si$_{2c}$	0.05667	0.05667	0.05667	0.05667	0.05667
Occ-S$_{2c}$	-	0.00167	0.00333	0.00500	0.00667
Occ-P$_{1b}$	0.05333	0.05333	0.05333	0.05333	0.05333
Occ-Si$_{1b}$	0.03000	0.03000	0.03000	0.03000	0.03000
Impurity1 ((MnFe)₃Si; *wf %*)	0.75 (2)	1.08 [0.5 (1)]	1.32 [2.2 (2)]	2.01 [3.9 (2)]	2.34 [3.8 (2)]
Impurity2 ((MnFe)S; *wf %*)	0	0.62 [1.1 (2)]	0.58 [1.8 (2)]	0.50 [2.8 (2)]	1.08 [4.1 (2)]
FM state	99.25 (1)	98 (2) [98 (1)]	98 (2) [96 (1)]	97 (2) [93 (1)]	96 (3) [92 (1)]
Rp (%)	4.57	4.94	5.34	5.30	5.39
Rwp (%)	5.32	5.67	6.23	6.22	6.07
M_{total} (*M-T*) ($\mu_B/f.u.$)	2.87	2.67	2.59	2.34	2.00
M_{total} (Neutron) ($\mu_B/f.u.$)	2.82 (6)	2.61 (10)	2.44 (10)	2.31 (10)	1.93 (10)
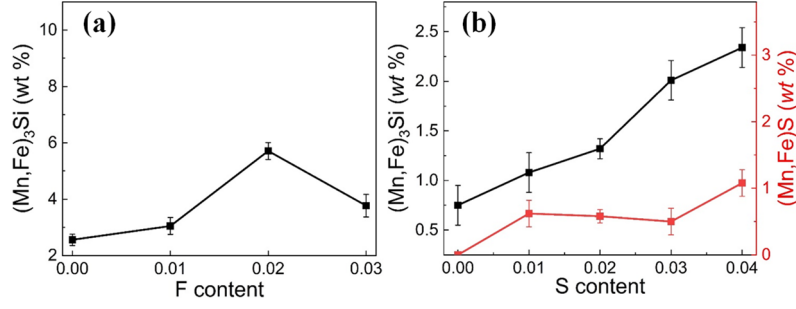
Figure S4.4 Phase fraction of the main impurities for (a) $Mn_{0.60}Fe_{1.30}P_{0.64}Si_{0.36}F_x$ (x = 0.00, 0.01, 0.02, 0.03) and (b) $Mn_{0.60}Fe_{1.25}P_{0.66-y}Si_{0.34}S_y$ (y = 0.00, 0.01, 0.02, 0.03, 0.04) alloys derived from powder neutron diffraction.

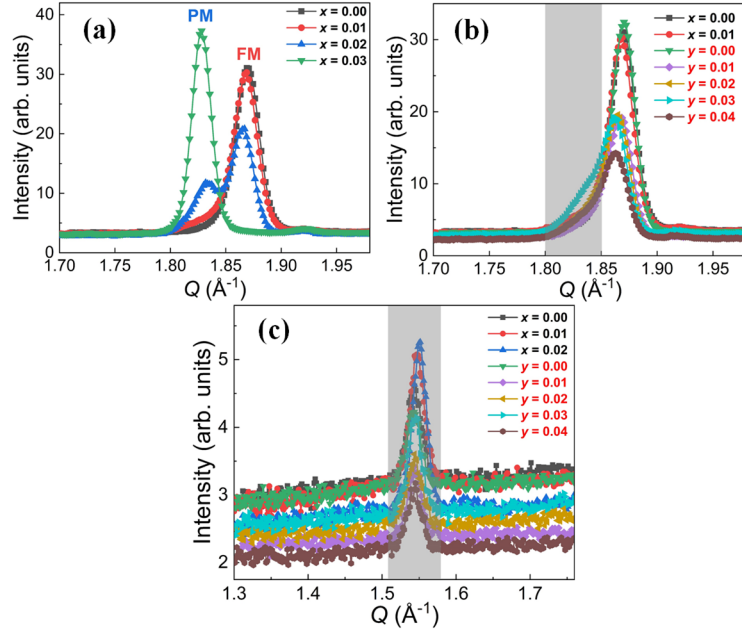**Figure S4.5** (a) (001) Neutron diffraction peak in different magnetic states for $Mn_{0.60}Fe_{1.30}P_{0.64}Si_{0.36}F_x$ with x = 0 (black, FM), x = 0.01 (red, FM), x = 0.02 (blue, two phase coexistence) and x = 0.03 (green, PM) alloys. (b) (001) Neutron diffraction peak in the FM state for $Mn_{0.60}Fe_{1.30}P_{0.64}Si_{0.36}F_x$ (x = 0.00, 0.01) and $Mn_{0.60}Fe_{1.25}P_{0.66-y}Si_{0.34}S_y$ (y = 0.00, 0.01, 0.02, 0.03, 0.04) alloys. The grey area demonstrates the anisotropic broadening of the (001) peak. (c) Neutron diffraction peak at $Q \approx 1.55$ Å^{-1} for $Mn_{0.60}Fe_{1.30}P_{0.64}Si_{0.36}F_x$ (x = 0.00, 0.01, 0.02) and $Mn_{0.60}Fe_{1.25}P_{0.66-y}Si_{0.34}S_y$ (y = 0.00, 0.01, 0.02, 0.03, 0.04) alloys.

As shown in **Figure S4.5a**, a (001) peak is observed for the $Mn_{0.60}Fe_{1.30}P_{0.64}Si_{0.36}F_x$ (x = 0.00, 0.01, 0.02, 0.03) samples with an obvious shift from the pure FM to the pure PM state. In contrast, the two-phase coexistence state for the F-doped (x = 0.02) sample at RT shows a characteristic double diffraction peak. The (001) peaks of all FM state samples for F-doping

95

and S-doping illustrates an asymmetric broadening, as shown in the grey area in **Figure S4.5b**, which could possibly be ascribed to the introduced stacking faults during the strong first-order phase transition. This phenomenon can also be seen for *in-situ* field-dependent neutron diffraction [1]. Ungár *et al*. demonstrated that introducing intrinsic stacking faults (ISFs) and extrinsic stacking faults (ESFs) will cause an asymmetric broadening for different peaks. More recently, Wang *et al*. [2, 3] found that for a *fcc*-to-*hcp* phase transformation in CrCoNi a similar asymmetric peak broadening was found during tensile loading were mainly resulted from ISFs. Furthermore, based on high-resolution STEM-HAADF measurements, Miao *et al* [4] observed distributed dislocations along the (001) basal plane, which could be ascribed to stacking faults of the *3g* and *3f* layers along the hexagonal *c* axis as a result of the quenching process. As shown in **Figure S4.5c** an unknown weak neutron peak appeared at $Q \approx 1.55$ Å^{-1}, which is not observable in XRD and cannot be labeled by either the main phase or an impurity phase. This peak may correspond to a superstructure reflection [5] of the (MnFe)₃Si impurity, which may depend on Mn/Fe site ordering [6, 7].
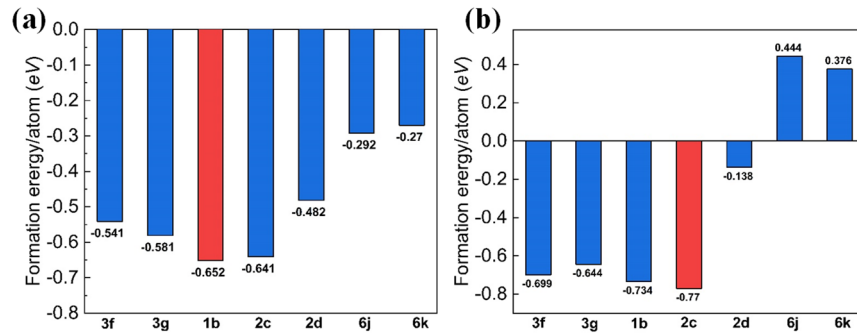

Figure S4.6 Formation energies E_f of various site occupation models for the (a) F-doped and (b) S-doped Mn$_{0.5}$Fe$_{1.5}$P$_{2/3}$Si$_{1/3}$.

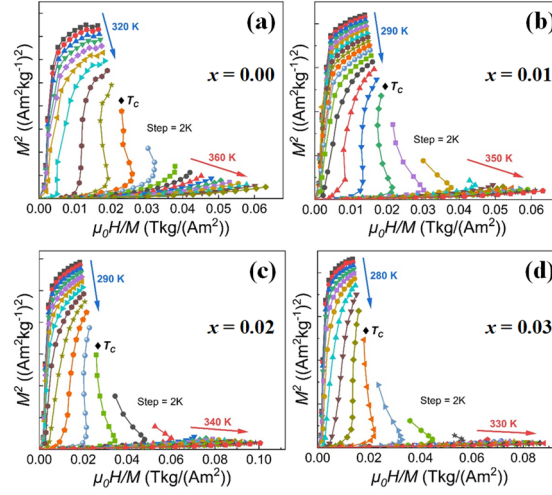**Figure S4.7** Arrott plots for the $Mn_{0.60}Fe_{1.30}P_{0.64}Si_{0.36}F_x$ (x = 0.00, 0.01, 0.02, 0.03) alloys derived from isothermal M-T curves in different applied magnetic fields.
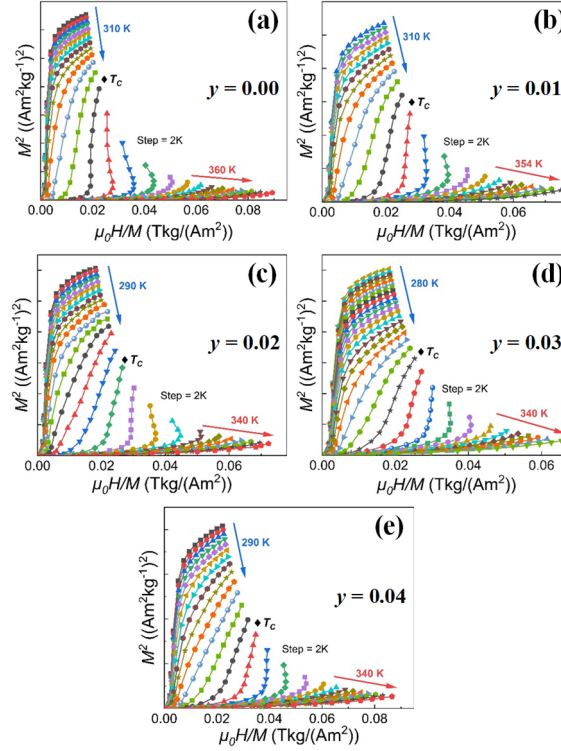

Figure S4.8 Arrott plots for the $Mn_{0.60}Fe_{1.25}P_{0.66-y}Si_{0.34}S_y$ (y = 0.00, 0.01, 0.02, 0.03, 0.04) alloys derived from isothermal M-T curves in different applied magnetic fields.
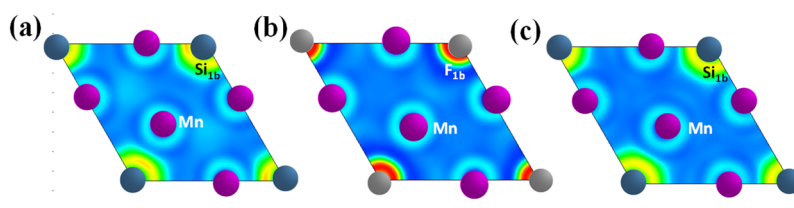
**Figure S4.9** Calculated contour maps of the Electron Localization Function (ELF) for MnFeP$_{2/3}$Si$_{1/3}$ showing the *3g* (Mn) layer with (a) no doping, (b) F doping and (c) S doping. The contour maps are sliced along (001) direction.

References:

[1] X.F. Miao, Y. Gong, F.Q. Zhang, Y.R. You, L. Caron, F.J. Qian, W.H. Guo, Y.J. Zhang, Y.Y. Gong, F. Xu, N.H. van Dijk, E. Brück, Enhanced reversibility of the magnetoelastic transition in (Mn,Fe)$_2$(P,Si) alloys via minimizing the transition-induced elastic strain energy, *J Mater Sci Technol* 103 (2022) 165-176.

[2] L. Balogh, G. Ribarik, T. Ungar, Stacking faults and twin boundaries in fcc crystals determined by x-ray diffraction profile analysis, *J Appl Phys* 100 (2006) 023512.

[3] H.Y. He, M. Naeem, F. Zhang, Y.L. Zhao, S. Harjo, T. Kawasaki, B. Wang, X.L. Wu, S. Lan, Z.D. Wu, W. Yin, Y. Wu, Z.P. Lu, J.J. Kai, C.T. Liu, X.L. Wang, Stacking fault driven phase transformation in CrCoNi medium entropy alloy, *Nano Lett* 21 (2021) 1419-1426.

[4] X.F. Miao, H. Sepehri-Amin, K. Hono, Structural origin of hysteresis for hexagonal (Mn,Fe)2(P,Si) magneto-caloric compound, *Scripta Mater* 138 (2017) 96-99.

[5] A.Y. Volkov, Structure and mechanical properties of CuAu and CuAuPd ordered alloys, *Gold Bull* 37 (2004) 208-215.

[6] V. Niculescu, K. Raj, T.J. Burch, J.I. Budnick, Correlation of the internal fields, magnetic moments, and site preferences in Fe$_{3-x}$Mn$_x$Si alloys, *Phys Rev B* 13 (1976) 3167-3174.

[7] S. Yoon, J.G. Booth, Magnetic properties and structures of some ordered (FeMn)$_3$Si alloys, *J Phys F Met Phys* 7 (1977) 1079-1095.

Chapter 5 The second-order magnetic phase transition and magnetocaloric effect in all-*d*-metal NiCoMnTi-based Heusler alloys
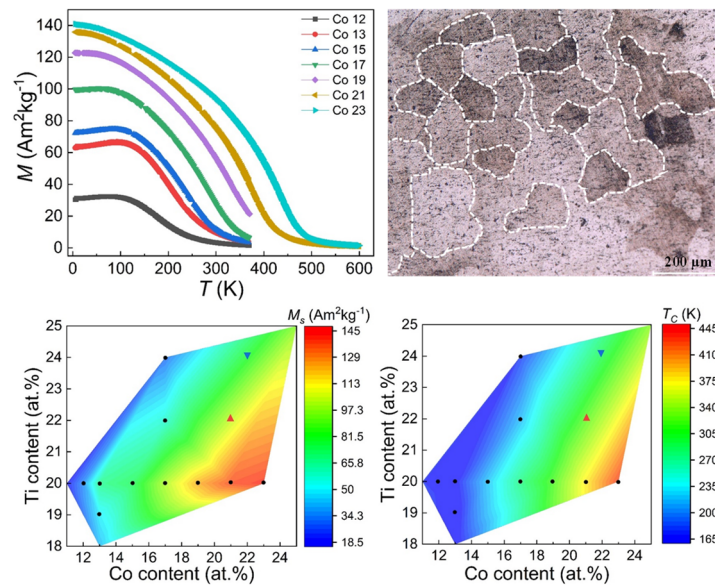
This chapter is based on:

Abstract

The novel all-*d*-metal Ni(Co)MnTi based magnetic Heusler alloys provide an adjustable giant magnetocaloric effect and good mechanical properties. We report that the second-order magnetic phase transition can be tailored in this all-*d*-metal NiCoMnTi based Heusler system by optimizing the Mn/Ti ratio, resulting in a reversible ferromagnetic-to-paramagnetic magnetic transition. A candidate material $Ni_{33}Co_{17}Mn_{30}Ti_{20}$ with a magnetic entropy change ΔS_m of 2.3 Jkg^{-1}K^{-1} for a magnetic field change of 0-5 T, has been identified. The T_C and saturation magnetization M_S can be controlled by adjusting the Ni/Co concentration and doping non-magnetic Cu atoms. The compositional maps of T_C and M_S have been established. Density functional theory (DFT) calculations reveal a direct correlation between the magnetic moments and the Co content. By combining XRD, SQUID, SEM and DFT calculations, the (micro)structural and magnetocaloric properties have been investigated systematically. This study provides a detailed insight in the magnetic phase transition for this all-*d*-metal Ni(Co)MnTi-based Heusler alloy system.

5.1 Introduction

The giant magnetocaloric effect (GMCE) is characterized by an adiabatic temperature change (ΔT_{ad}) and an isothermal magnetic entropy change (ΔS_m) when a magnetocaloric material (MCM) is exposed to a changing magnetic field. The GMCE can be utilized to design promising environmental-sustainable and eco-friendly applications like waste heat recovery, a thermomagnetic generator (TMG) and solid-state magnetic refrigeration (SSMR). The GMCE has been widely observed in various MCMs like Gd-Si-Ge [1], Fe_2P-type [2], La-Fe-Si [3], Ni-Mn-*X* (*X* = In, Sn, Sb, Ga, Al) based Heusler alloys [4] and Mn-*M*-X based (*M* = Co or Ni, X = Si or Ge) ferromagnets [5]. These materials demonstrate a strong first-order magnetic transition (FOMT) with a discontinuous change in the first derivative of the Gibbs free energy resulting from the coupling between the magnetic and crystal lattice degrees of freedom (in the form of a magnetoelastic or magnetostructural coupling). Even though the MCMs that show a FOMT exhibit the giant and sharp ΔS_m and ΔT_{ad}, the associated undesirable intrinsic thermal and magnetic hysteresis inevitably results in a low energy efficiency during cooling cycles as a result of the irreversibility. Furthermore, the strong crystal lattice distortion accompanied by the structural transition generally makes these MCMs subject to cracking and fatigue, which limits the lifetime of these materials.

Compared with the FOMT, the second-order magnetic transition (SOMT) with a discontinuous change in the second derivative of the Gibbs free energy show a reversible magnetic transition from the low-temperature ferromagnetic (FM) to high-temperature paramagnetic (PM) state. The SOMT materials can thereby avoid some of the intrinsic disadvantages of the FOMT materials, although the magnetocaloric performance is relatively moderate. Currently, some interesting SOMT materials like $(LaSr)MnO_3$ based perovskites [6], Fe-based amorphous alloys [7], $AlFe_2B_2$ based intermetallic compounds [8], MnSb based half-Heusler alloys [9, 10] and NiMn based Heusler alloys [11-16] have been investigated. Singh *et al.* found that the off-stoichiometric $Ni_2Mn_{1.4}In_{0.6}$ Heusler alloys can simultaneously demonstrate a large saturation magnetization (M_S = 6.17 μ_B/f.u.) and a high ΔT_{ad} (of about 1.5 K for a field change of 0-2 T) near room temperature, which makes it competitive with some FOMT shape-memory Heusler alloys [11]. Additionally, the SOMT properties of the Si substituted $Ni_{50}Mn_{36}Sn_{14-x}Si_x$ (*x* = 1, 2, 3) and $Ni_{50}Mn_{35}In_{15-x}Si_x$ ($1 \leqslant x \leqslant 5$) Heusler systems have been studied [12, 15]. Recently, the unique all-*d*-metal Ni(Co)MnTi based magnetic Heusler alloys have been discovered [17, 18]. In comparison to the traditional NiMn-*X* (*X* = In, Sn, Sb, Ga, Al) based magnetic Heusler alloys, where the 3rd element is mainly occupied by *p*-block elements, the structural transition temperature can be significantly decreased by introducing Ti and ferromagnetism can be established by

forming strong Mn-Co-Mn magnetic interactions in these all-*d*-metal Ni(Co)MnTi based Heusler alloys. Like other Heusler systems, this all-*d*-metal Heusler alloy system also shows a large thermal hysteresis [19-21]. Because the Ti in the system can effectively stabilize the austenite phase [22], we therefore expect that tuning the Mn/Ti ratio could decouple the first-order magnetostructural transition, resulting in a reversible SOMT. Recent studies in this Heusler system mainly focus on regulating the FOMT [19, 23]. Studies associated with the SOMT in this system are still scarce and could deepen our understanding of the functionality of this material system for future applications.

By optimizing the Mn/Ti ratio all-*d*-metal NiCoMnTi based magnetic Heusler alloys with a SOMT have been produced successfully. We systematically investigate the magnetocaloric properties (including compositional maps of T_C and M_S), the structural properties and the microstructure information of these alloys by XRD, SQUID, SEM and Density functional theory (DFT). Our results show T_C and M_S can be controlled by adjusting the Ni/Co concentration and by doping non-magnetic Cu atoms. The present study provides new insight into the magnetic phase transition for this all-*d*-metal Ni(Co)MnTi based Heusler alloy system.

5.2 Experimental methods

The SOMT all-*d*-metal NiCoMnTi based magnetic Heusler alloys with a composition of $Ni_{50-x}Co_xMn_{30}Ti_{20}$ (x = 11, 12, 13, 15, 17, 19, 21, 23), $Ni_{37}Co_{13}Mn_{30+x}Ti_{20-x}$ (x = 1, 2), $Ni_{33}Co_{17}Mn_{30-x}Ti_{20+x}$ (x = 2, 4) and $Ni_{37-y}Co_{13}Mn_{30}Ti_{20-x}Cu_{x+y}$ (x,y = 0.5, 1) samples were prepared from high-purity elements (Ni 99.99%, Co 99.9%, Mn 99.99%, Ti 99.99% and Cu 99.9%) employing the arc-melting technique under Ar atmosphere. For homogenization the melted ingots were flipped and remelted for five times. An extra 4% Mn was added to compensate for evaporation losses during melting. Subsequently, the as-cast ingots were sealed into quartz ampoules under Ar atmosphere and annealed at 1173 K for 6 days followed by cold-water quenching to further enhance homogeneity and short range order. The room temperature X-ray diffraction (XRD) patterns were collected on a PANalytical X-pert Pro diffractometer with Cu-K_α radiation. The crystal structure refinement of XRD patterns was performed using the Rietveld refinement method [24] implemented in the Fullprof software package. The microstructure of the alloys was analyzed by a Scanning Electron Microscope (SEM, JEOL JSM IT100LA) equipped with Energy Dispersive X-ray Spectroscopy (EDS), and line-scans were used to determine the elemental distribution of different phases. To visualize the grain boundaries of the materials two drops of etching solvent (0.5 g $FeCl_3$ mixed with 9.9 mL methanol (CH_3OH)) were spread on the surface of

metallographic specimens and then rapidly removed with ethanol after 15-20 seconds. After that, optical microscopy (Olympus Corporation) was applied. The temperature and magnetic field dependence of the magnetization curves were characterized by a superconducting quantum interference device (SQUID) magnetometer (Quantum Design MPMS 5XL) using the reciprocating sample option (RSO) mode. For measurements on the magnetic properties above 370 K a vibrating sample magnetometer (VSM, Quantum Design Versalab) was applied. The ΔS_m and ΔT_{ad} can be derived from the calorimetric measurements based on a home-built in-field DSC machine, details can be found in Ref. [25].

First-principles electronic structure calculations were performed in the framework of the density functional theory (DFT). The Vienna *ab initio* simulation package (VASP) [26, 27] in the projector augmented wave (PAW) method [28, 29] was employed to perform the DFT calculations using the generalized gradient approximation of Perdew-Burke-Ernzerhof [30] for the exchange correlation functional. The valence electron configuration was $3p^6 4s^2 3d^5$ for Mn, $3p^6 4s^2 3d^2$ for Ti, $4s^2 3d^7$ for Co and $4s^2 3d^8$ for Ni. A 2×2×1 supercell, built from a 16-atom unit cell, was utilized in all calculations. The structural degrees of freedom were fully relaxed on a *k*-grid of 10×10×10. The *k*-space integrations were performed with the Methfessel-Paxton method [31] of second order with a smearing width of 0.05 eV. The lattice parameters and atomic positions were relaxed for a force convergence of 0.1 meV/Å, the energies were converged to 1 μeV. The kinetic energy cutoff was set at 350 eV.

5.3 Results and discussions

5.3.1 Structural analysis

The room temperature XRD patterns for the $Ni_{50-x}Co_xMn_{30}Ti_{20}$ (*x* = 12, 13, 15, 17, 19, 21, 23) samples are shown in **Figure 5.1(a)**. All diffraction peaks correspond with the cubic *B2*-type austenite (space group *Fm-3m*) crystal structure, confirming that a stable austenite phase is formed. No signal from the modulated martensite structure or from an impurity phase was found, indicating a pure austenite phase. Wei *et al.* demonstrated that samples contained less than 16% Co could hold martensite at low temperatures [17], while in our case the martensite to austenite structural transition can be tuned to disappear and only the parent *B2*-type austenite is left by optimizing the Mn/Ti ratio to a lower Mn level (higher Ti). The lattice parameter *a* decreases from 5.928 Å to 5.914 Å when the Co content increases from 12% to 23%, as illustrated in **Figure 5.1(b)**. Considering the covalent radius of Ni (1.24 Å) and Co (1.26 Å) [32], more Co with a larger radius should expand the unit-cell volume, which is in conflict with the experimental results. Similar results were also observed

in $Ni_{50-x}Co_xMn_{35}Ti_{15}$ (x = 13, 13.5) ribbon samples with a FOMT [20]. This decrease in cell volume is also confirmed by our DFT calculations see below. The Rietveld refinement of the room-temperature XRD pattern for the $Ni_{33}Co_{17}Mn_{30}Ti_{20}$ sample is presented in **Fig 5.1(c)** and the main diffraction planes are labeled as (220), (400) and (422). In **Fig 5.1(d)** the cubic *B2* austenite crystal structure with space group *Fm-3m* is shown. The various metallic atoms follow specific crystal occupancy rules. The Ni/Co atoms occupy the 8*c* site at (1/4, 1/4, 1/4) and (1/4, 1/4, 3/4) while the Mn/Ti atoms occupy the 4*b* site at (1/2, 1/2,1/2) and the 4*a* site at (0, 0, 0), where Mn preferentially occupies the 4*b* position.
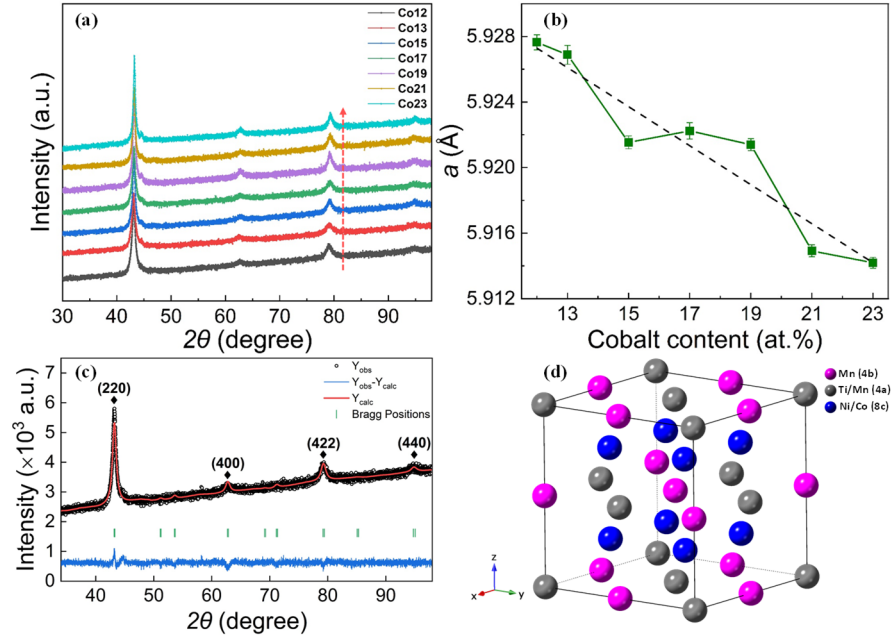

Figure 5.1 (a) Room-temperature XRD patterns for $Ni_{50-x}Co_xMn_{30}Ti_{20}$ (x = 12, 13, 15, 17, 19, 21, 23) alloys with different Co concentrations. (b) Lattice parameter a derived from the XRD refinement results as a function of the Co concentration for the $Ni_{50-x}Co_xMn_{30}Ti_{20}$ (x = 12, 13, 15, 17, 19, 21, 23) alloys. (c) Room-temperature refined XRD measurement of the $Ni_{33}Co_{17}Mn_{30}Ti_{20}$ sample. (d) Schematic crystal structures of *B2* austenite phase.

5.3.2 Magnetic properties and magnetic phase diagram

In **Figure 5.2(a)** the temperature-dependent magnetization (*M-T*) curves of the materials that vary in Ni/Co ratio (x = 12, 13, 15, 17, 19, 21, 23) are shown. The heating and cooling curves coincide, which suggests that the transition corresponds to a SOMT. The results show that the magnetic behavior is significantly affected by its composition. For instance, a higher

104

Co content attributes to an obvious enhancement in magnetization. By comparing the samples with the lowest Co (12%) and the highest Co (23%) it is found that the saturation magnetization shows a fivefold increment, from 32.4 to 144.5 Am^{2}kg^{-1}. Similar to the case of all-*d* metal NiCoMnTi system with a FOMT, the so-called "Co-activated ferromagnetism" also plays a crucial function in the SOMT system where Co can effectively help to build a strong ferromagnetic coupling in the local Mn-Co-Mn configuration [33, 34]. In **Figure 5.2(b)**, the *M-T* curves at 0.01 T are presented. The Curie temperature T_C of austenite can be determined from the maximum in $|dM/dT|$ in these low-field *M-T* curves (see the inset of **Figure 5.2(b)**). As illustrated in **Figure 5.2(c)**, it can be seen that with increasing Co content the T_C of austenite increases and closely follows a linear relation of about 27 K/*at.*% Co. Interestingly, in **Figure 5.2(b)** we observe for almost all samples a distinct difference between zero-field-cooling (ZFC) and field-cooling (FC) curves when temperature is below 100 K. This has also been observed in other Mn-based Heusler alloys like Fe-Mn-Si [35] and Ni-Mn-In [13] and should be ascribed to magnetocrystalline anisotropy. The maximum observed in the temperature dependence of the magnetization for Co ≤ 19 should be ascribed to a change in magnetic interactions from FM at high temperatures to antiferromagnetic (AFM) at lower temperature. Note, that the parent austenite of NiMnTi based Heusler alloys is an antiferromagnet [17, 19]. In **Figure 5.2(d)** the isothermal field-dependent magnetization (*M-H*) curves at 5 K are presented, which demonstrate that an increase in Co concentration leads to a higher magnetization. Furthermore, it can be also deduced that considerably less magnetic field is needed to reach its maximum magnetization for samples with a higher Co content. For example, the sample containing 23% Co can be saturated at around 1 T while the 15% Co sample is still not saturated at 5 T. It is worth to note that for the samples with the lowest Co content (such as 12% and 15%) the magnetization and demagnetization curves fail to overlap each other below 1 T, which should also be attributed to the magnetocrystalline anisotropy mentioned above.
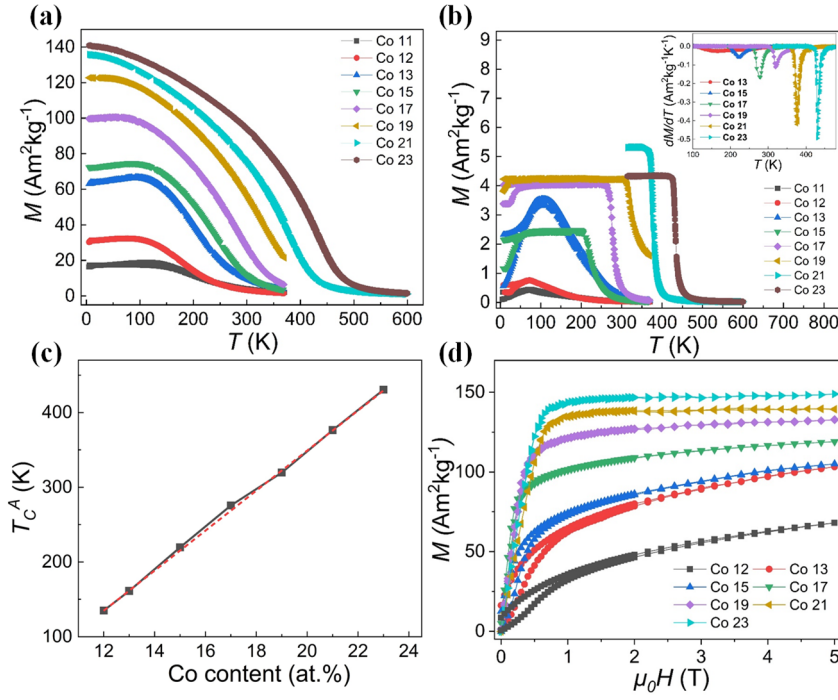
Figure 5.2 (a) Temperature-dependent magnetization (*M-T*) curves at 1 T for Ni$_{50-x}$Co$_x$Mn30Ti20 (*x* =11, 12, 13, 15, 17, 19, 21, 23) samples. (b) *M-T* curves at 0.01 T for Ni$_{50-x}$Co$_x$Mn$_{30}$Ti$_{20}$ (*x* =11, 12, 13, 15, 17, 19, 21, 23) samples. The inset shows *dM/dT* versus temperature. (c) Curie temperature as a function of the Co content. (d) Field-dependent magnetization (*M-H*) curves at 5 K for Ni$_{50-x}$Co$_x$Mn$_{30}$Ti$_{20}$ (*x* = 12, 13, 15, 17, 19, 21, 23) samples.

Controlling T_C to cover a certain temperature range is a fundamental requirement for cooling applications. The Curie temperature can be tuned via optimizing different intrinsic and extrinsic parameters, such as composition [36], particle size [37], chemical element pressure [38], electron valence [23], and external mechanical (hydrostatic) pressure [39]. Within these factors, the chemical pressure, which is closely related to a change in unit-cell volume, and electron valence effects could be distinctly affected by magnetic/non-magnetic metal substitution or interstitial (light-element) doping. For example, the substitution of Mn by Cr has been applied to tailor the magnetic and structural transitions in Mn$_{1-x}$Cr$_x$CoGe compounds [40]. Recently, it has been found that Cu substitution in Ni-Mn-In based Heusler alloys can effectively modify the FOMT [41-43]. Therefore, we expect that T_C could also be efficiently tailored through Cu substitution of Ni/Mn in the Ni-Co-Mn-Ti system with a SOMT. In **Figure 5.3(a)**, the *M-T* curves at 1 T for the Ni$_{37-y}$Co$_{13}$Mn$_{30}$Ti$_{20-x}$Cu$_{x+y}$ (*x, y* = 0, 0.5, 1) samples are presented. It is observed that the magnetization decreases when Cu replaces

106

Ti or Ni. In **Figure 5.3(b)** it is shown that compared with the parent $Ni_{37}Co_{13}Mn_{30}Ti_{20}$ (T_C = 202 K) alloy, Cu substitution of Ti shows a remarkable decrease in T_C. A substitution of 0.5% Cu shifted T_C to 179 K (and 1% Cu to 171 K), while a 0.5% Cu substitution of Ni results in a reduction in T_C to 190 K (and 1% Cu to 178 K). The reduction in T_C is about 24 K/*at.*% Cu. The shift in T_C by Cu substitution could result from the weakened magnetic exchange interaction between the Mn-Co-Mn configuration, rather than the chemical pressure effect because the covalent radius of Cu (1.32 Å) is in between that of Ti (1.60 Å) and Ni (1.24 Å) [32], even though Cu ($3d^{10}4s^1$) atoms have more electrons than Ti ($3d^24s^2$)/Ni ($3d^84s^2$). Therefore, Cu substitution and tuning the Ni/Co ratio are both efficient ways to optimize the T_C shift. In addition, **Figure 5.3(c)** and **3(d)** show the *M-T* curves at 1 T for the $Ni_{37}Co_{13}Mn_{30+x}Ti_{20-x}$ (x = 0, 1, 2) and $Ni_{33}Co_{17}Mn_{30-x}Ti_{20+x}$ (x = 0, 2, 4) samples.
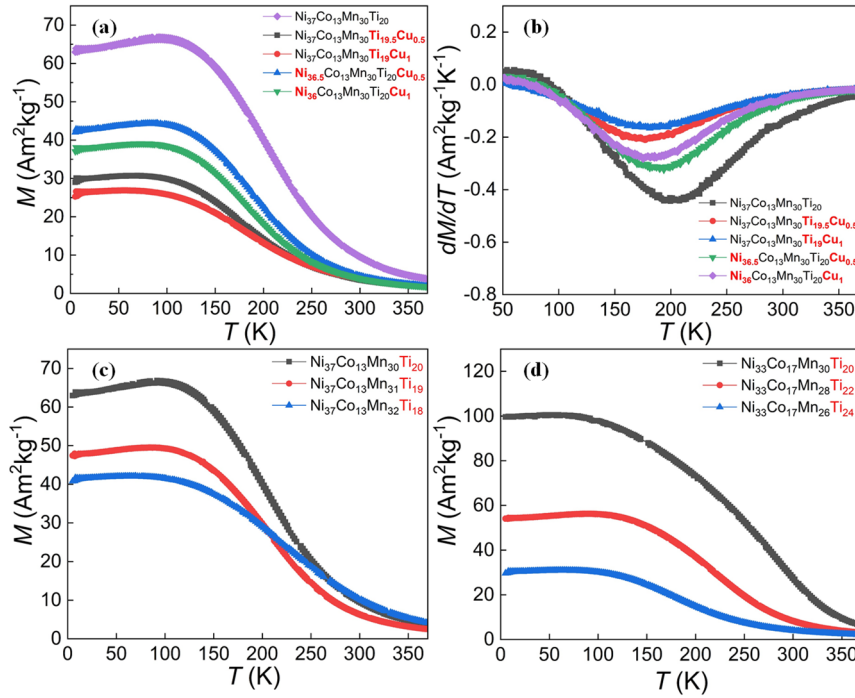
Figure 5.3 (a) Isofield *M-T* curves at 1 T for $Ni_{37-y}Co_{13}Mn_{30}Ti_{20-x}Cu_{x+y}$ (x,y = 0, 0.5, 1) series samples. (b) Relationship between *dM/dT* and temperature for the Cu-doped samples. (c) Isofield *M-T* curves at 1 T for $Ni_{37}Co_{13}Mn_{30+x}Ti_{20-x}$ (x = 0, 1, 2) samples. (d) Isofield *M-T* curves at 1 T for $Ni_{33}Co_{17}Mn_{30-x}Ti_{20+x}$ (x = 0, 2, 4) samples.

From the above results it can be seen that T_C and the magnetization can be regulated by composition in the $Ni_{50-x}Co_xMn_{30}Ti_{20}$ (x = 12, 13, 15, 17, 19, 21, 23) samples with a SOMT. This indicates that Co substitution for Ni is effective in increasing T_C and the magnetization

for the NiCoMnTi Heusler alloys with a SOMT. This may be attributed to the strong coupling between Co and Mn atoms. A similar phenomenon was also observed in other NiMn-based Heusler alloys with a FOMT, such as Ni(Co)MnGa [44], Ni(Co)MnIn [45], Ni(Co)MnSn [46] and Ni(Co)MnSb [47]. In **Figure 5.4(a)** and **5.4(b)** we summarized the changes in T_C and magnetization as a function of Co content. Once Co content is above 12 *at.%* T_C and magnetization data show an increasing tendency with increasing Co concentration, and T_C of 11% Co is close to 12% one.
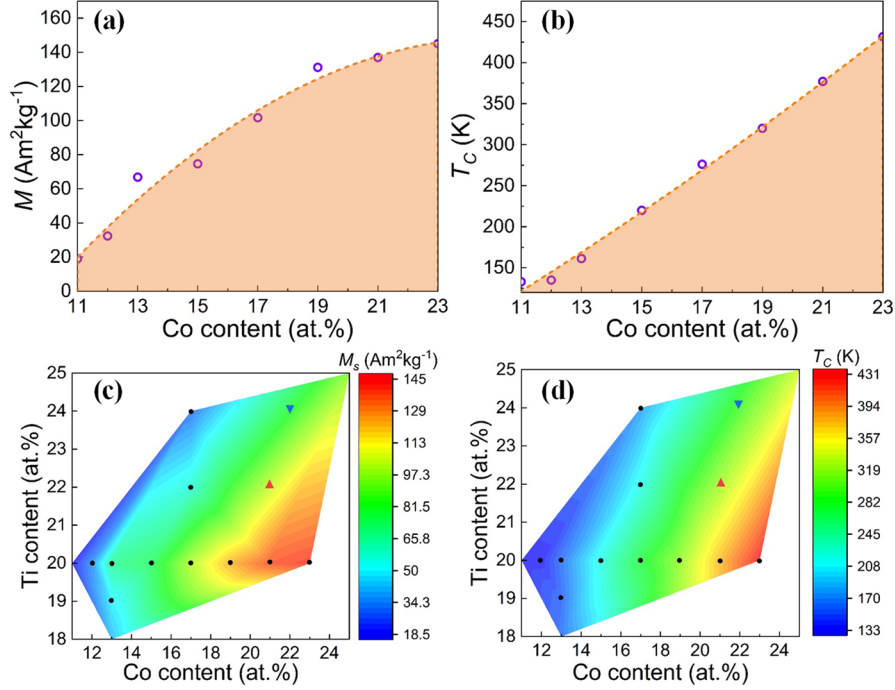

Figure 5.4 Effect of the Co concentration on the (a) saturation magnetization and (b) transition temperature at 5 K derived from *M-T* measurements. Effect of the amount of Co and Ti substitution on (c) the saturation magnetization and (d) the phase transition temperature the *2D* compositional maps. The black marks indicate which compositions were measured, and (▲), (▼) in the top corner stands for two test samples to confirm the trends.

To better guide the optimization of the all-*d*-metal NiCoMnTi magnetic Heusler alloys with a SOMT, it is useful to determine compositional maps of the saturation magnetization MS and the Curie temperature T_C with respect to different Co/Ti content (in *at.%*), as presented in **Figure 5.4(c)** and **5.4(d)**, respectively. On the other hand, to verify the usefulness of these phase diagrams, two new alloys with a designed composition (Ni$_{29}$Co$_{21}$Mn$_{28}$Ti$_{22}$ and

$Ni_{28}Co_{22}Mn_{26}Ti_{24}$) are utilized. For example, **Figure 5.5** shows the *M-T* curves at 1 T for these two samples and the inset corresponds to the *M-T* curves at 0.01 T. The values of M_S at 5 K are 114 and 88 Am^2kg^{-1}, and the values of T_C are 333 and 311 K for $Ni_{29}Co_{21}Mn_{28}Ti_{22}$ and $Ni_{28}Co_{22}Mn_{26}Ti_{24}$ compounds, respectively. These experimental data points are marked in **Figure 5.4(c)** and **4(d)**. It is clear that the experimental data for these two samples are in good agreement with the compositional maps for T_C and M_S, which supports the reliability of our compositional maps.
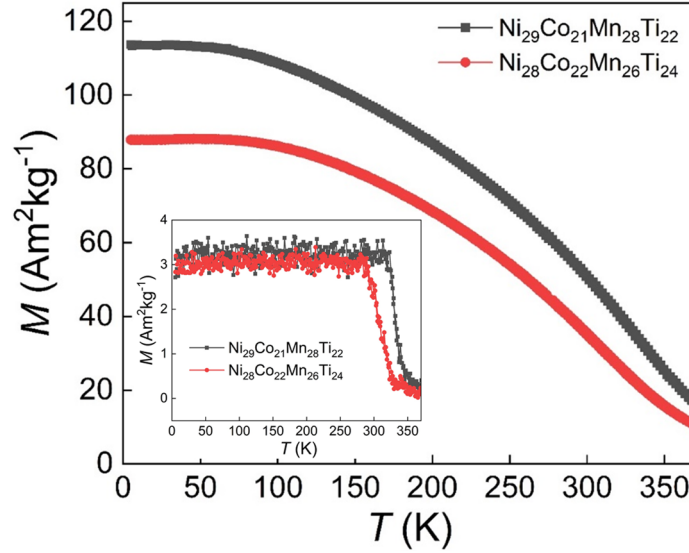

Figure 5.5 Isofield *M-T* curves at 1 T for the $Ni_{29}Co_{21}Mn_{28}Ti_{22}$ and $Ni_{28}Co_{22}Mn_{26}Ti_{24}$ samples. The inset corresponds to the *M-T* curves at 0.01 T for these two alloys.

Using DFT, the calculated lattice parameter *a*, the total magnetic moment and the lowest formation energy have been evaluated for the $Ni_{50-x}Co_xMn_{30}Ti_{20}$ (*x* = 12, 13, 15, 17, 19, 21, 23) samples, as listed in **Table 5.1**. A decrease in lattice parameter a is also observed for increasing Co content, which is in agreement with our experimental results shown in **Figure 5.1(b)**. Interestingly, the total magnetic moment (per formula unit) for this material system with a SOMT is predominantly controlled by the Co concentration and shows an increase with increasing Co content. For instance, the calculated moment was enhanced from 5.44 (*x* = 13) to 5.83 (*x* = 23) $\mu_B/f.u.$ This might be because a higher Co content can more sufficiently align the Mn atoms as the local Mn-Co-Mn configuration controls the introduced strong FM, which is similar to other Co-doping NiMn-based Heusler systems.

Table 5.1 DFT calculation results for the lattice parameters a, the total magnetic moment per formula unit and the lowest formation energy for the $Ni_{50-x}Co_xMn_{30}Ti_{20}$ (x = 12, 13, 15, 17, 19, 21, 23) samples.

x	13	14	16	17	19	20	22	23
a (Å)	5.91	5.91	5.90	5.89	5.88	5.88	5.87	5.87
Moment (μ_B/f.u.)	5.44	5.45	5.55	5.60	5.64	5.71	5.80	5.83
Energy (eV/atom)	-0.668	-0.641	-0.631	-0.612	-0.591	-0.575	-0.544	-0.517

Due to the relative high M_S at 1 T (102 Am^{2}kg^{-1}) and the near room temperature magnetic phase transition T_C (275 K) the 17% Co sample ($Ni_{33}Co_{17}Mn_{30}Ti_{20}$) seems to be the most promising candidate within this series for magnetic refrigeration applications. It is therefore of interest to further investigate the magnetocaloric properties of this $Ni_{33}Co_{17}Mn_{30}Ti_{20}$ alloy in terms of the magnetic entropy change (ΔS_m), adiabatic temperature change (ΔT_{ad}) and the relative cooling power (*CRP*). As shown in **Figure 5.6(a)**, the isofield *M-T* curves from 0.1 to 5 T have been collected. From these data the ΔS_m values can be calculated by using the Maxwell relation:

$$\Delta S_m(T,H) = \int_0^{\mu_0 H} \left(\frac{\partial M}{\partial T}\right)_H d\mu_0 H \tag{5.1}$$

From **Figure 5.6(b)** it can be seen that the sample shows a conventional MCE. As expected for a material with a SOMT the ΔS_m peak is obviously broad and moderate in size. For example, the maximum $|\Delta S_m|$ with an applied magnetic field change ($\Delta \mu_0 H$) of 0-1 T can reach only 0.6 Jkg^{-1}K^{-1} which is well consistent with the value extracted from DSC-in field measurement, and $|\Delta S_m|$ reaches a maximum value of 1.1 and 2.3 Jkg^{-1}K^{-1} with $\Delta \mu_0 H$ of 0-2 and 0-5 T, respectively. Although maximum value for $|\Delta S_m|$ only reaches about 22 % of the value obtained for pure gadolinium (5 Jkg^{-1}K^{-1} for $\Delta \mu_0 H$ = 2 T), it is comparable to other magnetic Heusler alloys with a SOMT [11-14, 48, 49]. The coefficient of refrigerant performance (*CRP*) reflects the MCE performance and can be determined by the following relation [50]:

$$CRP = \frac{\Delta S_m^{max} \Delta T_{ad}}{\int_0^{\mu_0 H} M(Tc, H) \, d\mu_0 H} \tag{5.2}$$

where $|\Delta S_m^{max}|$ is maximum peak value of $|\Delta S_m|$ and ΔT_{ad} is the maximum temperature change (extracted from in-field DSC measurements) due to an applied magnetic field (ΔT_{ad}

110

≈ 0.3 K for $\Delta\mu_0H$ = 1 T). Therefore, compared with commercial Gd (≈ 0.17(2) for $\Delta\mu_0H$ = 1 T) the calculated *CRP* value for $Ni_{33}Co_{17}Mn_{30}Ti_{20}$ alloy is only 0.01 which means this material is not suitable for potential magnetic refrigeration application.
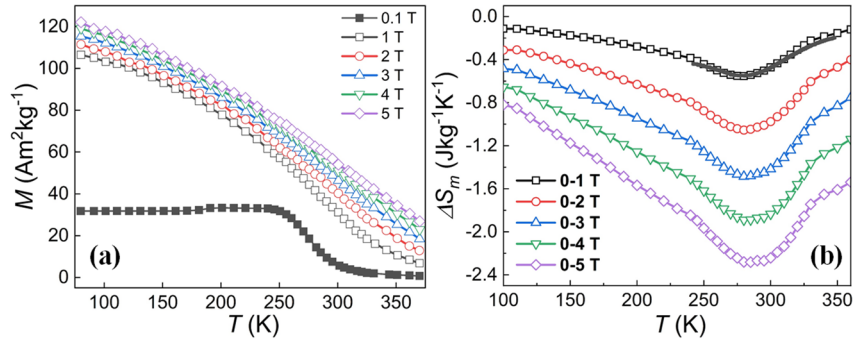

Figure 5.6 (a) Isofield *M-T* curves between 0.1 and 5 T for the $Ni_{33}Co_{17}Mn_{30}Ti_{20}$ sample. (b) Magnetic entropy change ΔS_m for different magnetic field changes as a function of temperature for the $Ni_{33}Co_{17}Mn_{30}Ti_{20}$ sample. The black solid curve was derived from DSC-in field measurement with $\Delta\mu_0H$ = 1 T.

5.3.3 Microstructural information

If the crystal structure and the macroscopic property change, then it is useful to obtain a deeper insight into the microstructure. For some traditional NiMn-*X* (*X* = In, Sn, Sb, Ga, Al) based magnetic Heusler alloys, the average grain size can reach several hundreds of µm up to the mm-range [23]. As demonstrated in **Figure 5.7(a)**, the grain boundaries of the material are distinguishable in the optical microscopy image, and the average grain size is approximately 100 to 200 µm. Compared with other NiMn-*X* (*X* = In, Sn, Sb, Ga, Al) based Heusler alloys, this grain size is significantly smaller. Considering the Hall-Petch relation (inverse relation between the grain size and the material strength) [51] the noticeable reduction in grain size for the NiCoMnTi MCMs with a SOMT could lead to an enhanced mechanical strength. Grain refinement has been utilized in NiCoMnTi ribbon samples with a FOMT to improve micro-hardness [20]. Additionally, as shown in the SEM image of **Figure 5.7(b)**, pure austenite is observed and there is no slat-like martensite at room temperature. Worth mentioning is the presence of several µm (below 10 µm) secondary phase precipitates within the main matrix. Because the concentration of precipitates is very limited (< 1%), it is insufficient to be detected by XRD. EDS measurements were utilized to determine the composition of main matrix phase and the secondary phase, as illustrated in **Table 5.1**. The chemical composition of the main matrix phase ($Ni_{32.57}Co_{16.33}Mn_{31.87}Ti_{19.06}$) is close to the nominal composition ($Ni_{33}Co_{17}Mn_{30}Ti_{20}$). Meanwhile, the small fraction of

precipitates corresponds to a Ti-rich impurity ($Ni_{2.69}Co_{1.33}Mn_{4.76}Ti_{91.22}$). The concentration of Ti-rich second phase particles can be controlled by the annealing conditions. For instance, a lower heat-treatment temperature would generate more Ti-rich impurities. The enlarged SEM image in **Figure 5.7(c)** shows the morphology of the Ti-rich secondary phase. Along the yellow arrow a line scan measurement was performed at various locations along the yellow dashed line to confirm the elemental distribution of the main matrix phase and the Ti-rich secondary phase, as shown in **Figure 5.7(d)**. The line scans indicate that the Ti-rich impurities are quite homogeneous.

Table 5.2 Elemental composition of the $Ni_{33}Co_{17}Mn_{30}Ti_{20}$ alloy determined by EDS measurements.

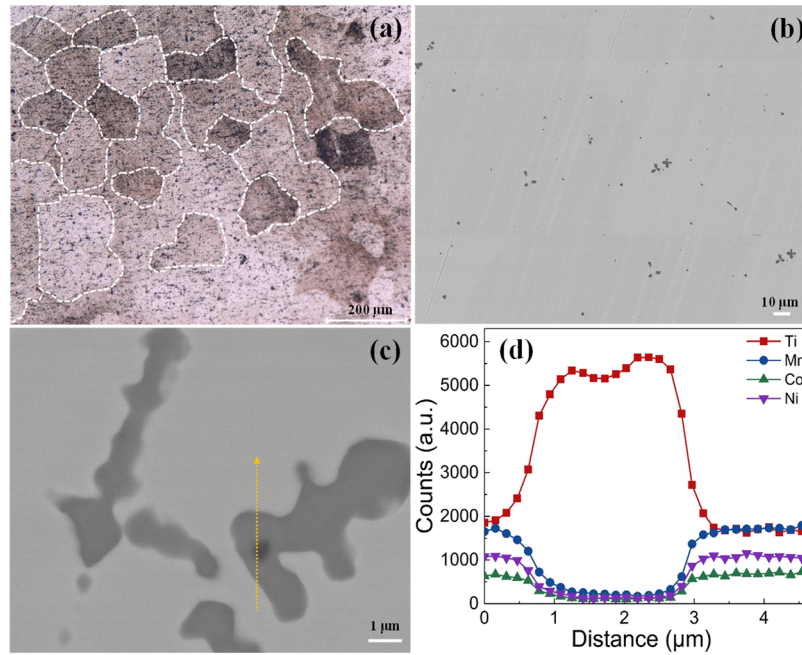| Phases	Ni (*at.%*)	Co (*at.%*)	Mn (*at.%*)	Ti (*at.%*)
Main phase	32.57 (±0.99)	16.33 (±0.87)	31.87 (±0.88)	19.06 (±0.47)
Ti-rich impurity	2.69 (±0.61)	1.33 (±0.44)	4.76 (±0.44)	91.22 (±1.00)

Figure 5.7 (a) Optical microscope image for the etched $Ni_{33}Co_{17}Mn_{30}Ti_{20}$ sample. (b) Back-scattered SEM image for the $Ni_{33}Co_{17}Mn_{30}Ti_{20}$ sample. (c) Enlarged back-scattered SEM image for the $Ni_{33}Co_{17}Mn_{30}Ti_{20}$ sample. (d) SEM line scan measurements based on (c) for the $Ni_{33}Co_{17}Mn_{30}Ti_{20}$ sample.

5.3 Conclusions

In summary, by utilizing XRD, SQUID, SEM measurements and DFT calculations the crystal structural, the magnetocaloric properties and the microstructure information have been investigated systematically in the novel all-*d*-metal NiCoMnTi based magnetic Heusler alloys with a SOMT. The Mn/Ti ratio controls the FOMT/SOMT nature of transition. The SOMT in this alloy system is obtained by optimizing the Mn/Ti ratio. The values of T_C and M_S can be regulated by adjusting either by the Ni/Co ratio or by doping with non-magnetic Cu. The alloys with a high Co content show good soft magnetic properties with a reversible ferromagnetic transition and a moderate MCE. Compositional maps for T_C and M_S have been established. Microstructural measurements indicate a refined crystallite size and a limited volume fraction of the Ti-rich secondary phase. Our DFT calculations reveal that the total magnetic moment per formula unit is controlled by the Co content. Our study provides new insight into the second-order magnetic phase transition for these all-*d*-metal Ni(Co)MnTi based Heusler alloys.

References

[1] V.K. Pecharsky, K.A. Gschneidner, Giant magnetocaloric effect in $Gd_5(Si_2Ge_2)$, *Phys Rev Lett* 78 (1997) 4494-4497.

[2] O. Tegus, E. Brück, K.H.J. Buschow, F.R. de Boer, Transition-metal-based magnetic refrigerants for room-temperature applications, *Nature* 415 (2002) 150-152.

[3] F.X. Hu, B.G. Shen, J.R. Sun, Z.H. Cheng, G.H. Rao, X.X. Zhang, Influence of negative lattice expansion and metamagnetic transition on magnetic entropy change in the compound $LaFe_{11.4}Si_{1.6}$, *Appl Phys Lett* 78 (2001) 3675-3677.

[4] A. Planes, L. Mañosa, M. Acet, Magnetocaloric effect and its relation to shape-memory properties in ferromagnetic Heusler alloys, *J Phys-Condens Mat* 21 (2009) 233201.

[5] J. Liu, Y.Y. Gong, Y.R. You, X.M. You, B.W. Huang, X.F. Miao, G.Z. Xu, F. Xu, E. Brück, Giant reversible magnetocaloric effect in MnNiGe-based materials: Minimizing thermal hysteresis via crystallographic compatibility modulation, *Acta Mater* 174 (2019) 450-458.

[6] J. Mira, J. Rivas, F. Rivadulla, C. Vazquez-Vazquez, M.A. Lopez-Quintela, Change from first- to second-order magnetic phase transition in $La_{2/3}(Ca,Sr)_{1/3}MnO_3$ perovskites, *Phys Rev B* 60 (1999) 2998-3001.

[7] X.C. Zhong, H.C. Tian, S.S. Wang, Z.W. Liu, Z.G. Zheng, D.C. Zeng, Thermal, magnetic and magnetocaloric properties of $Fe_{80-x}M_xB_{10}Zr_9Cu_1$ (M = Ni, Ta; x=0, 3, 5) amorphous alloys, *J Alloy Compd* 633 (2015) 188-193.

[8] X.Y. Tan, P. Chai, C.M. Thompson, M. Shatruk, Magnetocaloric effect in $AlFe_2B_2$: Toward magnetic refrigerants from earth-abundant elements, *J Am Chem Soc* 135 (2013) 9553-9557.

[9] E.E. Levin, J.D. Bocarsly, K.E. Wyckoff, T.M. Pollock, R. Seshadri, Tuning the magnetocaloric response in half-Heusler/Heusler $MnNi_{1+x}Sb$ solid solutions, *Phy Rev Mater* 1 (2017) 075003.

114

[10] J.A. Cooley, M.K. Horton, E.E. Levin, S.H. Lapidus, K.A. Persson, R. Seshadri, From waste-heat recovery to refrigeration: Compositional tuning of magnetocaloric $Mn_{1+x}Sb$, *Chem Mater* 32 (2020) 1243-1249.

[11] S. Singh, L. Caron, S.W. D'Souza, T. Fichtner, G. Porcari, S. Fabbrici, C. Shekhar, S. Chadov, M. Solzi, C. Felser, Large magnetization and reversible magnetocaloric effect at the second-order magnetic transition in Heusler materials, *Adv Mater* 28 (2016) 3321-3325.

[12] G.R. Raji, A.P. Paulose, R.B. Job, S. Thomas, K.G. Suresh, M.R. Varma, Phase transformations, inverse magnetocaloric effect and critical behavior of $Ni_{50}Mn_{36}Sn_{14-x}Si_x$ Heusler alloys, *Intermetallics* 82 (2017) 59-67.

[13] B. Dahal, C. Huber, W.Y. Zhang, S. Valloppilly, Y. Huh, P. Kharel, D. Sellmyer, Effect of partial substitution of In with Mn on the structural, magnetic, and magnetocaloric properties of $Ni_2Mn_{1+x}In_{1-x}$ Heusler alloys, *J Phys D Appl Phys* 52 (2019) 1-8.

[14] B.R. Dahal, Z. Lehmann, Y. Huh, P. Kharel, Magnetocaloric effect in $Ni_2Mn_xFe_yIn_z$ Heusler alloys with second-order phase transition, *Aip Adv* 10 (2020) 015109.

[15] A.K. Pathak, I. Dubenko, S. Stadler, N. Ali, The effect of partial substitution of In by Si on the phase transitions and respective magnetic entropy changes of $Ni_{50}Mn_{35}In_{15}$ Heusler alloy, *J Phys D Appl Phys* 41 (2008) 202004.

[16] I. Dubenko, M. Khan, A.K. Pathak, B.R. Gautam, S. Stadler, N. Ali, Magnetocaloric effects in Ni-Mn-X based Heusler alloys with X = Ga, Sb, In, *J Magn Magn Mater* 321 (2009) 754-757.

[17] Z.Y. Wei, E.K. Liu, J.H. Chen, Y. Li, G.D. Liu, H.Z. Luo, X.K. Xi, H.W. Zhang, W.H. Wang, G.H. Wu, Realization of multifunctional shape-memory ferromagnets in all-d-metal Heusler phases, *Appl Phys Lett* 107 (2015) 022406.

[18] Z.Y. Wei, E.K. Liu, Y. Li, X.L. Han, Z.W. Du, H.Z. Luo, G.D. Liu, X.K. Xi, H.W. Zhang, W.H. Wang, G.H. Wu, Magnetostructural martensitic transformations with large volume changes and magneto-strains in all-*d*-metal Heusler alloys, *Appl Phys Lett* 109 (2016) 071904.

[19] H.N. Bez, A.K. Pathak, A. Biswas, N. Zarkevich, V. Balema, Y. Mudryk, D.D. Johnson, V.K. Pecharsky, Giant enhancement of the magnetocaloric response in Ni-Co-Mn-Ti by rapid solidification, *Acta Mater* 173 (2019) 225-230.

[20] K. Liu, S.C. Ma, C.C. Ma, X.Q. Han, K. Yu, S. Yang, Z.S. Zhang, Y. Song, X.H. Luo, C.C. Chen, S.U. Rehman, Z.C. Zhong, Martensitic transformation and giant magneto-functional properties in all-*d*-metal Ni-Co-Mn-Ti alloy ribbons, *J Alloy Compd* 790 (2019) 78-92.

[21] Y.X. Zhang, H. Zeng, G. Yu, K. Liu, S.C. Ma, K. Yang, X.W. Zhao, G. Yuan, X.H. Luo, C.C. Chen, Z.C. Zhong, Impact of annealing on the martensitic transformation and magnetocaloric properties in all-*3d*-metal $Mn_{50}Ni_{32}Co_8Ti_{10}$ alloy ribbons, *Intermetallics* 125 (2020) 106882.

[22] Z.Y. Wei, Design magnetic phase transition in MM'*X* -alloys and all-*d*-metal Heusler alloys, PhD thesis (2017).

[23] A. Taubel, B. Beckmann, L. Pfeuffer, N. Fortunato, F. Scheibel, S. Ener, T. Gottschall, K.P. Skokov, H.R. Zhang, O. Gutfleisch, Tailoring magnetocaloric effect in all-*d*-metal Ni-Co-Mn-Ti Heusler alloys: a combined experimental and theoretical study, *Acta Mater* 201 (2020) 425-434.

[24] H.M. Rietveld, A profile refinement method for nuclear and magnetic structures, *J Appl Crystallogr* 2 (1969) 65-71.

[25] G. Porcari, M. Buzzi, F. Cugini, R. Pellicelli, C. Pernechele, L. Caron, E. Brück, M. Solzi, Direct magnetocaloric characterization and simulation of thermomagnetic cycles, *Rev Sci Instrum* 84 (2013) 073907.

[26] G. Kresse, J. Hafner, *Ab* initio molecular dynamics for liquid metals, *Phys Rev B* 47 (1993) 558-561.

[27] G. Kresse, J. Furthmuller, Efficiency of ab-initio total energy calculations for metals and semiconductors using a plane-wave basis set, *Comp Mater Sci* 6 (1996) 15-50.

[28] P.E. Blochl, Projector augmented-wave method, *Phys Rev B* 50 (1994) 17953-17979.

[29] G. Kresse, D. Joubert, From ultrasoft pseudopotentials to the projector augmented-wave method, *Phys Rev B* 59 (1999) 1758-1775.

[30] J.P. Perdew, K. Burke, M. Ernzerhof, Generalized gradient approximation made simple, *Phys Rev Lett* 78 (1997) 1396-1396.

[31] M. Methfessel, A.T. Paxton, High-precision sampling for Brillouin-Zone Integration in Metals, *Phys Rev B* 40 (1989) 3616-3621.

[32] B. Cordero, V. Gomez, A.E. Platero-Prats, M. Reves, J. Echeverria, E. Cremades, F. Barragan, S. Alvarez, Covalent radii revisited, *Dalton T* 21 (2008) 2832-2838.

[33] S.L. Liu, H.C. Xuan, T. Cao, L.B. Wang, Z.G. Xie, X.H. Liang, H. Li, L. Feng, F.H. Chen, P.D. Han, Magnetocaloric and elastocaloric effects in All-*d*-Metal $Ni_{37}Co_9Fe_4Mn_{35}Ti_{15}$ magnetic shape memory alloy, *Phys Status Solidi A* 216 (2019) 1-7.

[34] Y. Li, S.Y. Huang, W.H. Wang, E.K. Liu, L.W. Li, Ferromagnetic martensitic transformation and large magnetocaloric effect in $Ni_{35}Co_{15-x}Fe_xMn_{35}Ti_{15}$ (x=2, 4, 6, 8) alloys, *J Appl Phys* 127 (2020) 233907.

[35] L. Pal, K.G. Suresh, A.K. Nigam, Effect of Mn substitution on the magnetic and magneto-transport properties of $Fe_{3-x}Mn_xSi$ ($0 <= x <= 1.25$) alloys, *J Appl Phys* 113 (2013) 093904.

[36] A.F. Manchon-Gordon, R. Lopez-Martin, A. Vidal-Crespo, J.J. Ipus, J.S. Blazquez, C.F. Conde, A. Conde, Distribution of transition temperatures in magnetic transformations: Sources, effects and procedures to extract information from experimental data, *Metals-Basel* 10 (2020) 1-23.

[37] G. Cavazzini, F. Cugini, D. Delmonte, G. Trevisi, L. Nasi, S. Ener, D. Koch, L. Righi, M. Solzi, O. Gutfleisch, F. Albertini, Multifunctional Ni-Mn-Ga and Ni-Mn-Cu-Ga Heusler particles towards the nanoscale by ball-milling technique, *J Alloy Compd* 872 (2021) 159747.

[38] P. Devi, C.S. Mejia, L. Caron, S. Singh, M. Nicklas, C. Felser, Effect of chemical and hydrostatic pressure on the coupled magnetostructural transition of Ni-Mn-In Heusler alloys, *Phy Rev Mater* 3 (2019) 122401.

117

[39] L. Caron, N.T. Trung, E. Brück, Pressure-tuned magnetocaloric effect in $Mn_{0.93}Cr_{0.07}CoGe$, *Phys Rev B* 84 (2011) 020414.

[40] N.T. Trung, V. Biharie, L. Zhang, L. Caron, K.H.J. Buschow, E. Brück, From single- to double-first-order magnetic phase transition in magnetocaloric $Mn_{1-x}Cr_xCoGe$ compounds, *Appl Phys Lett* 96 (2010) 162507

[41] P. Devi, C.S. Mejia, L. Caron, S. Singh, M. Nicklas, C. Felser, Effect of chemical and hydrostatic pressure on the coupled magnetostructural transition of Ni-Mn-In Heusler alloys, *Phy Rev Mater* 3 (2019) 1-7.

[42] Z.B. Li, J.J. Yang, D. Li, Z.Z. Li, B. Yang, H.L. Yan, C.F. Sanchez-Valdes, J.L.S. Llamazares, Y.D. Zhang, C. Esling, X. Zhao, L. Zuo, Tuning the reversible magnetocaloric effect in Ni-Mn-In-based alloys through Co and Cu Co-doping, *Adv Electron Mater* 5 (2019) 1800845.

[43] D.W. Zhao, J. Liu, X. Chen, W. Sun, Y. Li, M.X. Zhang, Y.Y. Shao, H. Zhang, A.R. Yan, Giant caloric effect of low-hysteresis metamagnetic shape memory alloys with exceptional cyclic functionality, *Acta Mater* 133 (2017) 217-223.

[44] T. Kanomata, Y. Kitsunai, K. Sano, Y. Furutani, H. Nishihara, R.Y. Umetsu, R. Kainuma, Y. Miura, M. Shirai, Magnetic properties of quaternary Heusler alloys $Ni_{2-x}Co_xMnGa$, *Phys Rev B* 80 (2009) 214402.

[45] L.M. Wang, Z.B. Li, J.J. Yang, B. Yang, X. Zhao, L. Zuo, Large refrigeration capacity in a $Ni_{48}Co_1Mn_{37}In_{14}$ polycrystalline alloy with low thermal hysteresis, *Intermetallics* 125 (2020) 1-6.

[46] D.Y. Cong, S. Roth, L. Schultz, Magnetic properties and structural transformations in Ni-Co-Mn-Sn multifunctional alloys, *Acta Mater* 60 (2012) 5335-5351.

[47] C. Salazar-Mejia, V. Kumar, C. Felser, Y. Skourski, J. Wosnitza, A.K. Nayak, Measurement-protocol dependence of the magnetocaloric effect in Ni-Co-Mn-Sb Heusler alloys, *Phys Rev Appl* 11 (2019) 054006.

[48] S. Ghosh, A. Ghosh, K. Mandal, Reversible magnetocaloric effect and critical exponent analysis in Mn-Fe-Ni-Sn Heusler alloys, *J Alloy Compd* 746 (2018) 200-205.

118

[49] P. Nehla, V.K. Anand, B. Klemke, B. Lake, R.S. Dhaka, Magnetocaloric properties and critical behavior of $Co_2Cr_{1-x}Mn_xAl$ Heusler alloys, *J Appl Phys* 126(20) (2019) 203903.

[50] E. Brück, H. Yibole, L. Zhang, A universal metric for ferroic energy materials, *Philos T R Soc A* 374 (2016) 1-6.

[51] S.-H. Whang, Nanostructured metals and alloys: processing, microstructure, mechanical properties and applications, Elsevier 2011.

Chapter 6 Reduced hysteresis and enhanced giant magnetocaloric effect in B-doped all-*d*-metal Ni-Co-Mn-Ti based Heusler materials
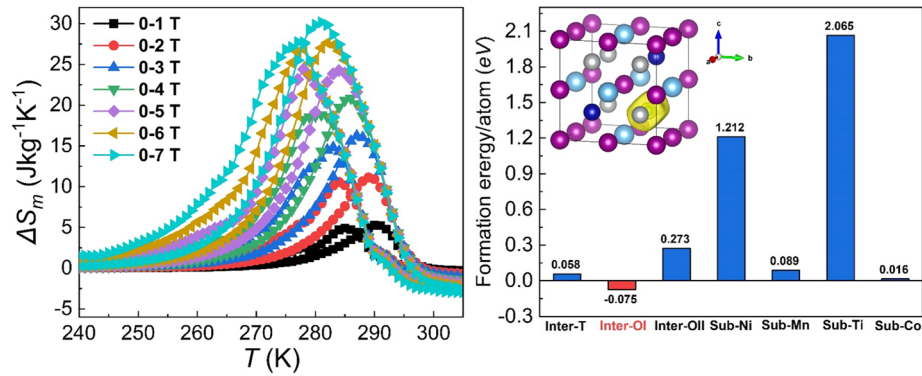
This chapter is based on:

Fengqi Zhang*, Ivan Batashev, Niels van Dijk, Ekkes Brück, Reduced hysteresis and enhanced giant magnetocaloric effect in B-doped all-*d*-metal Ni-Co-Mn-Ti based Heusler materials, *Physical Review Applied* 17, **(2022)** 054032.

Abstract

The all-*d*-metal Ni(Co)MnTi based Heusler alloys have been found to show a giant magnetocaloric effect near room temperature and are thereby potential materials for solid-state refrigeration. However, the relative large thermal hysteresis and the moderate ferromagnetic magnetization provide limitations for real applications. In the present study, we demonstrate that introducing interstitial B atoms within $Ni_{36.5}Co_{13.5}Mn_{35}Ti_{15}$ alloys can effectively decrease the thermal hysteresis ΔT_{hys} (down to 4.4 K), and simultaneously improve the saturation magnetization (maximum 40% enhancement) for low concentrations of B doping (up to 0.4 *at.*%). In comparison to the undoped reference material, the maximum magnetic entropy change (ΔS_m) for the $Ni_{36.5}Co_{13.5}Mn_{35}Ti_{15}B_{0.4}$ alloy shows a remarkable improvement from 9.7 to 24.3 $Jkg^{-1}K^{-1}$ for an applied magnetic field change ($\Delta\mu_0 H$) of 5 T (30.2 $Jkg^{-1}K^{-1}$ for $\Delta\mu_0 H$ = 7 T). Additionally, due to the obtained low thermal hysteresis ΔT_{hys}, the maximum reversible ΔS_m^{rev} amounts to 18.9 $Jkg^{-1}K^{-1}$ at 283 K for $\Delta\mu_0 H$ = 5 T (22.0 $Jkg^{-1}K^{-1}$ at 281 K for $\Delta\mu_0 H$ = 7 T), which is competitive to the traditional NiMn-*X* based Heusler alloys (*X* = Ga, In, Sn, Sb). The enhancement of the magnetic moments by B doping is also observed in first-principles calculations. These calculations clarify the atomic occupancy of B and the changes in the electronic configuration. Our current study indicates that interstitial doping with a light element (boron) is an effective method to improve the magnetocaloric effect in these all-*d*-metal NiCoMnTi based magnetic Heusler compounds.

6.1 Introduction

Magnetocaloric materials (MCMs), which hold a giant magnetocaloric effect (GMCE), enable promising application scenarios such as solid-state magnetic refrigeration [1], magnetic heat pumps [2] and thermomagnetic generators to covert low-temperature waste heat to electricity [3]. In comparison to the conventional magnetocaloric effect (MCE), the "giant" MCE arises from an efficient coupling of different degrees of freedom (e.g. magnetic spin order-disorder, structural transformations, phonon excitations or changes in electronic state). The GMCE results in a large isothermal entropy change composed from magnetic, lattice and electronic contributions [4]. Depending on the type of coupling, the MCMs can be distinguished in magnetoelastic and magnetostructural MCMs. The magnetoelastic MCMs are mainly represented by $(Mn,Fe)_2(P,X)$-based (X = As, Ge, Si) [5], $La(Fe,Si)_{13}$-based [6], FeRh-based [7] and Eu_2In [8] compounds, while the magnetostructural MCMs are mainly found in $Gd_5(Si_2Ge_2)$ [9], NiMn-X based magnetic Heusler alloys (X = Ga, In, Sn, Sb) [10] and MnM-X (M = Co or Ni, X = Si or Ge) ferromagnets [11, 12].

Among these MCMs the NiMn-X based Heusler alloys (X = Ga, In, Sn, Sb) attract significant attention because of their fruitful multifunctionality with e.g. caloric effects [1] (magnetocaloric, elasticaloric, barocaloric, multicaloric), giant magnetoresistance [13] and exchange bias [14]. Aside from the traditional NiMn-based Heusler alloys, which are stabilized by *p-d* hybridization, the novel all-*d*-metal Ni(Co)MnTi-based Heusler alloys functionalized by *d-d* covalent hybridization were successfully introduced. This resulted in an obvious enhancement of the mechanical properties across the martensitic transition where the intrinsic brittleness of the traditional Heusler alloys could efficiently be prevented [15, 16]. Encouraged by this progress, some studies have been reported to further optimize the experimental MCE performance, in combination with electronic structure calculations [17, 18]. For example, by applying a rapid-solidification technique (melt-spinning) Bez and coworkers demonstrated that $Ni_{37.5}Co_{12.5}Mn_{35}Ti_{15}$ ribbons show a magnetic entropy change (ΔS_m) as high as 27 Jkg^{-1}K^{-1} for a moderate magnetic field change ($\Delta\mu_0H$) of 2 T [19]. Simultaneously, Taubel and coworkers reported that an optimized heat treatment can significantly affect the magnetocaloric properties in $Ni_{35}Co_{15}Mn_{37}Ti_{13}$ with a ΔS_m of 20 J kg^{-1}K^{-1} and an maximum adiabatic temperature change (ΔT_{ad}) of -4 K for $\Delta\mu_0H$ = 1.93 T [20]. Combining a MCE with hydrostatic pressures or uniaxial stresses can result in an enhanced magnetocaloric performance through a multicaloric cycle [21, 22]. However, a relatively large thermal hysteresis (10– 40 K) is observed in the above mentioned materials, which will dramatically reduce the heating/cooling efficiency in a practical thermodynamic cycle, which compromises the advantages (excellent mechanical properties

[23], rare-earth-free composition and non-toxicity) of these all-*d*-type Heusler alloys. Additionally, apart from the current so-called "Co ferromagnetism activation effect", there are no other known substitutions that can efficiently optimize the ferromagnetic ordering.

Consequently, inspired by the effect of doping with light elements (e.g. B, C, N) in other MCMs systems [24-29], in the present study interstitial B doping is investigated. A series of $Ni_{36.5}Co_{13.5}Mn_{35}Ti_{15}B_x$ (*x* = 0, 0.2, 0.4, 0.6 and 0.8) alloys has successfully been produced and their thermodynamic, magnetic, GMCE properties have been reported. Density Functional Theory (DFT) modeling, is applied to determine the atomic occupancy of B and theoretical Electron Localization Function (ELF) calculations provide information on the changes in electronic environment in the surroundings of the main atoms. Our current study demonstrate the positive influence of interstitial B doping for the all-*d*-metal Ni(Co)MnTi-based Heusler alloys and shows how B affects the GMCE performance, which deepens our understanding of this all-*d*-metal type Heusler system.

6.2 Methods and experimental procedure

High-purity (99.9%) raw materials were used to prepare polycrystalline samples with a nominal composition of $Ni_{36.5}Co_{13.5}Mn_{35}Ti_{15}B_x$ (*x* = 0, 0.2, 0.4, 0.6 and 0.8) using the arc melting method under Ar atmosphere. The samples were melted for five times. To compensate the over-evaporation of Mn during melt processing, 4 *at.%* extra Mn were introduced. To ensure the homogeneity the as-cast ingots were sealed in quartz ampoules under 20 kPa Ar and annealed at 1173 K for 6 days in a vertical furnace and then quickly quenched into cold water.

Zero-field differential scanning calorimetry (DSC) measurements were carried out using a commercial TA-Q2000 DSC calorimeter. The DSC measurements under different applied magnetic fields (up to 1.5 T) were performed in a home-built Peltier cell-based DSC, where the calorimetric ΔS_m and ΔT_{ad} were derived from specific heat measurements [30, 31]. X-ray diffraction (XRD) patterns at different temperatures were collected using an Anton Paar TTK450 temperature-tunable sample chamber and a PANalytical X-pert Pro diffractometer with Cu K_α radiation. The XRD patterns were processed using Fullprof's implementation of the Rietveld refinement method [32]. Temperature-dependent magnetization (*M-T*) and field-dependent magnetization (*M-H*) curves were measured in a superconducting quantum interference device (SQUID, Quantum Design MPMS 5XL) magnetometer. The so-called loop method has been used for isothermal *M-H* measurements at different temperatures to eliminate the influence of thermal history [33]. The samples were initially cooled down

to 200 K (the complete martensite region) and then subsequently heated to the target temperature at a rate of 2 K/min.

Density functional theory (DFT) calculations were performed using the Vienna *ab initio* simulation package (VASP) [34, 35]. The ion-electron interactions were described via the projector augmented-wave (PAW) [36, 37] method and the generalized gradient approximation of Perdew-Burke-Ernzerhof [38] was used for the exchange correlation functional. 3*d* and 4*s* electrons were treated as valence electrons for Ni and Co. 3*d*, 3*p* and 4*s* for Mn, and 3*s*, 3*p*, 3*d*, 4*s* for Ti, while for B 2*s* and 2*p* were set as valence electrons. A 2×2×1 supercell based on a 16-atom unit cell was relaxed on a gamma-centered ***k***-grid of 6×6×9 using the Methfessel-Paxton method of the second order [39] with a smearing width of 0.05 eV (*B2* austenite structure with partial disorder of excess Mn and Ti is considered). The kinetic energy cutoff was set at 520 eV with the force convergence criteria at 0.1 meV/Å and the energies convergence criteria at 1 μeV.

To deduce the site preference, the formation energies of the structures with a B atom placed on several possible crystallographic sites were compared. The energy cost corresponding to each structure was calculated as the difference between energies of doped (E_{doped}) and pure (E_{pure}) compounds minus the chemical potential of boron (μ_d) plus the chemical potential of the atom substituted by boron (μ_s).

$$E_f = E_{doped} + \mu_s - \left(E_{pure} + \mu_d\right) \qquad (6.1)$$

To study the changes in the electronic environment the Electron Localization Function (ELF) was analyzed [40]. The ELF allows for accurate characterization of the bond nature based on electron densities. This characterization is based on topological analysis of local quantum-mechanical functions related to the Pauli exclusion principle. ELF effectively states the possibility of finding a second electron with the same spin close to where the reference electron is located. High ELF values point to areas with more localized electrons and indicate stronger covalent bonding.

6.3 Results and discussion

The zero-field DSC curves of the $Ni_{36.5}Co_{13.5}Mn_{35}Ti_{15}B_x$ (x = 0.0, 0.2, 0.4) alloys are shown in **Figure 6.1a**. Sharp exothermic and endothermic peaks indicate the presence of a first-order phase transition. The corresponding characteristic temperatures (A_s, A_f, M_s, M_f), thermal hysteresis (ΔT_{hys}), transformation entropy changes (ΔS_{tr}) and valence electron concentration (e/a) are summarized in **Table 6.1**. The thermal hysteresis is defined as ΔT_{hys} = (A_s +A_f -M_s -

M_f)/2, and the entropy change as $\Delta S_{tr} = \int_{A_s}^{A_f} \frac{1}{T}(Q - Q_{base})(\frac{\partial T}{\partial t})^{-1}dT$, where Q is the heat flow and Q_{base} the baseline for the heat flow [41, 42]. With increasing B doping ΔS_{tr} increases from 29.22 to 35.82 Jkg^{-1}K^{-1} (18 % increment) for a B doping (x) from 0 to 0.4 *at.%*. This could indicate that the magnetic entropy change ΔS_m also has the potential to increase with B doping as ΔS_{tr} is mainly attributed to the configuration entropy from structural and magnetic contributions [4]. From **Table 6.1** it is observed that ΔT_{hys} decreased continuously from 13.0 K (x = 0.0) to 9.6 K (x = 0.4) for an increasing B doping content. For comparison, the ΔT_{hys} value extracted from SQUID measurement is found to demonstrate a similar reduction from 9.7 K (x = 0.0) to 6.8 K (x = 0.4). The lower ΔT_{hys} values should be ascribed to the slower heating/cooling rates for the SQUID (2 K/min) in comparison to the DSC (10 K/min) measurements.
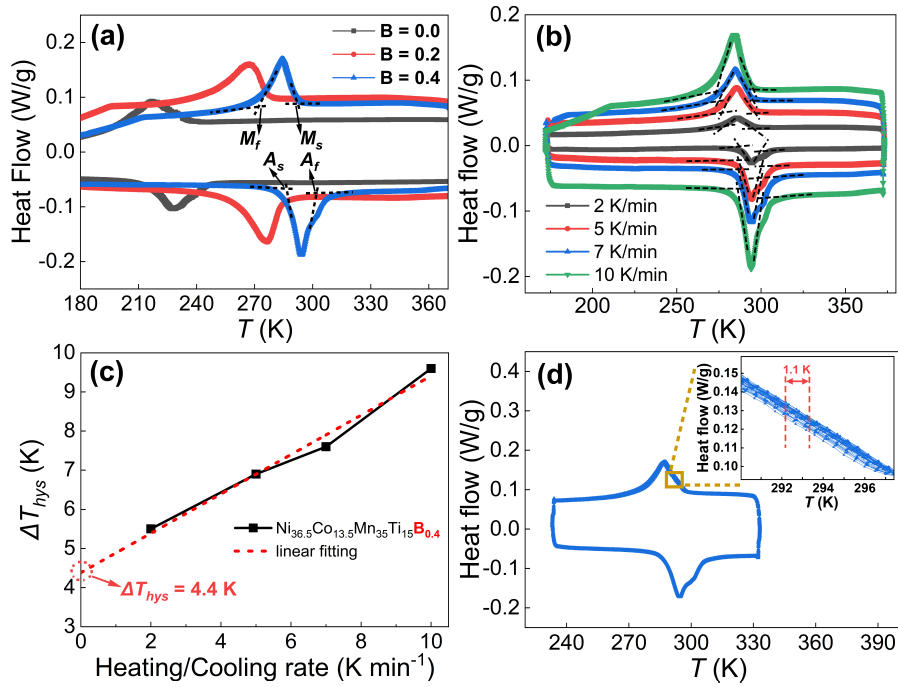
Figure 6.1 (a) DSC curves of Ni$_{36.5}$Co$_{13.5}$Mn$_{35}$Ti$_{15}$B$_x$ (x = 0.0, 0.2, 0.4) for heating and cooling at a rate of 10 K/min. (b) DSC curves of Ni$_{36.5}$Co$_{13.5}$Mn$_{35}$Ti$_{15}$B$_{0.4}$ at different heating/cooling rates. (c) Linear fitting of the ΔT_{hys} obtained at different sweep rates for Ni$_{36.5}$Co$_{13.5}$Mn$_{35}$Ti$_{15}$B$_{0.4}$. (d) DSC curves and characteristic transformation temperatures in 35 subsequent thermal cycles for Ni$_{36.5}$Co$_{13.5}$Mn$_{35}$Ti$_{15}$B$_{0.4}$. The inset presents an enlarged part of the curves.

As shown in **Figure 6.1b**, the sweeping rate can affect the determination of ΔT_{hys}. At different DSC scanning rates (10, 7, 5, 2 K/min) the thermal hysteresis of

126

$Ni_{36.5}Co_{13.5}Mn_{35}Ti_{15}B_{0.4}$ alloy is found to grow at higher sweeping rates, which is caused by thermal lag problems during the measurement. The intrinsic value of ΔT_{hys} for the $Ni_{36.5}Co_{13.5}Mn_{35}Ti_{15}B_{0.4}$ alloy is identified as 4.4 K by extrapolating the results at different sweeping rates towards zero, as demonstrated in **Figure 6.1c**. This low value for ΔT_{hys} for B doped NiCoMnTi-based alloys is comparable to the best NiMn-*X* (*X* = In, Sb, Sn) based magnetic Heusler alloys [42, 43] and is superior to the previously reported all-*d*-metal NiCoMnTi-based compounds synthesized and optimized by appropriate heat treatment [20] or rapid-solidification [19] techniques. The general non-linear theory of martensite (GNLTM) was successfully proposed to explain the relationship of ΔT_{hys} and the interfacial compatibility between the austenite and martensite lattices [44, 45]. The interfacial lattice properties of these two phases are related to a 3×3 transformation stretch matrix $\boldsymbol{U}$, as described below:

$$\boldsymbol{U} = \begin{bmatrix} \tau & \sigma & 0 \\ \sigma & \rho & 0 \\ 0 & 0 & \delta \end{bmatrix} \qquad (6.2)$$

where the controlling parameters of the interfacial lattice mismatch are τ, ρ, σ and δ, which can be derived from the experimental lattice parameters. Note that the above matrix $\boldsymbol{U}$ depends on the symmetry of martensite. The modulated monoclinic structure of martensite can be found in **Figure S6.1** and **Table S6.1** (Supplementary Information [46]). The calculated middle eigenvalue (λ_2) of this matrix $\boldsymbol{U}$ for *x* = 0.4 sample is 0.9913 in comparison to 0.9812 for undoped sample, which indicates a good geometric compatibility condition. A low value ΔT_{hys} is correlated with a reduced additional free energy to overcome both the stored elastic energy and interfacial energy due to the incompatibility between austenite and martensite (as reflected by a λ_2 close to 1). As these compounds hold a good geometric compatibility for the austenite and the martensite at the phase transition, they are expected to show a longer fatigue life, consistent with our cycled DSC results (only 1.1 K temperature shift after 35 cycles), as shown in **Figure 6.1d**.

Table 6.1 Characteristic temperatures A_s, A_f, M_s, M_f for starting and finishing points of forward martensitic (*M*) and reverse austenitic (*A*) transformations, entropy change of the transformation ΔS_{tr}, thermal hysteresis ΔT_{hys} and *e/a* for the $Ni_{36.5}Co_{13.5}Mn_{35}Ti_{15}B_x$ (*x* = 0.0, 0.2, 0.4) alloys.

	A_s^{DSC} (K)	A_f^{DSC} (K)	M_s^{DSC} (K)	M_f^{DSC} (K)	ΔT_{hys}^{DSC} (K)	ΔT_{hys}^{SQUID} (K)	*e/a*	ΔS_{tr} (Jkg^{-1}K^{-1})
x = 0.0	217.0	243.1	239.4	194.8	13.0	9.7	7.915	29.22
x = 0.2	259.8	285.1	278.2	244.3	11.2	8.8	7.921	35.58
x = 0.4	285.6	300.5	292.7	274.1	9.6	6.8	7.927	35.82

To investigate the influence of B doping on the magnetic properties of NiCoMnTi-based Heusler alloys, **Figure 6.2a** and its inset show the temperature-dependent magnetization (*M-T*) curves for the $Ni_{36.5}Co_{13.5}Mn_{35}Ti_{15}B_x$ (*x* = 0.0, 0.2, 0.4) alloys measured during cooling and heating in magnetic field of 1 T (main panel) and 0.01 T (inset). Interestingly, the structure transition temperatures (T_{tr}) of the martensitic transformation shows a clear increase with B doping. Similarly, the Curie temperatures (T_C) for the ferromagnetic (FM) to paramagnetic (PM) transition present a remarkable increase from 265 K (*x* = 0.0) to 352 (*x* = 0.2) and 361 K (*x* = 0.4). It is well known that for NiMn-based Heusler alloys T_{tr} illustrates a proportional relationship with *e/a* [47]. As present in **Table 6.1**, with B ($2s^2 2p^1$) doping the increase in *e/a* results in the positive shift of T_{tr}. The increase in T_C could however reflect an enhanced magnetic exchange interaction among the magnetic atoms. Compared with the undoped sample, the magnetization shows a significant enhancement from 64.4 Am^2kg^{-1} (*x* = 0.0) to 90.2 Am^2kg^{-1} (*x* = 0.2) and 82.9 Am^2kg^{-1} (*x* = 0.4), which demonstrates that interstitial B doping can enhance the magnetic moments and further strengthen the alignment of ferromagnetic spins, and thereby shows similar effect as substitutional Co doping (the so-called "FM activation effect") [15, 48]. The Clausius-Clapeyron relation $dT_{tr}/d(\mu_0H) = -\Delta M/\Delta S_{tr}$, relates the jump in the magnetization ΔM and the entropy change ΔS_{tr} to the field dependence of the transition. The derived values of $dT_{tr}/d(\mu_0H)$ at 1 T are 2.2 K/T (*x*= 0.0), 2.5 K/T (*x* = 0.2), 2.3 K/T (*x* = 0.4). As illustrated in **Figure 6.2b**, for the $Ni_{36.5}Co_{13.5}Mn_{35}Ti_{15}B_{0.4}$ alloy it is found that ΔM can reach 87.9 (5 T) and 93.3 (7 T) Am^2kg^{-1}. The temperature difference between A_s = 268.4 K (5 T) and M_s = 288.4 K (0.05 T) is about 20 K, which suggests a substantial reversibility of the magnetic field-induced transformation [49].

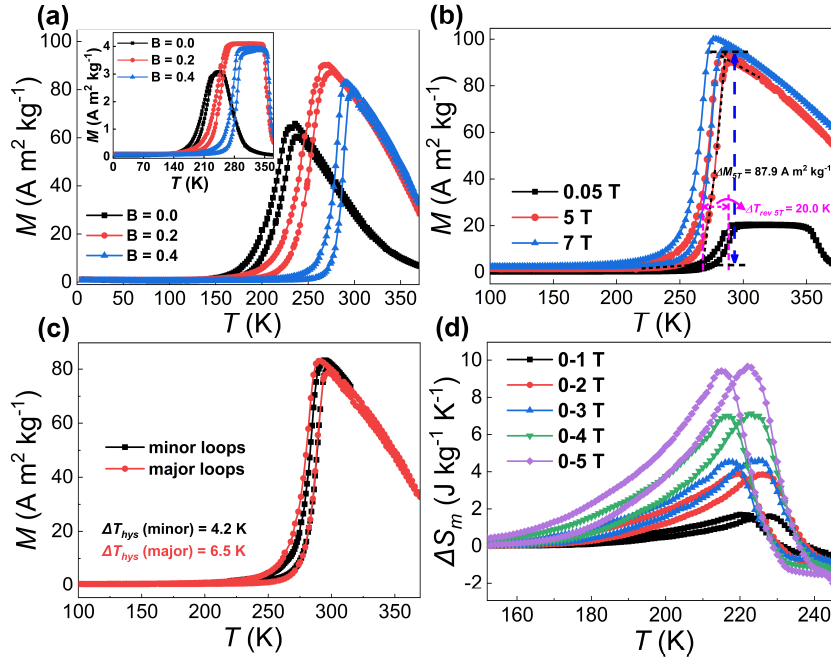**Figure 6.2** (a) *M-T* curves measured in 1 T for $Ni_{36.5}Co_{13.5}Mn_{35}Ti_{15}B_x$ (x = 0.0, 0.2, 0.4) alloys. The inset corresponds to the *M-T* curves at 0.01 T. (b) *M-T* curves for $Ni_{36.5}Co_{13.5}Mn_{35}Ti_{15}B_{0.4}$ in applied magnetic fields of 0.05, 5 and 7 T. The determination of ΔM is illustrated in the figure. (c) *M-T* curves of $Ni_{36.5}Co_{13.5}Mn_{35}Ti_{15}B_{0.4}$ for minor and major hysteresis loops in different temperature ranges at 1 T. (d) ΔS_m of $Ni_{36.5}Co_{13.5}Mn_{35}Ti_{15}$ as a function of temperature for both heating and cooling, determined in magnetic fields ($\Delta\mu_0 H$) ranging from 1 to 5 T.

Gottschall and coworkers reported that the minor loop method can further minimize the ΔT_{hys} [49]. In **Figure 6.2c** scanning with major loops (100 to 370 K) is compared with scanning with minor loops (210 to 315 K). The reduced ΔT_{hys} of 4.2 K for the minor loop (in comparison to the value of 6.5 K for the major loop) can be ascribed to the fact that less nucleation is required for an incomplete martensitic transformation. As shown in **Figure 6.2d**, the maximum ΔS_m of the parent $Ni_{36.5}Co_{13.5}Mn_{35}Ti_{15}$ alloy can only attain 3.8 and 9.7 $Jkg^{-1}K^{-1}$ for a $\Delta\mu_0 H$ of 2 and 5 T, respectively. These relatively low values originate from the relative low magnetization and sluggish magnetostructural phase transition. After B doping the transition sharpens and ΔM increases, resulting in an improvement of ΔS_m in comparison to the undoped sample (x = 0).

Figure 6.3a presents the calculated ΔS_m as a function of temperature in the vicinity of the martensitic transition. Here, the $Ni_{36.5}Co_{13.5}Mn_{35}Ti_{15}B_{0.4}$ alloy shows the largest ΔS_m peak at 24.3 $Jkg^{-1}K^{-1}$ for $\Delta\mu_0 H$ = 5 T (for heating), and even reaches 30.2 $Jkg^{-1}K^{-1}$ for $\Delta\mu_0 H$ = 7 T (for

heating). Compared with the undoped compound (x = 0.0), the maximum value of ΔS_m of the doped $Ni_{36.5}Co_{13.5}Mn_{35}Ti_{15}B_{0.4}$ sample shows a remarkable improvement by a factor 2.5 from 9.7 to 24.3 $Jkg^{-1}K^{-1}$ for a field change of $\Delta\mu_0 H$ = 5 T. For the application scenarios the reversible ΔS_m should be considered. As shown in **Figure 6.3b**, the isothermal magnetic field-cycled *M-H* loops (1st cycle is indicated by the solid symbols and the 2nd cycle by the open symbols) were measured in the temperature range from 268 to 288 K. It is found that the *M-H* curves do not overlap with each other during the 1st increase and 2nd decrease of the magnetic field cycles. This could result from the presence of some residual austenite that does not contribute to the transformation of the field cycles. The so-called transformation fraction (TF_MB) method can be applied on the basis of the assumption that the total magnetization originates from the ferromagnetic austenite phase fraction [48, 50]. Consequently, the reversible ΔS_m (ΔS_m^{rev}) can then be estimated by combining Eqs. (6.3) and (6.4):

$$f_{aus}(T,H) = \frac{M(H) - M_m(H)}{M_a(H) - M_m(H)} \qquad (6.3)$$

$$\Delta S_m^{rev} = \Delta f \cdot \Delta S_{tr} = \left(f(T,H_f) - f(T,H_i) \right) \cdot \Delta S_{tr} \qquad (6.4)$$

where $f_{aus}(T,H)$ is the austenite fraction at certain temperature and field, ΔS_{tr} donates the entropy change of the transformation (see **Table 6.1**), Δf is the transformed austenite fraction, $M(H)$ is the measured magnetization, and $M_m(H)$ is the magnetization of pure martensite (see the extrapolated black dotted lines in **Figure 6.3b**). Correspondingly, $M_a(H)$ is the magnetization of pure austenite. Note that the *M-H* curve at 300 K is chosen as the benchmark for pure austenite to avoid an underestimation of the austenite fraction at low fields, as shown in **Figure S6.2a** (Supplementary Information [46]). Consequently, for the $Ni_{36.5}Co_{13.5}Mn_{35}Ti_{15}B_{0.4}$ alloy the f_{aus} of the 1st and 2nd field cycle at different constant temperature have been derived, as in **Figure 6.3c** and **6.3d**.
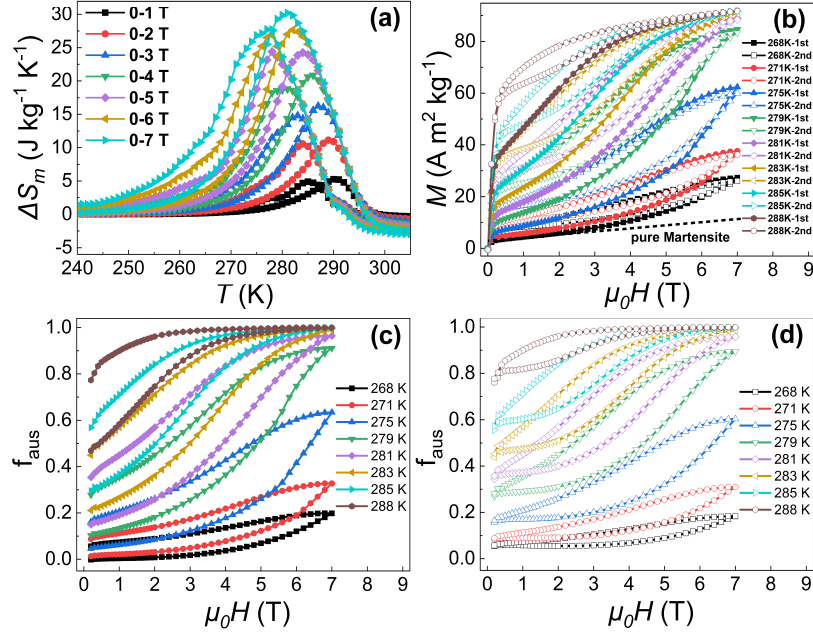
Figure 6.3 (a) Magnetic entropy change ΔS_m of the $Ni_{36.5}Co_{13.5}Mn_{35}Ti_{15}B_{0.4}$ alloy as a function of temperature for both heating and cooling determined for magnetic field changes $\Delta\mu_0H$ ranging from 1 to 7 T. (b) Isothermal *M-H* curves for the $Ni_{36.5}Co_{13.5}Mn_{35}Ti_{15}B_{0.4}$ alloy measured during the 1st (solid symbols) and 2nd (open symbols) cycle for increasing and decreasing magnetic fields at different temperatures. The dotted lines denote the extrapolated magnetization for pure martensite. Fraction of austenite f_{aus} for (c) the 1st field cycle and (d) 2nd cycle at different constant temperatures determined from (b).

Nevertheless, even though B doping significantly improve ΔS_m as mentioned above, it is important to note that its low field sensitivity of transition temperature $dT_{tr}/d(\mu_0H)$, which ranges from 1 to 3 K/T for this all-*d*-metal NiCoMnTi Heusler alloys system, could be detrimental to low-field (less than 2 T) applications [19, 20]. In our present study the $Ni_{36.5}Co_{13.5}Mn_{35}Ti_{15}B_{0.4}$ alloy shows a moderate $dT_{tr}/d(\mu_0H)$ value of 2.3 K/T. It has been reported that the reversible ΔS_m can roughly be determined by the overlap area of the heating and cooling branches in the ΔS_m-temperature curves [42, 52, 53]. Due to its low ΔT_{hys}, as shown in **Figure 6.4a**, the maximum reversible ΔS_m for the $Ni_{36.5}Co_{13.5}Mn_{35}Ti_{15}B_{0.4}$ alloy (see grey area) is estimated at 21.2 and 27.5 Jkg^{-1} K^{-1} for a field change of $\Delta\mu_0H = 5$ and 7 T, respectively. For comparison, in **Figure 6.4b** the ΔS_m for 1st and 2nd field cycles has been extracted by applying the TF_MB method. In comparison to the ΔS_m obtained from the Maxwell relation (1st cycle), the ΔS_m with $\Delta\mu_0H = 7$ T obtained by the TF_MB method (1st cycle) shows consistent results, while the 2nd cycle ΔS_m (corresponding to the reversible part and indicated by the red dashed line) shows a slightly reduction (22.0 Jkg^{-1}K^{-1} at 281 K). The

maximum reversible ΔS_m^{rev} value is determined as 18.9 Jkg^{-1}K^{-1} at 283 K with $\Delta\mu_0 H$ = 5 T as presented in **Figure S6.2b-d** (Supplementary Information [46]), which is competitive with traditional NiMn-based Heusler alloys like Ni$_{49.8}$Co$_{1.2}$Mn$_{33.5}$In$_{15.5}$ (14.6 Jkg^{-1}K^{-1}) [54], Ni$_{41}$Ti$_1$Co$_9$Mn$_{39}$Sn$_{10}$ (18.7 Jkg^{-1}K^{-1}) [49], Ni$_{48.1}$Co$_{2.9}$Mn$_{35.0}$In$_{14.0}$ (12.8 Jkg^{-1}K^{-1}) [55], Ni$_{43}$Co$_6$Mn$_{40}$Sn$_{11}$ (19.3 Jkg^{-1}K^{-1}) [56], Ni$_{46}$Co$_3$Mn$_{35}$Cu$_2$In$_{14}$ (16.4 Jkg^{-1}K^{-1}) [57].

Additionally, we applied calorimetric measurements (in-field DSC) to obtain ΔS_m and ΔT_{ad} for the Ni$_{36.5}$Co$_{13.5}$Mn$_{35}$Ti$_{15}$B$_{0.4}$ alloy at low applied magnetic fields (up to 1.5 T). As shown in **Figure S6.3a** (Supplementary Information [46]), with increasing applied magnetic field the specific heat peak shows a decrease, which is characteristic for an inverse MCE. In **Figure S6.3c** the extracted ΔS_m for $\Delta\mu_0 H$ = 1 T (5.0 Jkg^{-1}K^{-1}) extracted from the in-field DSC is in close agreement with the value obtained from the Maxwell relation (5.2 Jkg^{-1}K^{-1}). From **Figure S6.3d** the value of ΔT_{ad} can be determined as -1.1 K ($\Delta\mu_0 H$ = 1 T) and -1.8 K ($\Delta\mu_0 H$ = 1.5 T). As shown in **Figure S6.4b** (Supplementary Information [46]) by applying the equation $\Delta T_{ad} = -\frac{T}{c_p}\Delta S_m$ values of ΔT_{ad} for different B content samples can be estimated. Compared to the non-doped sample (x = 0.0), the x = 0.4 sample shows the maximum $|\Delta T_{ad}|$ value for a field change of 5 T, with an increase from 3.2 K (x = 0.0) to 7.4 K (x = 0.4).
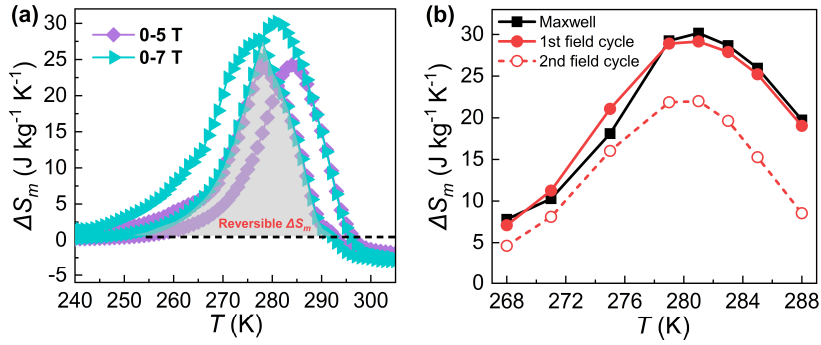
Figure 6.4 (a) Magnetic entropy change ΔS_m as a function of temperature for the Ni$_{36.5}$Co$_{13.5}$Mn$_{35}$Ti$_{15}$B$_{0.4}$ alloy upon heating and cooling in high magnetic field changes of 5 and 7 T. The shaded area corresponds to the reversible ΔS_m. (b) ΔS_m for a magnetic field change of 0-7 T obtained from the Maxwell relation and the TF_MB method during the 1st and 2nd cycles. In the 2nd cycle ΔS_m is reversible.

Although a colossal elastocaloric effect [58] and giant barocaloric effect [59] have been achieved by boron doping (substitutional method), the underlying mechanism associated with the doped B atoms was not studied. To further investigate the mechanism responsible for the positive influence of B doping on the MCE in the NiCoMnTi system, it is crucial to understand what lattice site the B occupancies (interstitial or substitutional). For the

(Mn,Fe)$_2$(P,Si)-type MCMs both experimental and computational studies indicate that light atoms, like B, C, and N, have a distinctly different effect on the MCE for interstitial or substitutional doping [60]. As illustrated in **Figure 6.5a**, based on the typical *L2$_1$* cubic austenite structure for NiMn-based Heusler alloys, the supercell shown in the inset of **Figure 6.5a** has been constructed for our B-doped NiCoMnTi system. The formation energies E_f of different site-occupation models have been calculated on the basis of *ab initio* first-principles calculations, as shown in **Figure 6.5a**. Based on *L2$_1$* crystal structure, three kinds of interstitial sites have been considered [61]: one tetrahedral interstice (labeled as *T*) and two octahedral interstices (labeled as *O*-I and *O*-II). It is found that for our case the B atoms prefer to enter structure at an interstitial site rather than substitutional site. The B atoms are found to preferentially occupy the *O*-I octahedral interstitial site (24*d* site of the *Fm-3m* space group). The experimental XRD results shown in **Figure S6.5b** (Supplementary Information [46]) also prove that B enters interstitially as the unit cell linearly expands with increasing B content (up to 0.4 *at*.%). Note that for a B content above 0.4 *at*.% the doping reaches its limitation (indicated by the yellow area). The corresponding DSC curves and *M-T* curves at 0.01 and 1 T are presented in **Figure S6.6** and **S6.7** (Supplementary Information [46]). An extra Mn$_2$B impurity phase (space group: *I4/mcm*) appeared with a concentration of about 3.3(7) *wt*.% for the *x*= 0.8 sample, as shown in **Figure S6.8** (Supplementary Information [46]). From the Mn-B binary phase diagram [62] we know Mn$_2$B is very stable between 600-1120 °C (the annealing temperature is 900 °C). The created impurity phase has a significant influence for the system. For instance, in **Figure S6.7b** (Supplementary Information [46]) an obvious decrease in magnetization and transition temperature has been observed for the *x*= 0.8 sample as the Mn atoms are mainly responsible for the magnetic moments for NiMn-based magnetic Heusler alloys. The interstitially doped B increases the Mn-Mn distance, which is found to control the size of the magnetic moments [63, 64]. B doping will further improve the strong FM ordering based on Mn-Co-Mn configuration ("Co activation effect"). Interestingly, this B improvement of the magnetic moment is also observed computationally. DFT calculations indicate that the magnetic moment increases from 4.62 μ_B/f.u. in the undoped system to 4.75 μ_B/f.u. in the B doped system (1.6 *at*.% B).

To further investigate the underlying mechanisms of interstitial B doping on the local electronic environment, the electron localization function (ELF) has been calculated, providing a visualization of the valence electron pair repulsion theory. ELF values for the slice along the (110) direction for the undoped and the B doped NiCoMnTi alloys, are displayed in **Figure 6.5b** and **6.5c**, respectively. It is observed that more localized electrons

are concentrated in the surrounding of the B located at the *O*-I interstitial site. To quantitatively study the variation in bonding character between covalent and metallic bonding, line profiles of ELF values between nearest-neighbor atom pairs are illustrated in **Figure 6.5d** and **6.5e**. Note that a higher ELF value means more electron localization. Compared to the undoped system, the most prominent features for the maximum ELF values of the doped system are: an 33.3% increment of Mn-Mn (from 0.12 to 0.16) and an 21.4% increment of Mn-Ni (from 0.14 to 0.17), which suggest a stronger covalent-like bonding between the Mn-Mn and Mn-Ni atoms. In contrast to NiMn-*X* (*X* = Al, Ga, In, Sn) based Heusler alloys stabilized by *p-d* covalent hybridization, the all-*d*-metal NiCoMnTi-based alloys are essentially associated with *d-d* covalent hybridization [15]. Consequently, after B doping the coordination electronic environment of Mn-Mn and Mn-Ni will be affected.
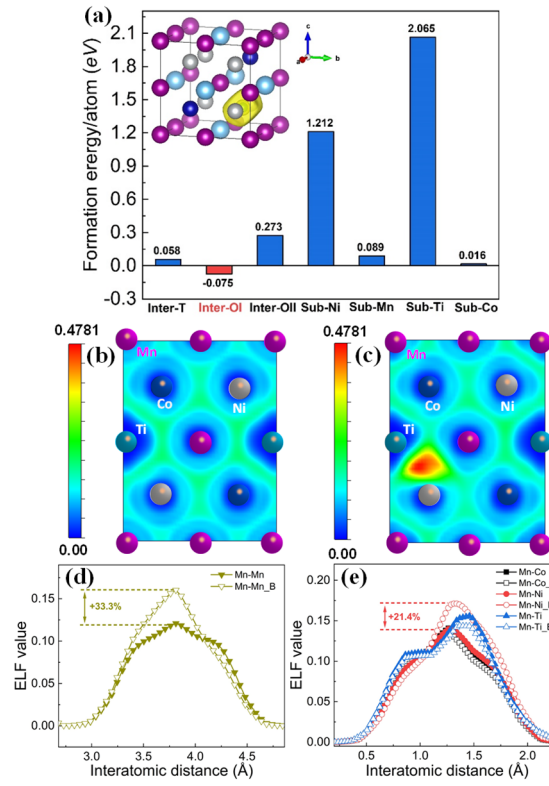
Figure 6.5 (a) Formation energy E_f for different site-occupation models for B-doped NiCoMnTi materials. Calculated ELF contour maps sliced along the (110) direction for (b) no dopant and (c) B doped NiCoMnTi-based alloys. (d)

Line profiles of the ELF values between Mn and its nearest Mn atom. (e) Line profiles of the ELF values between Mn and its nearest Co/Ni/Ti neighbors.

6.4 Conclusions

In summary, interstitial B doping has successfully been applied for all-*d*-metal $Ni_{36.5}Co_{13.5}Mn_{35}Ti_{15}B_x$ (x = 0, 0.2, 0.4, 0.6 and 0.8) magnetic Heusler alloys. It is demonstrated that doping with the light element B provides an efficient method to positively influence the magnetocaloric properties of the system. B doping significantly reduces the thermal hysteresis ΔT_{hys}, which could be ascribed to the good geometric compatibility between martensite and austenite. B doping also significantly improves ΔS_m by strengthening the FOMT. The low value for ΔT_{hys} obtained by B doping directly causes an excellent reversibility performances for the $Ni_{36.5}Co_{13.5}Mn_{35}Ti_{15}B_{0.4}$ alloy with a maximum ΔS_m^{rev} that can reach 18.9 $Jkg^{-1}K^{-1}$ (283 K) and 22.0 $Jkg^{-1}K^{-1}$ (281 K) for a field change $\Delta\mu_0 H$ of 5 and 7 T, respectively. This in combination with the favourable mechanical properties makes it a competitive candidate compared with traditional NiMn-*X* based Heusler alloys (*X* = Ga, In, Sn, Sb). The experimentally observed enhanced magnetic moments are in line with DFT calculations. Combining XRD and first-principles calculations, the site preference for doping of B atoms has been identified as the *O*-I octahedral interstitial site. Furthermore, ELF calculations illustrate the changes in electron localization before and after B doping. Our studies pave the way for further optimization of the GMCE, and provide insights in this all-*d*-metal NiCoMnTi magnetic Heusler alloy system.

References

[1] X. Moya, N.D. Mathur, Caloric materials for cooling and heating, *Science* 370 (2020) 797-803.

[2] H. Johra, K. Filonenko, P. Heiselberg, C. Veje, S. Dall'Olio, K. Engelbrecht, C. Bahl, Integration of a magnetocaloric heat pump in an energy flexible residential building, *Renew Energ* 136 (2019) 115-126.

[3] D. Dzekan, A. Waske, K. Nielsch, S. Fahler, Efficient and affordable thermomagnetic materials for harvesting low grade waste heat, *Apl Mater* 9(1) (2021) 011105.

[4] M.E. Gruner, W. Keune, B. Roldan Cuenya, C. Weis, J. Landers, S.I. Makarov, D. Klar, M.Y. Hu, E.E. Alp, J. Zhao, M. Krautz, O. Gutfleisch, H. Wende, Element-resolved thermodynamics of magnetocaloric $LaFe_{13-x}Si_x$, *Phys Rev Lett* 114(5) (2015) 057202.

[5] O. Tegus, E. Brück, K.H.J. Buschow, F.R. de Boer, Transition-metal-based magnetic refrigerants for room-temperature applications, *Nature* 415 (2002) 150-152.

[6] F.X. Hu, B.G. Shen, J.R. Sun, Z.H. Cheng, G.H. Rao, X.X. Zhang, Influence of negative lattice expansion and metamagnetic transition on magnetic entropy change in the compound $LaFe_{11.4}Si_{1.6}$, *Appl Phys Lett* 78 (2001) 3675-3677.

[7] E. Stern-Taulats, A. Planes, P. Lloveras, M. Barrio, J.L. Tamarit, S. Pramanick, S. Majumdar, C. Frontera, L. Mañosa, Barocaloric and magnetocaloric effects in $Fe_{49}Rh_{51}$, *Phys Rev B* 89 (2014) 1-8.

[8] F. Guillou, A.K. Pathak, D. Paudyal, Y. Mudryk, F. Wilhelm, A. Rogalev, V.K. Pecharsky, Non-hysteretic first-order phase transition with large latent heat and giant low-field magnetocaloric effect, *Nat Commun* 9 (2018) 2925.

[9] V.K. Pecharsky, K.A. Gschneidner, Giant magnetocaloric effect in $Gd_5(Si_2Ge_2)$, *Phys Rev Lett* 78 (1997) 4494-4497.

[10] A. Planes, L. Mañosa, M. Acet, Magnetocaloric effect and its relation to shape-memory properties in ferromagnetic Heusler alloys, *J Phys-Condens Mat* 21 (2009) 233201.

[11] E.K. Liu, W.H. Wang, L. Feng, W. Zhu, G.J. Li, J.L. Chen, H.W. Zhang, G.H. Wu, C.B. Jiang, H.B. Xu, F.R. de Boer, Stable magnetostructural coupling with tunable magnetoresponsive effects in hexagonal ferromagnets, *Nat Commun* 3 (2012) 1-10.

[12] J. Liu, Y.Y. Gong, Y.R. You, X.M. You, B.W. Huang, X.F. Miao, G.Z. Xu, F. Xu, E. Brück, Giant reversible magnetocaloric effect in MnNiGe-based materials: Minimizing thermal hysteresis via crystallographic compatibility modulation, *Acta Mater* 174 (2019) 450-458.

[13] S. Pandey, A. Quetz, A. Aryal, I. Dubenko, D. Mazumdar, S. Stadler, N. Ali, Large inverse magnetocaloric effects and giant magnetoresistance in Ni-Mn-Cr-Sn Heusler alloys, *Magnetochemistry* 3 (2017) 1-7.

[14] J. Sharma, K.G. Suresh, Observation of giant exchange bias in bulk $Mn_{50}Ni_{42}Sn_8$ Heusler alloy, *Appl Phys Lett* 106 (2015) 072405.

[15] Z.Y. Wei, E.K. Liu, J.H. Chen, Y. Li, G.D. Liu, H.Z. Luo, X.K. Xi, H.W. Zhang, W.H. Wang, G.H. Wu, Realization of multifunctional shape-memory ferromagnets in all-*d*-metal Heusler phases, *Appl Phys Lett* 107 (2015) 022406.

[16] V.G. de Paula, M.S. Reis, All-*d*-metal full Heusler alloys: A novel class of functional materials, *Chem Mater* 33 (2021) 5483-5495.

[17] Z.N. Ni, X.M. Guo, X.T. Liu, Y.Y. Jiao, F.B. Meng, H.Z. Luo, Understanding the magnetic structural transition in all-*d*-metal Heusler alloy $Mn_2Ni_{1.25}Co_{0.25}Ti_{0.5}$, *J Alloy Compd* 775 (2019) 427-434.

[18] Z.Q. Guan, J. Bai, J.L. Gu, X.Z. Liang, D. Liu, X.J. Jiang, R.K. Huang, Y.D. Zhang, L.D. Esling, X. Zhao, L. Zuo, First-principles investigation of *B2* partial disordered structure, martensitic transformation, elastic and magnetic properties of all-*d*-metal Ni-Mn-Ti Heusler alloys, *J Mater Sci Technol* 68 (2021) 103-111.

[19] H.N. Bez, A.K. Pathak, A. Biswas, N. Zarkevich, V. Balema, Y. Mudryk, D.D. Johnson, V.K. Pecharsky, Giant enhancement of the magnetocaloric response in Ni-Co-Mn-Ti by rapid solidification, *Acta Mater* 173 (2019) 225-230.

[20] A. Taubel, B. Beckmann, L. Pfeuffer, N. Fortunato, F. Scheibel, S. Ener, T. Gottschall, K.P. Skokov, H.R. Zhang, O. Gutfleisch, Tailoring magnetocaloric effect in all-*d*-metal Ni-Co-Mn-Ti Heusler alloys: a combined experimental and theoretical study, *Acta Mater* 201 (2020) 425-434.

[21] T. Gottschall, E. Bykov, A. Gracia-Condal, B. Beckmann, A. Taubel, L. Pfeuffer, O. Gutfleisch, L.I. Mañosa, A. Planes, Y. Skourski, J. Wosnitza, Advanced characterization of multicaloric materials in pulsed magnetic fields, *J Appl Phys* 127 (2020) 185107.

[22] Y. Li, L. Qin, S.Y. Huang, L.W. Li, Enhanced magnetocaloric performances and tunable martensitic transformation in $Ni_{35}Co_{15}Mn_{35-x}Fe_xTi_{15}$ all-*d*-metal Heusler alloys by chemical and physical pressures, *Sci China Mater* (2021).

[23] Z.Q. Guan, X.J. Jiang, J.L. Gu, J. Bai, X.Z. Liang, H.L. Yan, Y.D. Zhang, L.D. Esling, X. Zhao, L. Zuo, Large magnetocaloric effect and excellent mechanical properties near room temperature in Ni-Co-Mn-Ti non-textured polycrystalline alloys, *Appl Phys Lett* 119 (2021) 051904

[24] F. Guillou, G. Porcari, H. Yibole, N. van Dijk, E. Brück, Taming the first-order transition in giant magnetocaloric materials, *Adv Mater* 26 (2014) 2671-2675.

[25] N.V. Thang, X.F. Miao, N.H. van Dijk, E. Brück, Structural and magnetocaloric properties of $(Mn,Fe)_2(P,Si)$ materials with added nitrogen, *J Alloy Compd* 670 (2016) 123-127.

[26] H.Z. Luo, F.B. Meng, Q.X. Jiang, H.Y. Liu, E.K. Liu, G.H. Wu, Y.X. Wang, Effect of boron on the martensitic transformation and magnetic properties of $Ni_{50}Mn_{36.5}Sb_{13.5-x}B_x$ alloys, *Scripta Mater* 63 (2010) 569-572.

[27] Y. Zhang, J. Liu, Q. Zheng, J. Zhang, W.X. Xia, J. Du, A.R. Yan, Large magnetic entropy change and enhanced mechanical properties of Ni-Mn-Sn-C alloys, *Scripta Mater* 75 (2014) 26-29.

[28] S. Pandey, A. Quetz, I.D. Rodionov, A. Aryal, M.I. Blinov, I.S. Titov, V.N. Prudnikov, A.B. Granovsky, I. Dubenko, S. Stadler, N. Ali, Magnetic, transport, and magnetocaloric properties of boron doped Ni-Mn-In alloys, *J Appl Phys* 117 (2015) 183905.

[29] S. Kavita, V.V. Ramakrishna, P. Yadav, S. Kethavath, N.P. Lalla, T. Thomas, P. Bhatt, R. Gopalan, Enhancement of martensite transition temperature and inverse magnetocaloric effect in $Ni_{43}Mn_{47}Sn_{11}$ alloy with B doping, *J Alloy Compd* 795 (2019) 519-527.

[30] G. Porcari, F. Cugini, S. Fabbrici, C. Pernechele, F. Albertini, M. Buzzi, M. Mangia, M. Solzi, Convergence of direct and indirect methods in the magnetocaloric study of first order transformations: The case of Ni-Co-Mn-Ga Heusler alloys, *Phys Rev B* 86 (2012) 104432.

[31] G. Porcari, M. Buzzi, F. Cugini, R. Pellicelli, C. Pernechele, L. Caron, E. Brück, M. Solzi, Direct magnetocaloric characterization and simulation of thermomagnetic cycles, *Rev Sci Instrum* 84 (2013) 073907.

[32] H.M. Rietveld, A profile refinement method for nuclear and magnetic structures, *J Appl Crystallogr* 2 (1969) 65-71.

[33] L. Caron, Z.Q. Ou, T.T. Nguyen, D.T.C. Thanh, O. Tegus, E. Brück, On the determination of the magnetic entropy change in materials with first-order transitions, *J Magn Magn Mater* 321 (2009) 3559-3566.

[34] G. Kresse, J. Hafner, Ab initio molecular dynamics for liquid metals, *Phys Rev B* 47 (1993) 558-561.

[35] G. Kresse, J. Furthmuller, Efficiency of ab-initio total energy calculations for metals and semiconductors using a plane-wave basis set, *Comp Mater Sci* 6 (1996) 15-50.

[36] P.E. Blochl, Projector augmented-wave method, *Phys Rev B* 50 (1994) 17953-17979.

[37] G. Kresse, D. Joubert, From ultrasoft pseudopotentials to the projector augmented-wave method, *Phys Rev B* 59 (1999) 1758-1775.

[38] J.P. Perdew, K. Burke, M. Ernzerhof, Generalized gradient approximation made simple, *Phys Rev Lett* 77 (1996) 3865-3868.

[39] M. Methfessel, A.T. Paxton, High-precision sampling for Brillouin-Zone integration in metals, *Phys Rev B* 40 (1989) 3616-3621.

[40] B. Silvi, A. Savin, Classification of chemical-bonds based on topological analysis of electron localization functions, *Nature* 371 (1994) 683-686.

[41] B.D. Ingale, Y.K. Kuo, S. Ram, Phase transformation, microstructure and magnetocaloric properties in polycrystalline bulk $Ni_{50}Mn_{50-z}Sn_z$ alloys, *IEEE T Magn* 47 (2011) 3395-3398.

[42] J. Liu, X.M. You, B.W. Huang, I. Batashev, M. Maschek, Y.Y. Gong, X.F. Miao, F. Xu, N. van Dijk, E. Brück, Reversible low-field magnetocaloric effect in Ni-Mn-In-based Heusler alloys, *Phys Rev Mater* 3 (2019) 084409.

[43] A.A. Mendonca, L. Ghivelder, P.L. Bernardo, H.L. Gu, R.D. James, L.F. Cohen, A.M. Gomes, Experimentally correlating thermal hysteresis and phase compatility in multifunctional Hensler alloys, *Phys Rev Mater* 4 (2020) 114403

[44] J. Cui, Y.S. Chu, O.O. Famodu, Y. Furuya, J. Hattrick-Simpers, R.D. James, A. Ludwig, S. Thienhaus, M. Wuttig, Z.Y. Zhang, I. Takeuchi, Combinatorial search of thermoelastic

shape-memory alloys with extremely small hysteresis width, *Nat Mater* 5 (2006) 286-290.

[45] Y.T. Song, X. Chen, V. Dabade, T.W. Shield, R.D. James, Enhanced reversibility and unusual microstructure of a phase-transforming material, *Nature* 502 (2013) 85-88.

[46] See Supplemental Material at [http://link.aps.org/supplemental/10.1103/PhysRevApplied.17.054032]. Figure S6.1 shows the refined powder XRD patterns for the $x = 0.0$ (204 K) and $x = 0.4$ (room temperature) alloys with a two-phase coexistence of the modulated monoclinic martensite and cubic austenite. Figure S6.2 presents (a) *M-H* curves of the austenite phase at different temperatures for the $x = 0.4$ alloy. The *M-H* curve at 300 K is chosen as the benchmark for the pure austenite state when the "TF_MB" method is applied. (b-d) *M-H* curves in magnetic fields up to 5 T for different cycles and corresponding austenite fractions. Figure S6.3 shows the calorimetric ΔS_m and ΔT_{ad} estimation. Figure S6.4 shows the ΔS_m and ΔT_{ad} changes as a function of B content. Figure S6.5 presents powder XRD patterns of high-temperature pure austenite and lattice parameters. Figure S6.6 and S6.7 show DSC and *M-T* curves for different B-doped samples, respectively. Figure S6.8 shows refined powder XRD patterns of pure austenite for (a) $x = 0.4$ (393 K) and (b) $x = 0.8$ (room temperature) alloys. Table S6.1 and S6.2 show lattice parameters of martensite and austenite, respectively.

[47] M. Khan, J. Jung, S.S. Stoyko, A. Mar, A. Quetz, T. Samanta, I. Dubenko, N. Ali, S. Stadler, K.H. Chow, The role of Ni-Mn hybridization on the martensitic phase transitions in Mn-rich Heusler alloys, *Appl Phys Lett* 100 (2012) 172403.

[48] Z.Y. Wei, E.K. Liu, Y. Li, X.L. Han, Z.W. Du, H.Z. Luo, G.D. Liu, X.K. Xi, H.W. Zhang, W.H. Wang, G.H. Wu, Magnetostructural martensitic transformations with large volume changes and magneto-strains in all-*d*-metal Heusler alloys, *Appl Phys Lett* 109 (2016) 071904

[49] Y.H. Qu, D.Y. Cong, X.M. Sun, Z.H. Nie, W.Y. Gui, R.G. Li, Y. Ren, Y.D. Wang, Giant and reversible room-temperature magnetocaloric effect in Ti-doped Ni-Co-Mn-Sn magnetic shape memory alloys, *Acta Mater* 134 (2017) 236-248.

[50] T. Gottschall, K.P. Skokov, B. Frincu, O. Gutfleisch, Large reversible magnetocaloric effect in Ni-Mn-In-Co, *Appl Phys Lett* 106 (2015) 021901

[51] K. Xu, Z. Li, Y.L. Zhang, C. Jing, An indirect approach based on Clausius-Clapeyron equation to determine entropy change for the first-order magnetocaloric materials, *Phys Lett A* 379 (2015) 3149-3154.

[52] B. Kaeswurm, V. Franco, K.P. Skokov, O. Gutfleisch, Assessment of the magnetocaloric effect in La,Pr(Fe,Si) under cycling, *J Magn Magn Mater* 406 (2016) 259-265.

[53] M. Fries, L. Pfeuffer, E. Bruder, T. Gottschall, S. Ener, L.V.S. Diop, T. Grob, K.P. Skokov, O. Gutfleisch, Microstructural and magnetic properties of Mn-Fe-P-Si (Fe_2P-type) magnetocaloric compounds, *Acta Mater* 132 (2017) 222-229.

[54] L. Huang, D.Y. Cong, L. Ma, Z.H. Nie, Z.L. Wang, H.L. Suo, Y. Ren, Y.D. Wang, Large reversible magnetocaloric effect in a Ni-Co-Mn-In magnetic shape memory alloy, *Appl Phys Lett* 108 (2016) 1-5.

[55] Y.H. Qu, D.Y. Cong, Z. Chen, W.Y. Gui, X.M. Sun, S.H. Li, L. Ma, Y.D. Wang, Large and reversible inverse magnetocaloric effect in $Ni_{48.1}Co_{2.9}Mn_{35.0}In_{14.0}$ metamagnetic shape memory microwire, *Appl Phys Lett* 111 (2017) 1-5.

[56] Y.H. Qu, D.Y. Cong, S.H. Li, W.Y. Gui, Z.H. Nie, M.H. Zhang, Y. Ren, Y.D. Wang, Simultaneously achieved large reversible elastocaloric and magnetocaloric effects and their coupling in a magnetic shape memory alloy, *Acta Mater* 151 (2018) 41-55.

[57] Z.B. Li, J.J. Yang, D. Li, Z.Z. Li, B. Yang, H.L. Yan, C.F. Sanchez-Valdes, J.L.S. Llamazares, Y.D. Zhang, C. Esling, X. Zhao, L. Zuo, Tuning the reversible magnetocaloric effect in Ni-Mn-In-based alloys through Co and Cu Co-doping, *Adv Electron Mater* 5 (2019) 1800845.

[58] D.Y. Cong, W.X. Xiong, A. Planes, Y. Ren, L. Mañosa, P.Y. Cao, Z.H. Nie, X.M. Sun, Z. Yang, X.F. Hong, Y.D. Wang, Colossal elastocaloric effect in ferroelastic Ni-Mn-Ti alloys, *Phys Rev Lett* 122 (2019) 255703.

[59] A. Aznar, A. Gràcia-Condal, A. Planes, P. Lloveras, M. Barrio, J.L. Tamarit, W.X. Xiong, D.Y. Cong, C. Popescu, L. Mañosa, Giant barocaloric effect in all-*d*-metal Heusler shape memory alloys, *Phys Rev Mater* 3 (2019) 044406.

[60] X.F. Miao, S.Y. Hu, F. Xu, E. Brück, Overview of magnetoelastic coupling in $(Mn,Fe)_2(P,Si)$-type magnetocaloric materials, *Rare Metals* 37 (2018) 723-733.

[61] H.L. Yan, H.X. Liu, Y. Zhao, N. Jia, J. Bai, B. Yang, Z.B. Li, Y.D. Zhang, C. Esling, X. Zhao, L. Zuo, Impact of B alloying on ductility and phase transition in the Ni-Mn-based magnetic shape memory alloys: Insights from first-principles calculation, *J Mater Sci Technol* 74 (2021) 27-34.

141

[62] P.K. Liao, K.E. Spear, The B−Mn (Boron-Manganese) system, Bulletin of Alloy Phase Diagrams 7 (1986) 543-549.

[63] E.C. Passamani, F. Xavier, E. Favre-Nicolin, C. Larica, A.Y. Takeuchi, I.L. Castro, J.R. Proveti, Magnetic properties of NiMn-based Heusler alloys influenced by Fe atoms replacing Mn, *J Appl Phys* 105 (2009) 033919.

[64] X. Wang, M.M. Li, J. Li, J.J. Deng, Y. Wang, L. Ma, D.W. Zhao, C.M. Zhen, D.L. Hou, E.K. Liu, W.H. Wang, G.H. Wu, Design of Mn-Mn distance for tunable spontaneous exchange bias in Heusler alloys, *Intermetallics* 132 (2021) 107170.

Supplementary Information for Chapter 6
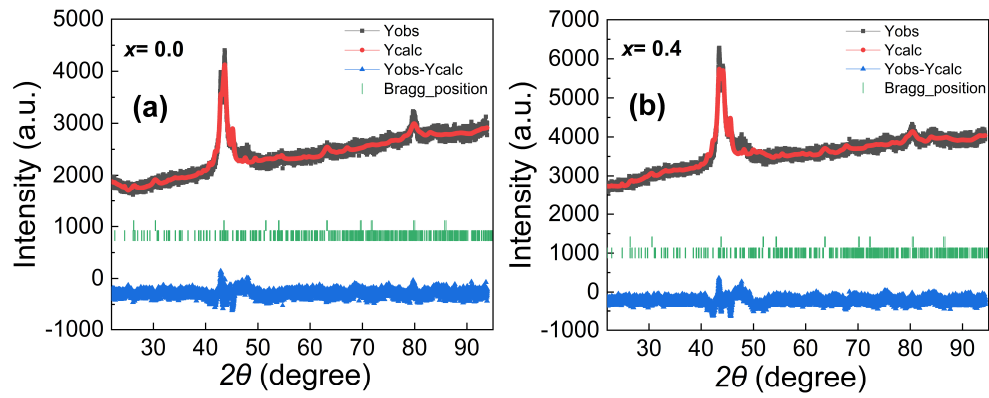
Figure S6.1 (a-b) Refined powder XRD patterns indicating a two-phase coexistence of the modulated monoclicnic martensite and cubic austenite for the *x*= 0.0 (204 K) and *x*= 0.4 (room temperature) alloys.

Table S6.1 The lattice parameters of modulated martensite from XRD refinement for the *x* = 0.0 and *x* = 0.4 alloys

Sample	*a* (Å)	*b* (Å)	*c* (Å)	*α*	*β*	*γ*	Chi2
x = 0.0	4.2383(10)	5.5800(6)	12.6811(6)	90°	93.95(1)°	90°	1.87
x = 0.4	4.1862(4)	5.5300(2)	12.5333(1)	90°	93.59(1)°	90°	2.08
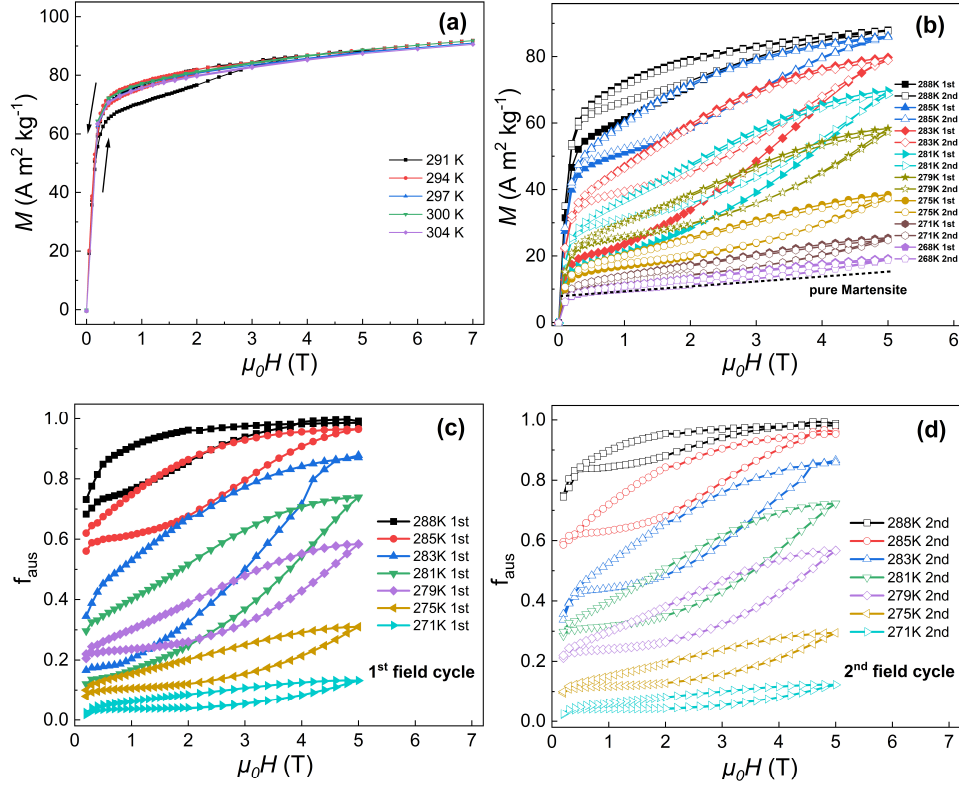
Figure S6.2 (a) Isothermal *M-H* curves of the austenite phase at different temperatures for the Ni$_{36.5}$Co$_{13.5}$Mn$_{35}$Ti$_{15}$B$_{0.4}$ alloy. The *M-H* curve at 300 K is chosen as the benchmark for the pure austenite state when the "TF_MB" method is applied. (b) Isothermal *M-H* curves in magnetic fields up to 5 T for the Ni$_{36.5}$Co$_{13.5}$Mn$_{35}$Ti$_{15}$B$_{0.4}$ alloy measured during the 1st (solid symbols) and 2nd (open symbols) cycle for increasing and decreasing magnetic field at different temperatures. The dotted lines denote the extrapolation of the magnetization for pure austenite and pure martensite (as indicated). The fraction of austenite f_{aus} for (c) the 1st field cycle and (d) 2nd field cycle at different constant temperatures determined from (b).
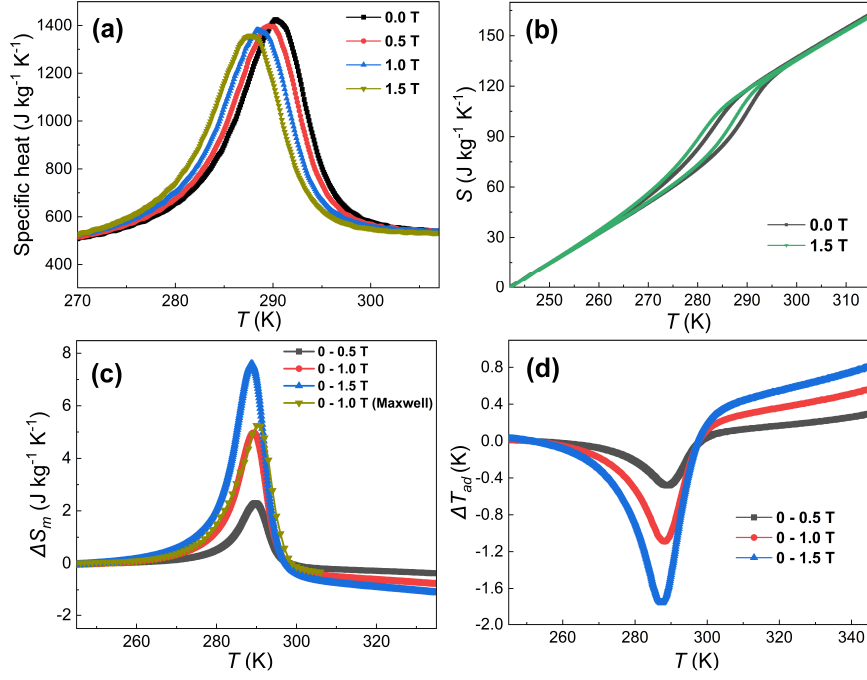
Figure S6.3 (a) Temperature dependence of specific heat from in-field DSC measurements in different applied fields for the $Ni_{36.5}Co_{13.5}Mn_{35}Ti_{15}B_{0.4}$ sample. (b) *S-T* curves obtained upon heating (solid symbols) and cooling (open symbols) in fields of $\mu_0H = 0$ T and $\mu_0H = 1.5$ T for $Ni_{36.5}Co_{13.5}Mn_{35}Ti_{15}B_{0.4}$ sample. (c) ΔS_m as a function of temperature for the $Ni_{36.5}Co_{13.5}Mn_{35}Ti_{15}B_{0.4}$ alloy extracted from in-field DSC measurements for different magnetic field changes. For comparison, the dashed olive curve presents the ΔS_m calculated by the Maxwell equation. (d) Temperature dependence of ΔT_{ad} in different applied field changes derived from in-field DSC measurements.
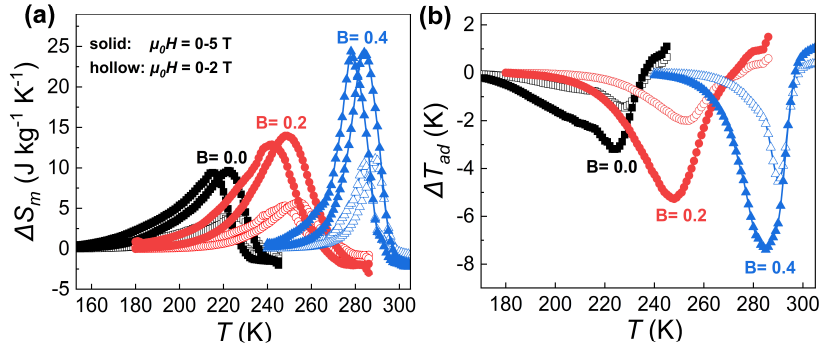
Figure S6.4 (a) ΔS_m values as a function of temperature for $Ni_{36.5}Co_{13.5}Mn_{35}Ti_{15}B_x$ (*x* = 0.0, 0.2, 0.4) alloys. (b) ΔT_{ad} values as a function of temperature for $Ni_{36.5}Co_{13.5}Mn_{35}Ti_{15}B_x$ (*x* = 0.0, 0.2, 0.4) alloys.
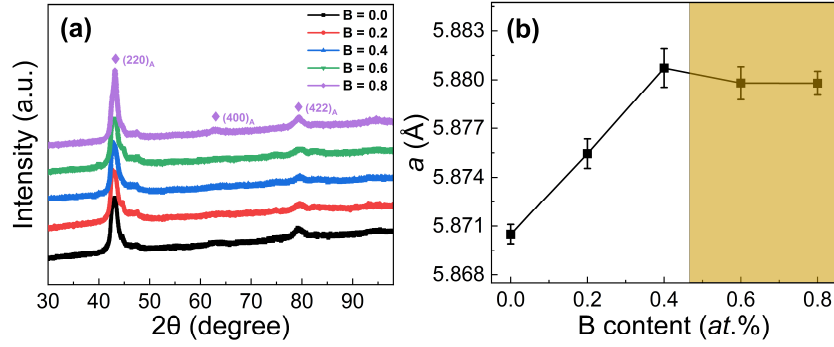
Figure S6.5 (a) Powder XRD patterns of high-temperature pure austenite for $Ni_{36.5}Co_{13.5}Mn_{35}Ti_{15}B_x$ (x = 0.0, 0.2, 0.4, 0.6, 0.8) alloys. (b) Derived lattice parameters as a function of B content for $Ni_{36.5}Co_{13.5}Mn_{35}Ti_{15}B_x$ (x = 0.0, 0.2, 0.4, 0.6, 0.8) alloys.

Table S6.2 The lattice parameters a of cubic austenite at 453 K from XRD refinement for the $Ni_{36.5}Co_{13.5}Mn_{35}Ti_{15}B_x$ (x = 0.0, 0.2, 0.4, 0.6, 0.8) alloys.

Sample	Lattice parameters a (Å)	Chi2
x = 0.0	5.8705(6)	2.65
x = 0.2	5.8755(9)	3.03
x = 0.4	5.8807(12)	3.14
x = 0.6	5.8798(10)	2.94
x = 0.8	5.8798(7)	2.89
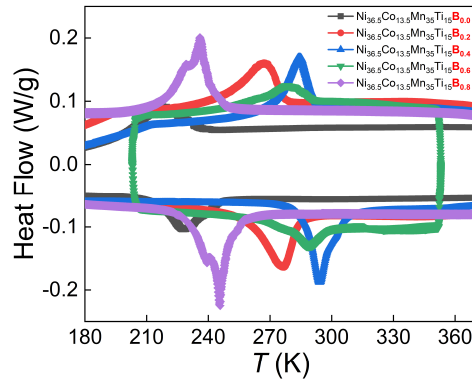
Figure S6.6 Temperature dependent DSC curves of $Ni_{36.5}Co_{13.5}Mn_{35}Ti_{15}B_x$ (x = 0.0, 0.2, 0.4, 0.6, 0.8) alloys for heating and cooling at a rate of 10 K/min.
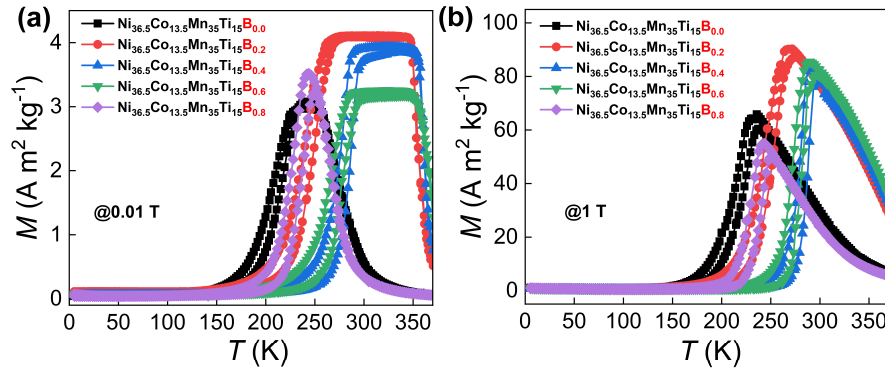
Figure S6.7 (a) *M-T* curves measured in 0.01 T for $Ni_{36.5}Co_{13.5}Mn_{35}Ti_{15}B_x$ (x = 0.0, 0.2, 0.4, 0.6, 0.8) alloys. (b) Corresponding *M-T* curves at 1 T for $Ni_{36.5}Co_{13.5}Mn_{35}Ti_{15}B_x$ (x = 0.0, 0.2, 0.4, 0.6, 0.8) alloys.
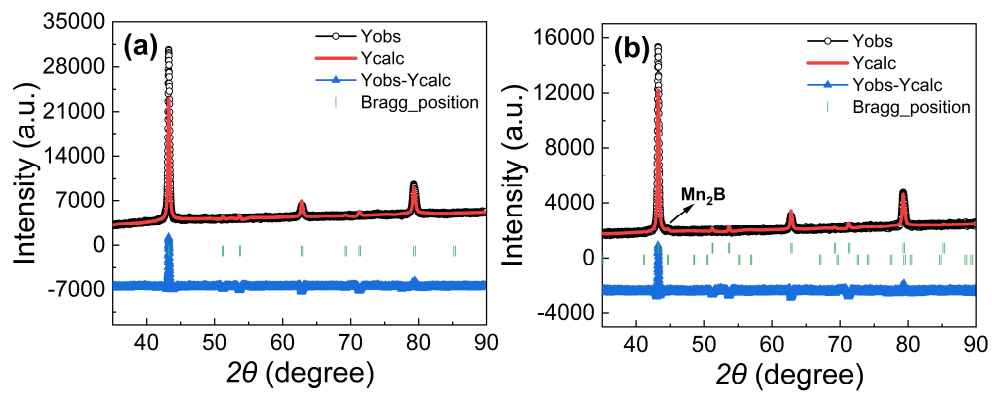
Figure S6.8 Refined powder XRD patterns of pure austenite for (a) x = 0.4 (393 K) and (b) x = 0.8 (room temperature) alloys.

Summary

Solid-state caloric effects as intrinsic responses from different physical external stimuli (magnetic-, uniaxial stress-, pressure- and electronic- fields) have been evaluated near magnetic phase transformations. In the last decades the magnetically driven caloric changes in various magnetocaloric materials (MCMs) have been exploited extensively for magnetic refrigeration and magnetic heat pumping scenarios near room temperature. This thesis systematically investigates the magnetocaloric effect (MCE) for the representative magnetoelastic $(Mn,Fe)_2(P,Si)$ system. Special emphasis has been directed towards the giant MCE in nanoscale particles and the influence of doping with elements that show a strong electronegativity on the magnetic properties of this metal-metalloid system. Meanwhile, two optimization strategies (decoupling and light element B doping) are successfully introduced to regulate the thermal hysteresis ΔT_{hys}, the ferromagnetic phase transition T_C and improve the reversibility of the MCE for magnetostructural transition in the all-d-metal NiCoMnTi Heusler alloys.

The relationship between the magnetoelastic coupling and size effects is still pivotal for $(Mn,Fe)_2(P,Si)$ materials. In **Chapter 3** the change in crystallite size is found to be responsible for changes in T_C, ΔT_{hys} and the magnetization. Post-annealing within the temperature range 300 -600 ^{o}C combined with gaseous nitriding can result in a significant recovery of the lost magnetization. Such material demonstrates competitive MCE characteristics among nano MCMs reported in the literature. This behavior can be attributed to the synergetic effect of post-annealing and nitration, which effectively removes the edge dislocations inside the particles and introduces interstitial nitrogen. Interestingly, a core (crystalline) - shell (amorphous) type nanostructure, as well as superparamagnetic (SPP) nanoparticles, have directly been observed for the first time in $(Mn,Fe)_2(P,Si)$ based nano MCMs. These studies provide essential insight in $(Mn,Fe)_2(P,Si)$ based nano MCMs and open the possibility to further expand its potential for future applications in the field of microrefrigerators, ferrofluids, nanocomposites, heterogeneous catalysis and magnetic hyperthermia.

Doping with the light elements F and S, that show a strong electronegativity, has successfully been demonstrated in **Chapter 4**. For these two dopant systems T_C can be moved efficiently over a wide range of temperatures. Specifically, it is found that F doping enhances the magnetocaloric effect at the FOMT (by an increase in magnetic moments and an increase in the magnetic entropy change $|\Delta S_m|$), while for S doping the formation of impurities slowly weaken the first-order magnetic transition (FOMT). For F doping the increased ΔT_{hys} could be ascribed to the enhanced transition-induced elastic strain energy at the interface of the ferromagnetic (FM) and paramagnetic (PM) phases. The site

occupancy has been resolved by performing neutron diffraction (ND) experiments, indicating that F and S are substituted on the $1b$ and $2c$ sites, respectively. This site preference has also been confirmed by DFT calculations. The unexpected tunable MCE properties with F/S doping are analyzed in terms of the experimental atomic distances among different metal-metal or metal-metalloids atom pairs. Together with theoretical electron-localization function (ELF) calculations, these results clarify the subtle changes in atomic distance and in the strength of the covalent bonding. Together they determine the change in GMCE with doping in these magnetoelastic $(Mn,Fe)_2(P,Si)$-based materials. These findings provide important insight into the effect of doping with light elements (B, C, N, F and S) on the GMCE properties of $(Mn,Fe)_2(P,Si)$ based MCMs.

To avoid the large ΔT_{hys} that generally accompanies a first-order magnetostructural phase transformation, a decoupling of the magnetic and structural transition has been studied in all-d-metal NiCoMnTi based magnetic Heusler alloys with a second-order magnetic transition (SOMT). In **Chapter 5** it is found that the Mn/Ti ratio can control the FOMT/SOMT nature of the transition. The values of T_C and M_S can be regulated by adjusting either the Ni/Co ratio or doping with non-magnetic Cu. The alloys with a high Co content show good soft magnetic properties with a reversible ferromagnetic transition and a moderate MCE. However, the relatively low ΔS_m values prove that SOMT NiCoMnTi based materials may not be suitable for potential MCE applications in e.g. a magnetic heat pump. Compositional maps for T_C and M_S have been established. We refined the crystallite size and found the limited volume fraction of the Ti-rich secondary phase by microstructural measurements. Our systematic survey in combination with DFT calculations reveals that the total magnetic moment can solely be controlled by the Co content. These results provide new insight in the SOMT for these all-d-metal Ni(Co)MnTi based Heusler alloys.

Tailoring ΔT_{hys} and holding excellent GMCE performance can simultaneously be achieved by optimizing the geometric compatibility between martensite and austenite for the FOMT magnetostructural coupling MCMs. Interstitial B doping has successfully been applied for all-d-metal $Ni_{36.5}Co_{13.5}Mn_{35}Ti_{15}B_x$ (x = 0, 0.2, 0.4, 0.6 and 0.8) magnetic Heusler alloys. As shown in **Chapter 6** the light element B presents a positive influence on the magnetocaloric properties of the system. For example, they can help to significantly reduce the ΔT_{hys}, which results from the good geometric compatibility between martensite and austenite. They can also further improve ΔS_m by strengthening the FOMT. The low value for ΔT_{hys} obtained by B doping directly causes an excellent reversibility performance for the $Ni_{36.5}Co_{13.5}Mn_{35}Ti_{15}B_{0.4}$ alloy with a maximum ΔS_m^{rev} that can reach 18.9 $Jkg^{-1}K^{-1}$ (283 K) and 22.0 $Jkg^{-1}K^{-1}$ (281 K) for a field change $\Delta\mu_0H$ of 5 and 7 T, respectively. This in combination with the favorable mechanical properties makes it a competitive candidate compared with traditional NiMn-X

based Heusler alloys (X = Ga, In, Sn, Sb). The experimentally observed enhanced magnetic moments are in line with DFT calculations. Combining XRD and first-principles calculations, the site preference for doping of B atoms has been identified as the O-I octahedral interstitial site, which could affect the magnetic interactions among different magnetic atoms. Furthermore, ELF calculations illustrate the changes in electron localization before and after B doping. This study paves the way for further optimization of the GMCE, and provides insights in this FOMT all-d-metal NiCoMnTi magnetic Heusler alloy system.

Samenvatting

Calorische effecten kunnen zich in vaste stoffen manifesteren als intrinsieke gevolgen van verschillende externe fysische stimuli (magnetische velden, uniaxiale druk, hydrostatische druk en elektrische velden) en zijn bestudeerd in de buurt van magnetische faseovergangen. In de laatste decennia zijn magnetisch gedreven calorische veranderingen in magnetocalorische materialen (MCMs) intensief onderzocht voor toepassingen op het terrein van magnetisch koelen en magnetisch warmtepompen in het temperatuurgebied rond kamertemperatuur. Dit proefschrift geeft een systematisch onderzoek van het magnetocalorische effect (MCE) in het representatieve magneto-elastische (Mn,Fe)$_2$(P,Si) systeem. Speciale aandacht is gericht op het reusachtige MCE (GMCE) in nanoschaal deeltjes en de invloed van substituties met elementen die een sterke elektro-negativiteit vertonen, welke een groot effect op de magnetische eigenschappen van dit metallische systeem. Twee optimalisatie-strategieën zijn succesvol geïntroduceerd (ontkoppelen en doping met het lichte element B) om de thermische hysterese ΔT_{hys} te reguleren, de ferromagnetische faseovergang T_C in te stellen en de reversibiliteit van het MCE voor magneto-structurele overgangen enkel-d-metaal NiCoMnTi Heusler legeringen te verbeteren.

De relatie tussen de magnetoelastische koppeling en effecten van afmetingen is doorslaggevend voor het gedrag van (Mn,Fe)$_2$(P,Si) materialen. In **Hoofdstuk 3** is gevonden dat een verandering in kristalgrootte direct leidt tot veranderingen in T_C, ΔT_{hys} en de magnetisatie. Een gloeibehandeling achteraf in het temperatuurgebied van 300 tot 600 ºC in combinatie met gas-nitratie geeft aanleiding tot een significant herstel van de magnetisatie die verloren is gegaan bij het reduceren van de kristalgrootte en vertoont daarmee MCE karakteristieken die concurreren met eerder gerapporteerde nano MCMs. Dit gedrag kan worden toegeschreven aan het synergetische effect van een gloeibehandeling achteraf en nitratie, wat effectief leidt tot het verwijderen van een deel van de defecten binnen de deeltjes. Het is interessant dat zowel een kern (kristallijn) - schil (amorf) type nanostructuur als de aanwezigheid van super-paramagnetische nano-deeltjes (SPP), voor het eerst is waargenomen in op (Mn,Fe)$_2$(P,Si) gebaseerde nano MCMs. Deze studies geven een essentieel inzicht in het gedrag van (Mn,Fe)$_2$(P,Si) gebaseerde nano MCMs en maken nieuwe toepassingen mogelijk op het gebied van micro-koelers, ferro-vloeistoffen, nano-composieten, heterogene katalyse en magnetische hyperthermie.

Elektronen beïnvloeden in belangrijke mate de magneto-elastische faseovergang van de karakteristieke itinerante (Mn,Fe)$_2$(P,Si) gebaseerde MCMs. Doping met de lichte elementen F en S die een sterke elektro-negativiteit vertonen is succesvol aangetoond in

Hoofdstuk 4. Voor deze twee doping-systemen kan T_C voldoende worden verschoven om kamertemperatuur te bereiken. Er is gevonden F doping tot een versterking van het magnetocalorische effect ter plaatse van de eerste-orde magnetische faseovergang (FOMT) leidt (door een toename van de magnetische momenten en een toename van de magnetische entropie-verandering $|\Delta S_m|$), terwijl voor S doping de geïntroduceerde onzuiverheden tot een langzame verzwakking van de FOMT leiden. Voor F doping kan de toename in de thermische hysterese in de magnetische overgang ΔT_{hys} worden toegeschreven aan een versterking van de door de faseovergang geïnduceerde elastische energie op het grensvlak tussen de ferromagnetische (FM) en de paramagnetische (PM) fasen. Met behulp van neutronen diffractie (ND) experimenten is de atomaire bezetting van kristalposities bepaald, welke aangeeft dat F en S doping tot stand komt door substitutie op respectievelijk de *1b* en de *2c* kristalpositie. De voorkeur voor deze specifieke kristalposities is bevestigd met behulp van DFT berekeningen. De regelbare MCE eigenschappen die kunnen worden aangepast met F/S doping zijn geanalyseerd in termen van de experimentele atoomafstanden tussen verschillende metaal-metaal of metaal-metalloïde atoomparen. Samen met de theoretische elektron-lokalisatie functie (ELF) berekeningen, kunnen deze resultaten de subtiele veranderingen in de atoomafstanden en in de sterkte van de covalente binding verduidelijken. Samen zijn ze bepalend voor de verandering in het GMCE ten gevolge van de doping in deze magneto-elastische $(Mn,Fe)_2(P,Si)$ gebaseerde materialen. Deze resultaten geven belangrijk inzicht in de rol die doping van lichte elementen (B, C, N, F en S) heeft op de GMCE eigenschappen van $(Mn,Fe)_2(P,Si)$ gebaseerde MCMs.

Om de grote ΔT_{hys}, die over het algemeen samen gaat het een eerste-orde magneto-structurele faseovergang, te voorkomen is er voor gekozen om de magnetische en structurele overgang te ontkoppelen in volledig-*d*-metaal NiCoMnTi gebaseerde magnetische Heusler legeringen met een tweede-orde magnetische overgang (SOMT). In **Hoofdstuk 5** is gevonden dat de Mn/Ti ratio bepalend is voor het FOMT/SOMT karakter van de overgang. De waarden van T_C en M_S kunnen worden ingesteld door aanpassing van de Ni/Co ratio of door doping met niet-magnetisch Cu. De legeringen met een grote hoeveelheid Co geven geode zacht magnetische eigenschappen met een reversibele ferromagnetische overgang en een gematigde MCE. Echter, de relatief geringe waarden van ΔS_m tonen aan dat de SOMT NiCoMnTi gebaseerde materialen mogelijk niet geschikt zijn voor potentiele toepassingen in b.v. een magnetische warmtepomp. Op basis van de metingen zijn kaarten van T_C en M_S als functie van de samenstelling geconstrueerd. Metingen van de microstructuur laten een gereduceerde kristalgrootte en een beperkte fasefractie zien voor de Ti-rijke secondaire fase. In combinatie met DFT berekeningen is

gevonden dat het totale magnetische moment enkel bepaald wordt door de hoeveelheid Co. Deze resultaten geven nieuw inzicht in de SOMT van deze volledig-d-metaal Ni(Co)MnTi gebaseerde Heusler legeringen.

Het afregelen van ΔT_{hys} en tegelijkertijd behouden van een uitstekende GMCE performance kan worden bereikt door het optimaliseren van de geometrische passing aan het grensvlak van de martensiet en austeniet fasen voor de FOMT van MCMs met een magneto-structurele koppeling. B doping op interstitiële atoom-posities is succesvol toegepast voor de volledig-d-metaal $Ni_{36.5}Co_{13.5}Mn_{35}Ti_{15}B_x$ (x = 0, 0.2, 0.4, 0.6 en 0.8) magnetische Heusler legeringen. Zoals weergegeven in **Hoofdstuk 6** hebben lichte element B atomen een positieve invloed op de magnetocalorische eigenschappen op het systeem. Bijvoorbeeld kunnen ze helpen om ΔT_{hys} te verlagen, wat het resultaat is van de goede geometrische passing tussen martensiet en austeniet. Ze kunnen ook ΔS_m verbeteren door de FOMT te versterken. De lage waarde van ΔT_{hys} verkregen door B doping veroorzaakt direct een excellente reversibele performance voor de $Ni_{36.5}Co_{13.5}Mn_{35}Ti_{15}B_{0.4}$ legering met een maximum ΔS_m^{rev} die waarden van respectievelijk 18.9 $Jkg^{-1}K^{-1}$ (283 K) en 22.0 $Jkg^{-1}K^{-1}$ (281 K) kunnen bereiken voor een veldverandering $\Delta\mu_0H$ van 5 en 7 T. Dit in combinatie met de gunstige mechanische eigenschappen maken dit materiaal vergelijkbaar met traditionele NiMn-X gebaseerde Heusler legeringen (X = Ga, In, Sn, Sb). De experimenteel waargenomen verhoogde magnetische momenten zijn in overeenstemming met die van DFT berekeningen. Door XRD en *first-principles* berekeningen is de voorkeurspositie voor het dopen van B atomen bepaald als de O-I octahedrische interstitiële positie, welke bepalend is voor de magnetische interacties tussen de verschillende magnetische atomen. Verder illustreren ELF berekeningen de veranderingen in elektron-lokalisatie voor en na B doping. Deze studie maakt het mogelijk om het GMCE verder te optimaliseren en geeft inzicht in de FOMT van deze volledig-d-metaal NiCoMnTi magnetische Heusler legeringen.

Acknowledgements

"The tassel is worth the hassel"

Time flies, and there are no enough preparations for the graduation before I touch this part. Four years ago one youngster full of enthusiasm started his adventure in this land, and took along motivations to find his own "Mr. Science". During this wonderful journey, like "strain-stress curve" I also experience "accumulating- struggling- necking" procedures and luckily after undergoing severe training and hammering I did not enter "fracture". And it is my pleasure to complete one of the great milestone of my life so far. Let me take this opportunity to express my sincere gratitude to all of people lending a helping hand for me, and memorize my Dutch time.

First and foremost, I would like deliver my deepest appreciation to my daily supervisor Prof. Dr. Ekkes Brück who originally decide to give me the opportunity to pursue my PhD degree in FAME group. When time backed to 9th December 2017 I still remembered you arranged a warm welcome meeting with me, and introduced me a lot about MCE in West-lake (XiHu) Hotel in SCUT on a sunny Saturday morning. Your friendly and kind attitudes deeply impressed me a lot, and therefore a smooth decision was made to join your group without any consideration. Since I arrived at Delft thanks for your kind consideration of my life and "don't forget to buy two locks for your bicycle" was my first impression of the Netherlands. Most importantly, I really appreciate your strict academic training for me and fruitful discussions with me in the past four years. And I also keep in mind two crucial personalities for successful researchers: intelligence and hard-working, which you told me during our meeting with Enschede in 14th February 2019 (what a special day!). Meanwhile, your excellent organization and coordination abilities as a section leader make me admire, which will be a good mirror for me. The master initiates the apprentices but the cultivation depends on the individual. Thank you give me enough freedom to regulate my academic processes. For Ekkes, not only a great pioneer in GMCE field, emphatically but also a highly respectable man.

How my acknowledgement can continue without my another daily supervisor Dr. Niels van Dijk? I sincerely appreciate your guidance about my subjects during PhD career, and luckily I obtained enough trainings from you about solid-state physics which are what I want. However, at the first six months I feared to discuss with you because of the so-called "Amsterdam defense jury story". With increasing in mutual collaboration, I found some similar characteristics between you and me. Your ice-breaking stories about science, culture, history, family and even self-growth make you like an encyclopaedia and make conversation

vivacious. Your active mind always enlightened me on the deep thinking of one scientific question rather than drifting on the surface, and your abundant research experiences also expand my own interested research topics. I believe these multi-disciplined knowledge will be useful for me to find my own "academic blue sea" in the future. One of most enjoyable thing for me is polishing novel ideas and pushing progresses with you, and the brainstorming makes me think freely. And thanks to your encouragement I can attend the different international academic competitions in different scientific topics and further extend my academic networks. Specifically, I appreciate you introduce big science to me and let me enjoy the mysterious fascination of it. Two unique precious working experiences with you in Grenoble and Dresden will be definitely beneficial for my independence. As my supervisor I respect your endless patience to students and flexible strategies for complex matters. As my colleague you are a kind of England-type gentleman, and your passion and enthusiasm will encourage me continue to scale new heights. Sincerely, thank you Niels.

I also would like to thank the people who I closely collaborated during these four years. Dr. Jun Liu, who worked with me in FAME for almost 9 months, is a kind and friendly enough young researcher. Your personality of keeping thinking motivates me to efficiently catch knowledge, and a lot of constructive discussions between us at my starting stage were helpful and made me cast off the struggling. And special thanks to Dr. Xuefei Miao. An occasional chance during DDMC-2019 made us know each other and the well-built connections contribute to sequential projects. I must show my respects to your strong ambition, enthusiasm, tolerance and perseverance. Your advisement for my career is meaningful and hope I will follow the right track. Dr. Ivan Batashev is a quick-learner and share the same working office with me. Needless to say, thanks to your experienced theoretical calculation skills we can push forwards our works together to higher quality journals. Your easy-going personality further deepens our friendship and I am enjoyable for some off-site topics like games/videos/Russian history. Dr. Luana Caron, who is a great and strong mother as well as an outstanding scientist, always shows your unselfish assistance to my projects. Although we only met several times because of the pandemic, your arrangement of measurements is always in time. I appreciate your careful comments and suggestions for the manuscript, and the same appreciation for your student Chris Taake. Furthermore, I am grateful for the two students I supervised—Kevin Westra (master) and Sebas Smits (bachelor). Thanks both of you for your careful attitudes for science and significant contributions of solid data for MCE community. Also, extended sincere thanks to Dr. Ron I. Smith, Prof. Maxim Avdeev, Dr. Diadkin Vadim and Dr. Dmitry Chernyshov for sharing beam-time with us, and sufficient discussions improved my knowledge about neutron and synchrotron X-rays. For Dr. Tino Gottschall, thank you for the meticulous care,

Fengqi Zhang,

Delft. May. 2022

List of Publications

Publications related to the PhD study

1. **Fengqi Zhang*,** Ivan Batashev, Qi Shen, Ziying Wu, Ronald I. Smith, Gilles A. de Wijs, Niels van Dijk, Ekkes Brück, Impact of F and S doping on $(Mn,Fe)_2(P,Si)$ giant magnetocaloric materials, *Acta Materialia,* 234 (**2022**) 118057.

2. **Fengqi Zhang*,** Ivan Batashev, Niels van Dijk, Ekkes Brück, Reduced hysteresis and enhanced giant magnetocaloric effect in B-doped all-*d*-metal Ni-Co-Mn-Ti based Heusler materials, *Physical Review Applied*, 17 (**2022**) 054032.

3. **Fengqi Zhang*,** Kevin Westra, Qi Shen, Ivan Batashev, Anika Kiecana, Niels van Dijk, Ekkes Brück, The second-order magnetic phase transition and magnetocaloric effect in all-*d*-metal NiCoMnTi-based Heusler alloys, *Journal of Alloys and Compounds,* 906 (**2022**) 164337.

4. **Fengqi Zhang*,** Chris Taake, Bowei Huang, Xinmin You, Hamutu Ojiyed, Qi Shen, Iulian Dugulan, Luana Caron, Niels van Dijk, Ekkes Brück, Magnetocaloric effect in the $(Mn,Fe)_2(P,Si)$ system: From bulk to nano, *Acta Materialia*, 224 (**2022**) 117532.

5. Anika Kiecana, Ivan Batashev, Iulian Dugulan, Cees Kwakernaak, Levi Pieter, **Fengqi Zhang**, Niels van Dijk, Ekkes Brück, Effect of Co and Ni doping on the structure, magnetic and magnetocaloric properties of Fe-rich $(Mn,Fe)_2(P,Si)$ compounds, *Journal of Magnetism and Magnetic Materials*, 561 (**2022**) 169710.

6. Qi Shen, Ivan Batashev, Hamutu Ojiyed, **Fengqi Zhang**, Niels van Dijk, Ekkes Brück, Nonlinear influence of excess Mn on the magnetoelastic transition in $(Mn,Cr)_2Sb$, *Journal of Alloys and Compounds,* 903 (**2022**) 164011.

7. Xuefei Miao, Yong Gong, **Fengqi Zhang**, Yurong You, Luana Caron, Fengjiao Qian, Wenhui Guo, Yujing Zhang, Yuanyuan Gong, Feng Xu, Niels van Dijk, Ekkes Brück, Enhanced reversibility of the magnetoelastic transition in $(Mn,Fe)_2(P,Si)$ alloys via minimizing the transition-induced elastic strain energy, *Journal of Materials Science & Technology,* 103 (**2022**) 165–176.

8. Jun Liu, Yuanyuan Gong, **Fengqi Zhang**, Yurong You, Guizhou Xu, Xuefei Miao, Feng Xu, Large, low-field and reversible magnetostrictive effect in MnCoSi-based metamagnet at room temperature, *Journal of Materials Science & Technology,* 76 (**2021**) 104–110.

9. Qi Shen, Ivan Batashev, **Fengqi Zhang**, Hamutu Ojiyed, Niels van Dijk, Ekkes Brück, The antiferromagnetic to ferrimagnetic phase transition in $Mn_2Sb_{1-x}Bi_x$ compounds, *Journal of Alloys and Compounds,* 866 (**2021**) 158963.

10. Jun Liu, Yurong You, Ivan Batashev, Yuanyuan Gong, Xinmin You, Bowei Huang, **Fengqi Zhang**, Xuefei Miao, Feng Xu, Niels van Dijk, Ekkes Brück, Design of reversible low-field magnetocaloric effect at room temperature in hexagonal Mn*MX* ferromagnets, *Physical Review Applied*, 13 (**2020**) 054003.

……………….

Publications related to the Master study

11. Lin Huang, **Fengqi Zhang**, Wenming Sun, Xiongwu Kang, Nitrene-functionalized ruthenium nanoparticles: Spectral evidence for the conjugated ruthenium-nitrene π bonds and the impact on the catalytic activity, *Journal of Colloid and Interface Science,* 588 (**2021**) 761–766.

12. **Fengqi Zhang**, Jingjing Fang, Lin Huang, Wenming Sun, Zhang Lin, Zhenqing Shi, Xiongwu Kang, Shaowei Chen, Alkyne-functionalized ruthenium nanoparticles: Impact of metal–ligand interfacial bonding interactions on the selective hydrogenation of styrene, *ACS Catalysis,* 9 (**2019**) 98–104.

13. Jigang Wang[#], **Fengqi Zhang**[#], Xiongwu Kang, Shaowei Chen, Organic functionalization of metal catalysts: Enhanced activity towards electroreduction of carbon dioxide, *Current Opinion in Electrochemistry,* 13 (**2019**) 40–46. ([#] co-first author)

14. Yi Peng[#], Bingzhang Lu[#], Feng Wu, **Fengqi Zhang**, Jia En Lu, Xiongwu Kang, Yuan Ping, Shaowei Chen, Point of anchor: Impacts on interfacial charge transfer of metal oxide nanoparticles, *Journal of the American Chemical Society,* 140 (**2018**) 15290–15299. ([#] co-first author)

15. Peiguang Hu, Yinghui Ren, Limei Chen, **Fengqi Zhang**, Yi Peng, Hsiau-Wei Lee, Shaowei Chen, Ruthenium nanoparticles cofunctionalized with acetylene derivatives of coumarin and perylene: Dyad-like intraparticle charge transfer, *Journal of Nanoparticle Research,* 20 (**2018**) 184.

16. **Fengqi Zhang**, Lin Huang, Jiasui Zou, Jun Yang, Xiongwu Kang, Shaowei Chen, Isonitrile-functionalized ruthenium nanoparticles: Intraparticle charge delocalization through Ru=C=N interfacial bonds, *Journal of Nanoparticle Research,* 19 (**2017**) 308.

17. Kanghua Miao, Yun Luo, Jiasui Zou, Jun Yang, **Fengqi Zhang**, Lin Huang, Jie Huang, Xiongwu Kang, Shaowei Chen, PdRu alloy nanoparticles of solid solution in atomic scale: Outperformance towards formic acid electro-oxidation in acidic medium, *Electrochimica Acta,* 251 (**2017**) 588–594.

18. **Fengqi Zhang**, Lin Huang, Jiasui Zou, Jinwu Yan, Jiaying Zhu, Xiongwu Kang, Shaowei Chen, Nitrile-functionalized ruthenium nanoparticles: Charge delocalization through Ru−N≡C interface, *Journal of Nanoparticle Research,* 19 (**2017**) 106.

Conference presentations

1. Poster presentation: **Fengqi. Zhang**, Niels. van Dijk, Ekkes. Brück, *et al.*, "Magnetocaloric effect in the $(Mn,Fe)_2(P,Si)$ system: From bulk to nano", Delft Days on Magneto Calorics (DDMC), the Netherlands, 2019.

2. Oral presentation: **Fengqi. Zhang**, Niels. van Dijk, Ekkes. Brück, *et al.*, "Magnetocaloric effect in the $(Mn,Fe)_2(P,Si)$ system: From bulk to nano", The 64th Annual Conference on Magnetism and Magnetic Materials (MMM), USA, 2019.

3. Poster presentation: **Fengqi. Zhang**, Niels. van Dijk, Ekkes. Brück, *et al.*, "Magnetocaloric effect in the $(Mn,Fe)_2(P,Si)$ system: From bulk to nano", Physics@Veldhoven, the Netherlands, 2021.

4. Poster presentation: **Fengqi. Zhang**, Niels. van Dijk, Ekkes. Brück, *et al.*, "Investigation on the size effect and defects effect on the microstructural and magnetic properties of nanoscale $(Mn,Fe)_2(P,Si)$ based MCE material", Eurotherm: Heating and cooling, the Netherlands, 2021.

5. Oral presentation: **Fengqi. Zhang**, Niels. van Dijk, Ekkes. Brück, *et al.*, "Giant magnetocaloric effect in the $(Mn,Fe)_2(P,Si)$ system: From bulk to nano", Joint MMM-INTERMAG, USA, 2022.

6. Oral presentation: **Fengqi. Zhang**, Niels. van Dijk, Ekkes. Brück, *et al.*, "Impact of F and S doping on $(Mn,Fe)_2(P,Si)$ giant magnetocaloric materials", The Joint European Magnetic Symposia (JEMS), Poland, 2022.

7. Poster presentation: **Fengqi. Zhang**, Niels. van Dijk, Ekkes. Brück, *et al.*, "Reduced hysteresis and enhanced giant magnetocaloric effect in B-doped all-*d*-metal Ni-Co-Mn-Ti based Heusler materials", International Conference on Strongly Correlated Electron Systems (SCES), the Netherlands, 2022.

8. Oral presentation: **Fengqi. Zhang**, Niels. van Dijk, Ekkes. Brück, *et al.*, "Impact of F and S doping on (Mn,Fe)$_2$(P,Si) giant magnetocaloric materials", The 67th Annual Conference on Magnetism and Magnetic Materials (MMM), USA, 2022.

Curriculum Vitae

Fengqi Zhang was born on 13 March 1992 in Yantai city, a beautiful coastal city in north China. He started his research and got his Master degree majored in Environmental Engineering in July 2018 at South China University of Technology (SCUT) under the supervision of Prof. Xiongwu Kang (SCUT) and Prof. Shaowei Chen (University of California, Santa Cruz). During his Master period, his research interests mainly focus on surface functionalization of noble metal nanoparticles (e.g. Ru, Pd, Pt, Au and Ag) and its photoelectric properties at the interface (delocalization systems), and utilize these nanoparticles for potential heterogeneous catalysis (e.g. styrene hydrogenation). After that, at the same year, he successfully competed the scholarship from China Scholarship Council (CSC) and continued to pursue his PhD degree on "novel giant magnetocaloric materials for magnetic refrigeration" in the group of Fundamental Aspects of Materials and Energy (FAME) at the Delft University of Technology, co-supervised by Dr. Niels van Dijk and Prof. Dr. Ekkes Brück. "Spur with long accumulation" is his favourite motto.